Development of Novel Scintillation Detection Techniques for Use in Nuclear Physics and Medical Applications

Nuray Yavuzkanat

Doctor of Philosophy

University of York
Physics

September 2015

Abstract

This thesis describes the practical application of scintillation detector techniques and focuses on how to enhance their potential for use in the new concept spectroscopy method called HELIOS, combination of the magnetic resonance image (MRI) and positron emission tomography (PET) called PET-MRI system, and other medical applications.

Optically coupled $LaBr_3(Ce)$ with Hamamatsu avalanche photomultiplier first tested inside a (nearly) 1T magnetic field, resulting in the field does not have an adverse impact on the performance of the detector. A magnetic resonance image was also successfully obtained when a scintillation detector system interfaced with a homogeneous magnetic field inside the brain phantom, but detector current influenced on the MR image. In Chapter 2, there are the further investigations into various scintillation detector systems such as Phoswich-PMT, CsI and LYSO coupled with SensL position sensitive SiPM.

SensL new-generation blue sensitive B and C series SiPMs have an innovative silicon photomultiplier structure resulting in an additional readout signal for fast timing application. SensL SiPMs with the large photosensitive area studied regarding their characteristics and coincidence time measurement. According to the measurement result, the dependencies of bias voltage, temperature, gain and dark current were consistent with the literature. Coincidence time resolution was gradually improved from 512 ps to 276 ps for 6 mm C-SiPM by changing set-up and adding transformer in the circuit.

A novel antimatter detector system developed for medical applications. GEANT4 based GATE 7.0 simulation was used for optimum scintillator thickness investigation to measure the activity directly from positrons rather than gamma radiation without any interference between scintillator and radiopharmacy. Various detector designs successfully tested for microfluidic chip and blood counter applications (measured volume from $94\mu\ell$ to $0.11\mu\ell$). The half-life of ^{68}Ga was experimentally calculated to be 62.11 ± 8 minutes resulting in agreement with the literature if they overlap within their uncertainties. The new detector is cost-effective, based on very simple working principle, user-friendly, easy to modify into another system, and achievable nanoscale volume. Therefore, the objective of this research is to aid significantly in deciding a final design for the detector system before serial manufacturing and before applying for the patent.

Contents

List of Figures

List of Tables

Acknowledgements

First, I would like to thank my supervisor, Professor David Jenkins, for his help, advice, and suggestions; he has supported me unconditionally throughout this thesis. I credit my PhD work to his considerable encouragement and great advice. Without his guidance, this thesis would not exist.

I would also like to thank Pankaj Joshi for his assistance in the first few years of my PhD studies, especially during experiments in the lab. I must also thank Nara Singh for helping me to complete the process and giving useful feedback as well as his great advice for timing measurements.

I am also very grateful for the help received from various people with expertise in several different disciplines. Access to such people is the direct result of the close community of the nuclear physics groups in York. I have been very productive with these inspiring people. Paul Davies and Edward Martin always offered me all the support and encouragement with writing code in C++. I must also mention how grateful I am to the Department of Physics and its supporting technicians for providing equipment and technical advice. Especially, I would like to thank John and Dave for their concerted effort and technical advice, which led to the development of antimatter detector systems. I must relay my greatest thanks to the individuals involved with the University of Hull PET Research Centre for providing radioisotopes to complete my experimental measurements, for help with the patent application, and for their joint collaboration between York and Hull. In particularly, I would like to thank Professor Steve J Archibald and fellow collaborators, Mark and Nasr, both of whom assisted me in the experiment in Hull.

Finally, I thank my parents for supporting me throughout my studies at university. I remain grateful to the Turkish embassy for giving me the incredible opportunity to receive my PhD abroad. I must also convey thanks to my friends for encouraging me when I was stressed, annoyed, and deterred during my PhD research. Thank you for your endless encouragement.

Declaration

This thesis has been submitted for the degree of Doctor of Philosophy in accordance with the regulations of the University of York. The work contained herein has not been previously submitted for any other degree or qualification. I declare that the work here is my own, and where other sources of information have been used, they are clearly marked and referenced.

The simulation and experimental work outlined in this thesis was performed solely by the author under the supervision of Professor D.G. Jenkins.

Chapter 1

Introduction

There is a trend to develop new scintillation crystals and photon counting devices, in order to construct a gamma-ray detector system that can work inside a solenoidal magnetic field. The successful integration of the functional imaging technique (positron emission tomography (PET)) into magnetic resonance imaging (MRI) has lead to a different approach to spectrometer technology, which has become an important part of research on nuclear physics. A large bore superconducting solenoidal spectrometer with a uniform axial field is now used in the investigation of the exotic nuclear structure and to achieve a deeper understanding of the stable nuclei by single nucleon transfer reactions, pair transfer, inelastic scattering, or even knockout-reactions.

This developing technique has strong synergies with current concepts in nuclear medicine. A PET-MRI detector system is used to obtain both functional and anatomical information within one medical image. Generating simultaneous PET and MRI images is helpful in obtaining accurate diagnostics and devising more efficient treatment for patients by improving in medical images. Scintillation detector systems (essentially PET detectors) also play a major role in the production of radiopharmacies and their quality controls in radioisotope centres. This chapter provides a concise overview of the key physical aspects of recently developed spectroscopy for studying critical subjects in nuclear physics and PET systems with novel detector technology of PET-MRI capability.

1.1 HELIOS (HELIcal Orbit Spectrometer)

HELIcal Orbit Spectrometer (HELIOS) was constructed at Argonne National Laboratory at ATLAS (Argonne Tandem Linac Accelerator System). This new concept spectroscopy is significantly important to the study of critical reactions with short-lived nuclei, particularly in the investigation of inverse kinematics reactions. The HELIOS spectroscopy provides a more detailed understanding of the structure of exotic nuclei with such phenomena as pair and single nucleon transfer reactions, inelastic scattering, and kick-out reactions. The superconducting solenoidal spectrometer has great advantages over more traditional measurement methods, including easier particle identification and availability for large solid angle and effective resolution improvement [1]. The basic component of this device is a bore diameter of a 60 cm solenoidal magnet (up to 5 Tesla), which is in fact a hospital MRI magnet. A simple configuration of the HELIOS spectroscopy is illustrated in Figure 1.1, complete with a target, silicon array detector, and recoil detector, which detects reaction products after bending inside a uniform magnetic field. Measured flight times, position and energy of detected particles are delivered to effective information regarding particle identification, excitation energy, and centre of mass angle. The HELIOS can be easily modified for existing accelerators with secondary beams, which will be very critical in research for future radioactive beam facilities.

1.1.1 Future Physics Cases for the HELIOS Spectroscopy

Nuclear structure research has recently focused on nuclei that are far away from the stability line. Around the world, over the past few decades research has resulted in improvements in a variety of methods for the production of beams, rare short-lived light exotic nuclei with satisfied intensity. The determination of nuclear properties in direct reactions is easier than in decay process and inverse kinematics reactions. The energy transfer and interaction time are very small in direct reactions compared to the incident beam energy.

When heavy nuclei beams are targeted to light nuclei, the reaction occurs in inverse kinematics. The velocity of the centre of mass system in the laboratory frame is higher than with conventional methods with light stable beams targeting

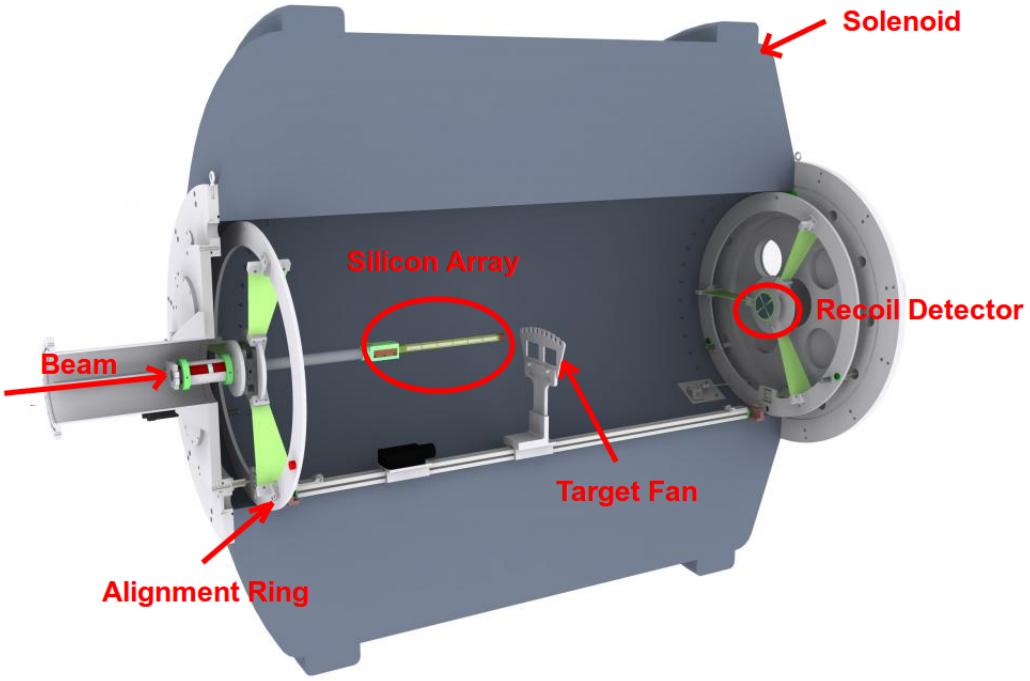

FIGURE 1.1: Configuration of the HELIOS spectrometer. Accelerated heavy-ion beams enter the spectrometer from the left side, and then bombard a light target in case of inverse kinematics reactions. The silicon array detector and rotating target fan are developed to detect particle and beam diagnostics respectively. The right side silicon detector array is present for recoil particle detection [2].

heavy stable nuclei, resulting in lower energies from emitted light ions at the relevant angles. Energy loss measurement in silicon detectors is used for identification of particles. In traditional method, front silicon detector thickness (ΔE) prefers to be thin compared to the stopping range of incoming particles, therefore only losing a fraction of their total energy. The rest of the incident particle energy is deposited by the other silicon detector which has enough thickness (E) to stop incident particles. The standard two layers silicon detector approach (ΔE - E) is problematic when the low energy light reaction product is identified in the critical angle range. In inverse kinematics, angular distribution of emitted particles with low energy is over a larger region of laboratory angles. This increases the detector array complexity and multi-segmentation. A large solid angle silicon array can also detect the backgrounds, scattering of beams, and large numbers of emitted particles from target and resulting undesirable measurement. Particle energy variations depend strongly on angle, so detector angular resolution is a critical parameter [3, 4]. The energy separation sensitivity between excited states (Q-value resolution) in the laboratory for inverse kinematics is very poor with traditional

spectroscopy method. HELIOS spectrometry addresses these issues while avoiding the drawbacks of standard methods (as will be discussed in the next sections) and as demonstrated in Figure 1.2 which aids in probing critical reactions.

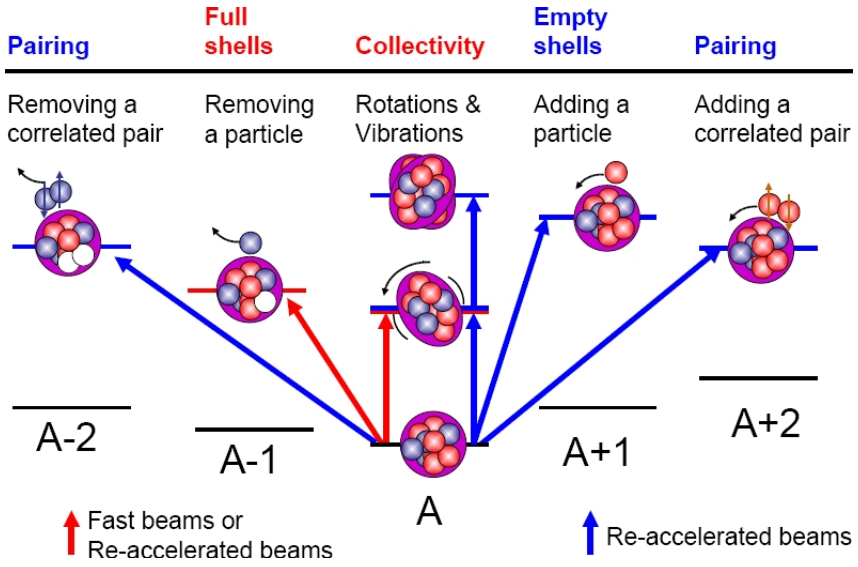

FIGURE 1.2: A new type of solenoidal spectroscopy yields an effective means to study unstable nuclei in inverse kinematics reactions with short-lived beams. Critical problems of such reactions hindering an understanding of nuclear structures are addressed through the novel concept of the HELIOS spectroscopy. The configuration of important reactions will be employed with solenoidal spectroscopy in future research projects [5].

1.1.1.1 Nucleon Transfer Reactions

A nucleon transfer reaction experiment involves the investigation of the single particle structure of nuclei, such as (d,p), (α,t) or (^{3}He,d) reactions, which are well-known reactions. Widespread improvements in accelerator facilities have both facilitated and altered the exploration of unstable nuclei with short-lived beams. Using the new solenoidal spectroscopy with novel accelerator facilities will improve the data quality in energy resolution and cleanliness, and require less beam time compared to the traditional approach. The identification of changing single particle structures on closed shell nuclei will be even clear with the HELIOS spectrometry, enhancing an understanding of the nuclear structure.

1.1.1.2 Pair Transfer Reactions

Pair transfer reactions, such as (p,t), (t,p) and (^{3}He,p) reactions, examine the nature and strength of pairing correlations for nuclei away from the stability line. The total isospin quantum number (T) is related to the strong interaction, which is independent of the particle electric charge (proton-neutron, proton-proton and neutron-neutron pairs are affected equally by the strong force). The HELIOS spectroscopy will be very useful in the study of T=0 pair transfer reactions in N=Z nuclei, particularly n-p pair transfers using (^{3}He,p) reactions in inverse kinematics [1].

This type of pairing is similar to the pairing between neutrons or protons coupling to T=1, strongly correlated 0^+ pairs, as well as electrons in BCS [1] superconductivity (boson-like behaviour of such electron pairs). The uncertainty may be higher for heavy N=Z nuclei in which both neutrons and protons fill the same orbits. Expected performance of solenoidal spectrometer was studied by Monte Carlo simulation for ^{3}He(^{56}Ni,p)^{58}Cu reaction, and then compared with result of the conventional silicon array detector. As shown in Figure 1.3, the centre of energy resolution was found to be 50 keV and 180 keV for silicon detectors in the HELIOS spectrometer and traditional silicon array, respectively. The HELIOS spectroscopy with better detector resolution provides an excellent opportunity to clarify excitation energy. The reaction Q-value is obtained from the measured proton energy and position which is detected particle distance, z, from the target. Different peaks in the spectra correspond to different excited states in ^{58}Cu. The separation of the proton energy between different groups of particles is equal to that between their excitation energies.

1.1.1.3 Inelastic Scattering

Inelastic scattering of protons or α particles is an alternate means of studying nuclear structure collectivity in cases when electromagnetic transition (Coulomb excitation) is not accessible. Detected recoil particles have low energy because

[1] The first microscopic theory of superconductivity describes as a microscopic effect caused by a condensation of Cooper pairs into a boson-like state. In nuclear physics, the theory describes the pairing interaction between nucleons in atomic nucleus.

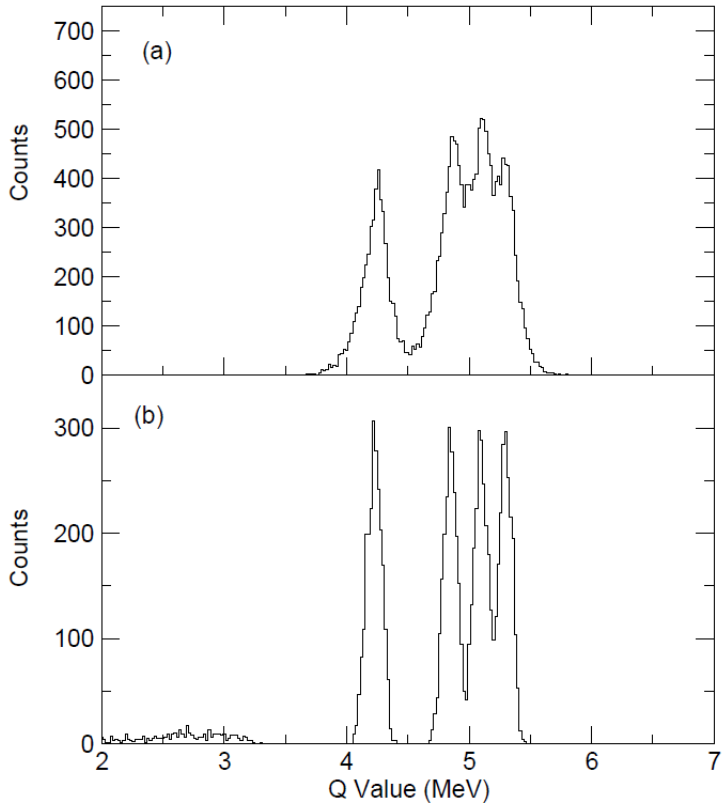

FIGURE 1.3: Expected representative Q-value spectra of ^{3}He(^{56}Ni,p)^{58}Cu reaction was obtained from : (a) detected proton energy of various states in ^{58}Cu from ^{3}He(^{56}Ni,p)^{58}Cu reaction with 2° resolution angle of traditional array detector measurement; (b) detected proton energy (or representative Q-values) and 1 mm position sensitivity of z in a magnetic field with the same detector energy resolution (assumed to be 50 keV energy resolution of the silicon detector in all simulation cases) [1].

momentum transfers are small during inelastic scattering. Particle scattering occurs forward of 90°, so detection with solenoid spectroscopy is an improvement over conventional methods.

1.1.1.4 Astrophysical Reactions

Astrophysical reactions can be probed by solenoid spectroscopic measurement to provide more information for the mapping of astrophysics processes such as s, r, and rp (rapid-proton capture) processes (Proposal for a solenoidal spectrometer to study reactions with short-lived beams, page 12 [1]). The HELIOS spectroscopy with its potential for superb Q-value resolution makes this concept a useful tool in the study of astrophysics processes.

1.1.1.5 Knockout Reactions

Knockout reactions are studied to gain additional information concerning single hole orbitals, such as proton knockout with (p,2p) reaction. Solenoid allows for the detection of protons over a large solid angle (4π) by two silicon array detectors placing before and after the target as explained in the next section, Operation Principle for The HELIOS spectrometer. However, the configuration must be modified to capture high energy protons by changing target and detector positions.

Studying these reactions with traditional approaches requires the construction of complex and large detector systems [4]. Improved Q-value energy resolution, large solid angle, easy particle identification, and reduced complexity in detector systems make the HELIOS spectroscopy a very attractive tool for upcoming research.

1.1.2 Operation Principle for the HELIOS Spectrometer

The charged particle spectroscopy is operated by a large-bore uniform magnetic field superconducting solenoid (from 2 to 5 Tesla). A heavy ion beam aligned with the magnetic axis passes through a hollow array of position-sensitive upstream Si detectors, before hitting the target as demonstrated in Figure 1.4. Almost all of

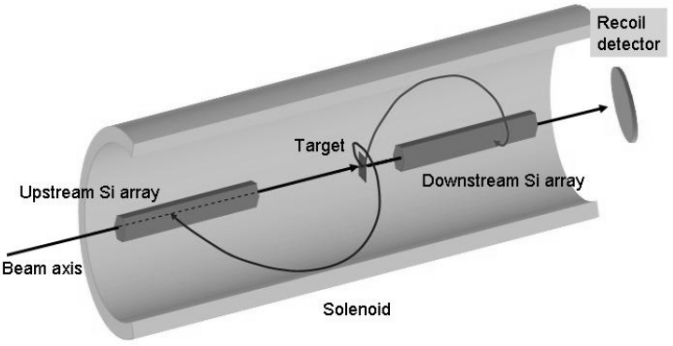

FIGURE 1.4: Scheme for the HELIOS solenoid charged particle spectrometer. The beam passes through the silicon detector before hitting the target. A hollow array of position-sensitive Si detectors is placed before and after the target to detect particles emitted either forward or backward. A heavy ions detector is fixed at the end of the solenoid to detect heavy recoiling ions [1].

the light ions emitted from the reaction either in a forward or backward direction

are detected by the position-sensitive upstream or downstream Si detectors after following helical trajectories in the magnetic field. The motion of charged particles depends on the strength of the uniform solenoidal field as given by Equation 1.1.

$$r = \frac{m\ V_{\perp}}{q\ e\ B} \tag{1.1}$$

The cyclotron period or one orbital rotation time is defined by Equation 1.2.

$$T_{cyc} = \frac{2\ \pi\ r}{V_{\perp}} = \frac{2\ \pi\ m}{B\ q\ e} \tag{1.2}$$

Where r is the radius of helical motion, m and $q.e$ are the mass and charged state of the particle, respectively, B is the strength of the magnetic field, and $V_{\perp}$ is the velocity of the particle perpendicular to the field line.

The time of flight of the detected particles is equal to the cyclotron period. In nanosecond time range, the cyclotron period is calculated by Equation 1.3, in which A/q denotes particle identification and A is the atomic mass number.

$$T_{cyc}(ns) = 65.5\ \mathrm{x}\ \frac{A}{q\ B} \tag{1.3}$$

In principle, the emitted particles that do not impact the inner wall of the solenoid chamber do not leave the magnetic field, but eventually go back to the solenoid axis after completing the helical motion. Returned particles are detected by two silicon array detectors, one before and one after the target, at close to a 4π solid angle [6]. As illustrated in Figure 1.5, the return distance can be defined as a vector diagram from the velocity of particles parallel to the field line ($V_{\parallel}$) with centre of mass velocity (V_{cm}), particle velocity (υ_0) and angles (θ_{cm} in the centre of mass frame and θ_{lab} in the laboratory frame) as detailed in Figure 1.6.

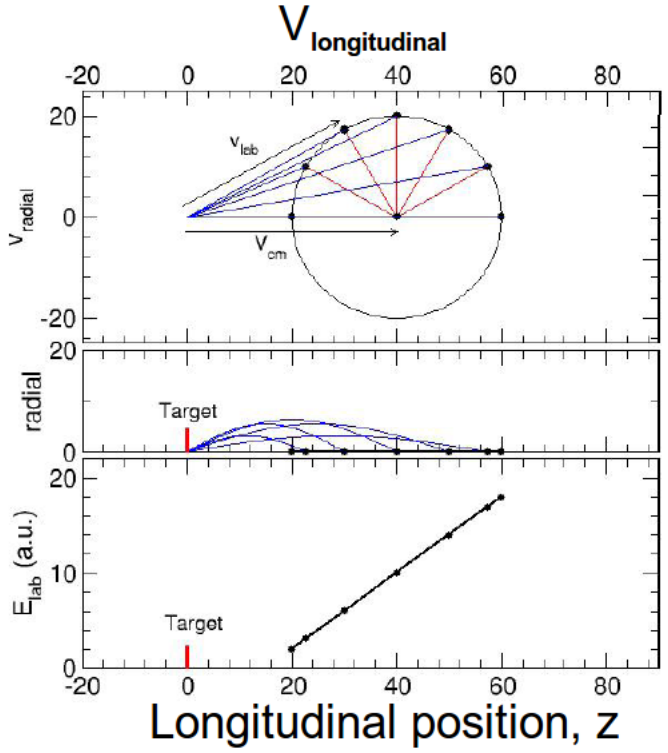

FIGURE 1.5: Plot is shown that target return position distance as a function of particle energy (atomic unit) in laboratory frame and radial. In the top graph, the velocity of particles parallel to the field line depends on centre of mass velocity (V_{cm}) and particle velocity (υ_0), as demonstrated on the vector diagram with angles (θ_{cm} and θ_{lab}) in Figure 1.6 [5].

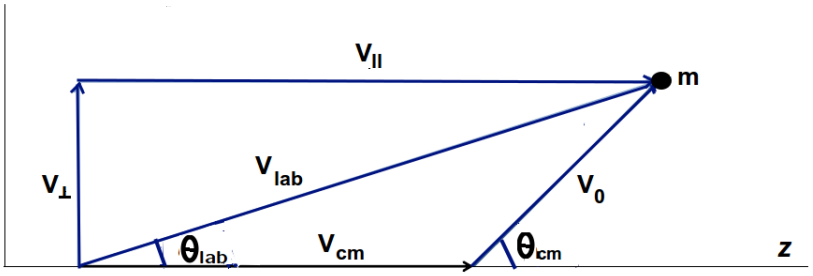

FIGURE 1.6: The vector diagram showing the velocities of the ejected m particle with $\vec{V_0}$ velocity. The velocity projections are illustrated with $V_{\parallel}$ and $V_{\perp}$. The velocity in the laboratory frame, V_{lab}, can be written by velocity in the centre-of-mass, V_{cm}, and the particle velocity ($\vec{V_{lab}} = \vec{V_{cm}} + \vec{V_0}$) [6].

Longitudinal position (z) is obtained from Equation 1.4.

$$z = T_{cyc} \;\; V_{\parallel} = T_{cyc} \;\; (V_{cm} + \upsilon_0 \; cos \; \theta_{cm}) \tag{1.4}$$

Another critical measured quantity is detected particle energy (E_{lab}), which is determined from the particle velocity as given by Equation 1.5:

$$E_{lab} = \frac{m}{2}\ (V_{\parallel}^2 + V_{\perp}^2) = \frac{m}{2}\ [(V_{cm} + \upsilon_0\ cos\ \theta_{cm})^2 + \upsilon_0^2\ sin^2\theta_{cm}] \tag{1.5}$$

If the expression of $\upsilon_0\ cos\ \theta_{cm}$ delivered from Equation 1.4 and centre of mass energy value (E_{cm}= $\frac{m.}{2}\ \upsilon_0\ ^2$) are inserted in Equation 1.5, particle energy in the centre of mass frame is expressed as:

$$E_{cm} = E_{lab}\ +\ \frac{m}{2}\ V_{cm}^2\ -\ \frac{V_{cm}\ m\ z}{T_{cyc}} \tag{1.6}$$

and centre of mass angle will be given as:

$$\theta_{cm} = \arccos\ (\frac{1}{2\ \pi}\ \frac{q\ e\ B\ z\ -\ 2\ \pi\ m\ V_{cm}}{\sqrt{2\ m\ E_{lab}\ +\ m^2\ V_{cm}^2\ -\ m\ V_{cm}\ q\ e\ B\ z\ /\ \pi}}) \tag{1.7}$$

The excitation energy is delivered from the centre of mass energy as defined in Equation 1.8. Where M is the mass of the reaction products (recoil mass), T_{cm} is the total kinetic energy in the centre-of-mass system and Q is the energy gain or loss in the system before and after the reaction.

$$E_{excitation} = T_{cm}\ +\ Q\ -\ E_{cm}\frac{m+M}{M} \tag{1.8}$$

Consequently, the measurements of time of flight, longitudinal position (z) and energy (E_{lab}) are used to obtain particle ID, centre of mass energy E_{cm} and angle θ_{cm}. In conventional silicon array detectors, the experimentally measured value is used to estimate the centre of mass energy and scattering angle resulting in uncertainty. However, using the solenoid method, Si array detectors measure particle energies from a more precisely valued flight time ($T_{flight} = T_{cyc}$ for small relativistic corrections) and distance from the target (z).

1.1.3 Comparisons Between the HELIOS Spectroscopy and Conventional Method

One of the important concepts in solenoid charged particle spectroscopy is the Q-value measurement with excellent energy resolution. The trajectory of detected particle groups and particle energies correspond to the different excitation states of

the residual nucleus. These energies will be separated by their centre of mass energies (Q-values). Particles with different energies are detected at different distances by array detectors because of different emission angles. Figure 1.7(a) illustrates that detected proton energy versus laboratory angle was obtained by conventional approach for states in ^{133}Sn from ^{132}Sn(d,p)^{133}Sn reaction. In Figure 1.7(b) shows

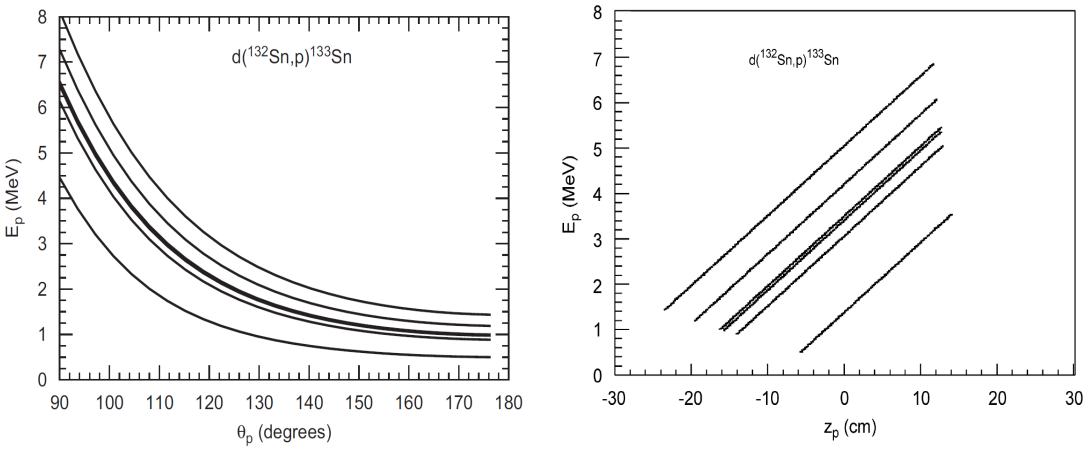

(a) Conventional method in simulation.

(b) HELIOS spectrometer in simulation.

FIGURE 1.7: A comparison energy spectrum for traditional method and new solenoidal approach. (a) Detected proton energy versus the emission angle of protons for states in ^{133}Sn from d(^{132}Sn,p)^{133}Sn reaction with conventional approach. (b) Energy separation between different kinematic groups for states in ^{133}Sn from d(^{132}Sn,p)^{133}Sn inverse kinematic reaction with the HELIOS.

that the same reaction is simulated for a solenoidal spectrometer method. Each straight line represents a kinematic line in the HELIOS. Energy separation between different kinematic groups is better than the energy versus angle plane in laboratory frame as compared in Figure 1.7. Excitation energy spectra are obtained from the centre-of-mass energy and shown in Figure 1.8 for both methods. Each peak represents different states in ^{133}Sn by separating energy difference equal to the separation in excitation energy.

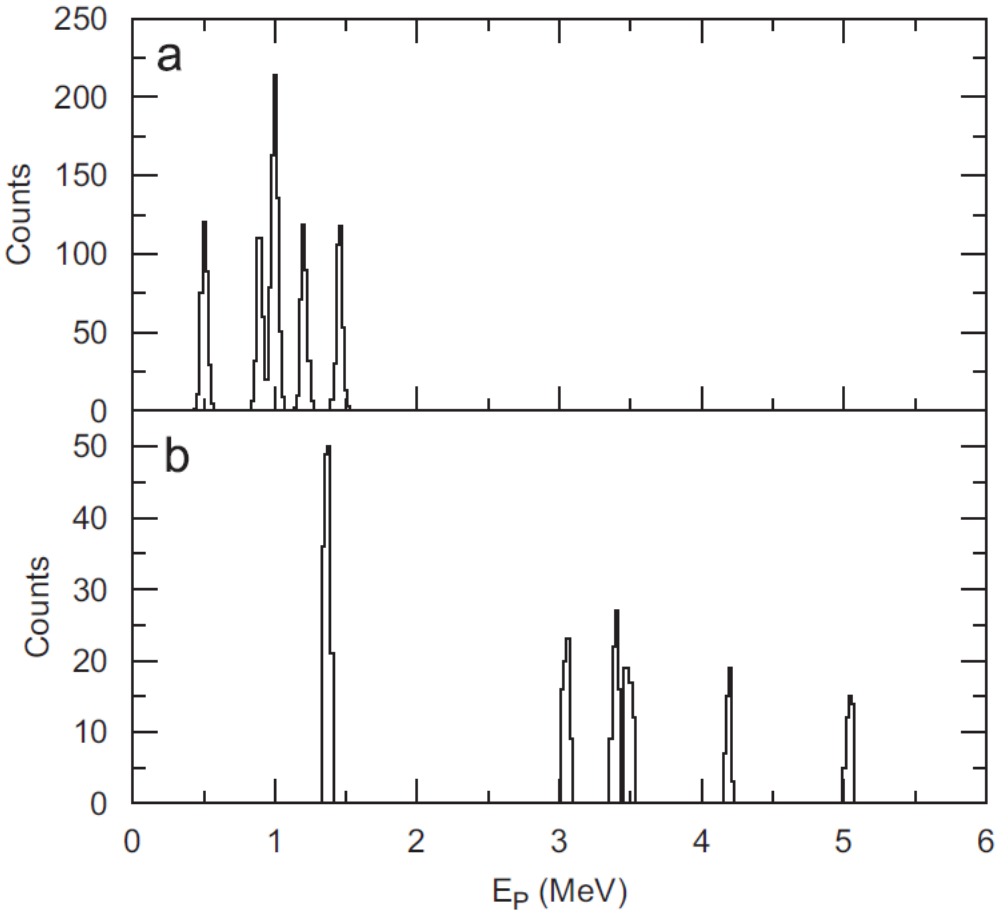

FIGURE 1.8: Projected proton energy spectra obtained from the data in Figure 1.7 for traditional method and the HELIOS. Excitation states for ^{132}Sn(d,p)^{133}Sn reaction (a) at 169°$< \theta <$171° with 8 MeV/u beam bombarding energy in conventional method, (b) at fixed z=0±1 mm.

1.1.3.1 Studying ^{28}Si(d,p)^{29}Si Reaction in Inverse Kinematics with the HELIOS

To verify untested characteristic and properties of the solenoidal spectrometer, the HELIOS was first studied with well-known (d,p) reaction in inverse kinematics. Figure 1.9 shows that the excitation energy spectrum for ^{28}Si(d,p)^{29}Si reaction in non-inverse kinematics was studied by Mermaz et al. Strongly popu-

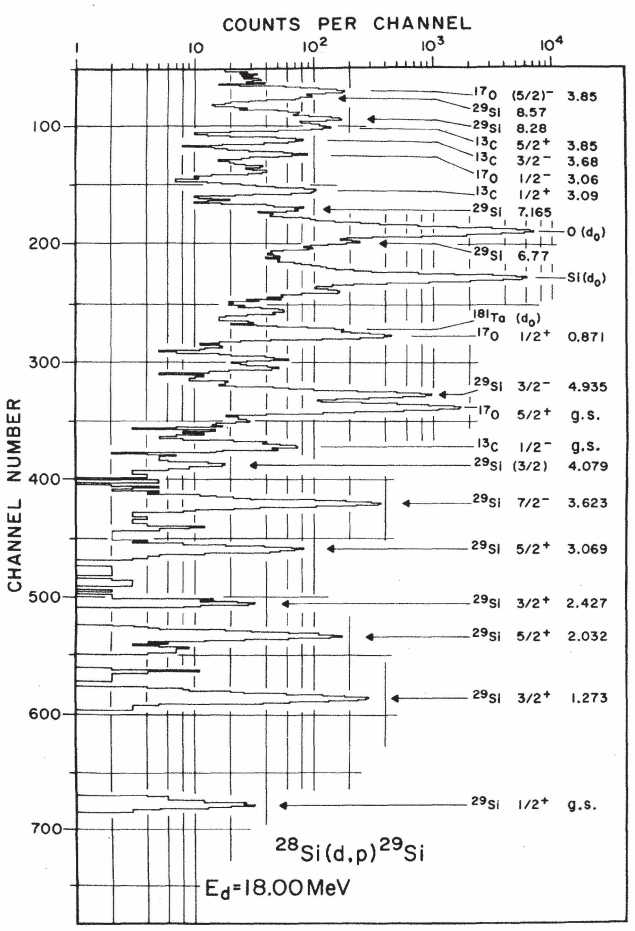

FIGURE 1.9: Energy spectrum for emitted protons from ^{28}Si(d,p)^{29}Si reaction in normal kinematics (measured at θ_{lab} =45°). In this experiment, the target was a silicon oxide with carbon contamination (that is why the states in ^{17}O and ^{12}C). Figure from Lighthall [5]

lated eight states in ^{29}Si from this reaction in inverse kinematics with excitation energy between 0 and 7 MeV were simulated and then measured with the HELIOS spectrometer. There is a pair of states near 6.2 MeV, and the best Q-value resolution is the order of 116 keV under ideal conditions of the traditional detection technique [6]. As we discussed in section 1.1.1.2 and stated in Reference [3], the

representative Q-value energy resolution for solenoidal spectrometer is equal to the order of intrinsic energy resolution of the silicon detector. Therefore, this pair states could be clearly separated by the HELIOS spectrometer.

Figure 1.10(a) shows that the detected particle energy (E_{lab}) versus the position for states in ^{29}Si obtained from simulation with defining the actual HELIOS field map. And Figure 1.10(b) illustrates the spectrum obtained from the experimental measurement. The active region of the array detector's leading edge was placed at -250 mm from the centre of the magnet. The target was positioned in three different places as indicated the line sets I, II, and III in Figure 1.10. An intercepted particle on the front of the detector array is defined as a low energy cut-off (acceptance limit) illustrated by the dashed curves.

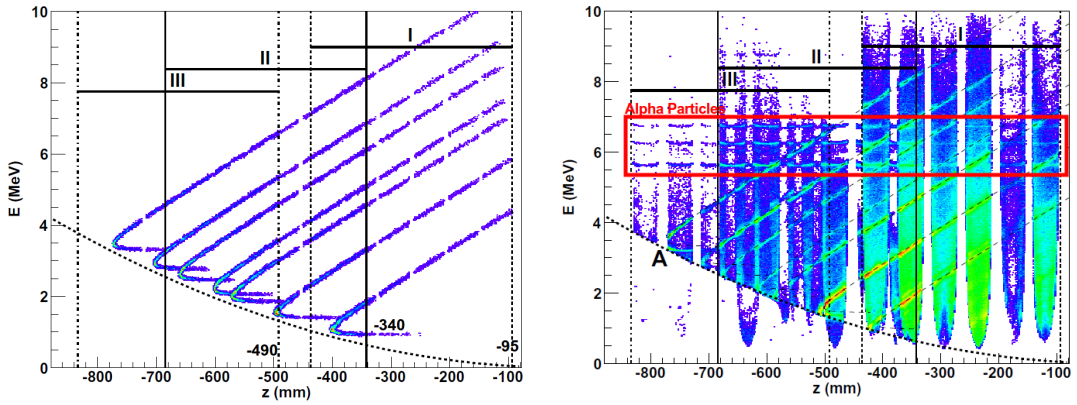

(a) Detected proton energy (E_{lab}) versus distance from target (z) spectrum was plotted using the actual HELIOS field map in the simulation. Populated seven states in ^{29}Si obtained from d(^{28}Si,p)^{29}Si reaction. [2]

(b) The spectrum obtained from the experimental measurement. The dash lines represent excitation of 0.00, 1.27, 2.03, 3.07, 3.62 and 4.9 MeV. The groups of detected alpha particle (orginate from calibration source (^{228}Th) cause the background with constant energy as indicated inside the red box. The other background throughout the plot arises from emitted protons from the fusion evaporation reactions of ^{28}Si+^{12}C. [6]

FIGURE 1.10: Detected particle energy versus the position (z) for three different target-detector separations by placing at -95 mm, -340 mm and -490 mm (to cover different centre of mass angle ranges [6]). The dash curves indicate the low energy cut-off in both plots. Energy spectrum for emitted protons from d(^{28}Si,p)^{29}Si reaction inverse kinematics obtained from (a) Monte Carlo simulation, and (b) experimental measurement [2].

Excitation energy is obtained from the centre-of-mass energy taking into account Q-value and recoil mass (M) as defined in Equation 1.8. Figure 1.11 shows the excitation energy spectra for ^{29}Si obtained with the HELIOS. The background, arising from the fusion evaporation, is subtracted from the data. Excitation energy levels are identified and labelled in keV with their spin number. Two states at 6194 and 6381 keV are resolved as shown in Figure 1.11. The response of the

spectrometer with simulation and experimental measurement are consistent with expectation. The HELIOS represents the powerful new tool for studying nuclear reaction in inverse kinematics with easy low-energy proton identification, better Q-value resolution, and large range of centre of mass angles with large solid angle coverage.

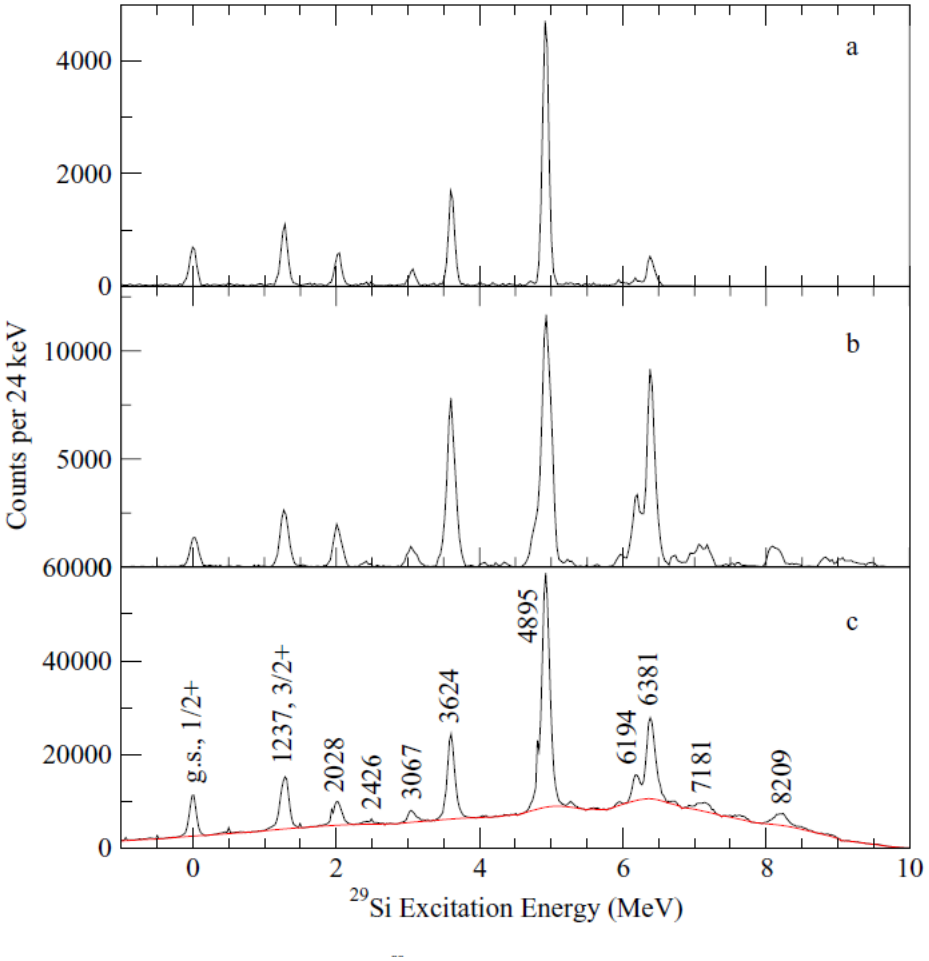

FIGURE 1.11: Excitation energy spectra of ^{29}Si obtained with HELIOS. (a) Fusion evaporation background is subtracted from the data which is the first separation line set (I) at $\triangle$Z=95mm. The energy resolution is approximately 103 keV FWHM. (b) Spectrum for entire array (one detector per position) at the same separation region. (c) Combination of all detectors at all three target-detector separations with indicating background subtraction. Excitation energy levels are identified and labelled in keV with their spin number. [6]

Excitation energy states in ^{13}B from ^{12}B(d,p)^{13}B reaction inverse kinematics are also studied with the HELIOS. Experimental centre of mass energy resolution is sufficient to separate closely 3.48 and 3.68 MeV positive parity excited states [7].

Measurements of solenoid axis position and the energy of detected particles are employed to obtain the emission angle of the particle in the laboratory frame, so effective angular resolution is also significantly better than traditional Si array detection. The magnetic field is beneficial for eliminating undesirable backgrounds (such as electrons and scattered beam particles), making solenoid charged particle spectroscopy an increasingly appreciated tool for use in nuclear research.

1.1.4 A HELIcal Orbit Spectroscopy for HIE-ISOLDE

As discussed in the previous section, the newly developed solenoid spectroscopy has many advantages over conventional methods. Accordingly, the HIE-ISOLDE project has invested in the production of a HELIcal Orbit spectrometer. The world's first 3T MRI scanner was moved from the University of Nottingham to Daresbury Laboratory for preliminary tests before it will be constructed to CERN. The first magnetic field measurement was not completed successfully due to the quenching of cooling liquid nitrogen (Figure 1.12). As shown in the HELIOS

FIGURE 1.12: (Left) The world first hospital MRI scanner was moved from the University of Nottingham to Daresbury Laboratory for preliminary tests. (Right) MRI scanner was being cooled with liquid nitrogen in Daresbury Laboratory. A magnetic field measurement could not be successfully carried out because of quenching, followed by the termination of liquid nitrogen a few minutes later.

configuration (Figure 1.1), only the silicon detector array system was constructed inside the uniform magnetic field. In addition to silicon detector systems, scintillator based gamma-ray detectors can be operated inside the magnetic field facilitating better understanding of nuclear structures through decay cascades. In many experiments the time-of-flight measurement is required. If the coincidence time resolution of this type of γ-ray detector is sufficiently higher than the lifetimes of excited nuclear states, in some cases, decay cascades can be ordered and identified,

which is why several aspects of the gamma-ray detector system were investigated for this thesis.

First, silicon photomultiplier, SiPM, (PN-junction of the semiconductor with silicon depletion region, which is detailed in Chapter 2) were optically coupled with different types of scintillation crystals. Some measurements were operated in the magnetic field from 1 Tesla to 3 Tesla in order to clarify interferences. The performance of a novel silicon photomultiplier was studied resulting in important measurements in terms of nuclear physics research. In order to stabilise time resolution, a new generation blue sensitive silicon photomultiplier with special fast timing output was used for coincidence time measurement. This research project is based on similar goals as the PET-MRI combination device, which is a very popular concept in medical physics.

1.2 PET and PET-MRI Capability

1.2.1 Positron Emission Tomography

Positron Emission Tomography (PET), a unique diagnostic method for producing 3D medical images of functional processes in the body is critically important in the diagnosis of illnesses. PET helps to define metabolic processes, which in oncology allows for the detection of primary tumours at the cellular level, as well as monitoring responses to therapeutic interventions. PET imaging is also useful in the diagnosis and evaluation of cardiovascular disease, and neurological, psychiatric, and other medical conditions [8]. Figure 1.13 shows a standard positron emission tomography model used in hospitals. Radioisotopes are generated in a cyclotron using proton or deuteron beams are labelled by different compounds (glucose, ammonia or water) depending on the biological properties of interested area. For instance, ^{18}F is labelled with glucose (Flurodeoxyglucose (FDG)) for brain images. Radioactively produced labelled pharmaceuticals are then injected into the patient's circulation system, following which the radioactive tracer substance accumulates inside a metabolically active place showing higher activity levels in abnormal regions (malignant tissue) than in others.

When an unstable nucleus decays through β^+ emission, one proton in the nucleus converts into a neutron while releasing a positron and an electron neutrino.

Emitted positron from the nucleus of an atom travels only several millimetres. This path length depends on the positron energy which is different for each PET radionuclide. The positron loses its energy by ionising many atoms in the medium during the path length. When the positron slows down, it pairs up with an electron in spiral motion towards each other (the annihilation event). The rest of the mass of both particles (matter and antimatter) is converted into electromagnetic energy called 511 keV annihilation photons (generated in 2 ns). The annihilation event produces back-to-back photons (Figure 1.14), though in rare cases (<1% probability) three annihilation photons can be emitted. The motion of the particles when the annihilation event occurs causes a minor variation from exactly 180 degrees. Therefore, back-to-back annihilation photons are not absolutely linear in direction; a small angular variation is called a non-collinearity ($180° \mp \approx 0.3$). The annihilation event occurs in a slightly different place from the actual location of the positron emitted atom, resulting in a different scan performance. For example, a scan performed with ^{18}F produces a higher resolution than ^{82}Rb because the maximum range is 2.4 mm for ^{18}F and 15.6 mm for ^{82}Rb [10]. Radionuclides should have sufficient half-life to distribute through interested regions, yet a short enough half-life to protect health tissues by reducing radiation exposure time. These two 511 keV photons are detected by a ring of gamma-ray detectors

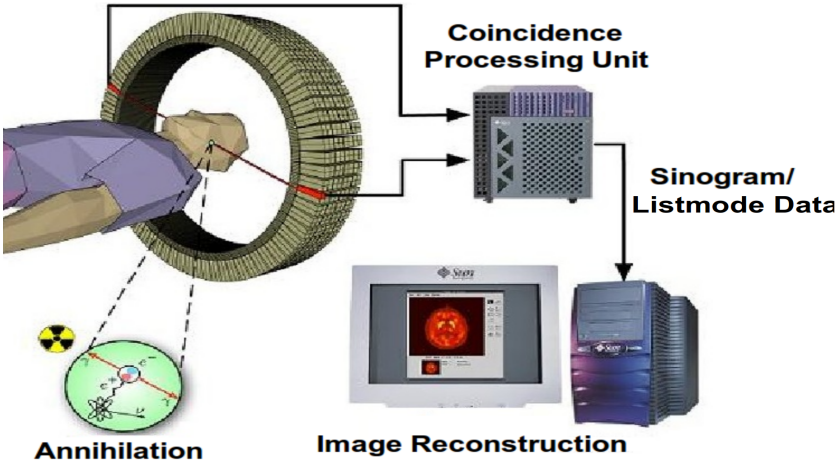

FIGURE 1.13: The configuration of a standard positron emission tomography system. After the injected radiotracer is collected in the interested region or organ, emitted positrons come across electrons in the medium, resulting in the annihilation of both and the production of two gamma rays passing in nearly opposite directions (because of the motion of the particles when annihilation occurs). These photons are detected by scintillation detector arrays as a ring system. Specific algorithms and data acquisition processes are applied in order to reconstruct the medical image without blurriness [9].

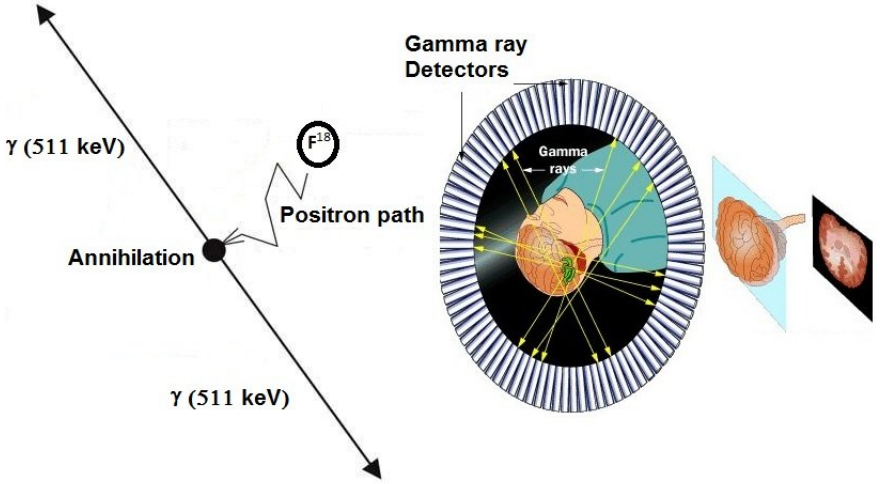

FIGURE 1.14: The positron losses its energy by ionising many atoms inside the brain during the path length, which is only several millimetres. When the positron slows down, it pairs up with an electron in spiral motion towards each other (the annihilation event). The rest of the mass energy of the positron and electron is converted into electromagnetic energy called 511 keV annihilation photons. After producing annihilation photons in the brain, all possible directions of gamma-ray pairs (coincidences) are recorded by ring scintillation detectors positioned to surround the patient. Consequently, the reconstructed slice-by-slice image is obtained after the application of algorithm processes [9].

to determine where the annihilation event occurs, resulting in a metabolic function map of the specific region. When the photons reach the scintillation crystals, visible lights are produced as a result of the scintillation process, as explained in Chapter 2. Scintillation photons are converted into electrical signals by a PMT (Photomultiplier Tube) or silicon photomultipliers (SiPMs). Finally, slice-by-slice images are obtained by reconstructing coincidence events with specific data acquisition processes and algorithms.

1.2.2 Properties of Positron Emission Tomography Gamma-ray Detectors

A PET detector must have sufficient sensitivity to detect annihilation photons and provide high spatial resolution, low dead-time, good timing and energy resolution with a cost effective scintillator. There are several critical properties that affect medical image quality such as energy and spatial resolution. Annihilation photon pairs would not travel in exactly opposite directions, thereby recording line of response (LOR, which defines a line through the decay event location) will not result

in accurate data. Furthermore, almost 30-50 percent of the total annihilation photons scatter in the medium, depending on the patient bone and tissue conditions. Annihilation photon pairs are detected by PET detectors in three different types of coincidence events: as a true coincidence; scattered or random as illustrated in Figure 1.15. If two annihilation photons reach the scintillators without any inter-

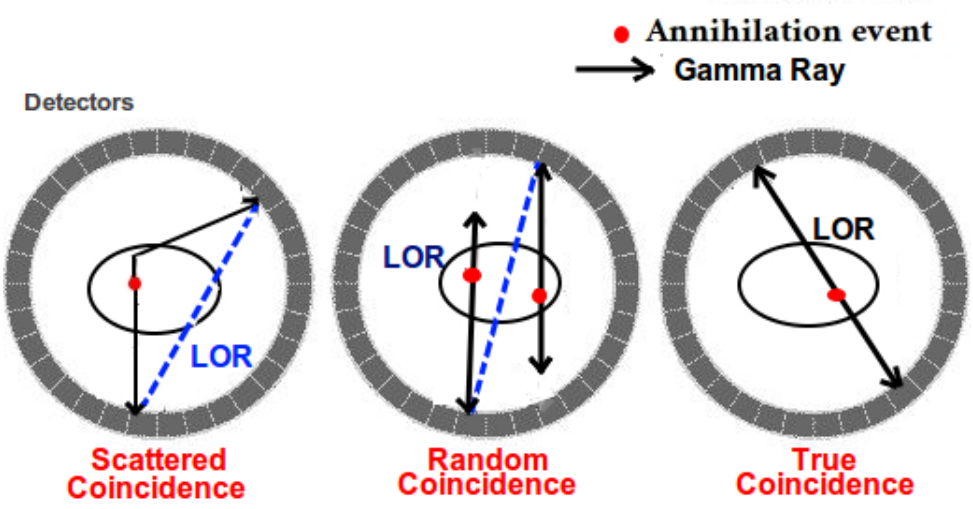

FIGURE 1.15: Gamma ray detectors record three different coincidence events (scattered, random and true coincidences respectively) depending on the path of annihilation photons. If Compton scattering occurs in the medium before photon detection, it will result in scattered coincidence and inaccurate LOR data. The photons of two different annihilation event can be detected as a one event, so line of response will again be recorded in inaccurately. Scattering and random coincidence contribute noise to the medical image.

action, this constitutes a true coincidence as a result of recording accurate LOR. When one of the annihilation photons scatters inside the medium before being detected by the gamma ray detector (Compton scattering), LOR will be recorded as a wrong line of response, causing noise in the image. Random coincidence happens when two photons occur in different annihilation events but are detected at the same time. It is again recorded as a wrong LOR, and results in noise in the image. Obtaining true coincidence events or recording accurate LOR gives the correct information about the annihilation events point. Therefore, the number of random and scattered coincidences will be reduced, and imaging quality improves with better spatial resolution. This is limited by positron range (depends on positron energy and type of nuclei) and non-collinearity of the annihilation photons.

The optical and physical properties of the inorganic scintillators most frequently used in PET detection are given in Table 1.1. To achieve better detection efficiency, effective atomic number and density of the scintillators must be as high

Properties \ Crystals	NaI(Tl)	BaF_2	LSO	BGO	CsI(Tl)	GSO	YAP	LYSO	$LaBr_3$
Density (g/cm^3)	3.67	4.89	7.4	7.13	4.51	6.71	5.37	7.10	5.29
Effective Atomic Number	51	53	65	75	54	59	26	63	47
Reflection Index	1.85	1.56	1.82	2.15	1.80	1.85	1.95	1.81	1.90
Decay Time (ns)	230	630	47	300	680	60	27	41	20
Emission Wavelength(nm)	415	310	420	480	540	440	370	428	380
Light Yield (Photons/MeV)	38000	9500	25000	8200	54000	9000	18000	32000	63000

TABLE 1.1: Properties of common scintillation crystals used in positron emission tomography for gamma ray detectors. LYSO and $LaBr_3$ (Lanthanum Bromide) have become very popular recently. LYSO is non-hygroscopic and a cheaper scintillator than $LaBr_3$, but properties of cerium doped lanthanum bromide are much preferred to other scintillators.

as possible. BGO (Bismuth Germanate) has excellent stopping power for gamma ray detections because of its higher atomic number and higher density than other scintillators. Incident radiation absorption is as much as possible. However, its timing performance is slightly poorer than NaI(Tl). Scintillators with fast decay times are preferred for good coincidence time performance, which allows for the reduction of dead time and the number of random coincidence resulting in improved medical image quality [11]. Intrinsic properties of LSO (Ce-doped Lutetium Orthosilicate; Lu_2SiO_5:Ce) and LYSO (Ce-doped Lutetium Yttrium Orthosilicate; $Lu_{0.6}Y_{1.4}SiO_5$:Ce) scintillators are different from other scintillators and include natural radioactive isotopes (^{176}Lu). Lu-176 decays to the excited state of Hf-176 by primarily emission of β^-. This isotope emits photons with energies from 88 keV to 307 keV, resulting of self emission inside the crystal. That causes the crystal to be excited and then produced scintillation light (the total self count rate is only 39 counts per second per gram (cps/g), so that is not a serious issue in application of PET) [11, 12]. Setting annihilation photon energy windows with these scintillators facilitates their use for coincidence counting due to their very fast decay time constants. In contrast, scintillators with a slower decay time constant cause a direct rise in detector dead time and the number of random coincidences. A higher light output influences the energy resolution and spatial resolution, leading to good quality medical images. It is important for scintillators to be non-hygroscopic, which means it is not damaged by exposure of the humidity. Therefore, scintillation material does not need to be sealed in a box. A non-hygroscopic scintillation

crystal facilitates easy packaging and mechanical ruggedness. Further content about scintillators will be provided in the next chapter.

1.2.3 PET-MRI Detector System

As previously discussed, over the last two decades positron emission tomography has been successfully integrated into MRI devices similar to gamma ray detectors construction inside HELIcal orbit spectrometers. When positron emission tomography is operated within a uniform high magnetic field, the positron range will be perpendicular to the field due to Lorentz force. Positron annihilation points do not spread over the interested region, so the spatial resolution of the PET detector improves depending on the force of the magnetic field [13]. An MRI integrated PET-CT image facilitates improved diagnosis in radiology, oncology and nuclear medicine. This new concept opens the door to addressing some biomedical issues affecting PET-MRI images. The magnetic resonance imaging technique provides details of physical structure and anatomical features similar to CT, but positron emission tomography (PET) depicts the contents of biological and metabolic processes inside organisms. When diagnosis is worked with PET-CT, many patients undergo X-ray exposure and PET radioisotopes. The combination of functional and anatomic imaging in a single image enables a more exact diagnosis providing significant information concerning soft tissue and anatomical detail from physiologic parameters, diffusion and changes in oxygenation levels, resulting in lower radiation exposure and much more effective treatment for patients [8, 14]. After treatment the activity of many diseases, such as cancer (tumour growth stages), brain atrophy and other abnormalities could be monitored with PET-MRI images.

The main difficulties in the PET detector system concern the effects of the magnetic field on PMTs in particular, and impairment of MRI image quality due to electromagnetic interference (EMI) between MRI and PET. In order to protect image quality, magnetic field homogeneity needs to be kept stable by eliminating interference. The literature review described various ways to achieve a simultaneous PET-MRI image. In early phases of technological development research groups were separated into two systems in order to reduce the effect of the magnetic field on PET systems. Separation was effected by, for example, splitting the magnetic field volume from PET so that the PMTs measure in the zero field, or using fibre-optic cables (a nonmagnetic component) to transfer light from the

scintillation crystals to PMTs placed outside of the magnetic field [15]. In earlier studies, forty-eight LSO scintillators were constructed as a 38 mm diameter ring PET detector system with one crystal of dimensions of 2x2x10 mm^3. Long fibre optic cabling was used to connect crystals with PMTs, and photomultiplier tubes were placed outside of the high magnetic field. Measurements were completed resulting in 2 mm, 41% and 20 ns spatial resolution, energy resolution and time resolution respectively. These results are not perfect, or even better than without magnetic field measurements, but it were nonetheless effective in acquiring the first simultaneous PET and MRI image. The effect of the electromagnetic interference is nearly nothing, but sensitivity is reduced with fibre optic cable because of resulting losses in light yield during the transfer of visible light from scintillator to PMTs.

The modern approach involves using solid-state photosensors such as avalanche photodiodes (APDs) or silicon photomultipliers (SiPMs) rather than PMTs. Several research groups have successfully developed prototype PET-MRI systems using APDs or SiPMs that are insensitive to the magnetic field [8, 16, 17]. A small animal tomography is called RatCAP was integrated into the MRI field by Woody (2006). RatCAP tomography consists of 12 detector modules each of which includes a 4 x 8 array of 2.3 x 2.3 x 5 mm^3 LSO crystals coupled to Hamamatsu S8550 APD. This research shows that RatCAP tomography and its various readout components can be successfully operated inside a high magnetic field and obtain individual PET and MRI images to search the effect of each system [17]. Similar to this approach, Catana and Procissi used 8x8 PET detector modules coupled to position sensitive avalanche photodiodes to examine magnetic field effects on PET imaging and found that the spatial resolution of PET was not deformed by the strong magnetic field. The effect of positron emission tomography on MRI imaging did not result in any obvious deterioration of the signal to noise ratio in that research, during which simultaneous PET-MRI imaging was carried out with cancer cells injected in mice.

Hong and Choi (2013) developed brain PET with 72 detector modules as a ring and insertable to MRI to achieve a simultaneous PET-MRI human brain image. Each detector module had a SensL Geiger mode avalanche photodiode array (see Figure 2.20) is optically coupled to 4x4 matrix LYSO crystals. The same PET detector module was constructed for this study, as discussed in section 2.5.3.1 of the next chapter. An almost 300 cm long flexible flat cable after shielded with aluminium sheet was used to connect each detector module to the preamplifier, thus placing all of the electronics outside of the MR. Research with the same brain PET scanner was carried out using improved software, hardware or hybrid filtering methods (combination of them). PET data acquisition filtered with hybrid was found to be the best technique to reduce the effect of the electromagnetic interference (EMI) [18]. Figures 1.16(a) and 1.16(b) illustrate that simultaneous MRI and PET images were successfully acquired independently without observing any noticeable deterioration [16], while Figure 1.16(c) demonstrates the simultaneous PET-MRI brain image. The performance of avalanche photodiode or Geiger mode avalanche photodiodes is very sensitive to temperature variations and magnetic resonance sequences cause increases in temperature or vibrations. The temperature of the shielded detector modules was therefore monitored to modify the gain drift depending on the temperature [19].

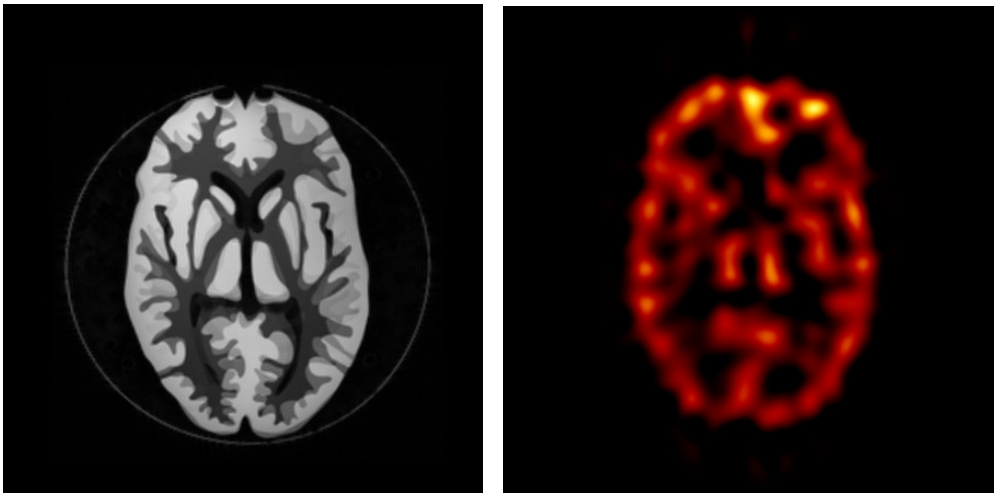

(a) MRI

(b) PET

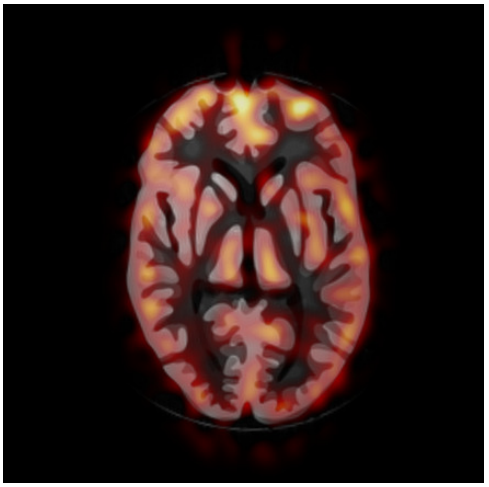

(c) PET-MRI

FIGURE 1.16: Brain images of 3D Hoffman phantom for three different systems: (a) Magnetic resonance imaging was acquired when PET was inserted into field. (b) Positron emission tomography imaging was acquired when MRI image was simultaneously acquired, and (c) simultaneous PET-MRI integrated image with MRI spin echo sequence [16].

A different approach is the redesigned gantry of PET-MRI system to operate photomultiplier tubes inside the MRI field after using magnetic shielding for the PMT systems which allow to operate in the normal flux level (close to the Earth′s magnetic field). The scientific measurements were found to be 12% and 520 ps energy resolution and timing resolution respectively for GEMINI TF PET-MRI scanner. These results are comparable with GEMINI TF PET-CT system measurements. Both scanners (GEMINI TF PET-CT and GEMINI TF PET-MRI) have a diameter of 90 cm, and each LYSO crystal element is 4x4x22 mm^3 in size. PET-CT scanner's energy resolution was averaged over all crystals 11.5 % FWHM at 511 keV with setting 440-665 keV energy window. Timing resolution for this system was found 585 ps for point source. Therefore, the performance of PET-MRI is very close to that of standard PET-CT [20, 21].

1.3 Quality Control of Positron Emission Tomography Radiopharmaceuticals

Positron emission tomography radioisotopes are generated from small cyclotrons, and are then formulated by specific chemical substances. Fluorine-18 FDG is a well-known radioisotopes used in positron emission tomography, others, such as Ga-68 and I-124 are also used in PET depending on the region of the interest. For example, I-124 is preferred in investigations of the thyroid due to its sensitivity to iodine. Therefore, iodine will accumulate in that region for suitable PET imaging. There must be acceptable quality control parameters to protect patients from extra radiation exposure before injecting them with radiopharmaceuticals. PET radioisotopes quality control parameters must be checked for radiochemical purity, radionuclide purity, pH level, sterility, safety, efficacy and radioactivity level before being used [22].

Radionuclide purity of a radiopharmaceutical is defined as the ratio of the radioactivity of the desired radionuclide to the total radioactivity of the source. Radionuclide impurities originate from the various nuclear reactions and impure target materials. Impurities in the radioisotopes can negatively affect image quality as well as expose patients to unnecessary radiation doses. Activity-time plot was used to determine contaminated radioisotopes from the half-life measurements by multichannel gamma spectrum. Thin layer chromatogram (radiochromatogram),

scintillation counter and dose calibrators are used in determination of radiochemical and radionuclide purity as a radiation detection instrument in the quality control protocol. A radiochromatogram scanner is used on a long narrow piece of radiochromatography paper for the quantification of the radioactivity distribution. These measurements take more time than with a scintillation detector equipment with an expensive radiochromatogram scanner [23]. The scintillation counter system will be detailed in Chapter 2. For better quality control a plastic scintillation detector was developed to measure the activity of PET radioisotopes directly from positrons rather than annihilation photons as discussed in Chapter 5, which also includes experimental measurements and simulations results.

1.4 Overview of the Thesis

The main aim of this project was to work with scintillation detector systems which are a combination of novel scintillators and new generation silicon photomultipliers, and can be operated inside a strong magnetic field. In this chapter, the motivation is presented in terms of number of nuclear physics cases and their application in the field of medical physics in the imaging and PET radioisotope quality control processes. Several important properties of scintillation detectors, which enhance their potential for use in the HELIOS spectrometer and PET-MRI systems, were investigated experimentally and a PET detector module was tested after a detailed construction process. Avalanche photodiodes and silicon photomultiplier were tested inside the magnetic field, and we successfully obtained a magnetic resonance image when a simple positron emission detector was located inside the phantom as explained in Chapter 2. That chapter includes a review of technical information about the nuclear instrumentation modules and signal shape processes that were used during the experimental measurements. Following this chapter, SensL blue sensitive B and C series silicon photomultiplier sensors are characterised as exhibiting important parameters such as temperature dependence and variation in gain.

Coincidence resolving time measurement is a critical measurement in nuclear research subjects and ToF-PET systems. Timing measurements were successfully completed using special fast timing output signals of SensL blue sensitive SiPMs, then compared with standard Hamamatsu avalanche photodiodes and PMTs. In

Chapter 4 describes how two different data acquisitions were used as an in analogue and digital timing measurements. Signal shape processes were carried out in ROOT, with the code written by myself. In order to obtain good time resolution, various methods were applied by improving the experimental setup step-by-step. After the investigation of scintillation detectors and characterisation of their properties, a new detector system was designed for measuring the activity of PET radioisotopes. The major difference between this detector and standard detectors used in PET research centre is that the measurement is obtained directly, without any interference from particles rather than secondary products (annihilation photons) through contact with radioactive substances. This increases detector efficiency, resulting in more accurate activity measurement, which is significantly important for checking PET radionuclide-radiochemical purity in the quality control procedure. This detector design is obviously cost effective, capable and based on very simple working principles. GEANT4 based Monte Carlo simulation work was performed in this study to investigate the effect of annihilation photons on the total scintillation photon number. In the last two chapters, there will be further discussion about the simulation work, final summary of the thesis providing experimental results, and future research plans.

Chapter 2

Scintillation Detector Systems

Scintillation detector systems are widely used in nuclear, particle, and medical physics for radiation detection spectroscopy, cross-sectional images, and quality control of medical radioisotopes. When ionising radiation, for example γ-rays, excite scintillation material and then visible or ultraviolet light appears by means of luminescent crystals during the energy absorption of the incident radiation. Then PMTs or photodiodes are used for converting light into an electrical pulse via photoelectric effects. If that amplified signal is analysed, it gives information about the interaction between incident radiation and scintillation crystals. Analysing this signal is critical because of the complicated behaviours of atomic nuclei, radioactive nuclei, γ-ray spectroscopy, and the high quality of medical images. They are directly provided by timing and energy spectra of detectors.

There are two types of scintillation crystals: organic scintillators and inorganic scintillators. Organic scintillators have a low light output and low stopping power for γ-rays. Therefore, inorganic scintillators are commonly preferred particularly in positron emission tomography [11, 24]. In this chapter, we will discuss scintillation mechanisms, photomultiplier processes, and signal shape processing with important nuclear instrumentation modules (NIM). In addition, experimental results will be presented by various scintillation detector systems.

2.1 Organic Scintillator

Organic crystals are the combination of aromatic hydrocarbon in benzene ring structures. Scintillation lights are produced by excited valance electrons that combine with molecules rather than a particular atom (in the case of inorganic scintillators). The most common bond in an aromatic carbon ring structure is π bond. Incident radiation can excite either an electron level or a vibrational level of the π molecular orbitals. There are various singlet and tripled states of the π molecular orbital state as shown in the energy level diagram in Figure 2.1.

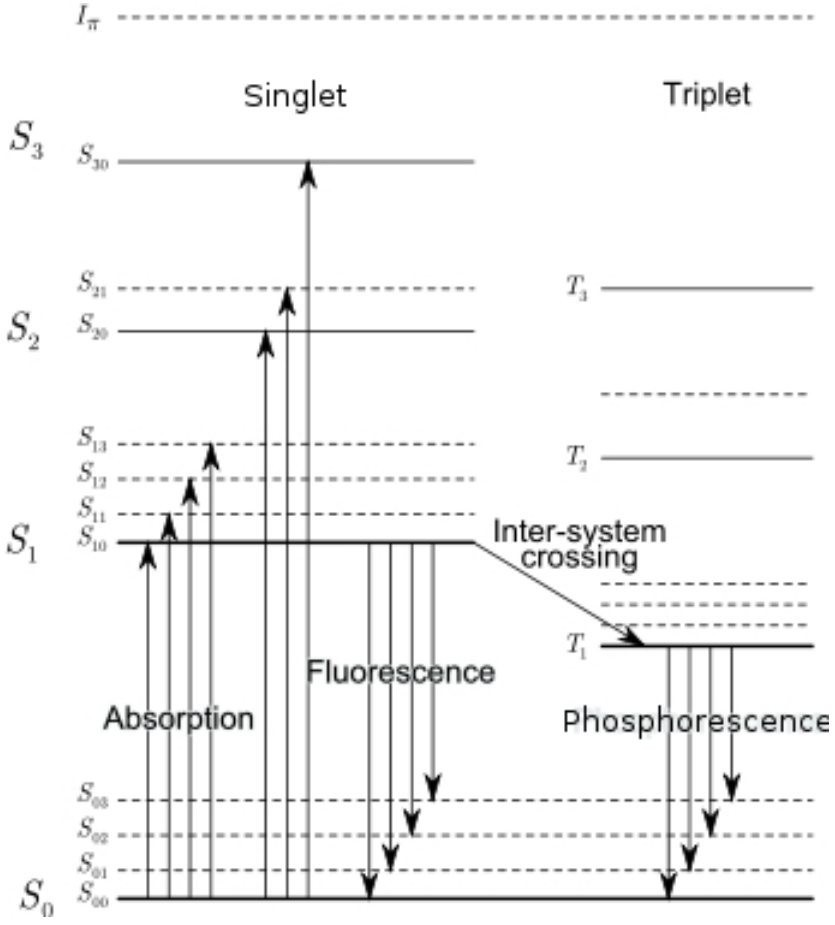

FIGURE 2.1: π-states of an organic molecule. The ground state is donated by S_0. Singlet excited states and tripled excited states are presented by S_1, S_2, S_3 and T_1, T_2, T_3 respectively. Vibrational sub-levels are also shown as S_{00}, S_{10}, S_{11} etc. [24]

Radiation absorption results in molecular vibration to the S_1 state and is followed by de-excitation to the ground state (S_0). The fluorescence mechanism arises by emitting scintillation photons from one of the vibrational levels above the S_0 state. The fluorescence process is also called the fast component. The slow

component of the decaying process is observed when one of the triplet state is excited (phosphorescence phenomena). Fast and slow components allow the use of the pulse shape discrimination method which is possible to identify the particle by looking at the pulse shape.

Organic crystals are long-lasting scintillators which are easily shaped, and they can be found in both liquid and crystal forms with a combination of a solvent, a scintillator, and other material, which helps to make it glow bright or places it on the right wavelength.

2.1.1 Plastic Scintillator

Plastic scintillator is combination of a solid polymer matrix (base) and fluorescent emitter (Fluor). The base material is generally acrylic, polystyrene (PS), or polyvinyltoluene (PVT). Convenient organic scintillators are homogeneously mixed with the base material to produce sufficient light yield and then the mixture is polymerized for plastic form. The plastic base material absorbs incoming radiation (ionisation) by transferring energy to the primary fluor through resonant dipole-dipole interaction (known as Forster energy transfer). As a result of that interaction, ultraviolet radiation with short attenuation length is produced in the plastic base (see Figure 2.2). Then secondary scintillator (fluor) shifts the wavelength from UV photons to light photons (mostly emits blue light) [25]. Increasing

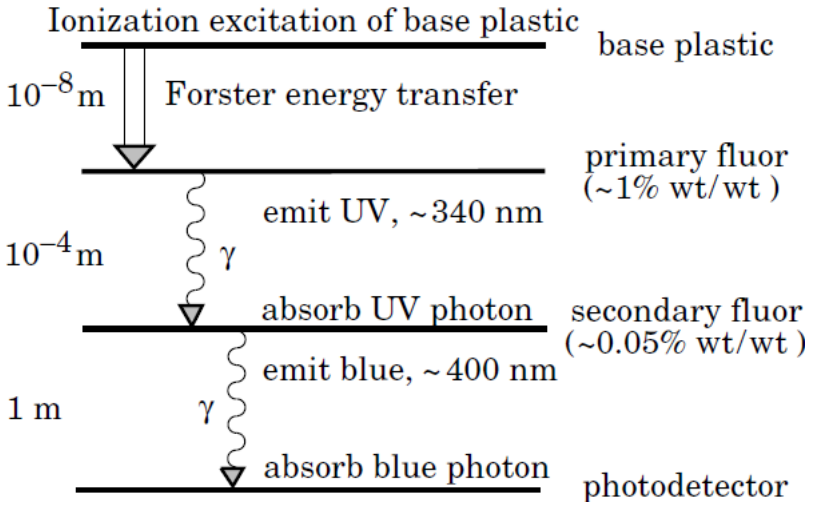

FIGURE 2.2: Operating system of an organic scintillator. Energy transfer distance for each process and approximate fluor concentrations are given in the diagram [26].

fluor concentration in the scintillator and resonant dipole-dipole interaction (strong

coupling the base and fluor) can shorten the decay time, so plastic scintillator has an extremely fast decay time constant (2-4 ns). The greatest advantage of using plastic scintillation is that they are shaped easily, especially if a large detection area is required, and that they are cost-effective. Generally, plastic scintillator

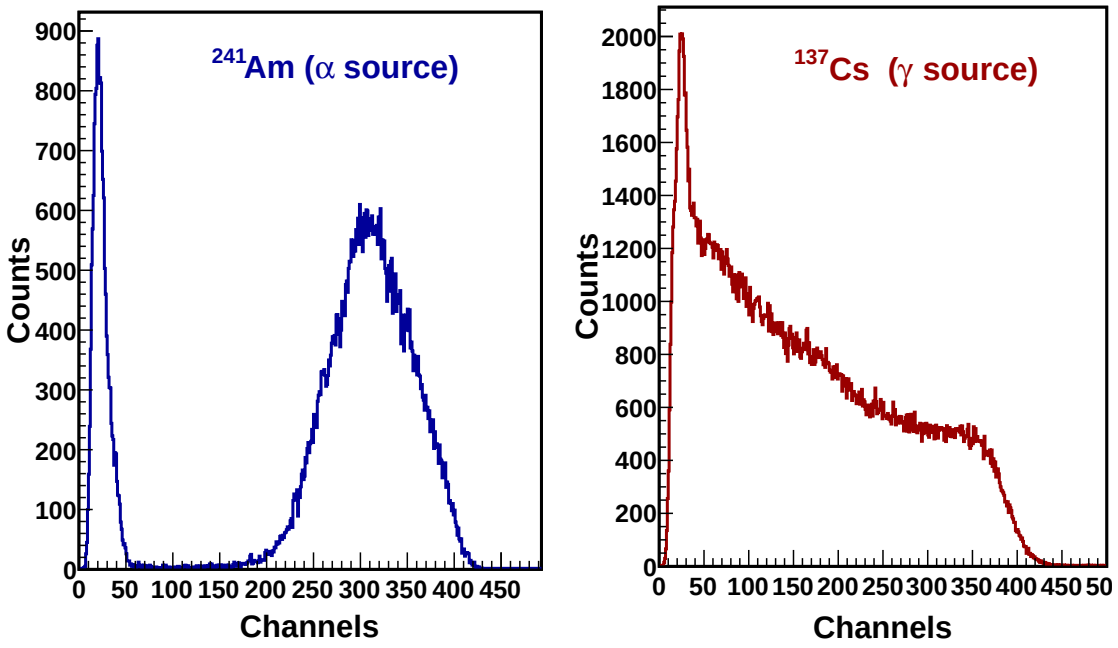

FIGURE 2.3: Energy response of plastic detector systems for α and gamma source separately. A full energy peak is not seen if a plastic scintillator interacts with gamma source. The probability of photoelectric effect is very low, so only the Compton edge is seen in the red spectrum. Plastic scintillator is generally used for charged particles as seen in the blue spectrum.

material is used for detection of charged particles. Figure 2.3 shows the energy response of plastic scintillation detectors for gamma and charged particles. There is no full energy peak when plastic scintillators interact with a gamma source because of its low density (1.02 g/cc) (Photoelectric effect is proportional to Z^4). Plastic scintillation material will be discussed in more detail in Chapter 5.

2.2 Inorganic Scintillator

Higher stopping powers for γ-rays, good energy resolution, higher light yields, a very fast decay time, and excellent linearity of inorganic crystals have made inorganic scintillators very popular in particle and nuclear physics. The biggest

disadvantages of inorganic scintillation crystals are the difficulty of making specific shapes and being hygroscopic.

Scintillation mechanisms for inorganic crystal occur in the electronic band structure of crystals not in a molecular bond. In organic scintillator, fluorescence mechanism occurs independently of the physical state of scintillators (can be observed in liquid, gas, and crystal structures). Pure inorganic scintillators (alkali halides) are not suitable for producing more visible light at room temperature. Incident radiation excites an electron from the valence band to the exciton band. Then it instantly returns to valence level emitting photons as shown in Figure 2.4(a) in the case of pure NaI scintillators. The energy gap between the

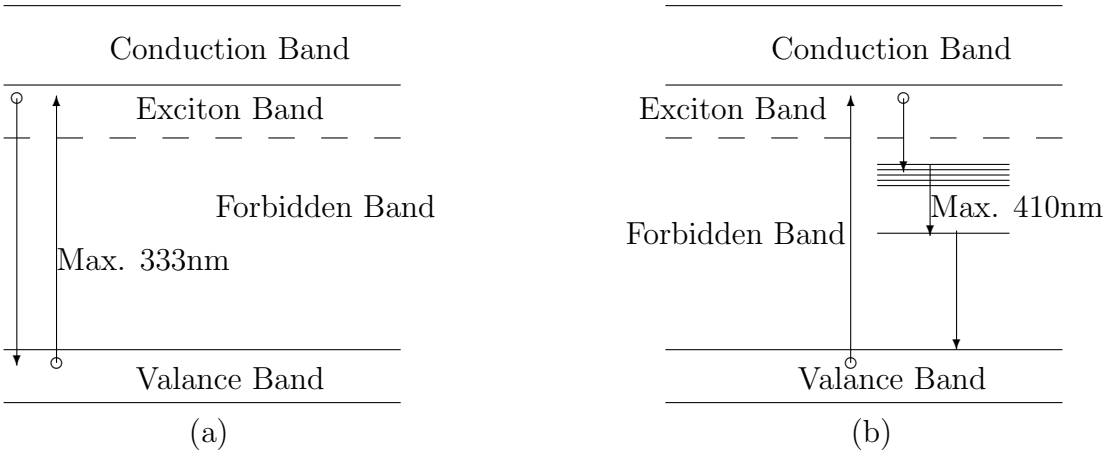

FIGURE 2.4: Electron energy level is maximum (a) 333 nm for pure sodium iodide (NaI) scintillator and (b) 410 nm for thallium activated sodium iodide.

valance band and conduction band (maximum 333 nm) are not in the visible light frequency range [27]. Therefore, photons can be absorbed by crystals themselves and the glass window of PMT or SiPM without converting signals. Pure crystals have to be doped with a heavy metal activator like thallium in order to produce more visible light. This causes interface energy levels to increase inside the forbidden band, and then photons emit with lower energy and longer wavelength (maximum 410 nm) as illustrated in Figure 2.4 (b). As a result, collecting more visible light improves the performance of the scintillation detector.

2.3 Photomultiplier Process

2.3.1 Photomultiplier Tube (PMT)

Vacuum photomultiplier tubes or PMTs are highly sensitive to visible light (photosensitive from ultraviolet to near-infrared range of the electromagnetic spectrum). PMTs are used for converting visible light (emission scintillation photons) into an electrical signal that is proportional to the incident radiation energy. There are several important parts of standard photomultiplier tubes as shown in Figure 2.5. Cathodes (photocathodes) are used for transferring visible light into electrical sig-

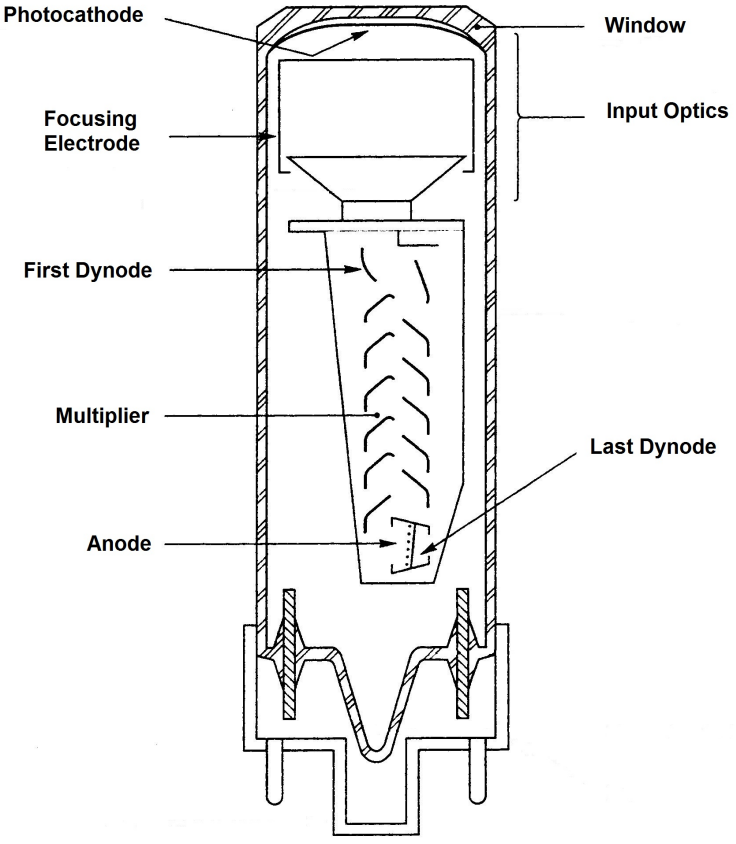

FIGURE 2.5: Configuration of a photomultiplier tube. Scintillation photons (visible light) first interact with photocathodes, so photoelectrons are produced via photoelectric effect. External resistance chains operate a desired output voltage between dynodes to accelerate and multiply electrons through anodes. Current obtained from accumulated and collected charges on anodes can be seen as signals [28].

nals via photoelectric effect, photocathode must be very sensitive to visible light. Furthermore, the emission of photon wavelengths, which occurs after the scintillation mechanism between crystals and ionising radiation, has to be well matched

with the PMTs sensitivity region [12]. Blue light sensitivity plays a critical role in terms of emission wavelength, coherences, and timing resolution, which will be discussed further in Chapter 4. The sensitivity of photocathodes is related to the quantum efficiency (QE) of the photocathode which depends on the incident radiation's frequency and collected number of photons as defined in Equation 2.1 [24].

$$QE = \frac{\text{the number of emitted photoelectrons}}{\text{the number of incident photons}} \tag{2.1}$$

The second important part of PMTs is a group of dynodes, which are used to accelerate photo electrons from the first dynode to the last. This process repeats itself until all electrons reach the anode. Consequently, the initial current is collected and amplified by dynodes. The other significant part is the anode, which accumulates all electrons after being multiplied by dynodes. All of these segments need to be placed inside the vacuum tube in order to reduce the pressure effect on the current.

2.3.2 Silicon Photomultiplier

2.3.2.1 PIN Diode

Incoming radiation produces 3-4 eV scintillation photons when interacting with crystals (see previous section "inorganic scintillator"), and the average energy to create an electron-hole (e-h) pair for silicon is about 3.6 eV (with 1.2 eV band gap energy). Therefore, the energy of the scintillation photon is enough to generate e-h pairs inside the undoped silicon wafer region (i-region), which is very sensitive to radiation [27], as shown in Figure 2.6. P-type semiconductors (positive charge of the hole) have a larger hole concentration than electron concentration by doping an intrinsic semiconductor with acceptor impurities or doping n-type semiconductor. In contrast, n-type semiconductors (negative charge of the electron) have a larger electron concentration than a hole concentration by doping intrinsic semiconductor with donor impurities or doping a p-type semiconductor. PN-junction structure is obtained by joining together opposite doped semiconductors (p and n type semiconductors). The width of the intrinsic region (i-region) should be larger than the space charge width of a normal PN-junction, when an external reverse

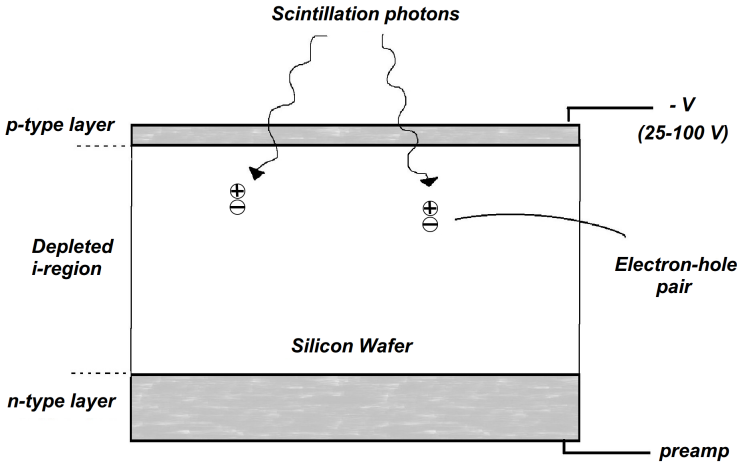

FIGURE 2.6: The basic structure of photodiodes. P-type layer refers to positive charge of the hole or p-type semiconductor. N-type layer (or n-type semiconductor) is the negative charge of the electron. Semiconductor diode allows charge to follow the current in only one direction. The region (i-region) between the p layer and n layer is filled with undoped silicon to produce electron-hole pairs. External potential is applied to accelerate electrons, and then a signal will be obtained with the preamplifier [24].

voltage is applied across the PN-junction. When scintillation light hits the PN-junction of the semiconductor, a current is generated by photodiodes, which easily and accurately detect the variation of the visible light.

The p-layer has to be as thin as possible ($< 1\ \mu$m), as the number of scintillation photons passing through the silicon region from the crystal dramatically increases with a thin p-layer. Optically transparent thin entrance window enhances the light transmission from scintillator to the active volume in photodiodes (silicon wafer region) [24].

If a bias voltage (25-100 V) between p and n-layers is applied, the electric field force accelerates photoelectrons from the p-layer and silicon wafer region to the n-layer. Applied external reverse voltage gives the advantage of measured low lights at a high speed and the multiplication of photoelectrons in the internal region. Multiplied electrons are collected on the pre-amplifier as a current, resulting in output pulse. Consequently, scintillation photons are transferred from p-layers to n-layers after being converted into photoelectrons.

2.3.2.2 Geiger Mode Avalanche Photodiode (APD)

Geiger mode avalanche photodiode (APD) is designed to support high electric fields, which is the main difference between ordinary PN-junction (PIN-diode). Generation of electron-hole pairs in the depletion region is similar to producing electron-hole pairs in PIN diode (section 2.3.2.1). Biasing voltage creates very high electric-field strength inside the region. As shown in Figure 2.7, generated electron

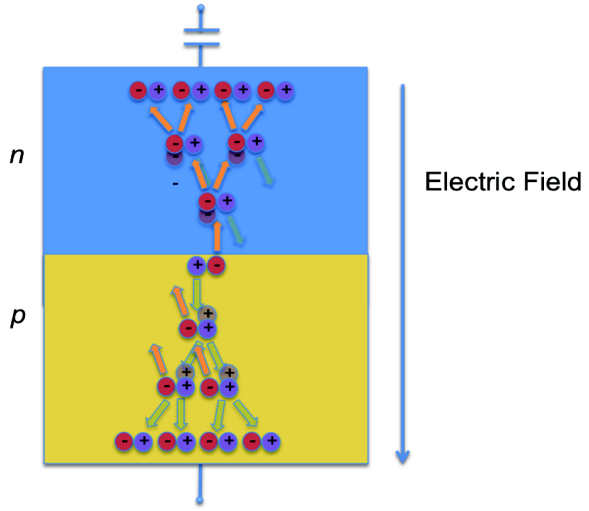

FIGURE 2.7: Schematic diagram of Geiger mode process in SensL silicon photomultiplier [29]

(or hole) gains the sufficient kinetic energy from the field to collide with crystal lattice, resulting generation of another electron-hole pair in the region. Electron-hole pairs are created more, this process is called as an impact ionisation. Impact ionisation mechanism causes an avalanche current in the depletion region.

Avalanche photodiode gain is stable until the breakdown voltage. At this operating bias (V_{BR}), the semiconductor junction breaks down and becomes a conductor called Geiger discharge as a result of more than 10^5 signal gain (because of a large single carries current). When the device is triggered, the junction breaks down and the avalanche photodiode is stopped or reset. A large current flows to the quenching resistor, then the voltage of the APD drops below the V_{BR}. A single photodiode device operates as a photo-triggered on and off switch by using this breakdown cycle [29]. However, a Geiger discharger current cannot distinguish between multiple photons and single photon trigger if multiple photons and a single photon are detected at the same time. Optically and electrically isolated Geiger mode photodiodes are integrated and then summed through the output

signal to distinguish between multiple photons and a single photon. APD with high single photon detection capabilities is defined as a pixel (or microcell) array system as illustrated in Figure 2.8. Each element of an array (microcell) has

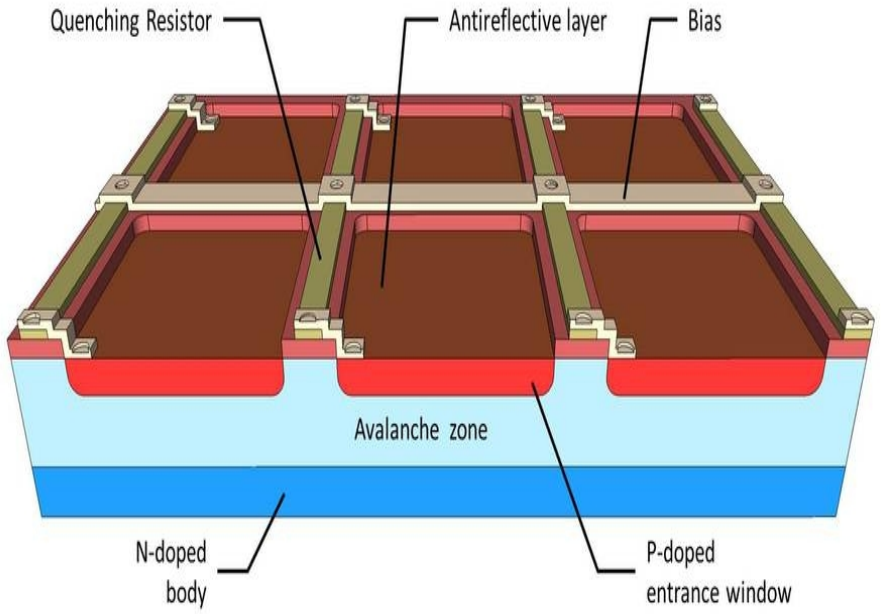

FIGURE 2.8: Standard Geiger mode APDs' microcell cross section for 3x2 array, which are connected together. Quenching resistor has been used to limit and rapidly reduce the signal current (active and passive quenching techniques) [30].

an independent quenching resistor. Every microcell detects photons identically and independently. The magnitude of the photon flux shows how many photons are detected at the same time as illustrated in Figure 2.9. Therefore, the silicon

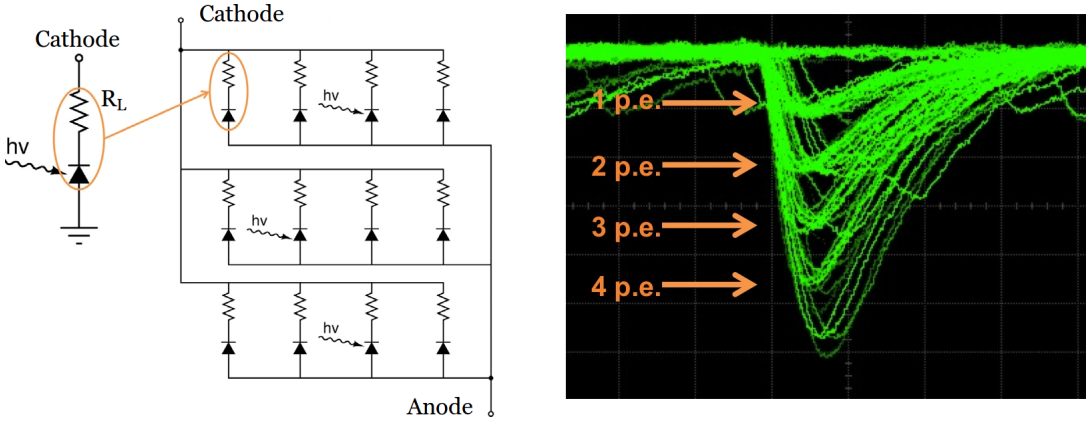

FIGURE 2.9: SensL Geiger mode avalanche photodiodes are integrated in parallel, and each microcell has individual quenching resistance as shown in the left side. Detected photon numbers are illustrated on the oscilloscope, which is obtained from SiPM output in the right side [29].

photomultiplier (SiPM), or multi pixel photon counter system, achieves to measure

the number of incoming photons per pulse, which is not possible with a single photon counting device (like an APD).

2.3.2.3 Technical Terms and Performance Parameters of SiPMs

This section will discuss important technical terms and several performance parameters of a silicon photomultiplier, which is used in the next two Chapters (3 and 4).

Overvoltage

When the Geiger discharge is created in the depletion region, this operating bias value is called the breakdown voltage (V_{BR}). Recommended working bias voltage is between 1V and 5V above the breakdown voltage to optimise the performance of SensL silicon photomultiplier [31]. That voltage range is called overvoltage (ΔV) and it can be expressed as;

$$\Delta V = V_{Applied\,Voltage} - V_{BR} \tag{2.2}$$

Gain

Applied bias voltage strongly effects the ionisation rate (gain), because the bias voltage increases the electric field strength across the avalanche layer. When the voltage is increased in the normal operation range, the gain increases and avalanche multiplication occurs. Even if a higher bias voltage is applied, PN junction voltage in the depletion region decreases due to series resistance, then the gain begins to drop [32]. The ratio of the total microcell output charge to an electron charge (q) gives the SiPMs gain or ionisation rate. The total charge is calculated by multiplying the microcells' capacitance (C) to overvoltage (ΔV) as given in Equation 2.3

$$Gain = \frac{Total\ Charge}{Electron\ Charge} = \frac{\Delta V.C}{q} \tag{2.3}$$

Quantum efficiency

If scintillation photon energy is higher than the band gap energy of depleted material, electron-hole pairs are generated when photon enters an avalanche photodiode. The band gap energy for silicon is 1.12 eV, so silicon avalanche photodiode

(APD) is sensitive to light wavelengths shorter than the cut-off wavelength ($\lambda_{(nm)} \cong$ 1100 nm) and is expressed by Equation 2.4;

$$\lambda_{(nm)} = \frac{h.c}{E} = \frac{1240_{(eV.nm)}}{E_{(eV)}} \tag{2.4}$$

where $h.c$ are the plank constant and the speed of light, E is the silicon band gap energy [32]. Quantum efficiency for APD is the ratio of generated electron-hole pairs to the number of incident photons in percent. Manufacturers often use photosensitivity or photon detection efficiency instead of quantum efficiency among their specifications. Photosensitivity " S " is given in electrical current generated per incident watt of the optical power (A/W). Therefore, quantum efficiency is defined with photosensitivity as expressed in Equation 2.5; where λ is wavelength (nm).

$$QE = \frac{S \,.\, 1240}{\lambda} \text{ x } 100 \ (\%) \tag{2.5}$$

Noise and dark count

Signal noise of silicon photodiode is a series problem, particularly in low energetic radiation measurements. A lower limit of light detection in silicon photodiode is defined as a noise characteristic of the detector and its amplifiers. Output signals are produced by either photoelectrons or thermally generated dark current electrons, and they are identical in signal. Silicon photodiode noise current (i_n) is the sum of the thermal noise current or Johnson noise current (i_J) of a resistor and shot noise currents (shot noise of the dark current (i_{SD}) and the photocurrent (i_{SP})) [32] as expressed in Equation 2.6;

$$i_n = \sqrt{(i_J)^2 + (i_{SD})^2 + (i_{SP})^2} \tag{2.6}$$

Unreal trigger level could be avoided from the noise by setting the appropriate threshold level (above the single photon level), but the dark counts always deteriorate the measured signal [29]. If the dark count rate is stable, it can be removed from the noise. However, if it fluctuates on the noise, the noise contribution will be the square root of the dark count rate due to existing Poissonian behaviour of dark pulses in time. This noise can be measured as a magnitude of pulse rate (kHz or MHz) or dark current (μ A). The shot noise of the dark current (i_{SD}) is

expressed by Equation 2.7;

$$i_{SD} = \sqrt{2q.I_D.B} \tag{2.7}$$

where q is electron charge, I_D is the dark current and B is the noise bandwidth. Thermal or Johnson noise can be expressed by the Equation 2.8;

$$i_J = \sqrt{\frac{4\kappa.T.B}{R}} \tag{2.8}$$

where κ is Boltzmann constant, T is the absolute temperature of photodiode and R is the resistance of the photodiode. Shot noise of the photocurrent (i_{SP}) is given by following Equation 2.9;

$$i_{SP} = \sqrt{2q.I_P.B} \tag{2.9}$$

where I_P is the incident light current. The electrical bandwidth of the detector and signal processing equipment is expressed as a bandwidth (B). Noise sources in the optical detector system are designed randomly in nature with very wide frequency distributions. When electrical bandwidth is increased, the noise of the detector system will be increased as given by Equation 2.10.

$$Noise = \sqrt{B} \tag{2.10}$$

The electrical bandwidth of the detector system should be close to the required bandwidth for reducing unnecessary noise. If applied bias voltage is constant, intrinsic gain of avalanche photodiode will be the average of each carrier's multiplication. Multiplication noise is known as an excess noise, so the shot noise of the avalanche photodiode (i_N) is larger than the shot noise of PIN photodiode as given in Equation 2.11;

$$i_N = \sqrt{2q(I_P + I_{DG})B.G^2.F + 2q.I_D.B} \tag{2.11}$$

Where I_{DG} is the current generated inside the substrate, which is the dark current component multiplied, G is gain and F is excess noise factor [12, 32]. The number of generated electron-hole pairs during the carries travel distance time is defined as an ionisation rate. The ionisation rate of electron is indicated with α, and β is the ionisation rate of holes. Each carries ionisation rate is not uniform and there is statistical fluctuation. Device noise parameter is called an ionisation rate ratio (k) which is the ratio of β to α ($k = \beta/\alpha$) [32, 33]. When electrons are injected inside the avalanche layer, the excess noise factor can be defined in terms of the

ionisation rate ratio as given in Equation 2.12.

$$F = G.k + (2 - \frac{1}{G})(1 - k) \tag{2.12}$$

If applied bias voltage is increased, this improves the photon detection efficiency, however, the dark count will also increase. The dark current can be reduced by lowering the temperate of photodiode. Another way to reduce the dark current is to use different wafer products like mercuric iodide [24]. Choosing a semiconductor material, which has a wider band gap (e.g 2.13 eV for mercuric iodide) than silicon, produces lower dark current. There are also two additional noise sources; afterpulse and crosstalk, which will be discussed in the next section.

Temperature Dependency

Temperature variation mainly affects the dark count rate and SiPM's breakdown voltage. Thermal generation of the electrons will increase with temperature, and that can be a limiting factor if a sensor is required to operate at high temperature applications [31]. As we discussed in the previous section, there are two ways to reduce the dark count rate: cooling and changing the semiconductor material inside the depletion region. Figure 2.10 shows the relationship between dark count

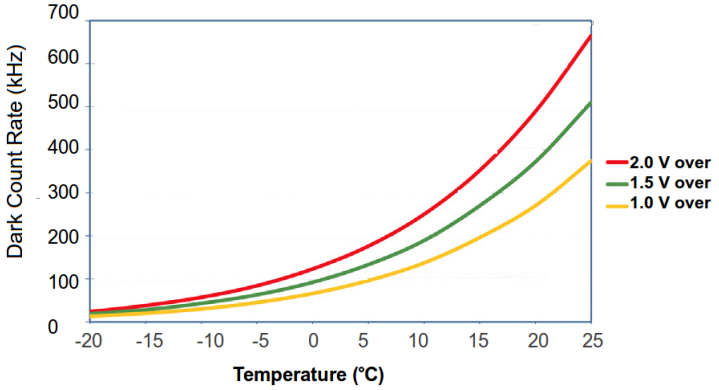

FIGURE 2.10: Dark count rate of SensL 1 mm, 35μm microcell silicon photomultiplier as a function of temperature and overvoltage [29].

rate of SensL silicon photomltiplier and temperature variation for three different overvoltage values. If the applied overvoltage remains constant over the measurement period at room temperature, SiPM gain, photo detection efficiency, and timing could be stable. However, a change in temperature with stable overvoltage will be altered by the dark count rate. Reducing the photodiode temperature by a thermoelectric cooling device will be decreased bt the dark count rate. Every 10°C

reduction in the temperature of the device provides a factor of a 50% decrease in the dark count rate for SensL silicon photomultiplier [29, 31].

Temperature variation also changes in the detector gain. When the temperature rises, the possibility of the collision between carries (electrons or holes) and crystal lattice increases before reaching the sufficient energy for ionisation. Therefore, detector gain at certain bias voltage decreases if the temperature increases. To obtain constant gain, bias voltage must be adjusted or the temperature must remain stable [31]. Figure 2.11 illustrates how overvoltage changes to minimise the bad effect of the temperature variation as a function of temperature that will result in a change of the breakdown voltage. SensL silicon photomultiplier has

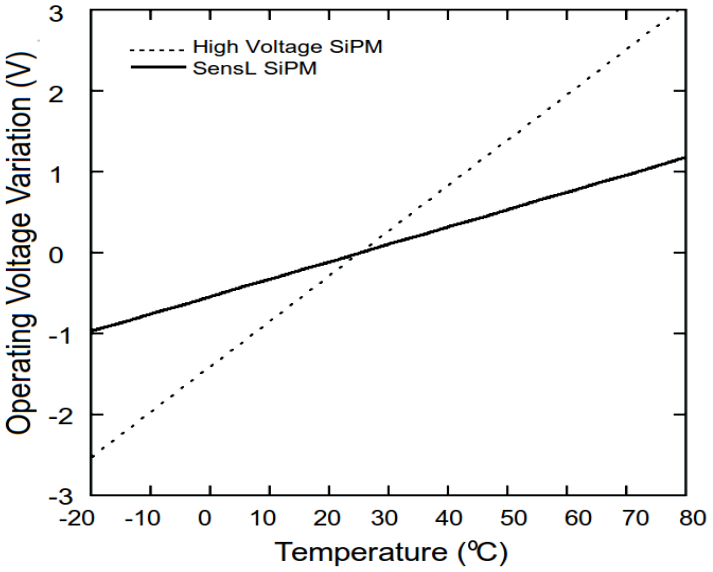

FIGURE 2.11: Temperature coefficients comparing SensL silicon photomultiplier and a high voltage SiPM [31]. Temperature variation for SiPM with high breakdown voltage is more influenced than SensL with a low breakdown voltage.

a low breakdown voltage (V_{BR}) because of having a narrow depletion layer and doping layer. Silicon photomultiplier sensors with higher breakdown voltage are very likely to be influenced by a change in temperature than SiPM with low V_{BR} as shown in Figure 2.11. A one degree variation in the temperature of the SensL SiPM will change only 21.5 mV. The temperature of SiPM can be fixed with either a thermoelectric cooling device or by regulating the device. If that is not possible, the bias voltage must be adjusted according to the altered breakdown voltage to keep the overvoltage value constant.

Pulse Shape

Signal rise time is a very important parameter in timing measurements. The rise time depends on the total area of the SiPM and capacitance which is caused from the total connection of microcells. They will be discussed in Chapter 4 in more detail. The rise time of 1 mm SensL SiPM is 1 ns, but 10 ns for 6 mm SiPM. Decay time or recovery time is expressed from the microcell reset period as given by the following equation;

$$\tau_{reset} = R_q \,.\, C \tag{2.13}$$

where R_q is quenching resistance and C is the microcells' effective capacitance. In Figure 2.12, a single photoelectron signal is demonstrated for SensL C series SiPM with a 6x6 mm^2 detection area and 35 μm microcell size detector coupled with a EJ212 plastic scintillator radiated by ^{137}Cs.

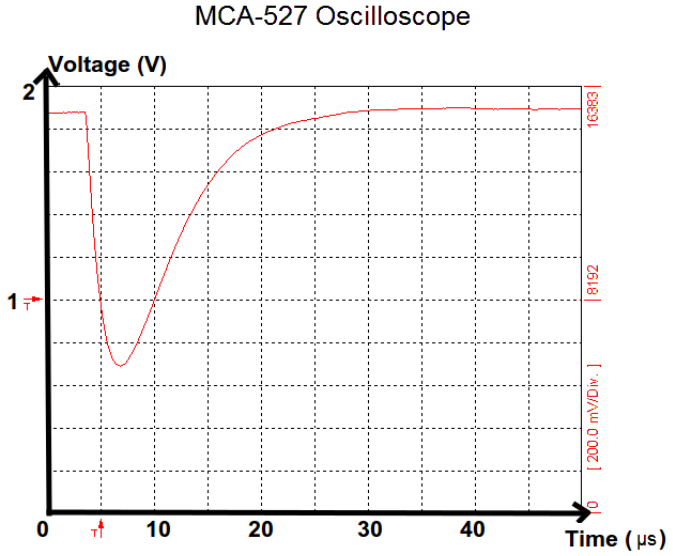

FIGURE 2.12: A single photoelectron pulse is generated by a 6 mm SensL C series. A Geiger mode silicon photomultiplier is coupled with a plastic scintillator.

Photon Detection Efficiency (PDE)

The photon detection efficiency (PDE) of SiPMs is defined as the statistical probability of converting incident photons into electrical signal. It is given by three factors: QE is the APDs' quantum efficiency as a function of incident photons wavelength, F is the filling factor of the device, which is the ratio of the photon sensitive area to the total pixel size with circuits, and $\in$ is the probability of the trigger a Geiger discharge with a function of bias voltage.

$$PDE = QE_{\lambda_{incident\ photon}} \,.\, F \,.\, \in_{v\,(Geiger)} \tag{2.14}$$

PDE is generally calculated by the average photo current generated per optical power from a detector response (R). That is defined as a fraction of measured photo current and incident optical power at a specific wavelength over the detection area. This method gives an over estimated value of PDE because it does not include the contribution of afterpulsing and crosstalk probability as defined in Equation 2.15 where G is expressed as SiPM microcells gain, h the Planck constant, c the speed of light, λ incoming light wavelength, and e charge.

$$R = \frac{PDE \,.\, G \,.\, \lambda \,.\, e_{electronic\ charge}}{h \,.\, c} \tag{2.15}$$

If crosstalk and afterpulsing probability contributions are taken into account in the APD response, photo detection efficiency will be calculated from Equation 2.16, where N is the number of incident photons, and ε and P_{ap} are the probability of crosstalk and afterpulse respectively.

$$R = PDE \,.\, G \,.\, (1+\varepsilon) \,.\, (1+P_{ap}) \,.\, N_{\lambda_{incident\ photon}} \tag{2.16}$$

Crosstalk

The crosstalk is one of the additional noise components in SiPM. Some photoelectrons generated in the avalanche process, can be produced by incoming photons which are initially incident on neighbour pixels of SiPM. Created photon reaches the neighbouring pixel in three ways; directly, inside the depletion layer, and through reflection [34]. A neighbour pixel might be triggered by another Geiger discharge. Consequently, there will be a higher number of photoelectrons in this event than normal. That can be seen as a large amplitude in the pulse (by factor two), and then deformation in device linearity will be observed. Crosstalk probability is defined as the ratio of the pulse rates from a SiPM measured at 1.5 times single photoelectron amplitude ($N_{1.5\ p.e.}$) to 0.5 times of that ($N_{0.5\ p.e.}$) as given in Equation 2.17;

$$\varepsilon = \frac{N_{1.5\ p.e.}}{N_{0.5\ p.e.}} \tag{2.17}$$

Crosstalk probability has almost no dependence on the temperature, but it increases with bias voltage and microcell size. Crosstalk and afterpulse events strongly depend on the current density [35]. A large pixel size will have a large gain, resulting in a high number of carries during the avalanche process as the same as the result of the high bias voltage. Therefore, the probability of crosstalk

and afterpulse become higher. Optically isolating each elementary pixel by trench technology and then filling with an opaque material is the best approach to reduce the optical crosstalk probability between neighbouring pixels. Crosstalk effects can also be reduced by improving the manufacturing process (e.g purity of the material reduces the defects).

Afterpulse

When microcell voltage is temporarily reduced by the quenching process to stop the Geiger discharge mechanism, not all photoelectrons can be cleaned in the sensitive area. Carries may be trapped by the lattice defects. After a certain time delay (recovery time), non-original pulses are realised following the true signal, which causes the detection error. Afterpulse depends on the bias voltage, doping level design of SiPM, recovery time, and temperature. At high temperature the trap carries lifetimes are shorter, so afterpulsing effect becomes weak at the fixed repetition time. The probability of trapping carries inside the crystal increases with lower temperature due to become long carries lifetime, therefore afterpulsing effect will increase [36]. A short detection width or large reputation period gives low released carries, hence afterpulse effect becomes weak according to the Equation 2.18;

$$N_r = P_D \,.\, N_{trap} \;\; \frac{exp(\frac{\Delta t}{\tau}) - 1}{exp(\frac{T}{\tau}) - 1} \tag{2.18}$$

where T is the repetition period, τ is trapped carrier lifetime, N_r is the average released carries within the detection width duration time ($\Delta\ t$), N_{trap} is the average trapped carrier in one breakdown, and P_D is the dark count probability.

2.4 Nuclear Instrumentation Module (NIM)

For the purpose of optimising the performance of a scintillation detector, signal shaping methods are essential to generate the appropriate pulse by nuclear instrumentation module (NIM) in particle and nuclear physics, particularly in timing measurement, as will be explained in Chapter 4. These electronic modules, such as amplifiers, MCA, and TAC, etc. can fit easily into the bin power, which supplies DC voltages during the measurements (Figure 2.13). This section will discuss the

general principle of signal shaping processes that are commonly used in radiation detection methods.

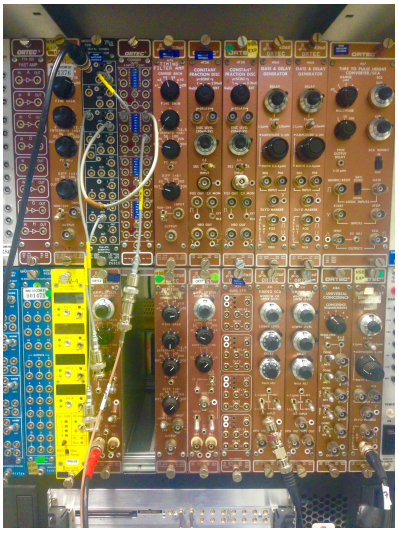

FIGURE 2.13: Common nuclear instrumentation modules are used worldwide in laboratories as a cost efficient experimental method, resulting in optimum pulse character in energy and timing spectroscopy.

2.4.1 Amplifiers

A pre-amplifier or amplifier are used for shaping the output signal of detector, and amplify the pulse amplitude for further signal processing. An amplifier is used to shape signals for optimum energy resolution and to reduce intersection between sequences of pulses. While long pulse widths are used to achieve an optimum energy resolution, short pulse widths are required for high counting rates. Therefore, different amplifiers are chosen according to which quality needs to be optimised in the measurements. See Appendix A.1 for common amplifiers used in nuclear and particle physics applications for pulse shaping processes.

The output pulse amplitude is deteriorated by pile-up phenomena, which occurs when two gamma rays arrive at the detector at the same time. Several pulses are seen inside the width of the amplifier output pulse at a high count rate. Delay-line pulse-shaping amplifier is well suited for avoiding a pulse pile-up phenomenon by returning immediately to the baseline. The basic delay-line shaping amplifier has replaced the original pulse after being inverted, delayed, and added back to the original pulse (Figure 2.14). As a result, the pulse in the last step will be a rectangular shape with a delay time the same size of the pulse width. A rectangular output pulse of a delay-line amplifier has the advantage of generating a fast

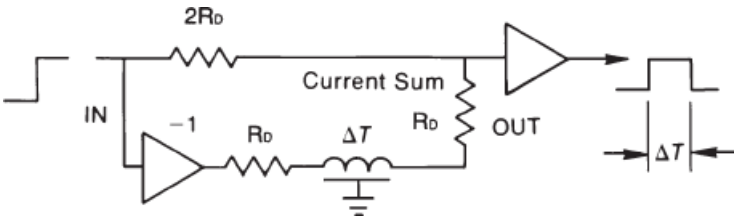

FIGURE 2.14: Pulse shaping circuit for single delay line [37]

rise time and fall time, so it is ideal for timing and pulse-shape discrimination measurement for scintillation detectors at low and high counting rates.

Figure 2.15 shows the basic circuit of a common pulse-shaping amplifier. The signal is first fed into a CR high pass filter, which improves the signal-to-noise ratio by attenuating a low frequency (Figure 2.15(a)). Then, a pulse passes through an RC low pass filter. A high frequency signal-to-noise ratio and the rise time of the pulse are improved by this second filter (Figure 2.15(b)). The last pulse shape is illustrated in Figure 2.15(c) after the signal has passed through both filters.

Generally, a CR-RC pulse-shaping amplifier is used for scintillation detector systems with the appropriate shaping time constant (τ), which should be at least three times the scintillation decay time constant in order to ensure complete integration of the scintillator signal for good resolution [25]. The pulse duration time of a CR-RC shaping amplifier is much longer than the output pulse of a delay-line shaping amplifier for scintillation detectors. In energy spectroscopy, for silicon and germanium detectors, the CR-RC pulse-shaping amplifier plays a critical role in the improvement of energy resolution by minimising noise.

2.4.1.1 Fast-Timing Amplifier

If the amplitude of a detector signal is sufficient for timing discriminator input, the best rise time and a low noise in timing resolution will be provided from raw output signals of the detector without an amplifier. When a detector signal requires amplification, a specific amplifier must be used to obtain an appropriate signal amplitude and output rise time (in a low nanosecond time range). A low noise and fast rise time play a critical role in timing measurements, but detector linearity and temperature stability are important characteristics of a detector. There are two different kinds of timing amplifiers: wideband and time filter. Wideband amplifiers are preferred because they can obtain good coincidence resolved time

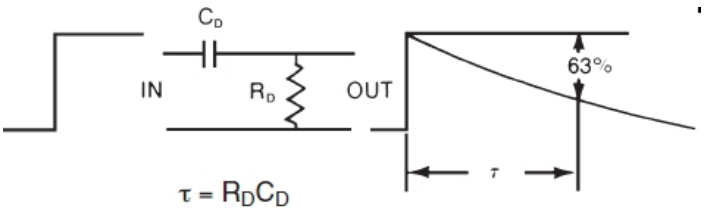

(a) CR high pass filter (differentiator).

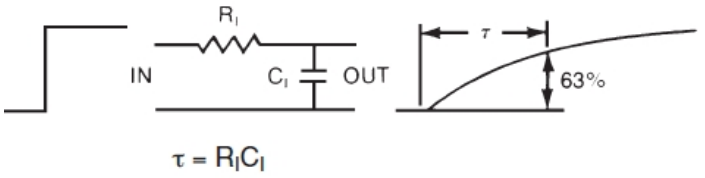

(b) RC low pass filter (integrator).

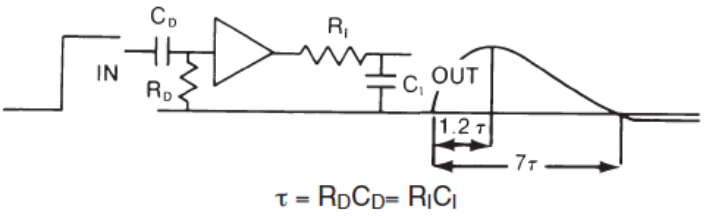

(c) Combination of CR-RC high pass and low pass filters.

FIGURE 2.15: CR-RC shaping amplifier circuit. (a) Improves signal-to-noise by attenuating the low frequency which is the source of the noise in the original signal. (b) Improves signal-to-noise by attenuating high frequency, (c) Combination of both filters and the output signal after applied CR-RC shaping amplifier [37].

for output signal of PMTs and silicon charged particle detectors. This type of fast-timing amplifier does not allow for control over the rise time or decay time of pulse. Both types of timing amplifiers (Ortec FTA820A, ZFL-1000 LN and ZX60-43+) have been used in timing measurement, and they will be detailed in Chapter 4.

Modification of the pulse shape is highly possible by timing filter amplifiers because CR high pass and RC low pass filters can be controlled separately. In timing resolution measurement, the intrinsic rise time of the preamplifier should be more than the rise time of the amplifier to avoid degradation of the signal rise time. If the rise time of the fast amplifier is excessive, that will result with more noise and will not improve the rise time of the signal. The differentiator time constant should be set to a time that is long enough to optimise signal amplitude. If the differentiator time constant is adjustable, it should be long enough to prevent

losing the signal amplitude.

2.4.2 Discriminator

Discriminators and single channel analysers are used for separation between pulse and noise.

2.4.2.1 Fast Timing Discriminator

If the signal is very narrow at high count rates and it is required to correctly define the arrival time of these pulses, a fast-timing discriminator must be used. The best time resolution and highest counting rates can be achieved with fast-timing discriminators. In counting applications, the analogue input pulses are converted into standard logic pulses by using timing discriminators. The applied threshold level, which is adjusted just above the noise, allows only real events to be counted without counting noise in the timer or a multichannel scaler. Fast detectors (such as PMTs, microchannel plate detectors, etc.) are used for single photon and ion counting applications. They have a very short pulse width, therefore 5 ns pulse-pair resolution can be achieved with the fastest discriminator. For scintillation, germanium and silicon charged particle detector systems have a much longer pulse width, so achieving pulse-pair resolution will be with a much higher threshold level. When a fast timing discriminator is used for counting and coincidence time measurements, the dead time will also limit the experimental results.

In timing applications, the essential principle of the timing discriminator is consistently and precisely determined by detected radiations' arrival times. The achievement of optimum time resolution is a very critical phenomenon for several applications, such as time spectroscopy and time-of-flight measurements in nuclear physics and positron emission tomography. The optimum time resolution can be achieved with the right timing discriminator, which depends on the characteristics of the detector. There are three important factors that affect optimum timing resolutions: jitter, walk, and drift as illustrated in Figure 2.16. A logic pulse is generated if the leading edge analogue pulse intersects with the threshold level. The initial point of the logic pulse is the analogue pulse arrival time. Many discriminators do not minimise electronic noise level, so noise creates time uncertainty or jitter in the pulse. In Figure 2.16, there are two similar shape pulses with different pulse amplitudes. The highest height signal first meets with the discriminator threshold level, and then the smallest pulse. This causes variation in the initial

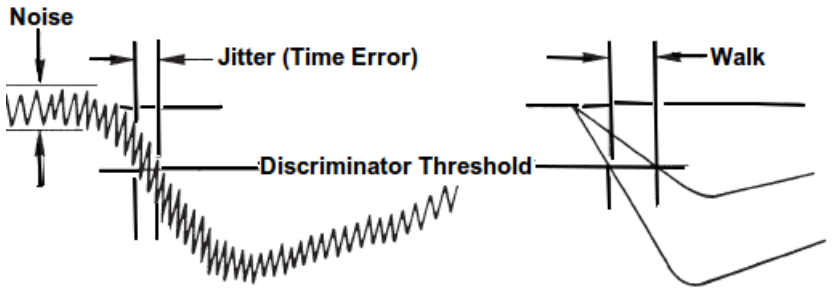

FIGURE 2.16: A simple leading-edge timing discriminator. The signal was set to an appropriate threshold level to generate a logic pulse. Jitter and walk occur during the generation of the logic pulse in a leading edge method [38].

arrival time of logic pulses, which is called time slewing or walk. If a logic pulse amplitude has a wide range, the walk will cause critical deterioration of the time resolution measurement. However, the effect of the walk in time resolution can be optimised by applying zero-crossing technique or constant fraction discriminator methods. The component age and temperature variations in the electrical circuits for long measurement periods will be contributed as a long term error or drift. As a result, the time resolution obtained will be worse.

2.4.2.2 Single Channel Analyser (SCA)

Analogue pulse amplitude is directly related to the detected radiation's energy. Therefore, a selected signal height will be directly proportional to energy range or event charge. Discriminators and single channel analysers are used for achieving energy selection.

An output logic pulse is generated when input signal takes over the threshold level in a discriminator. The output signal is produced if the input pulse amplitude is inside the window in a single-channel analyser. Therefore, there are two threshold levels, upper and lower, in an SCA module.

2.4.3 Time Amplitude Converter (TAC)

A time amplitude converter, or TAC, transfers small time intervals between two pulses into pulse amplitude. Electrical circuits of a TAC module have an on and off switch for the start pulse and stop pulse. When an input signal is fed to a TAC, a charged capacitor gives the voltage as proportional to the time interval. After

a few milliseconds, all switches close down for a short period of time to prepare for the next start-stop event. Therefore, one output pulse of a TAC will be a rectangular signal and the pulse height will be the time differences between the start and stop pulse. A TAC output pulse is fed to a multichannel analyser (MCA) or an analogue-to-digital converter (ADC) for the pulse height measurement.

2.4.4 Multi Channel Analyser (MCA)

Multi channel pulse height analysers are commonly used in nuclear physics for recording energy or time spectra. MCAs sort input signals according to the signal amplitude. The signals are divided into different channels based on an analysis of the analogue pulses. Each detected event produces an amount of electrical charge, so the charge will be proportional to the detected photon's energy. The charge is collected on a preamplifier to be converted into a voltage pulse with little added noise. Differentiators and integrators are applied with an amplifier to improve signal-to-noise ratio and increase the pulse height. Consequently, each output pulse has a duration in the order of microseconds. Filling the histogram according to the pulse amplitude and keeping records will give the energy spectrum of detected incident radiation. A MAESTRO multi channel analyser was used in experimental measurements. Acquisition data was converted in ROOT software to find the resolution and important parameters.

2.5 Various Inorganic Scintillator and Experimental Results

This section will discuss experimental results, which have been carried out with different types of scintillation detector systems. Figure 2.17 shows the experimental setup of detector systems. Various scintillation crystals are coupled with different types of photomultiplier devices such as APDs, SiPMs and PMTs.

2.5.1 NaI(Tl)

Thallium activated sodium iodide was used broadly as a detector inside positron emission tomography in its early period. The biggest advantage of using NaI(Tl) as

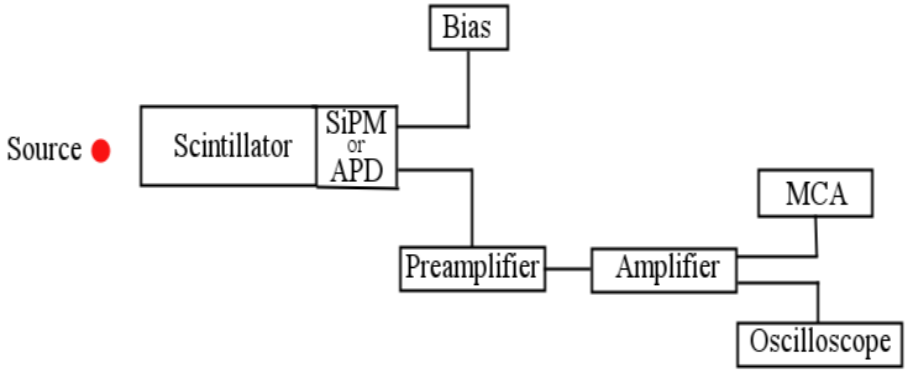

FIGURE 2.17: Experimental set-up for various scintillation detector systems.

a PET detector is that it had excellent light yields compared to other scintillators at that time. However, its popularity dramatically decreased after the discovery of new scintillation crystals, such as bismuth germanium oxide (BGO) because of their more valuable properties. NaI(Tl) has a lower detection efficiency than BGO for detecting 511 keV energy γ-rays (annihilation photons). In fact, it also has a relatively ineffective atomic number and density compared to other crystals (see Table 1.1 in Chapter 1). Thallium doped NaI is a hygroscopic scintillator and it is not easily packaged for a specific detection volume with keeping away from moisture for the long term.

2.5.2 BGO

The effective atomic number and density of BGO are much higher than that of NaI(Tl), so it has better detection efficiency. However, the decay time constant is very slow with low light output and it is a very costly crystal. Therefore, it is not preferred for coincidence measurement and BGO is not a particularly good choice for a PET detector, which is important for the detection of the annihilation.

2.5.3 LSO and LYSO

Lutetium oxyorthosilicate (LSO) and lutetium-yttrium oxyorthosilicate (LYSO) are different from other scintillators because of their intrinsic background radiation. They contain a natural radioactive element called ^{176}Lu, but this is not a serious problem for positron emission tomography. Background photons energy in LYSO or LSO is between 88 keV and 307 keV, which are absorbed by the crystal

itself. These photons create only 39 counts per second per gram (cps/g) [11, 12]. Setting energy window only for annihilation photons makes these scintillators suitable in PET devices to benefit from their very fast decay time constants. After NaI(Tl), these scintillators have been used in PET devices and have become more popular in nuclear medicine. They have better 511 keV γ-rays detection efficiency, coincidence timing resolution, and energy resolution. Being mechanically rugged and having non-hygroscopic properties also gives them an advantage over other scintillators. However, they can be very expensive if a large volume is required for the detector. Many research groups have successfully used these scintillators inside PET-MRI capability devices. As a result, high-resolution performance in brain tomography has been obtained [8, 16, 17, 39].

2.5.3.1 Making PET Detector

This section will discuss the making of a simple PET detector array process. In modern PET, TOF-PET, or PET-MRI devices include more than thousands of this detector array.

Cutting crystals and physical polishing

Hilger Crystal 3.5×4×60 mm^3 LYSO and BGO scintillators were cut by a low speed diamond wheel saw cutter as shown in Figure 2.18. There, different lengths of crystals were obtained (10, 20 and 30 mm). After cutting all scintillators, the York Nano Centre's lapping machine was applied on the crystals' cutting sides to make them smooth. This process was successfully carried out by thick pads for optical polishing, and then a 5 μm pad was used for fine polishing (Figure 2.18). Furthermore a polishing method called chemical polishing, is based on heating the crystals between 110-190°C with a concentrated acid solution such as phosphoric acid. The chemical polishing method is applied by a few research groups for the purpose of improvement of more than 1% scintillation efficiency and energy resolution while reducing cost and polishing process time. Slates et al reported that chemical polishing is a more suitable and effective way to increase light collection, which in turn improves energy and timing for narrow rectangular crystals [40]. We also considered applying chemical treatment to crystals. However, the improvement would be too significant; in addition, this facility is not accessible in the department.

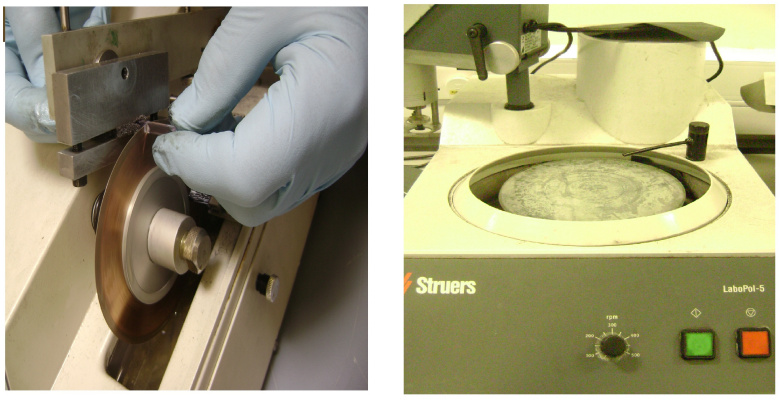

FIGURE 2.18: A diamond wheel saw cutter was used for cutting LYSO and BGO sticks without damaging the crystals (left). A lapping machine was employed to make the cutting face of crystals smooth (right).

Reflector

Reflectance materials with high reflectivity play a critical role in the improvement of light collection from the scintillator to the p-layer on the surface of the photomultiplier diodes (efficient light transportation). Generally, PTFE (Polytetrafluoroethylene) Teflon based reflector, Al foil, and black insulating tape are used as wrapping materials in detector application technique. First, the detector is wrapped with PTFE Teflon based reflector to minimise the scintillation light loss for obtaining optimal light collection. And then Al foil is used to minimise the ambient light effect. The last layer is wrapped with black insulating tape to ensure light-tightness. Detector energy resolution can be improved by 2% by wrapping carefully and using more effective reflector material. Covering the detector with six layers of Teflon tape and a backing layer with 3M VM2000 radiant mirror film around the detector successfully reduces the energy resolution from 11.6 % to 7.8 % for a BGO scintillator [41]. In our case, wrapping such a thick material is not suitable for array structures due to the 2 mm space between the array grid material and scintillator. Therefore, each crystal surface is wrapped in several layers with PTFE thread seal tape 0.075 mm thickness Teflon based reflector and then very thin radiant mirror film. The entire detector is finally wrapped with black isolating tape.

Making grid

A three dimension printer was used to make a 4×4 array grid. Each square size matched the crystal size exactly, adding extra space ($\approx$ 2 mm) for very thin

PTFE. First, a prototype array was drawn in SketchUp, a 3D modelling software program, and then it was printed, as demonstrated in Figure 2.19. After physically

FIGURE 2.19: An example of an array grid was drawn in Google SketchUp 3D modelling software program with a size similar to the crystals. The array was obtained from a 3D printer. The main material of the grid was plastic. $4.5\times3\times10$ mm^3 LYSO crystals were placed inside the grid after being covered with several layers of PTFE (thread seal tape 0.075 mm thickness Teflon based reflector [42]) and then a very thin radiant mirror film.

polishing and cutting scintillation crystals, 16 identical LYSO were placed inside the grid.

Testing the array detector

4x4 array LYSO crystals were optically coupled to position-sensitive SensL 4x4 array silicon photomultiplier. SensL SiPM array offers the determination of the depth-of-interaction (DOI), faster response, and high gain in the order of 10^6 for each pixel. Visible light sensitivity range is between 400 nm and 850 nm. Each pixel has 3640 microcells with 35 μm cell size and 200 μm space between two pixels. Optimum performance of SensL 4x4 array obtains at a low bias voltage $\sim$30V with 2V above the breakdown voltage. The dark count rate is 8 MHz per pixel and photo detection efficiency is 10-20% at maximum wavelength (λ_{max} = 520 nm) [12, 43]. The SensL SiPM is connected by flexible printed circuit (FPC) cables to four separate mother boards as demonstrated in Figure 2.20. This SiPM can be operated in the magnetic fields by using shielded FPC cables [43]. The main board reads either individual pixel signal or multiple signal outputs together (16 pixels) as a large pulse. Electrical circuits of 4x4 array SensL solid state silicon photomultiplier are shown in Figure 2.21. Each output is connected with other outputs to FPC cables by a crocodile clip. Therefore, every pixel can be read and analysed by an amplifier, time-filter amplifier, or oscilloscope. The energy spectrum was obtained by a radiated detector with a standard ^{137}Cs radioactive source. Only one pixel signal was sent to the Ortec 572 shaping amplifier and then fed to a maestro MCA. It only examined energy resolution, not position sensitivity.

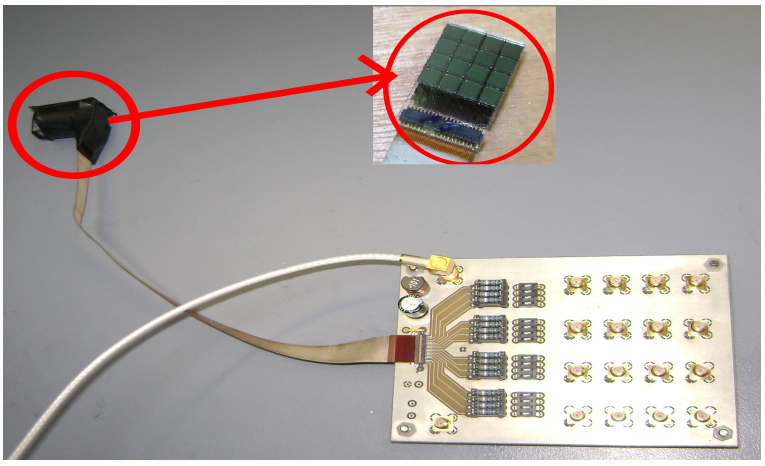

FIGURE 2.20: SensL 4x4 array of 2.8 x 2.8 mm^2 pixel position sensitive SiPM was connected to an electronic board via flexible printed circuit (FPC) cables. Output signal can be read either individual pixel or 16 pixels together by readout board.

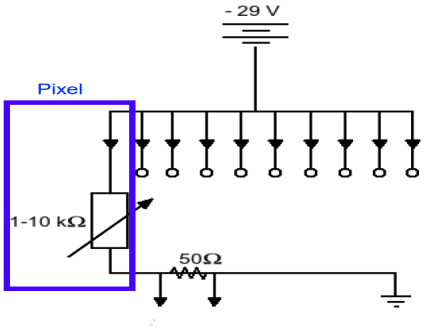

(a) Equivalent circuit diagram of SensL 4x4 array. Each pixel includes light sensitive Geiger mode avalanche photodiode connected in series with a quenching resistor.

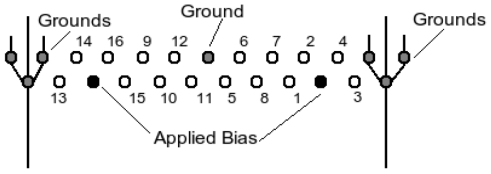

(b) Some outlets are grounded and the applied bias. Two channels are fed into the bias to power 8 of the 16 pixels, which are upper (1-8 pixels) and lower (9-16 pixels) as shown in Figure 2.21(c).

1	2	3	4
5	6	7	8
9	10	11	12
13	14	15	16

(c) Upper and lower 8 of the 16 pixels.

FIGURE 2.21: 4x4 array SensL position sensitive silicon photomultiplier electronic board circuit. It is used to read output pulses separately or together [12].

In Figure 2.22, the energy spectrum of Cs-137 was found to be very noisy, and poor energy resolution ($\sim$ 43.8 % at 662 keV). One of the pixel on array SiPM was broken, so it could cause a noise in the output signal. In addition, detector wrapping was not sufficiently completed because of significantly less space between the scintillator and plastic grid, therefore excessive loss of scintillation light.

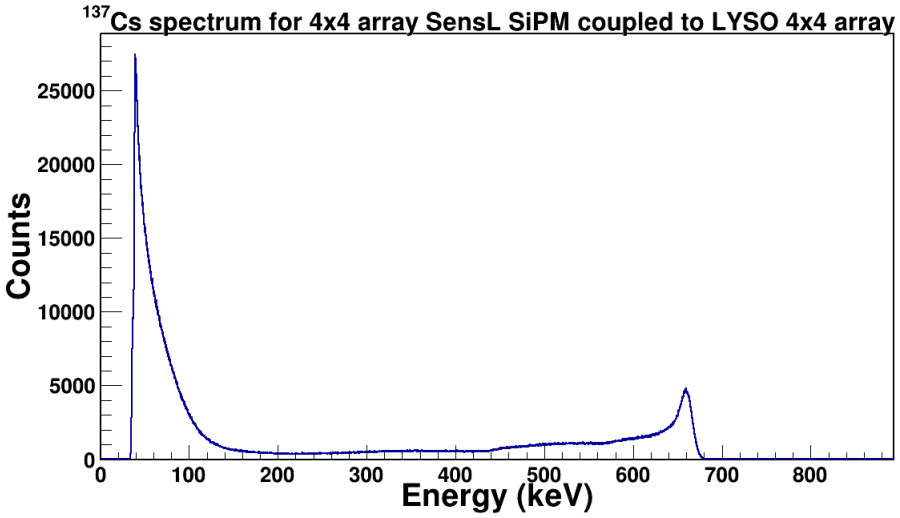

FIGURE 2.22: 4x4 array 16 LYSO scintillator (one crystal size is $4.5\times3\times10\text{mm}^3$) were coupled with the SensL 4x4 array silicon photomultiplier. Cs-137 energy spectrum took only one of the 16 pixel signal outputs. $\sim$ 43.8 % at 662 keV

2.5.4 CsI(Tl)

Thallium activated caesium iodide inorganic scintillation crystals have a low effective atomic number and density, but have very high light yield as illustrated in Table 1.1. Compared to NaI and BaF_2, CsI has higher stopping power because of its relative high density and atomic number, therefore, they have higher γ-ray stopping power. CsI is cost effective, less expensive, and less hygroscopic material than NaI(Tl) crystals, but it should still avoid contact with water and high humidity conditions. The physical properties of CsI are independent of the doping material, so it is easily machined in different shapes due to being soft and plastic. Generally, CsI is used in space instrumentation or applications in thermal shock conditions, because it is relatively quite rugged and more resistant to thermal and mechanical shock conditions [44, 45]. The average decay time constant is relatively slow (about 1 μs) compared to other scintillators, therefore timing resolution is undesirable as discussed further in Chapter 4. CsI(Tl) consists of two decay times with 0.6 μs the fastest component and 3.5 μs the slowest component. It can be used with suitable shaping time of the electronics, which is between 4 and 6 μs for the high count rate capability detector [45]. The ratio of the two decay time component intensities depends on the ionising power of the absorbed radiation if it is excited with highly ionising radiation such as α-particles or photons. Therefore, CsI(Tl) scintillation can be used for particle discrimination by pulse shape analysis [45].

One of the brightest scintillators, CsI, was obtained from Saint-Gobain crystals with a quoted 54 photons/keV light yield at 550 nm maximum peak emission. The optimum sensitivity for normal bialkali photocathode PMT is not well-suited with light output of the CsI scintillator; that is the reason the light yield is effectively low [44]. For instance, the amount of the photoelectron yield is only 45% of the value of NaI [45]. However, the emission wavelength range and sensitivity of CsI(Tl) is well-matched with photodiode or SiPM. A SensL 4x4 array silicon photomultiplier was optically coupled with CsI(Tl) scintillation crystal by silicon grease (EJ-550). All of the pixel output signals were sent to a shaping amplifier, and then the energy spectrum was acquired by an MCA as shown in Figure 4.27. Energy resolution was found to be very poor ($\sim$ 19.7 %), but this is unsurprising

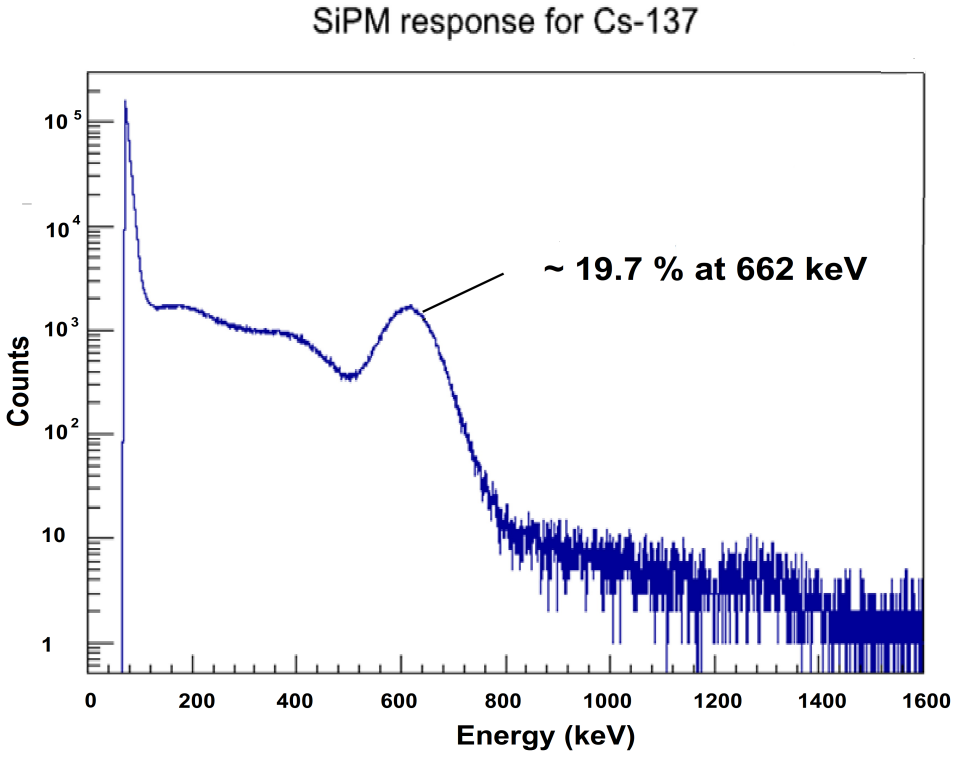

FIGURE 2.23: CsI(Tl) is tested with SensL 4x4 array SiPM. Energy resolution was found to be 19.7% at 662 keV.

because of its intrinsic resolution and slow component of the light pulses.

2.5.5 $LaBr_3$ (Ce)

Recently a new generation of inorganic caesium activated lanthanum bromide has become a very popular scintillator, with excellent timing ($\sim$200 ps) and energy

resolution (∼2.8 % at 662 keV) [12]. The very high light yields (60,700 photons/MeV) and the detection efficiency of lanthanum bromide give it a definite advantage over the other scintillators with its fast emission, high stopping power for γ-rays, and excellent temperature linearity. However, $LaBr_3$(Ce) has internal activity due to having natural unstable isotopes ^{138}La and ^{227}Ac contamination, so the background radiation energy range is between 1,500 keV and 2,750 keV [46]. It is also a very hygroscopic material, so it has to be housed in air-tight containers enclosed with aluminium to protect it from moisture in the air. Scintillation light transmission is provided by quartz window on the container for readout.

0.5" length x 0.5" radius $LaBr_3$(Ce) was optically coupled with single silicon avalanche photodiodes by silicon grease. Hamamatsu avalanche photodiodes with 5x5 mm^2 and 10x10 mm^2 photosensitive areas were used in this measurement, as illustrated in Figure 2.24. Several layers of PTFE, aluminium foil and black tape

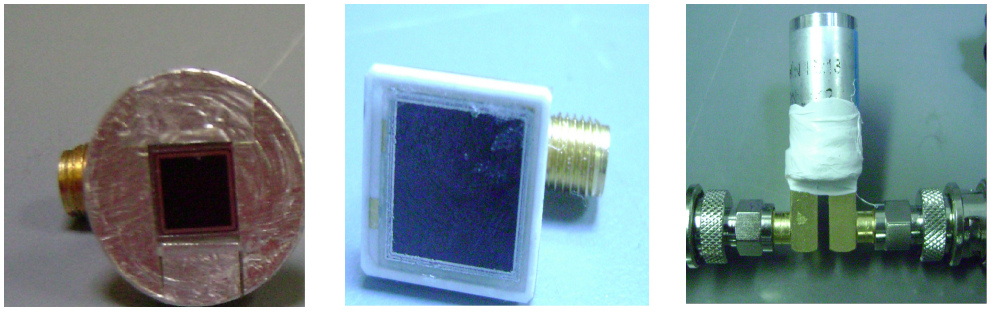

(a) Hamamatsu single avalanche photodiode with 5x5 mm^2 size.

(b) Hamamatsu single avalanche photodiode with 10x10 mm^2 size.

(c) Saint Gobain $LaBr_3$(Ce) crystal is optically coupled to APDs with silicon grease.

FIGURE 2.24: Hamamatsu avalanche photodiodes with (a) 5x5 mm ^{2} and (b) 10x10 mm ^{2} effective photosensitive area. (c) 0.5" length x 0.5" radius lanthanum bromide is optically coupled to Hamamatsu APDs.

were covered around the detector for light tight and optimum light output. Two identical detectors were prepared with different sizes of avalanche photodiodes. Standard ^{60}Co radioactive source (370 kBq) was placed at 0.5 cm distance from the detector. Radiation exposure time was set to approximately five minutes for both detector systems. A detector signal was first fed into the Ortec shaping amplifier, and then passed to a single-channel Ortec MCA running maestro software. The signals are then histogrammed into an energy spectrum for analysis. The energy resolutions were found to be 4.5% and 3.5%, that are the full-width-half-maximum (FWHM) of 1.17 MeV and 1.33 MeV photo-peaks respectively for 10x10 mm^2 APD (Figure 2.25). This result is better than the energy resolutions of 5x5

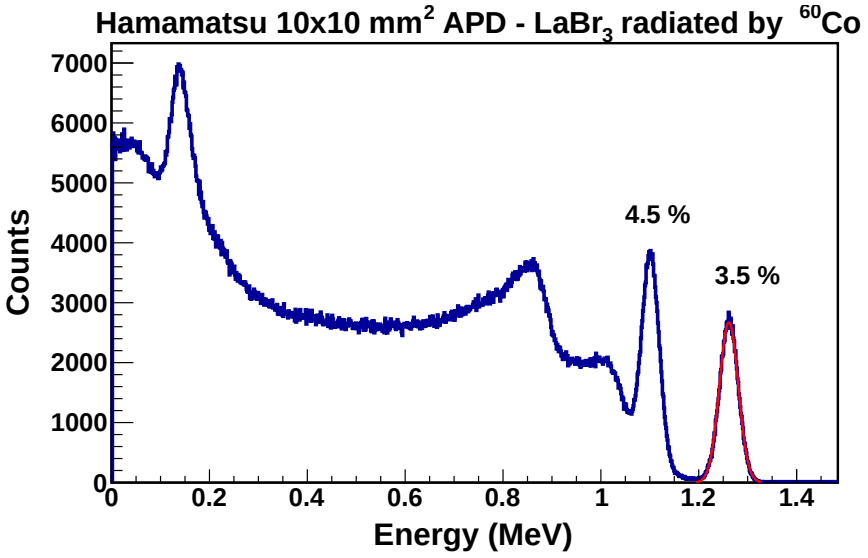

FIGURE 2.25: ^{60}Co energy spectrum was acquired by $LaBr_3$ optically coupled with 10x10 mm^2 APD.

mm^2, which were 5.4% for 1.17 MeV and 4.2% for 1.33 MeV. The energy resolution performance with 10 mm APD was better than a 5 mm APD, mainly as the quartz window surface area of the scintillation crystal was well-suited with a 10x10 mm^2 photosensitive area APD. When the window surface area is bigger than the sensitive area of the photodiode, the scintillation light transmission number from the crystal into the photodiode becomes lower than the similar size of photodiode and quartz window. The optimum obtainable energy resolution is influenced by the crystal heterogeneity, uniformity in light collection efficiency, photodiode performance, and the number of detected photons statistics. However, the primary limiting factor in the energy resolution is the scintillation light yield [47].

A 5x5 mm^2 APD-$LaBr_3$ detector system was examined inside $\sim$ 1 Tesla magnetic field. Two cylindrical pole electromagnets (dipole electromagnet) use the electric current to generate constant magnetic field as illustrated in Figure 2.26. Two coils are surrounded by electrically isolated water with an internal over temperature lock switch. Cooling coils with water allows to obtain higher coil current. At the university of York magnetism laboratory, one Tesla magnetic field was obtained by dipole electromagnet.

$LaBr_3$ and 5x5 mm^2 Hamamatsu avalanche photodiode were optically coupled by silicon grease. Then the detector system was placed in one Tesla magnetic field. Output signal was fed into the shaping amplifier and then sent to Ortec MCA running maestro software. A standard ^{137}Cs (370 kBq) was located in front

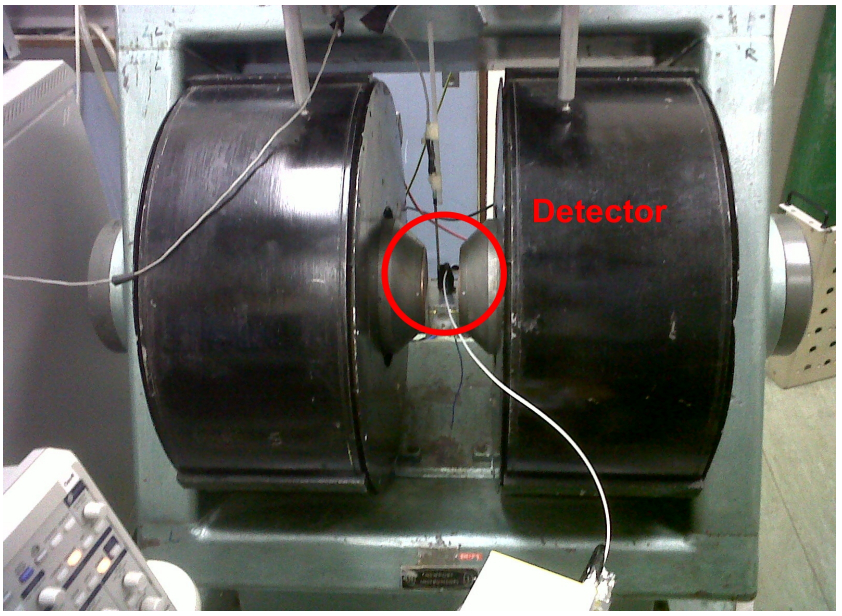

FIGURE 2.26: $LaBr_3$ and 5x5 mm^2 Hamamatsu avalanche photodiode were optically coupled by silicon grease. Then the detector system was placed in one Tesla magnetic field, which is obtained in the university of York magnetism laboratory. The electric current is used to generate constant magnetic field by dipole electromagnet (two cylindrical pole electromagnets (black)).

of the detector. The energy spectrum was obtained separately, with and without magnetic field. Energy resolutions at 662 keV were found to be 6.67% for magnetic field applied and 6.66% without magnetic field as shown in the statistical fitting parameters in Figure 2.27. Therefore, there is no magnetic field interference in the detector's energy performance.

After this satisfactory result, the same detector was tested in an MRI machine to examine the interference in the magnetic resonance image. The same set-up was established in the York Neuroimaging Centre without a radioactive source as demonstrated in Figure 2.28. A detector was put into a brain phantom, which is a plastic ball filled with paramagnetic substance. Nuclear magnetic resonance horizontal cross section images were successfully acquired as illustrated in Figure 2.29, when a scintillation detector system was interfaced in a homogeneous magnetic field. From top to bottom, there is 5.5 mm gap between each transaxial slices. The first image is taken in 5.5 mm depth of the phantom surface, and others going through the depth of the phantom with 5.5 mm gap. As illustrated in Figure 2.29, there is slight deterioration in the reconstructed MR image of the phantom (bright white pattern as illustrated by detector). Magnetic field homogeneity must be degraded by the detector current and few connectors.

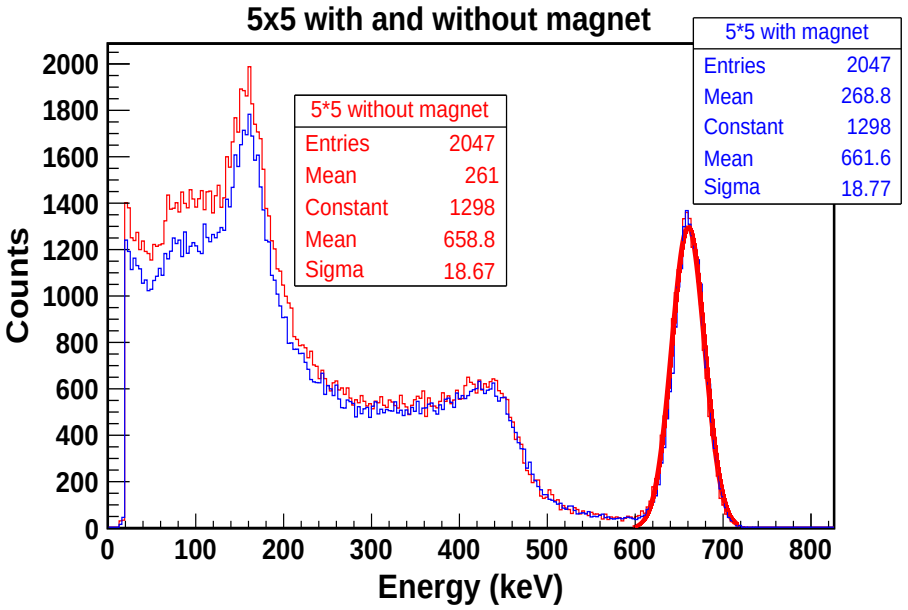

FIGURE 2.27: Cs-137 energy spectrum was obtained separately, with and without one Tesla magnetic field. Energy resolutions were found to be 6.67% when 1 Tesla magnetic field was applied. The energy resolution without the magnetic field was 6.66%.

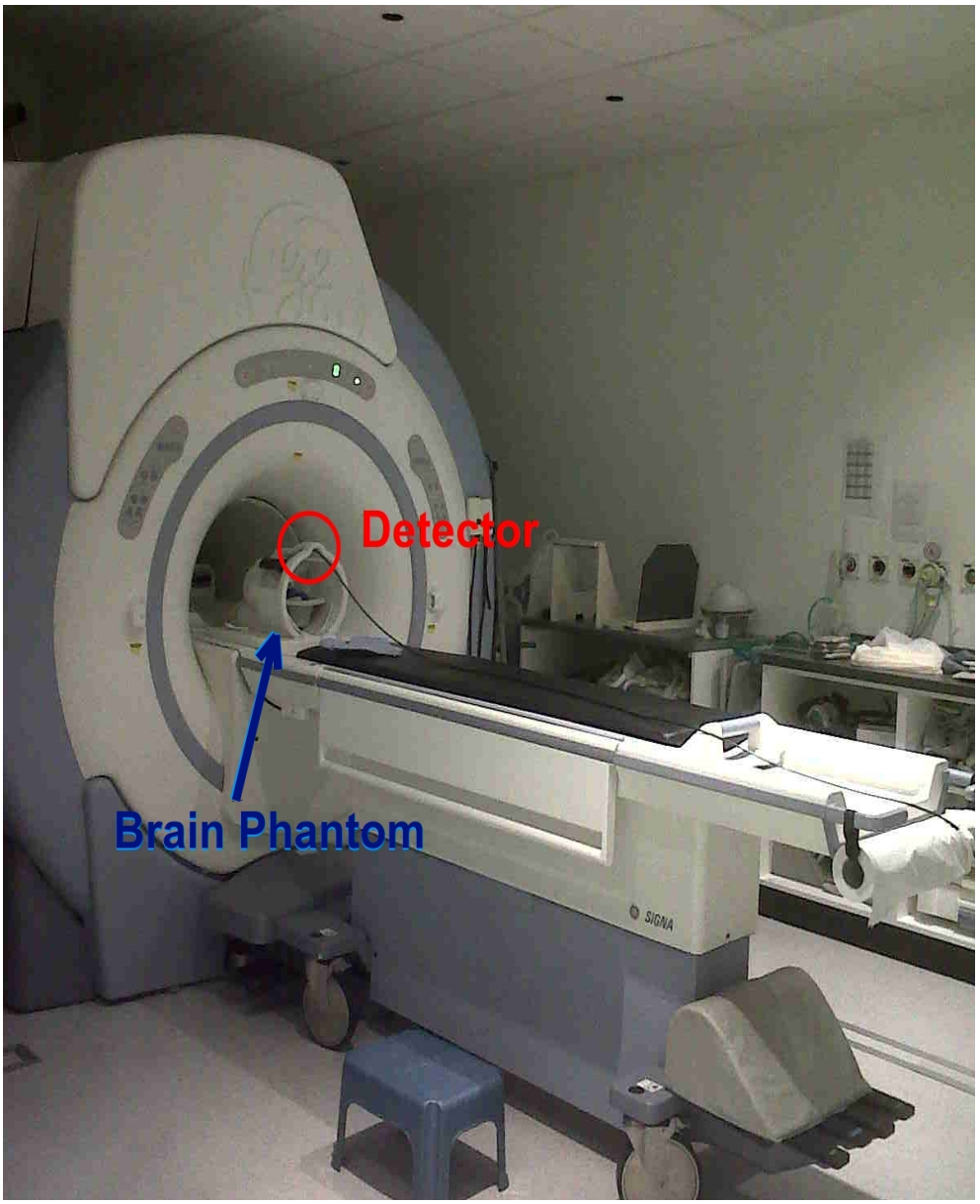

FIGURE 2.28: Magnetic resonance imaging scanner in the York NeuroImaging Centre. The detector system was placed into a brain phantom, and a cross-sectional medical image was obtained. While the MRI device was operated for medical imaging, the power supply of $LaBr_3$-APD detector system was set to work and each stage was checked on the oscilloscope.

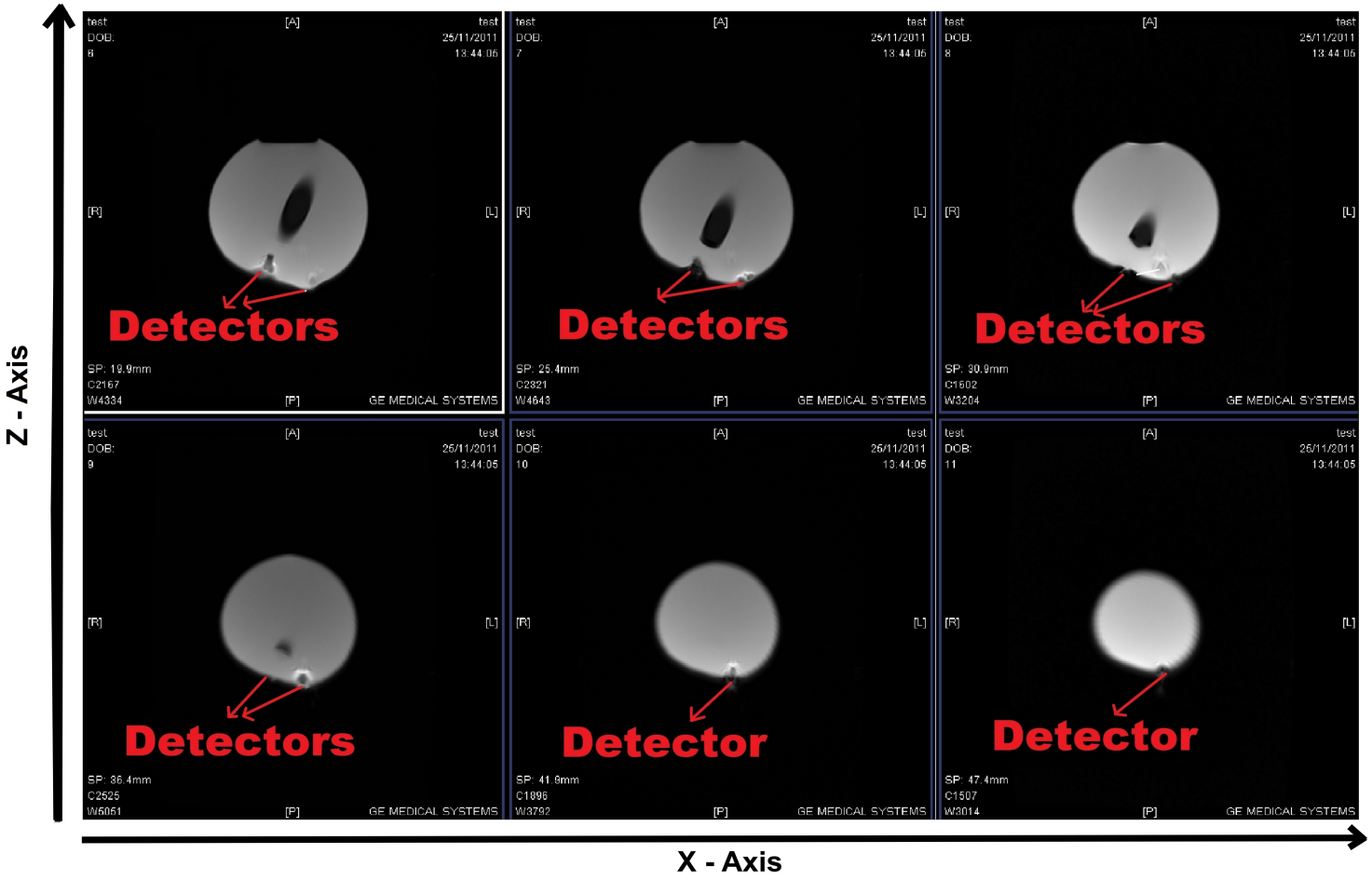

FIGURE 2.29: Nuclear magnetic resonance horizontal cross section images were successfully acquired after placing a scintillation detector system into the brain phantom at the York NeuroImaging Centre. From top to bottom, transaxial slices were obtained with 5.5 mm gaps in axial plane (transverse). The first image belonged to the top of the phantom, and going through the depth of the phantom. For this reason, the visible effect of the detector current on MRI image decreased by becoming away from the detector. There are sight scintillation detector influences on the last three MRI images.

Experimental measurements must be carried out without a radioactive source, because using a standard source in the NeuroImaging research centre is strictly forbidden due to health and safety local rules for ionising radiation. Therefore, an energy spectrum could not be taken with a scintillation detector inside 3 Tesla MRI field. However, as seen previously in Figure 2.27, we know that there is no significant magnetic field impact on the energy spectrum. Yet, there was a high frequency seen as a noise on the oscilloscope signal during the data acquisition time, which originated from the Larmor frequency. That frequency (127.7 MHz) is referred to the rate of precession of the magnetic moment of the proton around the external homogeneous fields in 3 Tesla MRI. Therefore, the shielding box could reduce of the noise on the detector caused by the radio frequency. It also needs to be shielded to avoid electronic oscillations such as power supply, amplifier, and MCA module. Non-magnetic and good electrical shielding materials, such as copper and aluminium can be used for shielding.

2.5.6 Phoswich (Phosphor Sandwich) and PARIS

Two or more scintillators optically coupled with each other like a sandwich is called a phoswich detector. This type of detector was developed for efficient detection of low energy radiation in a higher energy ambient background radiation. Some phoswich detectors were also designed to detect all energies simultaneously and separately. Phoswich scintillators must have dissimilar pulse shape characteristics and different rise and decay times. Therefore, rise time analysis of signals from a phoswich detector gives an opportunity to distinguish incident radiation, which can be a mixture of charged particles (β) and gamma rays. It also allows for the separation and identification of which events occurred in which scintillators.

PARIS (the Photon Array for studies with Radioactive Ion and Stable Beams) is a new, highly efficient gamma ray calorimeter used to detect gamma-rays in the large range energy from 100 keV to 50 MeV. The combination of a 2"x2"x2" size $LaBr_3$:Ce fast scintillator and a 2"x2"x6" size NaI(Tl) slow scintillator was sealed in an aluminium can with glass windows for light transfer. That is optically coupled with the PMT (Hamamatsu R7723-100), which in some cases can be easily modified for APD or SiPMs. Figure 2.30 demonstrates the PARIS phoshwich detector configuration.

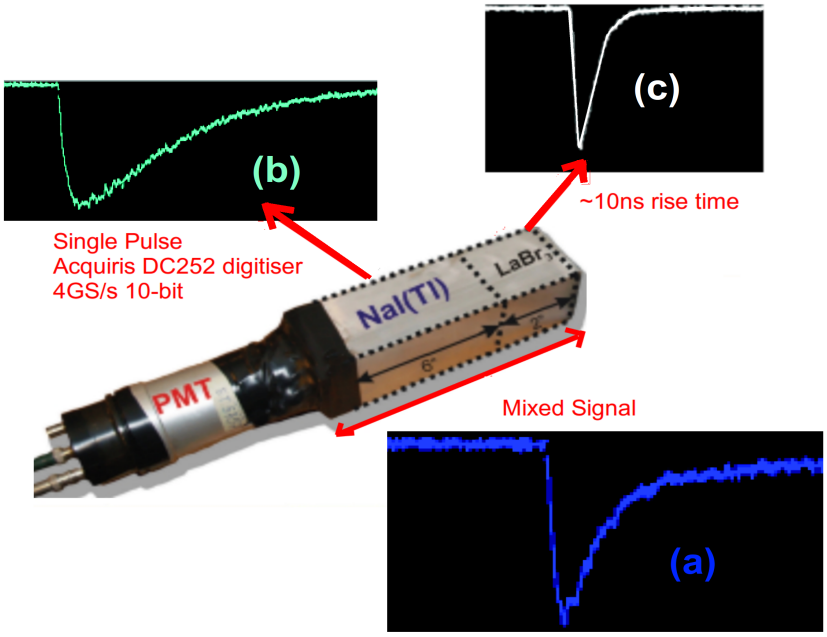

FIGURE 2.30: A single phoswich detector with a PMT is shown in the middle. The detector is designed by the combination of a fast scintillator $LaBr_3$ and slow scintillator NaI(Tl). Data accusation was acquired by DC252 digitiser. (a) The blue signal illustrates a single event detected by both scintillation detector combination, which is called phoswich. After applying the pulse shape analyser on the mixed signal, two separate pulses were acquired by using the difference between two scintillators' decay time. (b) The slow decay time component belongs to NaI(Tl), which is illustrated as cyan colour signal tracer. (c) The white signal with fast decay time constant (nearly 10 ns) was obtained by $LaBr_3$(Ce).

A Phoswich should give a good performance for high-energy range (to 50 MeV) gamma rays as well as low-energy range (from 100 keV). We have investigated the performance of the existing phoswich detector system and $LaBr_3$ response at high energy γ radiation, using radioactive source and nuclear reactions. Experimental set-up, which was performed with three phoswiches and a single $LaBr_3$(Ce) detector system is illustrated in Figure 2.31. ^{27}Al(p,γ)^{28}Si resonance reaction occurred with a 992 keV proton beam delivered by an accelerator at IFJ PAN in Kraków, Poland. Populated energy levels are clearly seen with $LaBr_3$ up to 12 MeV as illustrated in Figure 2.32.

Pulse shape discrimination had to be applied to define separate contribution of the slow (NaI(Tl)) and the fast component ($LaBr_3$) of the phoswich detector. An advanced Pulse Stretcher (APS) module, which was developed in Milano, was used for the discrimination method. Two Gaussian signals were obtained by the

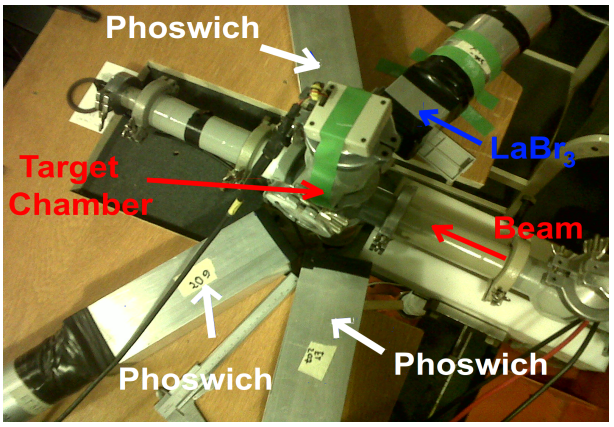

FIGURE 2.31: An experimental set-up is performed with three phoswiches and a single $LaBr_3$ detector system. Proton beam with 992 keV was conducted by Van de Graaff accelerator in Kraków.

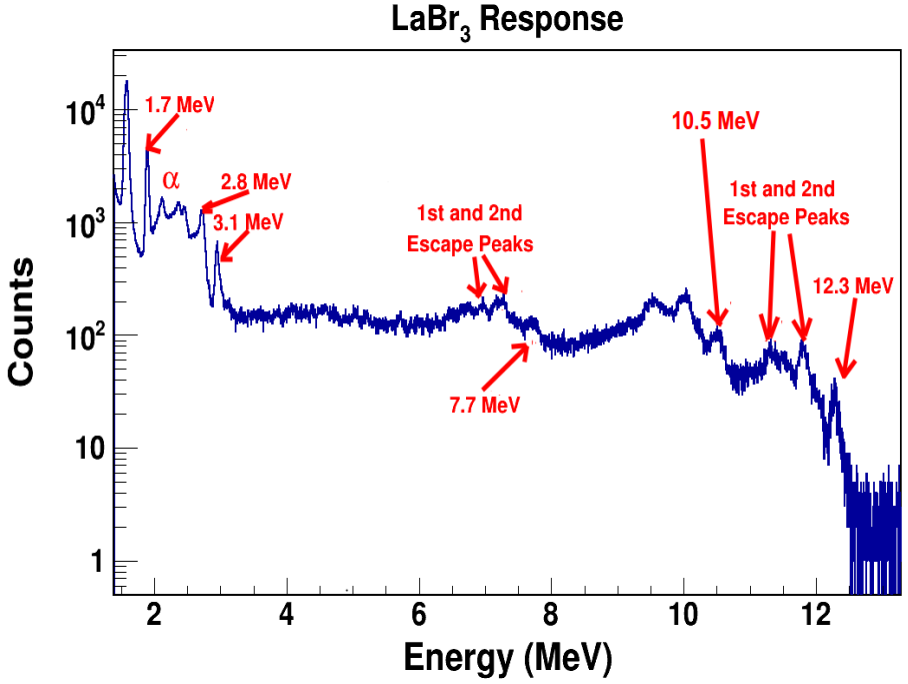

FIGURE 2.32: The populated energy levels for LaBr in $^{27}Al(p,\gamma)^{28}Si$ resonance reaction (E_p=992 keV).

APS module, which were proportional to the amplitude of the fast signal component (only $LaBr_3$(Ce)) and proportional to the energy of the entire signal (the combination of $LaBr_3$(Ce) and NaI(Tl)) [48]. These two amplitudes are obtained from the APS module as called Q_{fast} and Q_{slow} respectively, and then the 2D plot is acquired, which is the Q_{fast} amplitudes versus Q_{slow} amplitudes, as illustrated in Figure 2.33(a). Therefore, the separation between two different components of the phoswich ($LaBr_3$(Ce) and NaI(Tl)) is clearly seen in Figure 2.33(a). The events corresponding to the energy release only in fast scintillator $LaBr_3$ or slow crystal

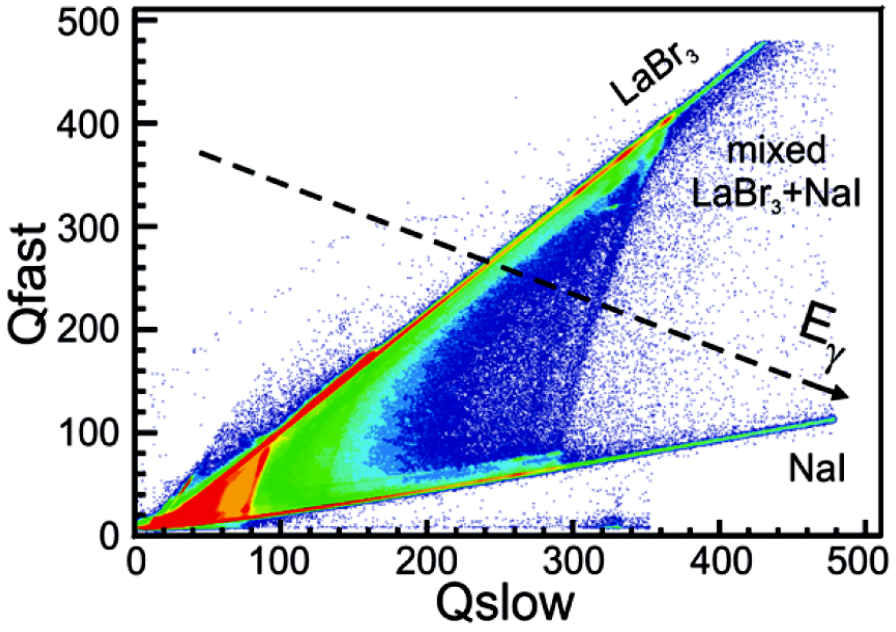

(a) Q_{fast} is proportional to the amplitude of the fast signal component. Q_{slow} is proportional to the energy of the combination of $LaBr_3$(Ce) and NaI(Tl) amplitude. 2D plot is obtained from the Q_{fast} amplitudes versus Q_{slow} amplitudes.

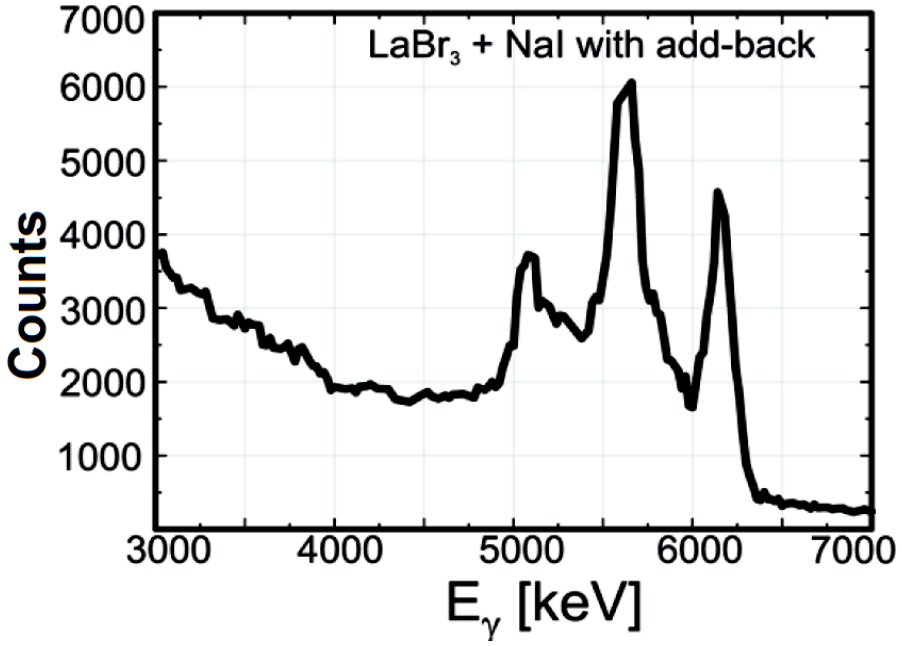

(b) Matrix points projection on tilted axis (indicated as a dash line collected charge in fast and slow gates for 6.13 MeV gamma rays in Figure 2.33(a)) gives the total energy spectra (the full addback spectrum).

FIGURE 2.33: (a) PARIS phoswich detector collected charge in fast and slow gates for 6.13 MeV gamma rays. (b) Addback spectrum acquired from the projection on the tilted axis (E_γ) [48].

NaI indicated as two semi-diagonal stripes. The events inside these two stripes regions demonstrated the shared energy deposition between two scintillations in

phoswich (Compton Scattering process). Each scintillation components of the phoswich had different energy gains; the gain matched gamma energies (E_γ) were defined as a tilted axis (indicated as a dash line) to obtain the total energy spectra. Matrix points projection on this axis gives the full addback spectrum as shown in Figure 2.33(b). If a gamma ray interacts with a single crystal ($LaBr_3$ or NaI), its full energy will be deposited resulting in collected charge proportional to this energy (Photoelectric effect is shown as semi-diagonal stripes in Figure 2.33(a)). In Compton scattering process, a gamma may interact with two or more crystals. Therefore, the energy of gamma ray will be shared by the crystals. In this case, the process is called addback, in which the collected charge by each crystal can be summed up to determine of the incident gamma ray energy. Consequently, the total deposit energy in the detector, is measured using the addback mode to produce clean γ-ray spectra with good energy resolution [48].

Phoswiches were tested for more than just resonance reaction using the proton beam facility in the PAN lab in Krakow. Three phoswiches' performances were also examined by using Agilent DC252 (10 bits, 4 GS/s) digitizer system. The Experimental setup is shown in Figure 2.34 with different PARIS detectors ($LaBr_3$(Ce)-NaI(Tl), $LaBr_3$(Ce)-CsI and $LaBr_3$(Ce) were optically coupled with Hamamatsu R7723-100 PMTs). The right of Figure 2.34 illustrates optically bond

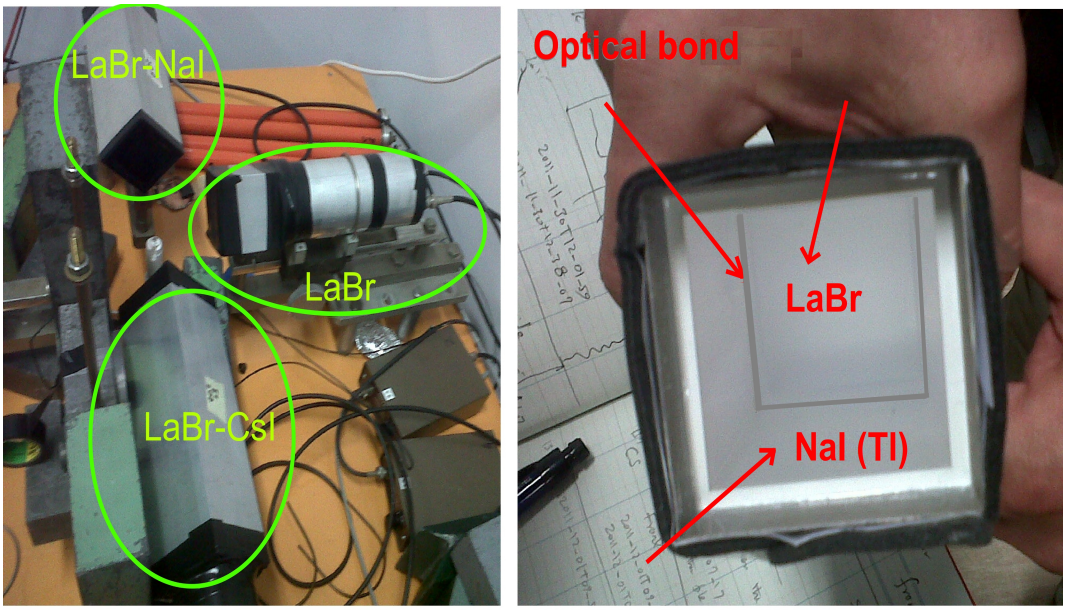

FIGURE 2.34: At the institute of nuclear physics in Krakow Poland, three phoswich detector systems were operated and tested. A radioactive source was placed in a different position than the detector. Coincidence time measurement was also successfully completed by using the Agilent DC252 digitiser system. On the right, the bond between NaI and LaBr scintillators is clearly visible.

surface between NaI and $LaBr_3$, and the glass window is coupled with PMT. The performance of detectors was studied with standard radioactive sources by placing these at different positions on the detector. Readout signals were recorded by the digital system (Agilent DC252 10 bits, 4 GS/s)) and analogue MCA module. Co-60 spectra for two PARIS detectors are obtained by MCA (see Figure 2.35(a)) and writing code in ROOT [1] software to analyse digitiser data (see Figure 2.35(b)).

[1]ROOT is a scientific software module to deal with big data processing, statistical analysis, and storage.

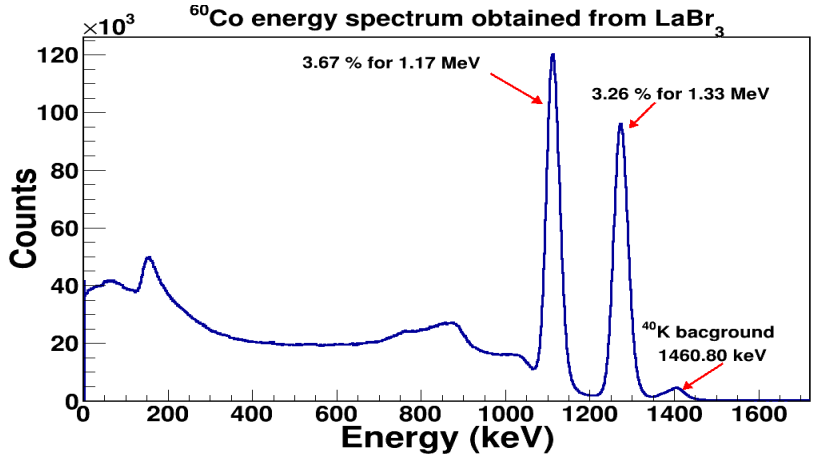

(a) 2"x2"x2" $LaBr_3$(Ce) PARIS scintillation detector was coupled with Hamamatsu R7723-100 PMT. Analogue MCA module was acquired for the spectrum.

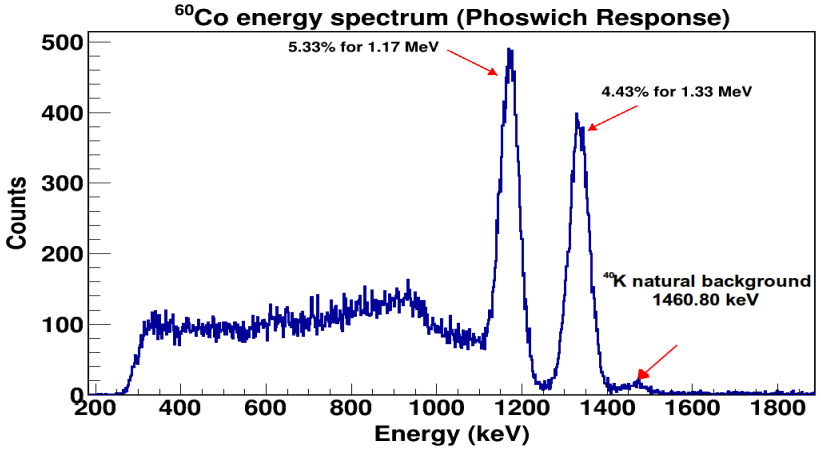

(b) 2"x2"x2" $LaBr_3$:Ce and backed 2"x2"x6" NaI(Tl) PARIS poswich scintillation detector was coupled with Hamamatsu R7723-100 PMT. Spectrum obtained with Acqiris DC252 (10 bits, 4 GS/s) digitiser.

FIGURE 2.35: Cobalt-60 energy spectra were taken separately using analogue and digital algorithms. (a) 3.67% and 3.26% energy resolution were found for only $LaBr_3$ detector at 1.33 MeV and 1.17 MeV respectively. (b) 5.33% and 4.43% energy resolution were found for phoswich detector system ($LaBr_3$(Ce)-NaI(Tl)) at 1.33 MeV and 1.17 MeV respectively. $LaBr_3$ detector system shows better energy performance and less signal-to-noise ratio.

$LaBr_3$ energy resolution is lower (3.67% at 1.17 MeV) than phoswich detector's energy resolution (5.31% at 1.17 MeV). A combination of $LaBr_3$ and NaI phoswich detector's signal-to-noise ratio is worse than only a $LaBr_3$ detector system noise ratio. In this experiment, the timing performance of PARIS detectors was also tested by using annihilation photons (Na^{22} radioactive source) in the PAN lab; however, digitiser data analysing in ROOT has not been completed. At the IPN in ORSAY, the original PARIS phoswich cluster (as shown in Figure 2.36) was tested with various targets and energetic proton beams. High energy addback

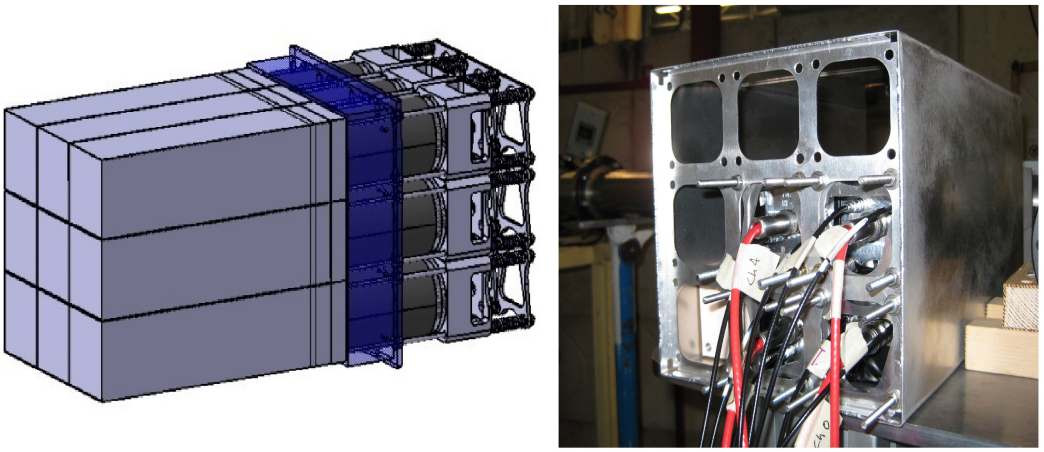

FIGURE 2.36: The cluster module comprising nine PARIS poswiches detector. Four phoswiches were tested in Tandem-ALTO at the IPN in Orsay, France.

capabilities (as detailed previously) were tested by using $^{11}Bi(p,\gamma)^{12}C$ reaction at 7.2 MeV with detecting gamma rays up to 22.56 MeV. In this experiment there was a GANAS collaboration, so the new generation scintillators were also tested such as, $CeBr_3$, SrI_2, CLYC, and GYGAY. The data, obtained from that experiment is yet to undergo analysis.

Chapter 3

Characterisation of SensL Blue-Sensitive Silicon Photomultipliers

3.1 SensL Silicon Photodiode

Semiconductor light sensors have gained a favourable position through photomultiplier tubes (PMTs) in the last few decades. SensL silicon photomultipliers (SiPMs) provide blue sensitivity and separate fast-timing signals beside standard output. These sensors are produced using innovative designs and employ novel manufacturing techniques. Figure 3.1 illustrates that the internal capacitance of each microcell is coupled with individual diodes, resulting in a low capacitance of fast output, which is a distinctive aspect of SensL's SiPMs (order of 2 to 4 percent of microcells' total capacitance). For instance, SensL silicon photomultiplier's capacitance for 6x6 mm^2 effective area is reduced from 3400 pF to 48 pF. That offers a significant advantage regarding coincidence-resolved time measurements (as discussed in Chapter 4). SensL SiPMs are also designed with minimal undesirable resistance. Fast output, capacitor and a quenching resistor for a single microcell are labelled in Figure 3.1. The electrical diagram (Figure 3.1) shows 12 microcells of SiPM, which form only a fraction of the total number of cells. The number of microchips included depends on the size of the silicon photomultiplier; for example, for the work presented in this thesis, we employed 6x6 mm^2 SiPMs (containing 18980 microcells).

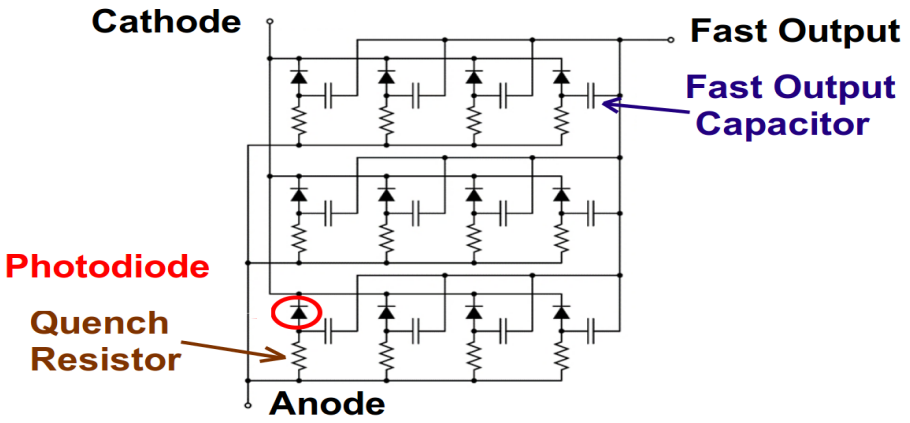

FIGURE 3.1: Schematic diagram of 3x4 microcell arrays for SensL blue sensitive silicon photomultiplier. A low light sensor has three separate terminals: cathode, anode, and fast output as labelled [49]. A unique modification in the standard SiPM structure is developed by SensL resulting in an additional terminal, ultra fast output signal.

Complementary metal-oxide-semiconductor (CMOS) technology is used in the manufacture of wafers, which are the main products of the SensL standard silicon photomultiplier. That holds several benefits: it allows for the provision of a high density of logic functions on the chip, maximum uniformity, and low heat waste. Moreover, the low temperature coefficient and the homogeneity of the SiPM structure reduce variations in the breakdown voltage of the sensor. Using CMOS technology, the P-N junction is extremely close to the surface of the SiPMs (Figure 3.2), thus, it can detect shorter wavelength photons (from blue light to UV) as a direct consequence of having excellent photo detection efficiency. In addition, when the silicon photomultiplier is fabricated in semiconductor materials, called the polysilicon, CMOS technology [49] minimise metal and oxide layers damage to the SiPM during the process. Therefore, dark current and noise are reduced with C-series SiPMs. Dark current is improved from 10-24 μA for SensL B series SiPM to 0.68-1.75 μA with SensL C-series SiPM as indicated in Table 3.1.

The performance of the blue sensitive silicon photomultiplier and comparison with the vacuum tube (PMT), or old generation SiPMs, such as Hamamatsu MPPC, are presented in this chapter. SensL first marketed the B-series blue-sensitive SiPM, and then made the C-series silicon photomultiplier available with an improvement in properties such as lower dark current, higher photon detection efficiency (PDE) and optimised breakdown voltage stability. Therefore, C-series photosensors were also examined to provide an improved comparison between B and C type SiPMs. Important properties of SiPMs are provided in Table 3.1.

Properties	**Photomultiplier**		
	SensL SiPMs		**Hamamatsu**
	B-series	**C-series**	**MPPC S12572-010P**
Breakdown voltage (V)	24.0-25.0	24.2-24.7	65∓10
Recommended maximum overvoltage(V)	V_{BR}+5	V_{BR}+5	V_{BR}+4.5
Spectral response range (nm)	300 - 800	300 - 800	320 - 900
Peak sensitive wavelength (nm)	420	420	470
Photon detection efficiency (%)	31-41	31-41	10
Dark count rate (MHz)	21.5	1.2-3.4	1-2
Dark current (μA)	10-24	0.68-1.75	0.022-0.044 [a]
Number of microcells	18 980	18 980	90 000
Terminal capacitance (Anode-Cathode) (pF)	3400	3400	320
Terminal capacitance (Fast Terminal-Cathode) (pF)	48	48	Not having Fast Terminal
Crosstalk at V_{BR}+2.5 V(%)	10	7	7
Afterpulsing at V_{BR}+2.5 V(%)	0.2	0.2	1
Gain (Anode-Cathode)	3x10^6	3x10^6	1.35x10^5
Gain (Fast Output)	4.3x10^4	4.3x10^4	Not having Fast Terminal
Temperature coefficient at V_{BR} (mV/°C)	21.5	21.5	60
Operating Temperature (°C)	-40 to +85	-40 to +85	0 to +40

TABLE 3.1: Technical information about 6x6 mm^2 active area SensL B and C series SiPMs, and Hamamatsu 3 mm S12572-010P MPPC [50–53].

[a]The dark count rate is used for estimation of the dark current as defined by Equation; $I_D \cong q \cdot G \cdot N_{0.5p.e} \frac{1}{1-P}$; where I_D is the dark current, q is electron charge, G is gain, $N_{0.5p.e}$ is the number of pulses generated in a dark state and exceed a threshold of 0.5 p.e., and P is the crosstalk probability [32]

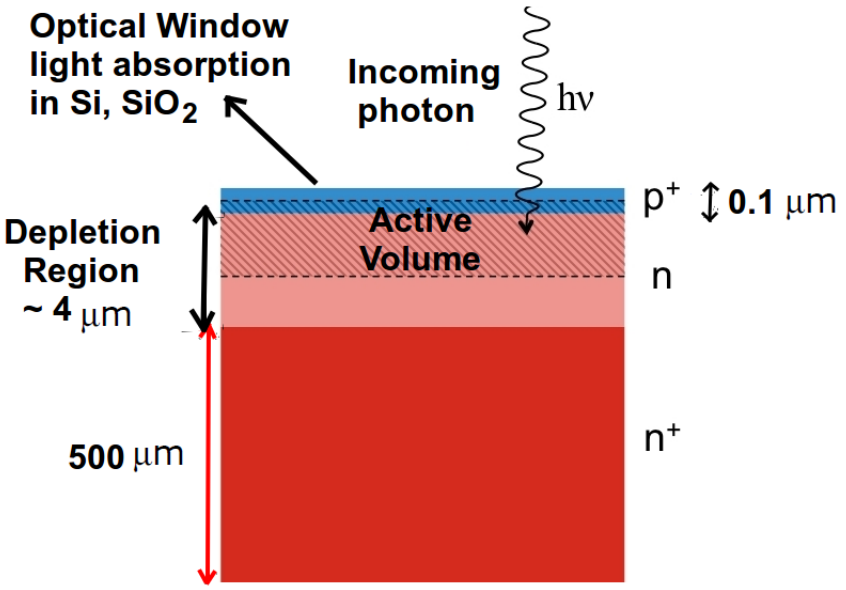

FIGURE 3.2: P-N junction structure for SensL B- and C-series silicon photomultiplier. Incoming scintillation photon (hν) first enter the positive charge of the hole region. The positively doped region is called p^+, and its thickness is extremely thin 0.1 μm. The depletion region is filled with undoped silicon to produce electron-hole pairs, which is labelled "n" in Figure with 4 μm thickness and 20%-80% filling factor. The depletion region is on the surface for optimisation of blue light (420 nm), which distinguishes it from standard SiPMs by detecting short wavelengths (sensitive range 300-800 nm). The average energy to create electron-hole pairs in silicon is about 3.6 eV with 1.2 eV band gap energy. If the incident radiation has enough energy to produce electron-hole pairs, applied reverse bias voltage accelerates generated electrons from p+ layer to n+ layer [54, 55].

3.2 Experimental Set-up

The SensL B-series blue sensitive silicon photomultiplier was coupled with $LaBr_3$ to evaluate the character of B-type SiPMs (Figure 3.3(a)). The SensL SiPM has an integrated cathode and built-in resistance; the read-out electronics were set-up according to the scheme is shown in Figure 3.3(b). The SensL blue sensitive silicon photomultiplier has two separate outputs: fast and standard terminals. A standard terminal, which is the signal from the cathode or anode terminal depending on the applied bias voltage polarity and application.

A standard terminal mode was used to obtain characterisation measurements of the SiPM, such as temperature dependency and energy measurement. While the fast output mode was studied in the coincidence-resolved time measurement (as detailed in chapter 4).

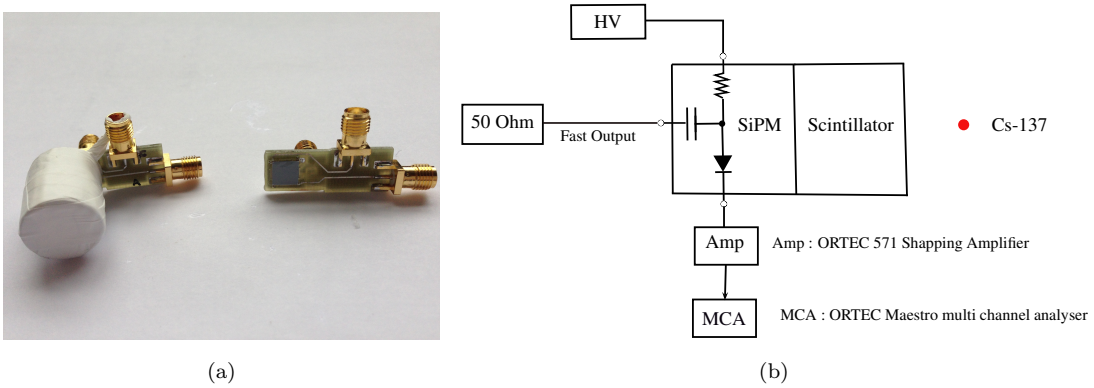

FIGURE 3.3: (a) SensL blue sensitive B series 6 mm SiPM with two separate outputs (standard and fast timing signals). A SiPM was coupled with 0.5 inch length x 0.5 inch diameter $LaBr_3$ and wrapped with PTFE. (b) Experiment setup used for initial SiPM tests. An Ortec 556 NIM power supply is used, which provides ± 1-2 mV stability in applied bias voltage. Readout in standard terminal, positive bias is applied to the cathode, so the signal was taken from the anode with positive polarity. When the standard terminal was used in the measurement, fast output was connected to a 50 ohm terminal.

When the negative bias is applied to the anode with the cathode at 0V, the signal polarity of the fast terminal will be positive, and a standard signal will obtain from the cathode with negative polarity. That is the recommended biasing and readout of SensL B- and C-series SiPMs in fast output mode as illustrated in Figure 3.4. In this measurement, we have used a standard readout mode. Positive bias is applied to the cathode, so the signal was taken from the anode with positive polarity. The value of the applied bias and the ambient temperature is changeable according to the measurement (as detailed in next sections). The variety of the standard radioactive source distance from the detector was fixed at 0.5 cm in the measurement.

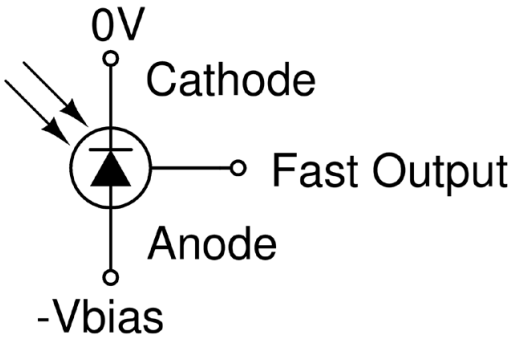

FIGURE 3.4: Recommended negative biasing and readout signal in fast terminal mode. In terms of standard readout mode, positive bias is applied to the cathode and readout signal is used from the anode with connecting 50 Ohm terminal to the fast readout terminal [50].

3.3 Energy Resolution - Voltage and Temperature Variation

The performance of the B-series SiPM detector system was investigated as a function of bias voltage at both room temperature (Figure 3.5(a)) and low temperature (Figure 3.5(b)). The experimental set-up is explained in the previous section. An Ortec 571 module (CR-RC pulse-shaping technique and amplifier) was fed by the standard readout signal of the sensor to generate a smooth pulse. All tests were conducted using 0.5 μs shaping time to produce spectra in Ortec MCA. Shaping

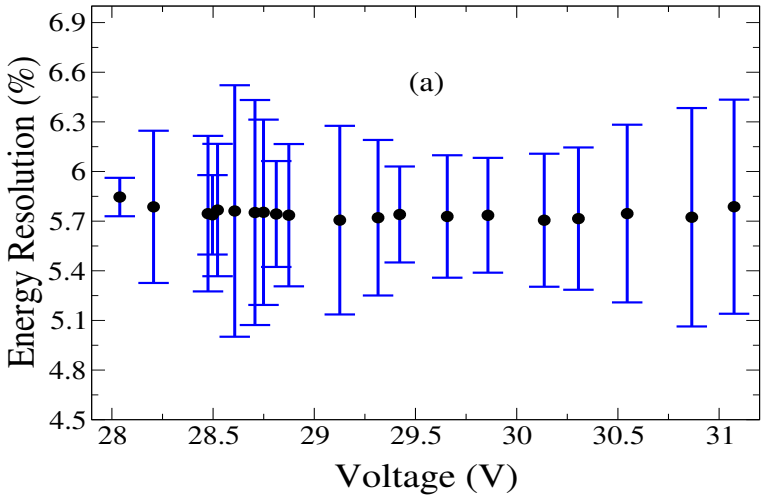

(a) Room temperature.

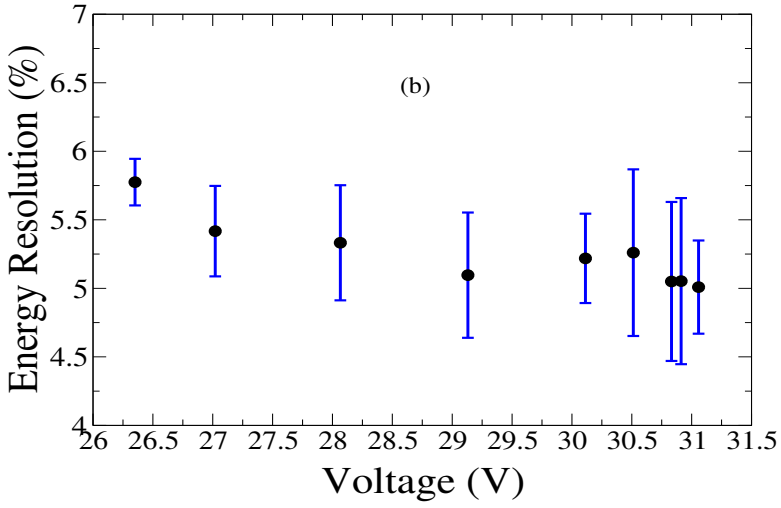

(b) Low temperature.

FIGURE 3.5: Energy resolution at 662 keV as a function of bias voltage for SensL B-series SiPM coupled to $LaBr_3$ crystal at (a) room temperature of 21.6 $\pm$ 0.1 °C and (b) lowered temperature of 6.1 $\pm$ 0.1 °C.

time constant should be chosen at least three times the scintillation decay time constant (∼26 ns decay time constant for $LaBr_3$) in order to ensure complete integration of the scintillator signal for good energy resolution. This shaping time constant is long enough to allow full light collection from the scintillator. To eliminate the effect of environmental conditions on the measurement (such as dark current), a temperature controlled chamber was used to stabilise the temperature and cooling or heating within ± 0.1°C uncertainty. A Fluke digital thermometer probe was attached on top of the SiPM board (after wrapping the detector system to make it light tight) using black tape to monitor the temperature. A detector system, which was an optical combination of $LaBr_3$ and SensL B series 6 mm^2 active area SiPM, was placed inside the temperature chamber (see Figure 3.7). A standard ^{137}Cs source (370 kBq) was located inside the chamber at a 0.5 cm distance from the detector system. The isolated lid then covered the temperature controller chamber; almost 10 minutes later, the temperature variation started to be stable. When the temperature stabilised, the measurement was acquired. The performance of the detector system was studied at two different temperatures (21.6 ± 0.1 °C room temperature and 6.1 ± 0.1 °C low temperature). The applied bias voltage uncertainty was ± 1-2 mV supplied by Ortec 556 NIM power.

Investigation of the bias voltage effects on the energy resolution at fixed temperature was studied as illustrated in Figure 3.5 for two different temperatures. The SiPM exhibits the best performance regarding energy resolution for bias voltages between 30 V and 31 V; if the voltage is increased above 31 V, the full energy peak resolution in the spectrum begins to deteriorate and the dark current rapidly increases, which was also observed during the measurement. However, energy resolution at 662 keV with an error at room temperature is not as fluctuated as at the low temperature measurement. Therefore, the performance at room temperature appears to be more stable than at a lowered temperature of 6.1° (see variation in Figures 3.5(a) and 3.5(b)). However, better energy resolutions were obtained at low temperature than room temperature. The best energy resolution was found to be at 30.592 ± 0.002 V bias value in the previous measurement. That is why the applied bias voltage was fixed at that bias voltage. The energy resolution was also found to be nearly stable with temperature variation from 5.0 ± 0.1°C to 40.0 ± 0.1°C as shown in Figure 3.6.

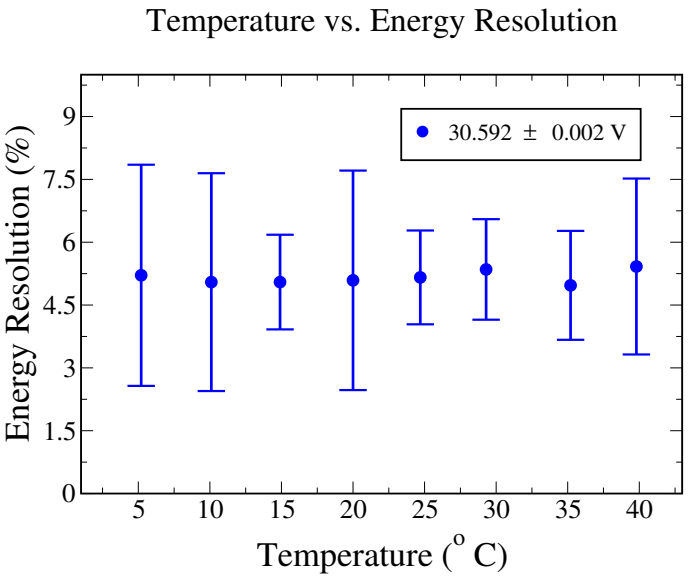

FIGURE 3.6: Energy resolution against temperature.

3.4 Voltage vs. Current Temperature Dependence

To stabilise the temperature during the data acquisition, a temperature controlled chamber, providing stability to ±0.1°C; was used (Figure 3.7). A Fluke digital thermometer probe was attached on top of the SiPM board using a black tape to monitor the temperature. A detector system was placed inside the temperature chamber. In this measurement, a radioactive source was not used, as we measured only dark current, without producing light yield. Then, the temperature

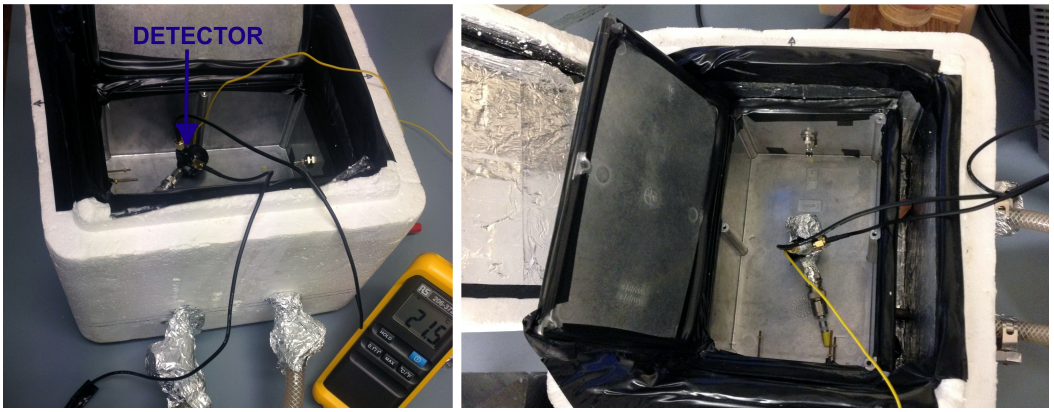

FIGURE 3.7: Detector system set-up inside the thermally-isolated temperature controlled chamber. (a) A Fluke digital thermometer probe was attached to the sensor board by a black tape, and it was then placed inside the chamber. (b) A thermally isolated lid was used to cover the chamber after the experimental set-up was completed.

controller chamber was covered by a thermally isolated lid. Almost 10 minutes later, the temperature variation started to stabilise, after setting the desired temperature. When the temperature appeared to stabilise on the digital and chamber thermometers, the measurement was acquired.

Figure 3.8 illustrates the bias voltage against the dark current for SensL B series 6 mm SiPM. The current measurement was performed by a Keithley model

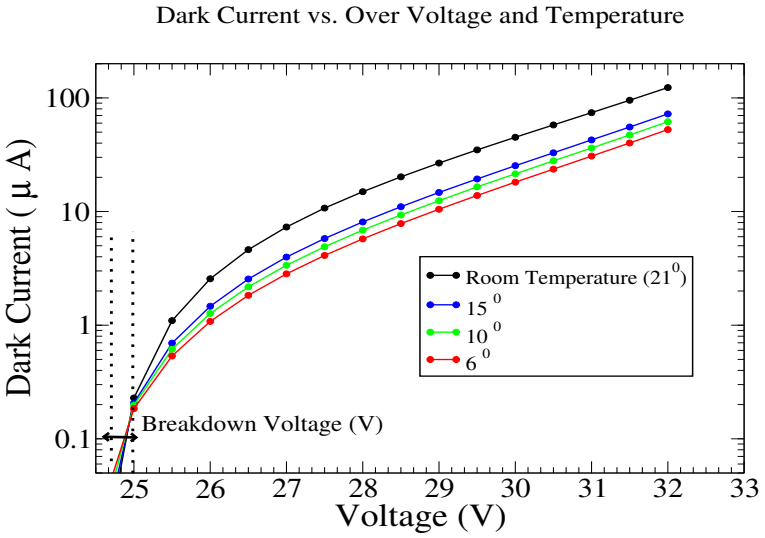

FIGURE 3.8: Bias voltage against the dark current for SensL B series. A Keithley model 6487 Picoammeter/Voltage supply and temperature controlled chamber are used at different ambient temperatures from 6°C to room temperature 21°C.

6487 Picoammeter/Voltage supply at different ambient temperatures from 6°C to room temperature 21°C. After a breakdown of voltage, thermally generated dark current electrons become more dominant. When the environment temperature rises, the dark current also increases as shown in Figure 3.8.

Figure 3.9(a) shows the dark current as a function of the applied bias voltage for SensL B and C series SiPMs. According to the graphs, the dark current of the C-series SiPM was improved by SensL manufacturing methods. CMOS technology reduces the damage to SiPM during the manufacturing process, so dark current is improved from 10-24 μA to 0.68-1.75 μA as detailed in the previous section. Dark current versus bias voltage for Hamamatsu 2x2 MPPC array (a single module has 3 mm^2 photosensitive area) was also examined as shown in Figure 3.9(b). After the breakdown on the plot's dark current suddenly increases, but before breakdown voltage, the dark current is very low almost zero. Overall, the dark

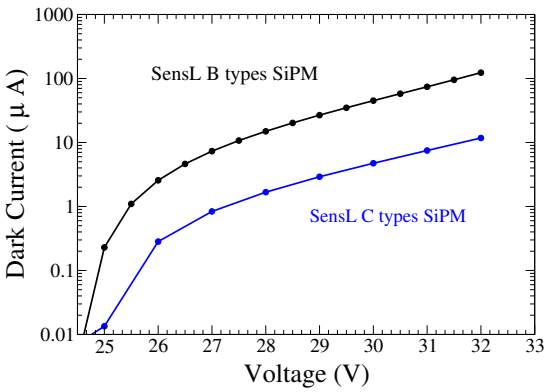

(a) SensL B- and C-series SiPMs.

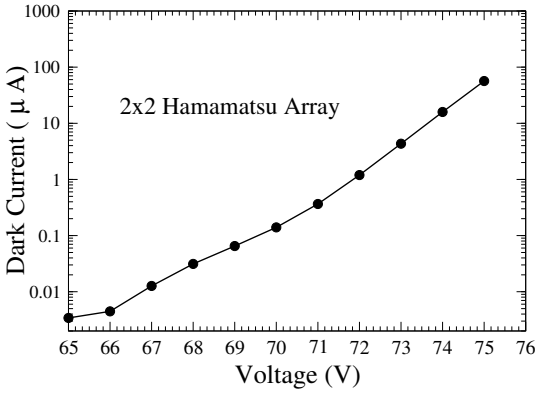

(b) The 2x2 array was made from four 3 mm S12572-010P Hamamatsu MPPC modules.

FIGURE 3.9: Dark current against bias voltage for different detector systems: (a) for B- and C-series SiPMs at room temperature; and (b) for 6 mm^2 size active area 2x2 array Hamamatsu MPPC at room temperature. The measurement was carried by a Keithley model 6487 Picoammeter/Voltage supply.

current increases as a square of the reverse voltage (V^2) as a similar trend with the literature [29].

3.5 Voltage vs. Gain and Gain vs. Temperature dependence

Voltage and temperature significantly influence the detector gain. If the detector is used in the high or low ambient temperature applications, the gain value of the detector has to be constant, because a change in temperature will vary the detector gain and detector performance. When temperature control is difficult, applied reversed voltage can be modified and vice versa; therefore, we studied gain relationship with temperature and bias voltage. The performance of the detector was examined between 5 and 40°C for SensL 6 mm B series SiPM by using the thermally-isolated chamber. A standard ^{137}Cs radioactive source (370 kBq) was placed inside the temperature chamber with a 0.5 cm detector distance as explained in the previous section. Photon spectra were acquired for various reverse voltage. An increase in each bias voltage value gives the extraction in the detector gain as a distance of the full energy peak in the spectrum [56]. Therefore, we have determined the full energy peak position (channels) as a detector gain.

Figure 3.10 illustrates the voltage variation with photoelectrons peak distribution (channels) at room temperature (Figure 3.10(b)) and at low temperature (Figure 3.10(a)). As indicated in Figures 3.10(b) and 3.10(a), linear fitting parameters are used to determine the breakdown voltage (horizontal intercept gives the breakdown voltage; $y = p0 + p1.x$). SensL B series SiPM's breakdown voltage is decelerated between 24-25 V in the technical data sheet as shown in Table 3.1. According to the plots, the calculated breakdown voltage was found to be 26.2 ± 0.6 V for room temperature measurement (4.8 % agreement with technical data value) and 25.8 ± 0.2V for low temperature measurement (3.2 % agreement with technical data value). Any deterioration during the ambient temperature stabilisation by a thermally isolated chamber could cause the shift in the breakdown voltage, which can create errors. The centroid of the 662 keV (mean value) shifts by one channel per 2.84 ± 0.05 mV and 1.94 ± 0.01 mV at room temperature and low temperature respectively according to the linear fitting parameters. Similar measurements were also carried out with SensL 6 mm C type SiPM and 6 mm Hamamatsu MPPC module (2x2 array which is made by four 3 mm S12572-010P MPPC). The breakdown voltage was found to be 26.23 ± 1.02 V for SensL C-SiPM and 66.3 ± 6.3 V for Hamamatsu MPPC (see the Table 3.1 for breakdown voltage value obtained from technical datasheet). Voltage dependence of the detector gain

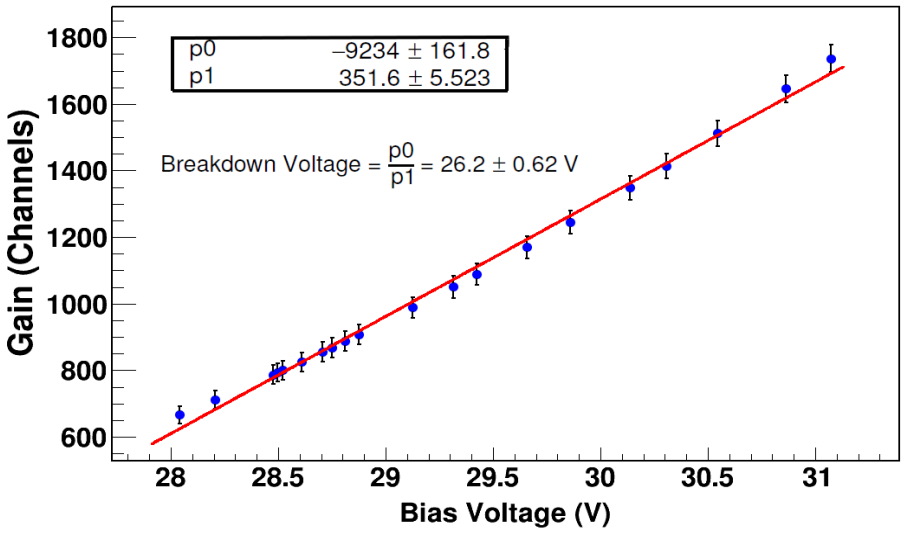

(a) Gain versus bias voltage at room temperature (21 ± 0.1 °C)

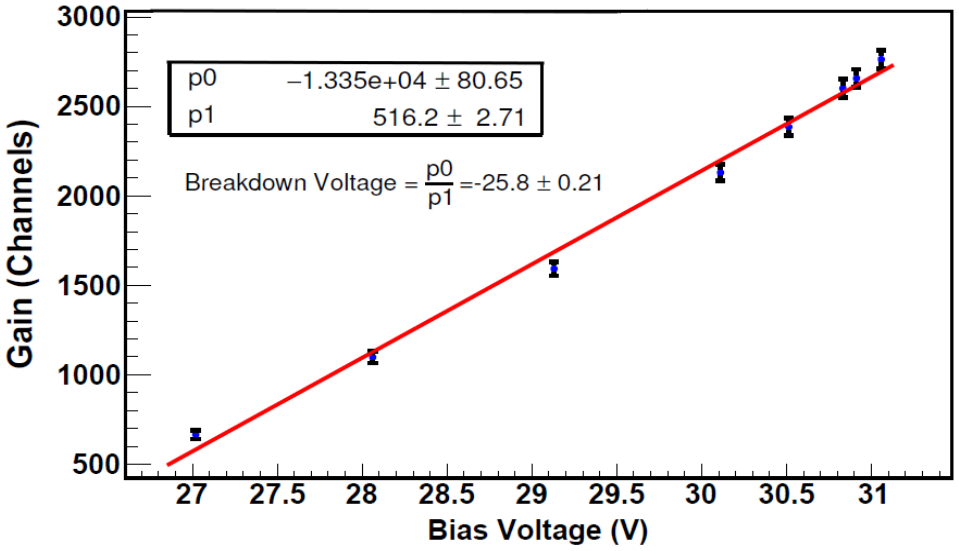

(b) Gain versus bias voltage at low temperature (6 ± 0.1 °C)

FIGURE 3.10: An optically coupled SensL B series 6 mm SiPM-$LaBr_3$ detector system, ^{137}Cs radioactive source and thermally isolated temperature controlled chamber were used in this measurement. Energy spectra with various bias voltage were recorded. Gaussian distribution mean value (channels), which is defined as a detector gain, was plotted as a function of bias voltage (a) at room temperature and (b) at a lowered temperature.

is also found to be 2.85 ± 0.10 mV for SensL C series SiPM that is very close to SensL B type SiPM voltage-gain relationship. Hamamatsu MPPC sensor is less affected by the change in voltage, one channel shifts per 8.5 ± 0.6 mV.

In this part of the measurements, we investigated temperature dependence of

the gain and bias voltage. The change in temperature also influences the detector gain. When the temperature rises, the possibility of collision between carries (electrons or holes) and crystal lattice increases. The hot electron-hole pairs passes through the depletion region losing their energy by more lattice scattering than cold caries scatters. Therefore, caries could not have sufficient energy to overcome a higher applied bias voltage (potential difference). Pairs with insufficient energy can not generate more electron-hole pairs and avalanche discharge in the depletion region [57], resulting in a decrease in the sensor breakdown voltage. The breakdown voltage of the SiPM changes with temperature variation, so the applied bias change will depend on the change of the temperature. Figure 3.11 shows linear re-

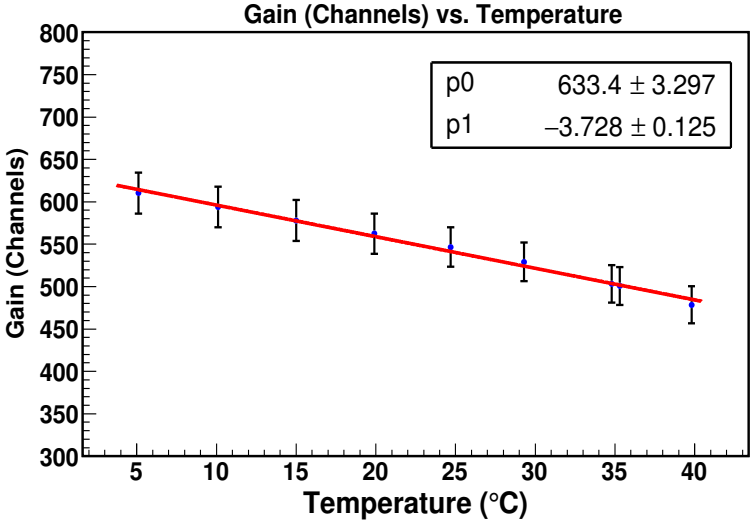

FIGURE 3.11: The temperature dependence of the detector gain (at 662 keV full energy peak position, mean value of the Gaussian distribution as a channel). An optically coupled B-series SiPM-$LaBr_3$ detector system was irradiated by standard ^{137}Cs (370 kBq), after placing the experimental set-up inside the thermally isolated temperature control chamber. Data acquisition was recorded between 5.0 ± 0.1 °C and 40.0 ± 0.1 °C at stable bias voltage (29.014± 0.001 V).

lationship between gain and temperature (inverse proportion). The gain increases with decreasing temperature and vice versa. A single centigrade variation will shift 3.72 ± 0.13 channels in the gain. According to the fitting parameters, 0.52 ± 0.02 percentage of gain changes per degree °C (-0.52 ± 0.02 %/°C), which is not very close to the measured value of SensL B series SiPM (-0.8%/°C [50]).

If it is not possible to keep the sensor temperature constant, the bias voltage must be modified to obtain the stable gain. The gain is not directly affected by the temperature; it is directly related to the breakdown voltage. The plot

in Figure 3.12 shows the linear correlation of the overvoltage with temperature. The breakdown voltage grows with a slope of 22.73 ± 0.72 mV/°C. In conclusion,

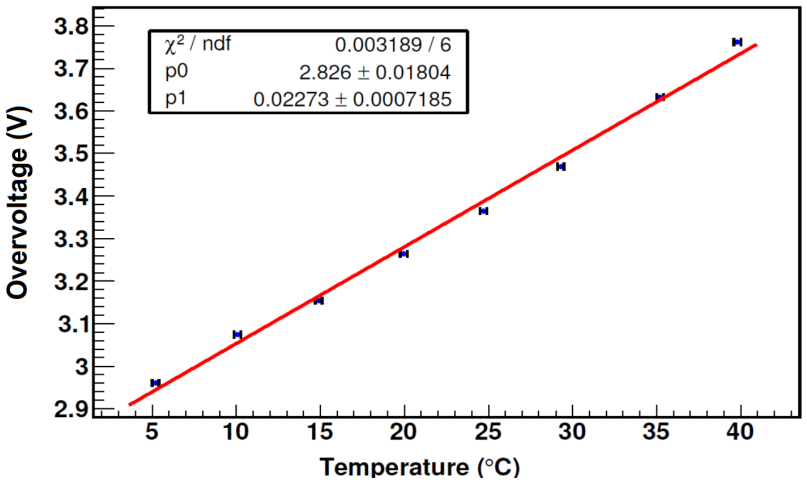

FIGURE 3.12: The temperature dependence of the breakdown voltage measurement at fixed centre of peak position (Channel number). Optically coupled SensL B series 6 mm SiPM-$LaBr_3$ and standard ^{137}Cs (370 kBq) radioactive source were located inside the thermally isolated temperature chamber as detailed in the introduction. At 662 keV full energy peak mean was fixed on the MCA and recorded voltage variation to shift the central of the peak for each temperature value. When the temperature increases, the applied bias voltage was increased until the full energy peak position matched with the reference spectrum peak position. Data acquisition was recorded between 5 and 40°C with 0.1 uncertainty.

temperature, bias voltage and breakdown voltage dependence of the detector gain were studied by using full energy peak position obtained from a radioactive source (Cs-137). Overall, measurement results are in agreement with the literature and the technical data provided by SensL and Hamamatsu.

3.6 Energy Resolution

Various scintillation detector systems were exposed to standard radioactive sources such as ^{241}Am (5.3 kBq activity and 59.54 keV gamma energy), ^{137}Cs (370 kBq activity and 661.73 keV gamma energy) and ^{22}Na (370 kBq and 511 keV - 1274 keV gamma energies). Different scintillation crystals were optically coupled with a photomultiplier (PMT or SiPMs) to compare the energy response of the scintillation detector systems. In this measurement, applied bias voltage was fixed with 1-2 mV uncertainty, and all measurements were taken at 22.2 ± 0.1 °C. An Ortec 572 amplifier amplified a readout signal with an appropriate shaping time (depending on the decay time constant of the scintillation), and then an amplified output signal was fed to an Ortec Maestro multichannel analyser to acquire the energy spectrum. Figure 3.13 illustrates the representative energy spectra of the ^{241}Am, ^{22}Na, and ^{137}Cs (with clearly seen 32 keV X-ray emitted from ^{137}Ba) for the $LaBr_3$-SensL C-SiPM detector system (data acquisition was acquired individually).

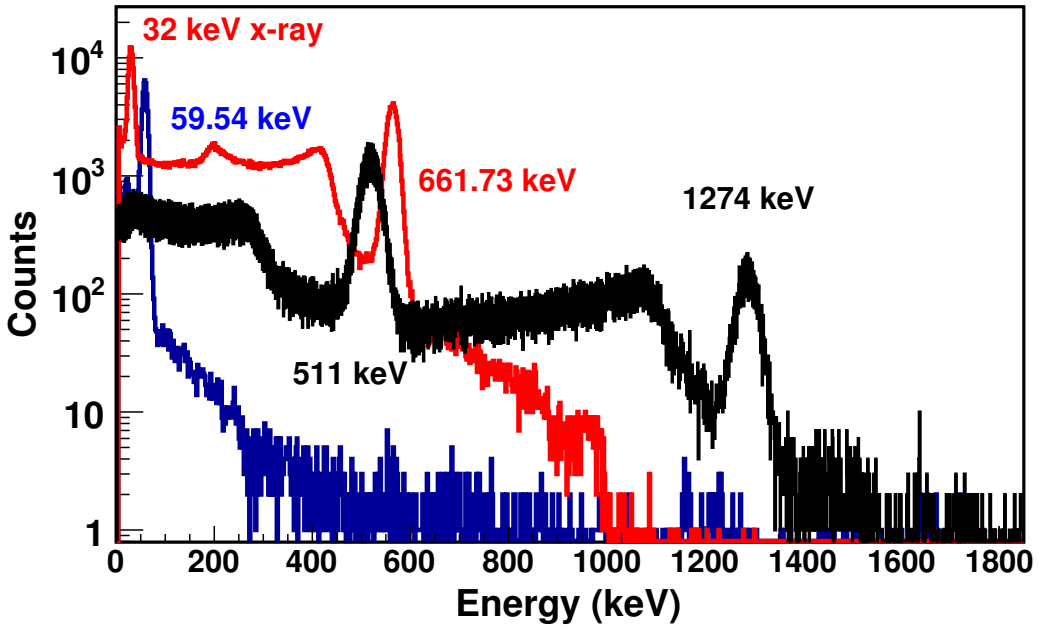

FIGURE 3.13: $LaBr_3$ was optically coupled with SensL 6 mm C-type SiPM, and the detector was irradiated by various radioactive sources. Applied bias voltage was set to 30 ± 0.001 V and all measurements were taken at 22.2 ± 0.1 °C. The readout signal was amplified by Ortec 572 amplifier with 0.5 μs shaping time; then an amplified output signal was fed to an Ortec Maestro multichannel analyser to acquire the energy spectrum.

The ability of differentiation between slightly different energies of gamma rays or characteristics of X-rays is one of the critical properties of the γ-rays spectrometer, which is called an energy resolution. It is defined as the width FWHM (Full Width Half Maximum) or % full width half maximum of the photopeak energy (E_γ: energy of the radiation). Recorded energy spectra were plotted in ROOT, and then energy resolutions were calculated by Equation 3.1;

$$FWHM(\%) = \frac{\Delta E}{E_\gamma} \times 100 \tag{3.1}$$

where ΔE is defined as the full width at half maximum height in photopeak. Table 3.2 provides the energy resolution of the detector systems in the energy range 32 keV to 1274 keV. According to the calculated energy resolution, the

Detector	**Energy (keV)**				
	32	**59.54**	**511**	**662**	**1274**
$LaBr_3$ - SensL B-SiPM	26.18 ± 0.62	-	7.38 ± 0.03	5.86 ± 0.02	3.95 ± 0.05
$LaBr_3$ - SensL C-SiPM	23.40 ± 0.46	12.04 ± 0.10	6.14 ± 0.02	5.09 ± 0.04	3.21 ± 0.04
$LaBr_3$ - Hamamatsu MPPC	-	-	13.44 ± 0.09	10.10 ± 0.02	7.49± 0.14
$LaBr_3$ - Hamamatsu PMT	33.35 ± 0.09	26.50 ± 0.73	6.80 ± 0.04	5.27 ± 0.02	2.07 ± 0.15
$CeBr_3$ - SensL C type SiPM	51.03 ± 0.47	-	7.37 ± 0.09	8.84 ± 0.71	4.06 ± 0.67
LYSO - SensL C type SiPM	55.44 ± 0.17	-	-	8.37 ± 0.02	-
CsI - SensL C type SiPM	30.55 ± 0.11	16.22 ± 0.46	6.33± 0.03	5.36 ± 0.02	3.57 ± 0.05

TABLE 3.2: Calculated energy resolutions for different detector systems at the different energy from 32 keV to 1274 keV. $LaBr_3$, $CeBr_3$, LYSO, and CsI scintillation crystals were optically coupled to Hamamatsu PMT (R9880U-210 fast photomultiplier tube as detailed in chapter 4) and MPPC, SensL B and C-series SiPMs. Detectors were irradiated using ^{22}Na and ^{137}Cs radioactive sources.

resolution of the higher energy gamma rays is better than the energy resolution of the lower energy γ-rays. The width of the FWHM is directly dominated by the created photoelectrons at the photocathode (for PMT) or depletion layer (for SiPM). Consequently, higher energy gamma rays create more electrons than lower energy radiation. Broad-full energy photopeaks were generated by the low energy gamma rays or X-rays, which will give poor energy resolution. Not only the energy resolution of the scintillation detector system is affected by the gamma ray energy, but it is also influenced by the scintillator light yield, detector size, light collection which are related to wrapping quality and optical interference between photomultiplier and scintillator, and photomultiplier properties such as quantum efficiency. In this measurement, we had to use diverse scintillation crystal sizes and shapes, for example, 6X6X10 mm^3 for CsI, and 0.5 inch length 0.5 inch diameter

cylindrical $LaBr_3$. Therefore, the photosensitive area of the photomultiplier tubes or SiPMs was not properly matched with the face of the scintillation crystals.

3.7 Detector Linearity and Efficiency

A ^{152}Eu (403 kBq) radioactive source was used to investigate detector linearity for both SiPMs and PMTs. Europium-152 disintegrates mainly by electron capture (72.1%) and β decays (β^- emission to ^{152}Gd (27.9%) and β^+ emission to ^{152}Sm (0.027%)). Table 3.3 shows the gamma emission energies and their yields[1] per 100 disintegration of the gamma rays emitted in each decay mode for $^{125}_{63}Eu_{89}$. Different

Gamma Emission	Energy (keV)	Yields [%]
$\gamma_{1,0}$ (Sm)	121.78	28.41
$\gamma_{2,1}$ (Sm)	244.70	7.55
$\gamma_{1,0}$ (Gd)	344.28	26.59
$\gamma_{3,1}$ (Gd)	411.12	2.24
$\gamma_{13,9}$ (Sm)	443.97	2.80
$\gamma_{7,1}$ (Gd)	778.90	12.97
$\gamma_{10,2}$ (Sm)	867.38	4.24
$\gamma_{9,1}$ (Sm)	964.08	14.50
$\gamma_{9,0}$ (Sm)	1085.84	10.13
$\gamma_{11,1}$ (Gd)	1089.74	1.73
$\gamma_{10,1}$ (Sm)	1112.08	13.41
$\gamma_{14,2}$ (Gd)	1212.95	1.42
$\gamma_{14,1}$ (Gd)	1299.14	1.63
$\gamma_{13,1}$ (Sm)	1408.01	20.85

TABLE 3.3: Strong gamma rays, emitted from ^{152}Eu decay, energies and their intensities (yields[%]) [58]

types of optically coupled detector systems were irradiated by ^{152}Eu source. Energy spectrum obtained in the range between 40.11 keV X-ray and 1408 keV gamma rays. Gaussian distribution fitted full energy peaks, and then pulse height photopeak centroid were determined as a channel number. The energy linearity was obtained for each detector system as illustrated in Figure 3.14. This data was recorded at a constant temperature of 21.6°C. A non-linear relationship was observed as expected, because of the contribution of the finite number of photocells into the signals. The quadratic fitting parameters (non-linearity correction)

[1]More than 1% gamma emission yields are listed in the Table 3.3.

will be used to convert the pulse amplitude histograms to the energy spectra. According to the plot, linearity of Hamamatsu MPPC (2x2 arrays)-$LaBr_3$ is much better than others and is particularly better than SiPM. This conclusion was also established in similar research [59]. The other interesting result is that the detector performance with the PMT is not as good as with the SiPM or MPPC. Each

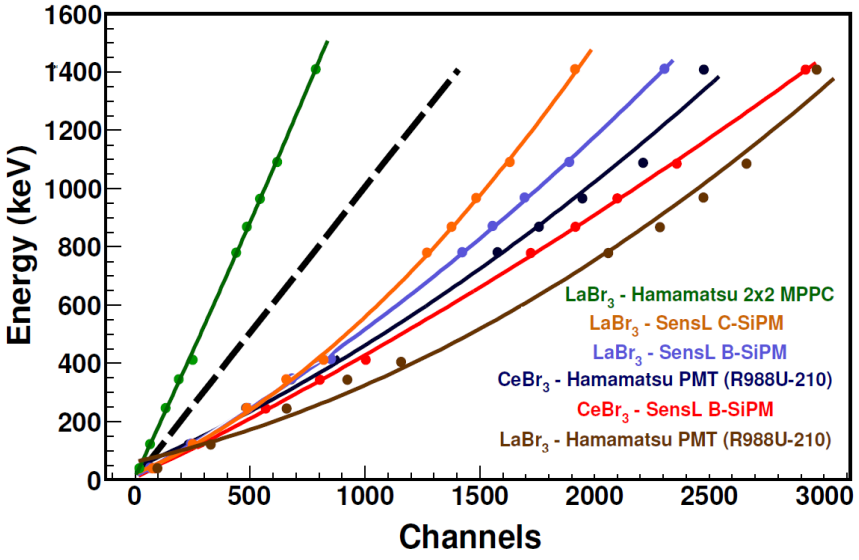

FIGURE 3.14: Pulse height photopeak centroid of the observed full energy peaks in the Eu-152 spectra as a channel number vs. input radiation energy. A non-linear relationship was observed as expected. A black dash line represents the lineal calibration line.

Eu-152 spectra was calibrated by its specific non-linearity corrections. Figure 3.15 shows the representative calibrated ^{152}Eu energy spectrum with its non-linearity corrections.

Furthermore, detection efficiency was investigated for three different detector systems: $LaBr_3$-PMT, $LaBr_3$-C SiPM, and $LaBr_3$-MPPC. The efficiency curve was generated by the calibrated energy spectrum of Europium-152, as illustrated in Figures 3.16(a), 3.17(a), and 3.18(a). The full energy peaks (except 40.11 keV X-ray, as we were only interested in gamma emissions) were fitted with the Gaussian distribution plus a continuous background function fitted with written sort code in ROOT. Therefore, the fitting parameters with their statistical errors of the photopeaks were determined, such as peak height, photopeak centroid (mean), and standard deviation (σ). If photopeak includes the combination of two or more full energy peaks because of the poor energy resolution of the detector as mentioned in Figure 3.15, combined Gaussian fitting function plus a continuous background should be used for peak fitting. Finally, a normalisation factor with

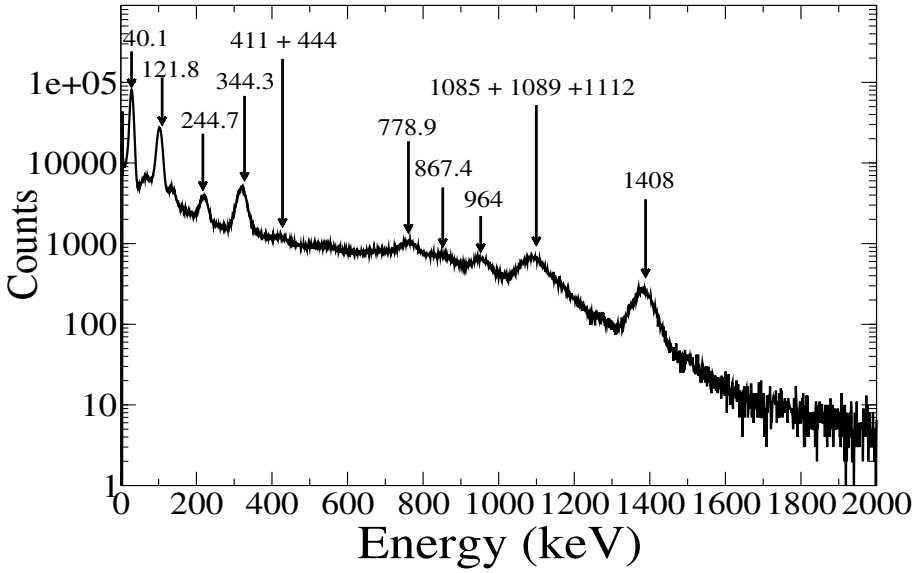

FIGURE 3.15: Optically coupled $LaBr_3$-SensL C-SiPM detector system was irradiated by ^{152}Eu source (403 kBq). Energy spectrum obtained in the range from 40.11 keV X-ray to 1408 keV gamma rays. The combination of the photopeaks in the spectrum is the results of the poor energy resolution. Nonlinear correction was found from the quadratic fitting parameters, which was $y=x^2 1.8\times10^{-4} + 0.34x + 23.38$; where x is the channel number, and y is the energy of the incident radiation. Therefore spectrum was calibrated using this non-linear correction.

its uncertainty was found from the Gaussian fitting parameters and the relative intensity of the interested source gamma ray. Each full energy peaks' intensities with their errors were recorded corresponding to the gamma rays' energy in keV. The efficiency data points with errors was fitted by the Equation 3.2,

$$\varepsilon = EXP[(P_0 + P_1. \times + P_2.\times^2)^{-P_3} + (P_4 + P_5.Y + P_6.Y^2)^{-P_3}]^{-\frac{1}{P_3}} \qquad (3.2)$$

where $\times$ is defined as a $\log(\frac{E_\gamma}{E_1})$, and Y is determined as a $\log(\frac{E_\gamma}{E_2})$; here E_γ is the gamma ray energy, E_1 is the low energy constant (100 keV), and E_2 is the high energy constant (1000 keV). The values of the seven fitted parameters (from p0 to p6) are represented in Figures 3.16(b), 3.17(b), and 3.18(b). In the fitted parameters, p0, p1, and p2 give the efficiency at low energies, and p2 is not necessary can be default [60]. The other parameters (p4, p5, and p6) are defined as high energies efficiency. Between two regions (low and high energies efficiency curves) the interaction parameter is given by p3. If p3 is large, there will be sharper turnover at the top between two efficiency curves. In contrast, if p3 is small, the efficiency curve turns over gradually. At low energy, the efficiency of Hamamatsu MPPC is higher than the efficiency for PMTs and SensL C-SiPM. In

terms of the efficiency at the high energy, SensL C-SiPM and Hamamatsu PMT are similar to each other.

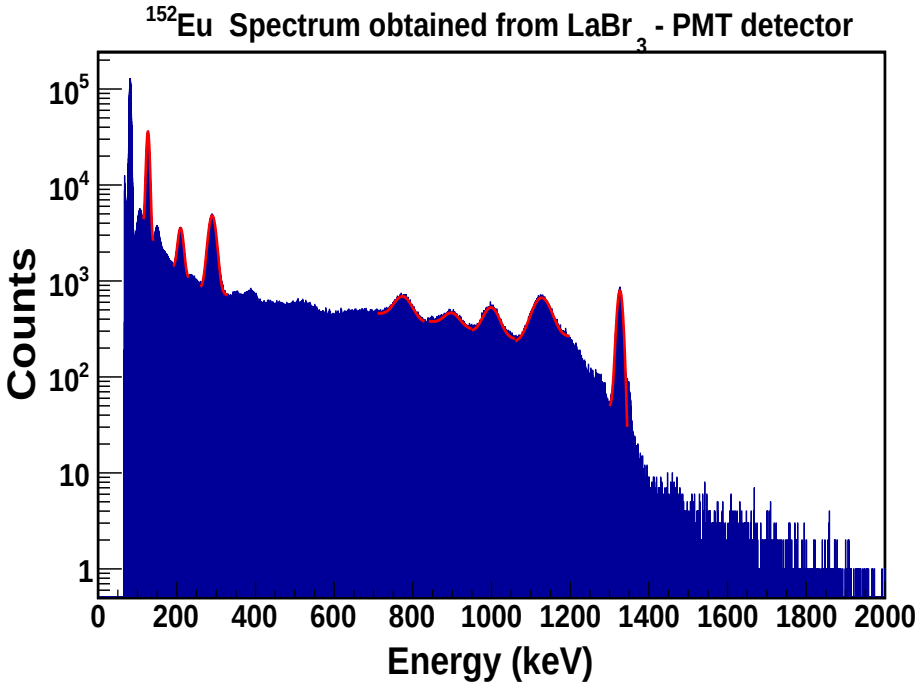

(a) Calibrated energy spectrum of Europium 152 for $LaBr_3$- Hamamatsu (R9880U-210) PMT detector.

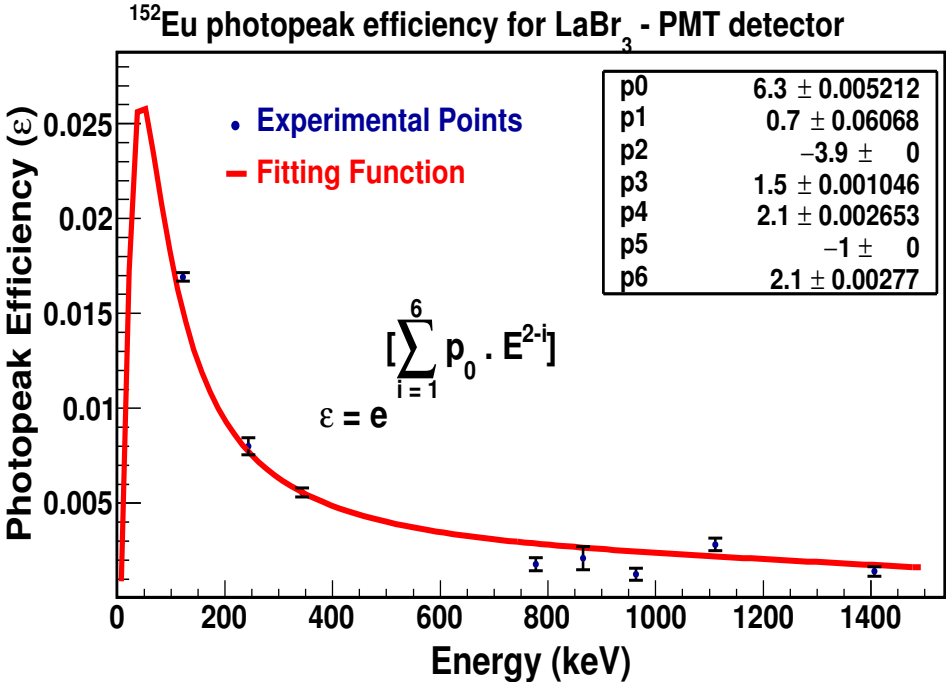

(b) Detector efficiency curve for PMT.

FIGURE 3.16: $LaBr_3$-Hamamatsu (R9880U-210) PMT detector efficiency curve. (a) Calibrated ^{152}Eu energy spectrum obtained from $LaBr_3$-Hamamatsu PMT detector. Gaussian fitting function included the background and some fitting function was accrued by a combined Gaussian function as detailed in the text. (b) Detection efficiency curve for PMT. These curve data points were obtained from eight photopeaks (Gaussian fitting curves labelled as red), which are clearly seen in the spectrum. p0, p1, and p2 are the efficiency at low energies; p4, p5, and p6 are the efficiency at high energies.

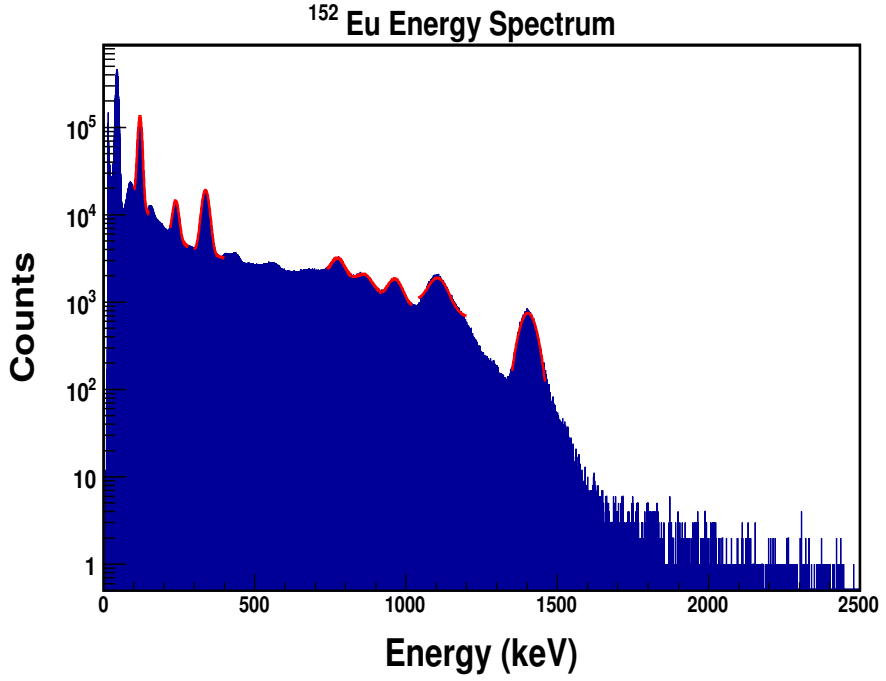

(a) Calibrated energy spectrum of Europium 152 for $LaBr_3$-C SiPM detector.

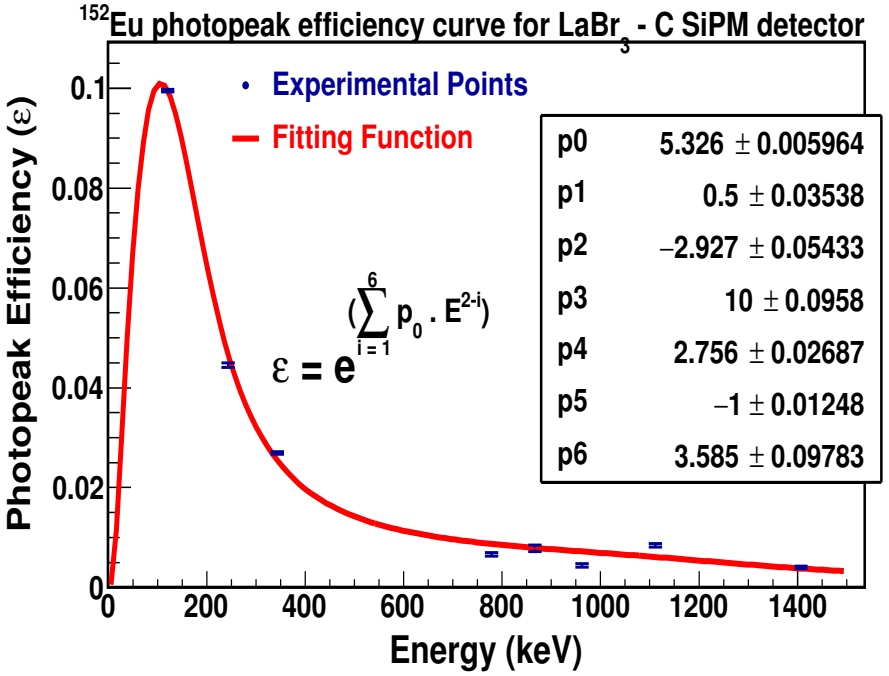

(b) Detector efficiency curve for SensL C-type silicon photomultiplier.

FIGURE 3.17: $LaBr_3$-C SiPM detector efficiency curve. (a) Calibrated ^{152}Eu energy spectrum obtained from $LaBr_3$-C SiPM detector system. (b) Detection efficiency curve for SensL C series SiPM.

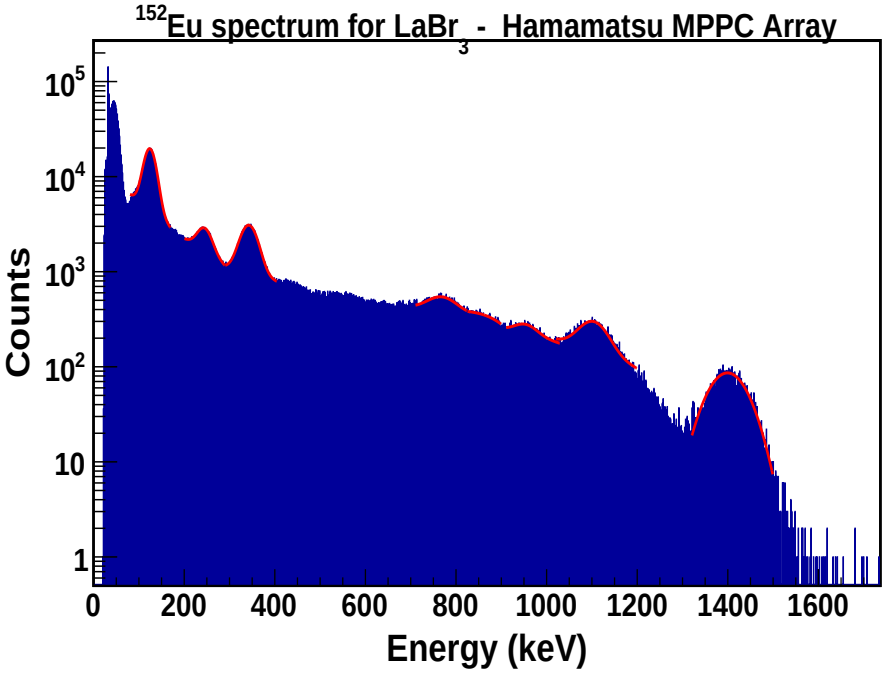

(a) Calibrated energy spectrum of Europium 152 for $LaBr_3$-Hamamatsu array of multi-pixel photon counter (S12572-010P) detector.

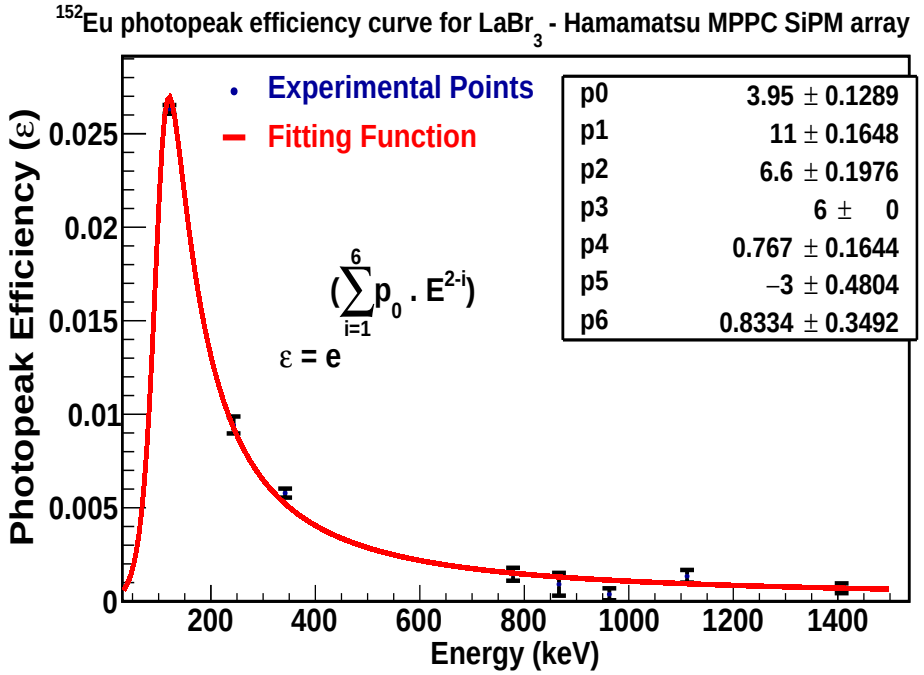

(b) Detector efficiency curve for Hamamatsu multi-pixel photon counter (S12572-010P).

FIGURE 3.18: $LaBr_3$-Hamamatsu array of multi-pixel photon counter (S12572-010P) detector efficiency curve. (a) Calibrated ^{152}Eu energy spectrum obtained from $LaBr_3$-Hamamatsu array of multi-pixel photon counter (S12572-010P) detector system. (b) Detection efficiency curve for Hamamatsu array of multi-pixel photon counter (S12572-010P).

3.8 Result

Several important properties, such as temperature dependency, gain dependence of voltage and temperature, and the effect of bias voltage on energy resolution and detector efficiency play a critical role in nuclear detection instrumentation. This chapter investigated important properties and compared the results obtained from standard silicon photomultiplier (Hamamatsu MPPC), PMTs, and SensL B and C-types SiPMs.

Energy resolution measurement with SensL silicon photomultiplier was found to be more stable at room temperature than at the low temperature. The energy resolution decreases with reducing the temperature due to the decline in the dark count rate or dark current. Regarding the dark current, SensL C-types SiPM has lower dark current than B-series SiPM (it reduces from 10-24 μA to 0.68-1.75 μA), because SensL improved their manufacturing methods by using CMOS technology. Therefore, SiPM homogeneity becomes better with reducing the damage on the detector during the production process. Dark current increases as a square of the bias voltage in our measurement, which is consistent with the literature.

Another important parameter gain was also studied, which found the linear correlation between the bias voltage and the detector gain at room temperature and low temperature respectively. If the temperature increases, the collision possibility between electron-hole pairs and silicon crystal lattice rises. Therefore, pairs could not have sufficient energy to overcome the reversed potential inside the depletion region and for the avalanche process resulting in a drop in the gain. As similar to the literature, we obtained the reverse proportional relationship between gain and temperature. However, a single centigrade temperature variation will shift 3.72 ± 0.13 centroid of the photopeak (change in the gain), which was not very close to the value provided by the manufacturer. The gain is not directly related to the temperature; it directly depends on the breakdown voltage. The breakdown voltage increases if the temperature increases, but the gain will reduce. Studied temperature, bias voltage, and breakdown voltage dependence of the gain were consistent with the literature and the scientific data values provided by the manufacturers (SensL and Hamamatsu).

Finally, we investigated the detector energy linearity with the best result with Hamamatsu MPPC, which is also in agreement with similar research. Furthermore, studies were presented in the Chapter 4 by focusing only on SensL C types

SiPM with its special readout signals for timing applications.

Chapter 4

Coincidence Resolved Time (FWHM) Measurement Based Scintillation Detectors

4.1 Silicon Photodiode Timing Performance

Coupling scintillator crystals with photomultiplier tubes is a well-established approach to γ-ray detection. The technology is, for example, used extensively in the field of nuclear physics and finds widespread application in medical imaging, where it is employed in PET (positron emission tomography) and SPECT (single-photon emission computed tomography). Silicon photomultipliers offer an attractive replacement for photomultiplier tubes in certain applications, particularly when it is desirable to operate in regions with high magnetic fields. Historically, the performance of silicon photodiode devices is poor in terms of timing resolution, which would disbar applications such as time-of-flight PET in medical imaging, or fast-timing measurements in nuclear physics [61]. The approach taken in PET is to determine lines of response through coincident detection of annihilation photons; hence, good timing resolution is crucial. If the timing resolution of the detectors is high enough (subnanosecond) then it enters the regime of time-of-flight PET (TOF-PET), in which the line of response can be reduced in length according to the time difference recorded between the detected photons [62]. Additionally, improving timing resolution reduces false coincidences. Therefore, there is a strong drive to improve the timing resolution of detector elements used in PET.

It is striking that the demands of contemporary medical imaging significantly overlap with those of experimental nuclear physics. Of great interest in nuclear physics are fast-timing measurements, which allow the lifetimes of excited states of the order of 100 ps to be measured. In the past, these were conducted with barium fluoride detectors, using the fast component of the BaF_2 signal to extract timing information. Increasingly, next-generation scintillators such as $LaBr_3$ are being used because they offer both excellent timing resolution and energy resolution, which makes it easier to select γ-ray transitions of interest [63, 64].

In summary, developing scintillation detector systems with excellent timing resolution that can operate in high magnetic fields is of great value in both medical imaging and nuclear physics. Attractive in this regard are newly-available blue-sensitive silicon photomultipliers such as the B-series or C-series available from SensL, since they will operate directly in a high magnetic field, but also have a fast timing ($<$ ns) output. Their blue sensitivity is particularly relevant, as they may be coupled with next-generation scintillators, such as $LaBr_3$, which are known for their excellent energy resolution and detection efficiency. Moreover, the number of collected photoelectrons is inversely proportional to the square of the time resolution. Quantum efficiency and gain times collection efficiency are two major factors in the timing resolution [65]. The quantum efficiency for silicon photomultiplier is higher than 80% in the blue light range, but it is required to reduce the absorption length from 5 μm for red light absorption to 1 μm for blue light absorption. That is why blue light sensitive photodiode junction must be located at a shallow at depth of 0.5 μm or less [61], as discussed in Chapter 3. Therefore, the blue sensitivity of the photomultiplier is critical for achieving optimal timing resolution. Several important parameters also indirectly affect the timing performance, such as the capacitance (C_d) of SiPM microcells, quenching resistance (R_q), and readout electronic noise (S/N). These parameters can play a critical role in the pulse decay time, and in particular, affect the pulse rise time. The exponential time constant (τ), timing resolution (σ_t) and signal-to-noise ratio (S/N) are described by Equations 4.1, 4.2 and 4.3 respectively [66, 67],

$$\tau = C_d.(R_q + R_{input}.N_{microcells}) \tag{4.1}$$

$$\sigma_t = \frac{N}{dV/dt} = \frac{\sqrt{k.T.(F-1)C_d}}{2.28.Q_c(e,h).BW_A} \tag{4.2}$$

$$\frac{S}{N} = \frac{Q_c(e,h)}{\sqrt{k.T.(F-1).C_d}} \tag{4.3}$$

where k is the Boltzmann constant, T is the temperature, Q_c(e,h) is the collected charge, and F and BW_A are the noise factor and bandwidth. The characteristic exponential time constant of a typical silicon photomultiplier is between 30 and 50 ns, depending on the type of scintillation crystals. However, PMTs' time constant can be a few nano seconds (lower than SiPM). According to Equations 4.2 and 4.3, time resolution (σ_t) is proportional to the square root of the detector capacitance ($\sqrt{C}$). The internal detector capacitance from the fast terminal to the cathode is 12 pF for 3x3 mm^2 active area SensL C type SiPM, which consists of 4774 microcells with 35μ size [54]. The internal capacitance increases to 48 pF with a larger dimension of 6 mm SiPM with 18980 microcells. As a result of the difference in the values of capacitance, the time resolution would be doubled when dimensions are increased from 3 mm to 6 mm SensL C type SiPMs. According to the result of the coincidence timing resolution measurement (which was successfully achieved by Kevin O'Neill et al.), the full width at high maximum (FWHM) was 226 ps for 3x3x15mm^3 LYSO crystals coupled to 3 mm SiPMs. Therefore, one would expect the FWHM to be approximately 452 ps for 6 mm SiPMs [68]. A similar timing measurement was completed with a 3 mm SiPM coupled with a 3x3x10 mm^3 LYSO crystal, and obtained 180 ps [66]. Yeom *et al.* report timing resolution of 290 ps for 10 mm-long LYSO crystals coupled with Hamamatsu MPPC S10931-050P 3 $\times$ 3 mm^2 silicon photomultipliers [69]. If 6 mm SiPMs were used in these measurements, then one would expect FWHM of 360 ps and 580 ps respectively for the SensL C-series SiPM and Hamamatsu MPPC (Multi-Pixel-Photon-Counter). It should be noted that although the time resolutions are worse for larger dimensions, for various nuclear physics and nuclear astrophysics applications, larger dimensions are needed and can be used for measurements that do not require the best possible time resolutions.

The primary focus of the present work is to compare the coincidence timing resolution of SensL SiPMs (both the B-series and C-series blue-sensitive types with 6 mm square active area [50, 54]), standard SiPMs (Hamamatsu S12572-010 with a 3 mm square effective area [52]) and fast PMTs, in conjunction with next-generation scintillators. A Hamamatsu 6 mm square active areas MPPC device was not available. Therefore, 2x2 array of MPPC (with a 3 mm square active area) was used (Figure 4.1(a)), thus allowing a comparison with SensL devices with 6

mm square active area (Appendix A.2). The PMTs were the Hamamatsu R9880U-210 and super bialkali R3998-100-02 (see Table 4.1 for the relevant parameters).

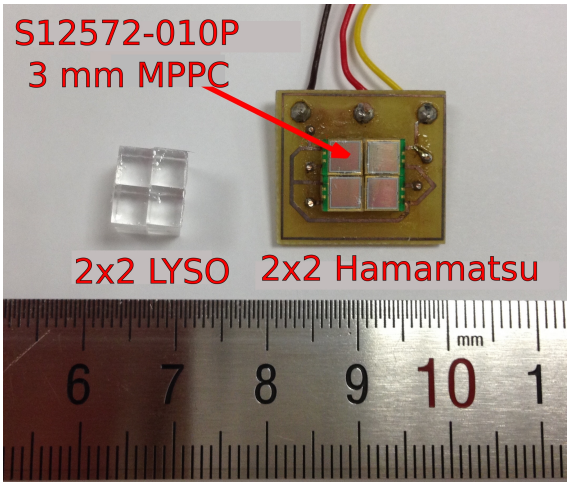

(a) 2x2 arrays were made from four 3 mm S12572-010P Hamamatsu SiPMs. Each SiPM is connected as a parallel to the circuit (to obtain proper combined readout signal because the circuit readout will be the total of the each MPPC currents with parallel connection). The electrical connection is shown in Appendix A.2

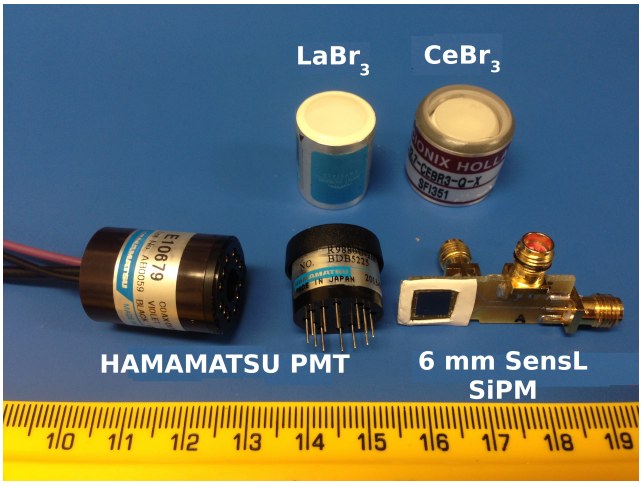

(b) Hamamatsu PMT, SensL blue-sensitive SiPM and scintillation crystals.

FIGURE 4.1: Photomultiplier and scintillator used for timing measurements.

The performance of these devices was evaluated in combination with crystals of novel scintillators: a 0.5 inch diameter x 0.5 inch long $LaBr_3$, a 0.4 inch diameter x 0.4 inch long $CeBr_3$, 6 x 6 x 25 mm^3 CsI and 3.5 x 4 x 10 mm^3 LYSO crystals (Figure 4.1). The measurements were conducted using analogue as well as digital systems. Timing measurement using a digitiser was successfully completed after improving the rise time of the C-series SiPM's fast-timing signals, as explained in

Properties	Hamamatsu SiPMs	SensL SiPMs B- and C-Series	Hamamatsu PMTs	
			R3998-100-02	R9880U-210
Bias Voltage (V_{BR}+V)	(65 ∓ 10) + 4.5	(24-25) + 5	1000	1000
Rise Time (ns)	-	1	3.4	0.57
Pixel Size (μm)	10	35	-	-
Pixel Number	90 000	18 980	-	-
Capacitance (pF)	320	48	-	-
Transit Time (ns)	-	-	23	2.7
Gain	$1.35x10^5$	$4.3x10^4$	$1.0x10^6$	$2x10^6$
Blue Sensitivity index	-	-	13.5	15.5
Peak Wavelength (nm)	470	420	350	400
Diameter (mm) or Active Area (mm^2)	3 x 3	6 x 6	25.4	16

TABLE 4.1: The properties of SiPMs and PMTs studied in the present work.

the section 4.3.5. Signal processing was completed using leading edge and constant fraction methods.

4.2 Timing Measurement with Analogue Setup

For subsequent timing resolution measurements, different combinations were explored for the 0.5 inch x 0.5 inch $LaBr_3$ and 0.4 inch x 0.4 inch $CeBr_3$ crystals optically coupled either with the 6 mm SensL B-series blue-sensitive silicon photomultipliers or with the Hamamatsu PMTs. Since the quality of crystal wrapping and surface treatment can change the timing resolution, a consistent technique was employed in which the crystal and photomultiplier were coupled using Bicron BC-630 silicone grease. The exposed areas were wrapped with a PTFE reflector with 3 mm effective thickness (optimum thickness for scintillation light-tight and reflection), and a few layers of black tape, to avoid interaction between the ambient light and the detector. Figure 4.2 shows the electronic block diagram used in the analogue timing measurement. A ^{22}Na (451 kBq) source was placed between two detector systems; all data were obtained with an Ortec maestro multichannel analyser. The fast output of the SiPM is fed into the Ortec 820 fast-timing amplifier, and then a signal is sent to the Ortec 473A CFD module. Ortec 416A gate delay generators are used for adjusting the time difference between the start and stop signals to the desired value, typically to place the peak in the middle of the ADC

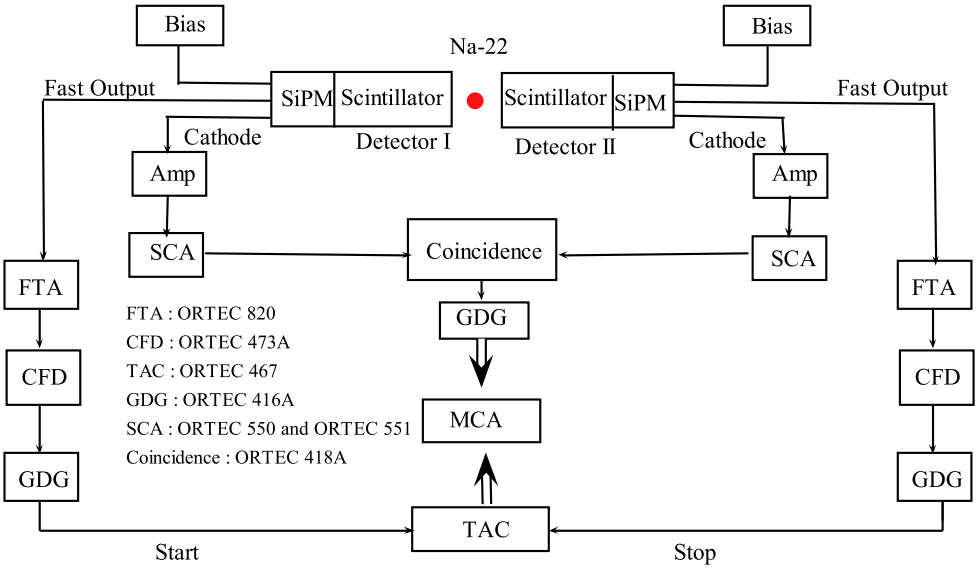

FIGURE 4.2: Electronic block diagram used for analogue coincidence timing measurements.

range. Cathode signals are used for the energy gate by applying an appropriate threshold level for picking up signals generated by 511 keV annihilation photons. Therefore, coincidence signals are sent to the MCA module with the energy gate to obtain a desirable timing spectrum. When the threshold level and energy gate are adjusted, each module output is checked step-by-step, with as low a threshold value as possible to eliminate signal noise. The intrinsic coincidence-resolved time (FWHM) of the electronics was found to be 76.28 ± 0.01 ps from the Gaussian-fitting parameters (Figure 4.3). For this measurement, a Philips PM5786 pulse generator was used for the initial pulses. Results from a systematic investigation of the coincidence-resolved time (FWHM) for different combinations of crystals and sensors are given in Table 4.2. The best result of 365 ps (at 511 keV) was obtained from a $LaBr_3$ crystal coupled to a fast Hamamatsu PMTs-R9880U-210, but the results listed in Table 4.2 were not close to literature values. SensL achieved the coincidence-resolved time measurement 180 ps for 3x3 mm^2 SiPM coupled to 3x3x10 mm^3 LYSO as discussed in the section 4.1. In addition, SiPM (3x3 mm^2) based in combination with $LaBr_3$ (3x3x5 mm^2) timing performance was found approximately to be 100 ps FWHM (nearly 15 mm positioning resolution in TOF-PET) for 511 keV annihilation photons emitted from ^{22}Na point source [70]. Another research in coincidence-resolved time measurement was conducted with a large effective area of 4x4 mm^2 near UV-SiPM (sensitive to ultraviolet) coupled with a 4x4x5 mm^3 30% Cerium doped $LaBr_3$ resulting with a 100 ps time resolution [71].

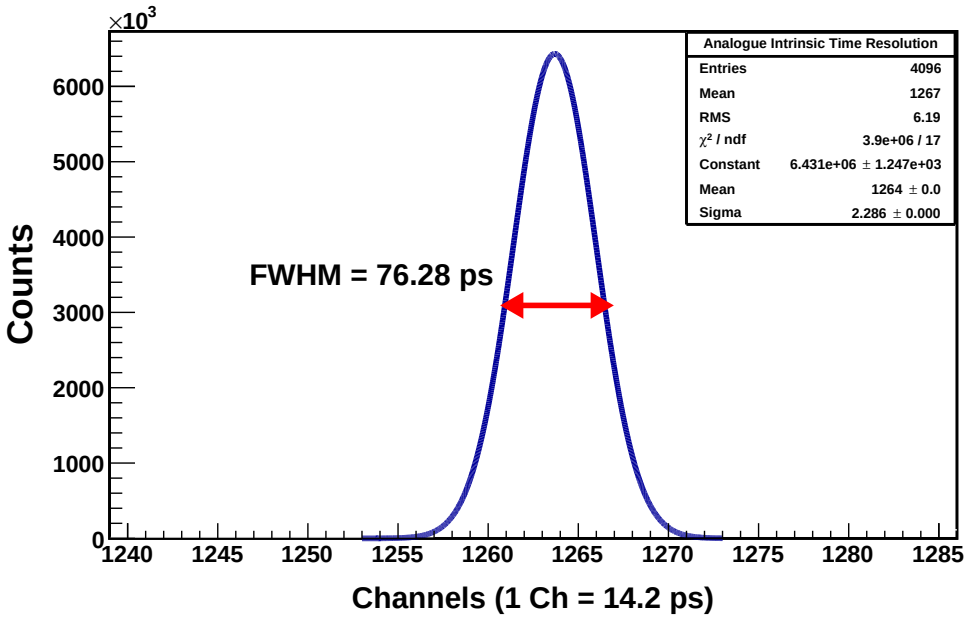

FIGURE 4.3: Intrinsic coincidence resolved time of the electronic modules (76.28 ± 0.01 ps).

Scintillator ⟷ Photomultiplier	**FWHM (ps)**	**FWHM after subtraction of intrinsic (ps)**
$LaBr_3$ ⟷ PMT-R9880U-210 **$LaBr_3$ ⟷ PMT-R9880U-210**	**373**	**365**
$LaBr_3$ ⟷ PMT-R9880U-210 **$CeBr_3$ ⟷ PMT-R9880U-210**	**381**	**373**
$LaBr_3$ ⟷ PMT-R9880U-210 **$LaBr_3$ ⟷ SiPM**	**518**	**512**
$LaBr_3$ ⟷ PMT-R3998-100-02 **$LaBr_3$ ⟷ SiPM**	**684**	**677**
$LaBr_3$ ⟷ PMT-R9880U-210 **$CeBr_3$ ⟷ SiPM**	**690**	**686**
$CeBr_3$ ⟷ PMT-R3998-100-02 **$LaBr_3$ ⟷ SiPM**	**720**	**716**
$LaBr_3$ ⟷ SiPM **$LaBr_3$ ⟷ SiPM**	**852**	**849**
$CeBr_3$ ⟷ SiPM **$LaBr_3$ ⟷ SiPM**	**1017**	**1014**

TABLE 4.2: Coincidence-resolved time for various detector systems measured by analogue setup.

NIM modules used in the analogue measurement were not perfectly suited for the type of fast signals present in these measurements. Therefore, there is room for improvement by using a digital acquisition and processing method. In addition, the active area of the PMTs and SiPM did not exactly match the surface area of the scintillation crystals, as unfortunately it 's hard to make specific shapes with

very hygroscopic inorganic scintillation crystals, such as $LaBr_3$ and $CeBr_3$. As a result, there was a loss of light collection by the sensor, which will also influence coincidence timing resolution.

4.3 Timing Measurement with DT5742 Digitiser

The SensL C type silicon photomultiplier was preferred to the B-series SiPMs for a digital timing measurement. Figure 4.4 shows that the signal-to-noise ratio improved with the C-series SiPMs from 6.6 to 12.9 with better signal amplitude. The SensL improved the manufacturing process in the C-SiPM. Less damage to the depletion region and better homogeneity are successfully developed by CMOS technology, resulting in a low dark current, and low noise, as detailed in Chapter 3. That novel technology does not influence the SiPM rise time because Geiger discharge time and the recovery time controls the decay time and the rise time of the signal. Both parameters increase with the photodetector capacitance; therefore, the large area of SiPM will be slower than a small area photodiode. Scintillation crystal rise and decay time are also affected by the readout signal shape.

A fast Hamamatsu R9880U-210 PMT, SensL C type SiPMs and Hamamatsu MPPC 2x2 arrays (6x6 mm^2 photosensitive area, as shown in Figure 4.1(a)) are coupled with various scintillation crystals such as $LaBr_3$, $CeBr_3$, LYSO and CsI for digital timing measurements (Figure 4.1(b)). A raw signal must be fed to an appropriate time filter amplifier such as an Ortec 820 FTA to optimise the signal and filter the noise. Digital signals are obtained by CAEN DT5742 16+1 channels 12 bit 5GS/s digitiser (Figure 4.5). The software was written in C++ and analysed in ROOT. Two different standard methods are applied separately to the analysis: leading edge and constant fraction (see sections 4.3.1 and 4.3.2 for more details). The electronic block diagram is shown in Figure 4.6 to stabilise time measurement with fast Hamamatsu $LaBr_3$-PMT detector systems. One $LaBr_3$-PMT detector system was fixed, while several others were tested one-by-one in combination with this reference detector.

Coincidence-resolved time (FWHM) of 136 ps for two identical $LaBr_3$-PMT detector systems was achieved (Figure 4.7). The leading edge method was applied, and a suitable threshold level was identified after the defined energy gate (511 keV annihilation photons).

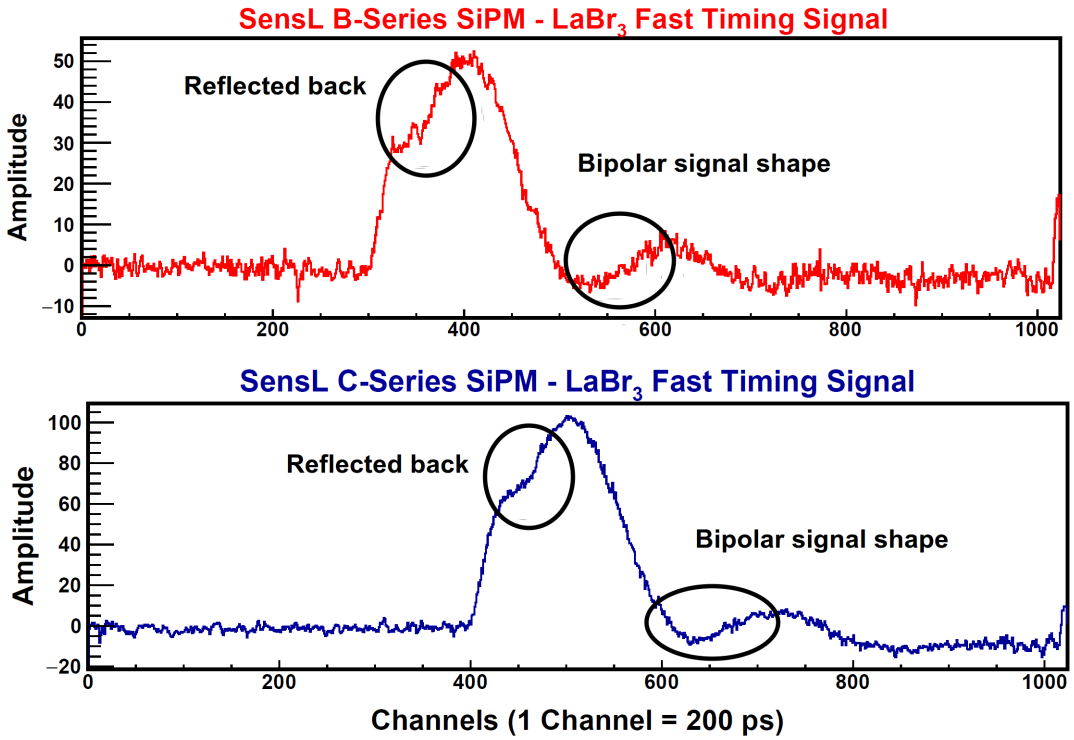

FIGURE 4.4: Fast-timing signals obtained by SensL B- and C-series SiPMs after coupled to $LaBr_3$. Bias voltage was at -28V for both silicon photomultipliers. Signal-to-noise ratio improved from 6.6 to 12.9 with C-series SiPMs. Therefore, the time resolution is reduced with SensL B-series SiPMs from C-series SiPMs. The fast readout signal shape is bipolar, and the rise time is much quicker than the standard readout signal (for standard mode and fast signal mode connections see Chapter 3.

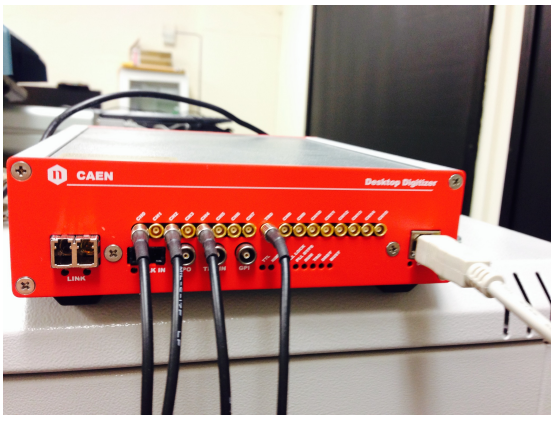

FIGURE 4.5: Picture of a DT5742 desktop waveform digitiser with 16 channels, a trigger, and other connections. A CAEN Waveform digitiser was used to obtain accurate and very fast time measurement (which can achieve few picoseconds time resolution).

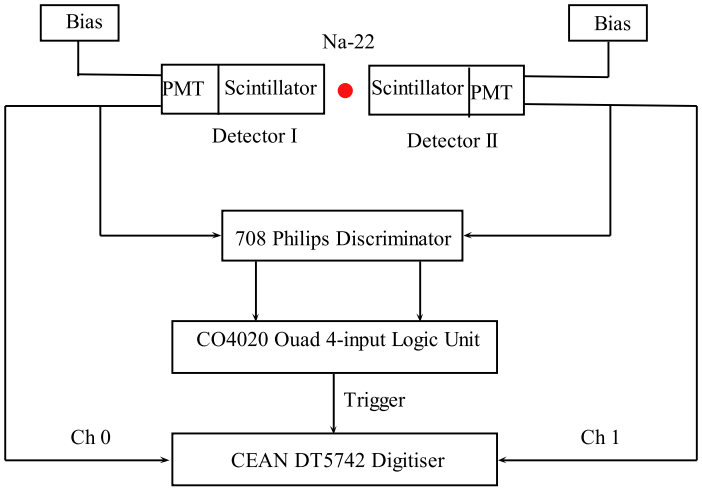

FIGURE 4.6: Electronic block diagram for two identical detector systems: the combination of $LaBr_3$-PMT detectors. The 708 Philips discriminator generated appropriate signals for the coincidence unit. A C04020 logic module gave AND signals for trigger input on the digitiser. If two signals were generated simultaneously, then the digitiser trigger allowed acquisition of signals fed to channel 0 and channel 1.

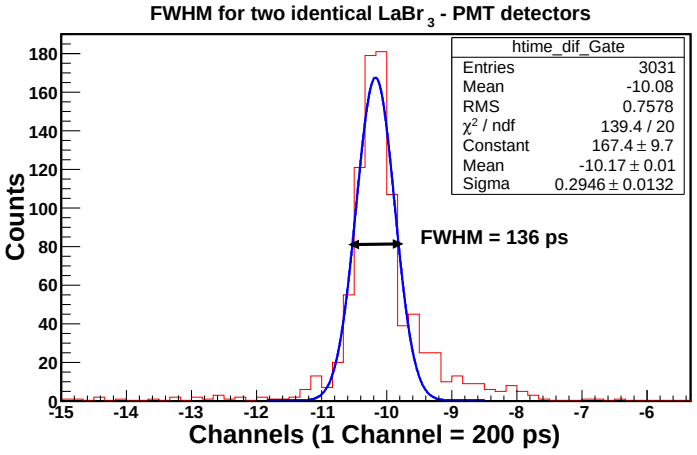

FIGURE 4.7: Gaussian fit function obtained from two identical $LaBr_3$-PMT detector systems after using the leading edge method and finding the best threshold level for two different spontaneous signals.

4.3.1 Leading Edge Method and Energy Gate

Two identical signals were generated by a Philips PM5786 pulse generator for intrinsic time resolution and two detector systems were radiated by a radioactive source for CRT (Coincidence Resolving Time) measurements. Digital data acquisition was conducted with suitable NIM modules such as an amplifier and discriminator. The recorded coincidence data were then analysed. The software

was written in C++ and run in conjunction with the ROOT package for an analysis of the signals according to the leading edge method. Several important steps were applied for the signal processing in the software. First, two signals, generated at the same time, inverted if they were negative, and then subtracted from the baseline. Second, the constant discriminator level (threshold) was applied as shown in Figure 4.8.

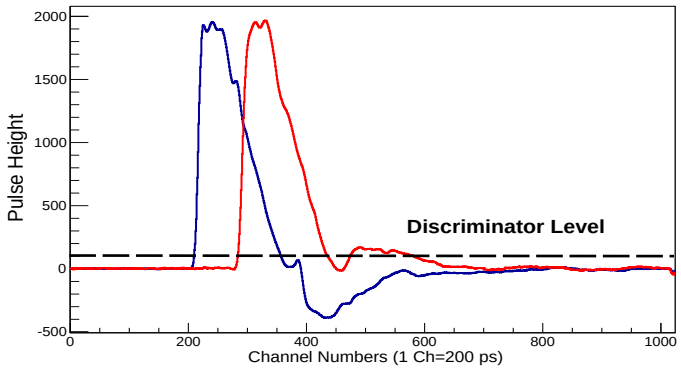

FIGURE 4.8: Two identical pulses generated from a Philips PM5786 pulse generator. The software was written in C++ and the analysis was carried out using the ROOT package in order to find crossing points. The time differences between the two pulses were then calculated.

Different values were chosen for the constant discriminator levels, depending on the signal height for non-identical pulses. In order to find the first crossing points, upper and lower threshold levels were recorded by using predefined thresholds. When the code found two bin numbers that were close to the threshold level, the crossing point was accurately calculated by a quadratic function, rather than a linear function (Figure 4.9). Then, the software calculated the time difference between the two different pulses and repeated the same calculation for 5000 coincidence pulses (Figure 4.10). Finally, the Gaussian distribution plotted and then obtained FWHM from the fitting parameters (FWHM = 2.35 x σ_t) [24]. However, plotted Gaussian distribution does not tell which energy gamma ray is in coincidence with which the other gamma ray. Recorded time coincidence of two logical signals can occur accidentally or from Compton scattering events in coincidence. In the analogue measurement, single-channel analysers were used to set only one gamma ray (511 keV for ^{22}Na) for each detector. In order to improve the timing resolution in the digital measurement, the energy filtering method must be used, and Compton scattering events and accidental coincidences must be separated from the annihilation events (511 keV). For this reason, another software was developed based on the pulse height. The amplitude versus time difference

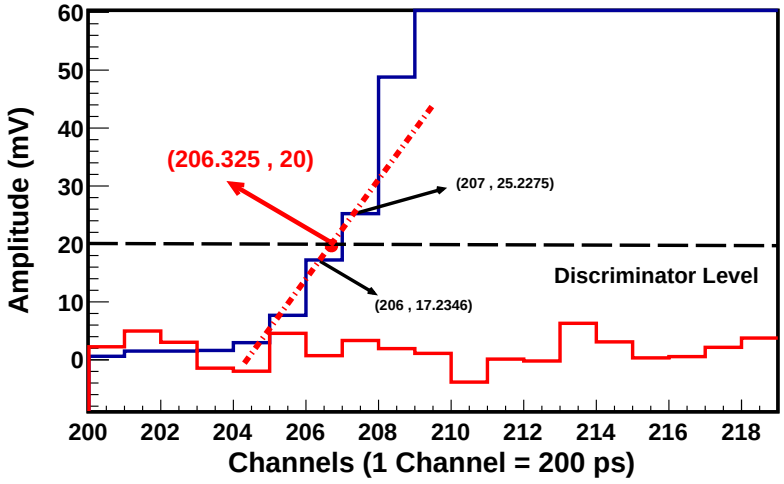

FIGURE 4.9: Blue and red colour two identical signals are produced by a Philips PM5786 pulse generator. A previously defined discriminator level was first crossed with blue signal and then a red signal. A quadratic fitting method was used to calculate the first crossing point at a discriminator level for each pulse separately.

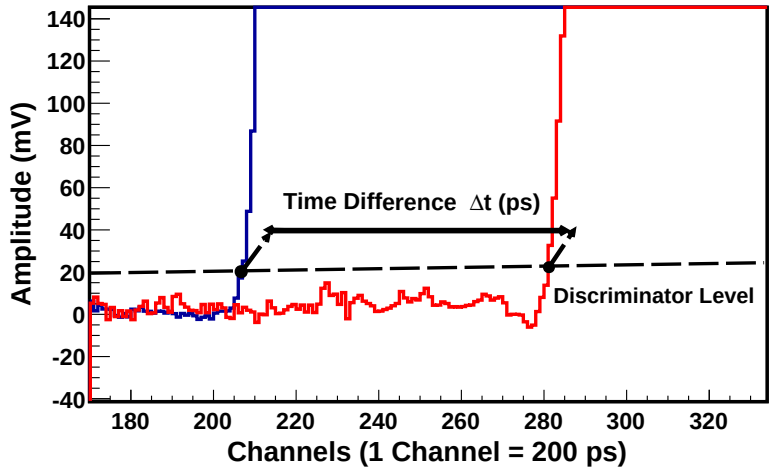

FIGURE 4.10: The identical two signals (blue and red) were generated by a Philips PM5786 pulse generator. After finding the first crossing points for each signal, the time differences between the two signals were recorded to create a Gaussian distribution for electronic time resolution (intrinsic time resolution) as illustrated in Appendix A.3.

was then plotted on a 2D histogram, which allowed us to define the energy gate (Figure 4.11). The software was modified to include the energy gate and then the Gaussian distribution of the time differences was plotted, as shown in Figure 4.12. In this plot, coincidence-resolving times for each case were found to be 409 ± 9 ps for without the energy gate and 371 ± 5 ps after applying the energy gate. It is clear that more accurate coincidence-resolved time measurement could be achieved

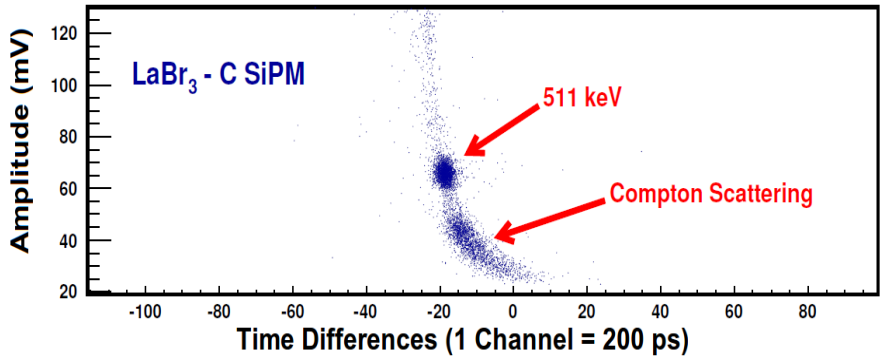

(a) Amplitude vs. time difference in 2D histogram for C-SiPM coupled to $LaBr_3$.

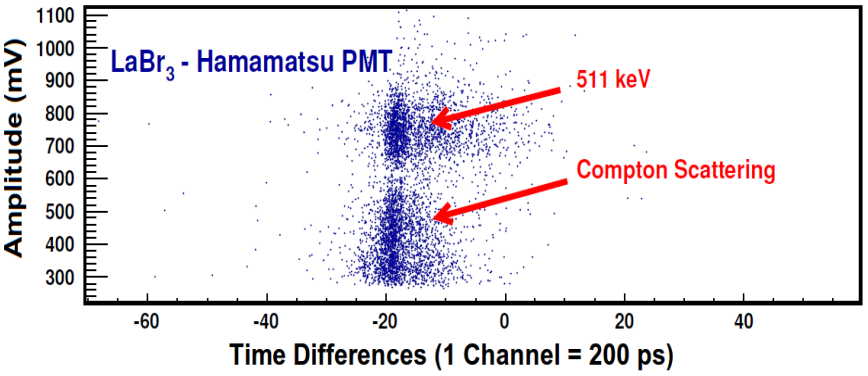

(b) Amplitude vs. time difference in 2D histogram for PMT coupled to $LaBr_3$.

FIGURE 4.11: Amplitude versus time difference 2D histogram corresponding to (a) SensL C-SiPM and (b) Hamamatsu PMT-R9880U-210 coupled to $LaBr_3$. Annihilation photons and Compton scattered photon events are clearly seen. Only the annihilation photons (511 keV gamma) were used for timing resolution calculations; the rest of the data were ignored in the software.

with the energy gate.

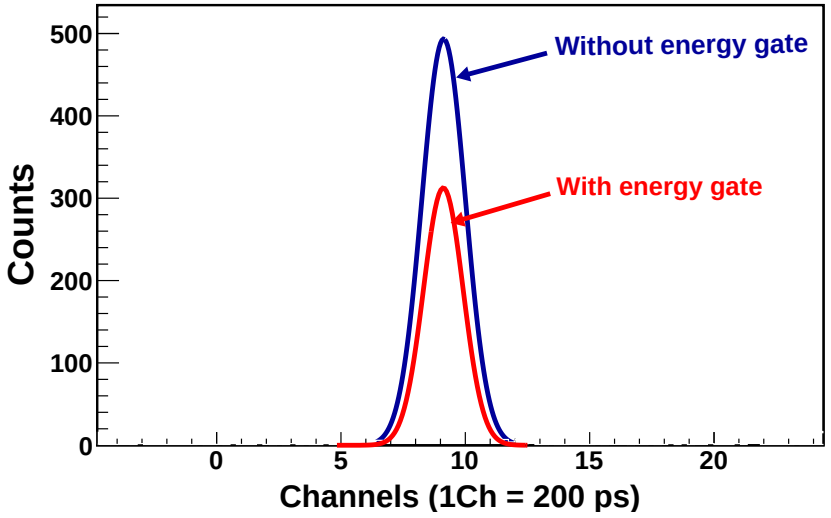

FIGURE 4.12: Gaussian distribution with and without an energy gate, so the sigma is improved by eliminating Compton scattering and noise during the data analysis process from 0.87 ± 0.02 to 0.79 ± 0.01 .

4.3.2 Constant Fraction Method

The second method is constant fraction: the pulse-shaping process is shown in Figure 4.13. The raw signal was inverted, delayed, and amplified with constant value, and was added to the raw-signal. The final signal (Figure 4.13 (bottom))

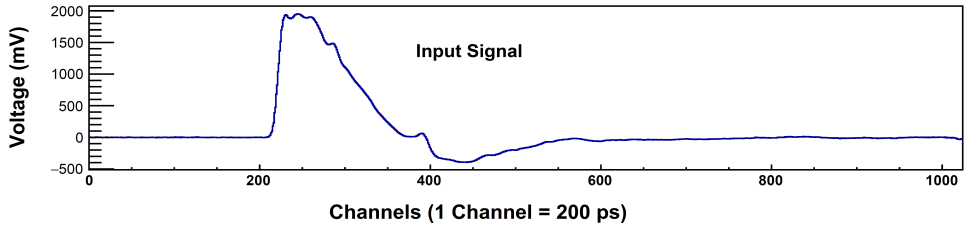

(a) Orginal $LaBr_3$-PMT detector fast timing readout signal without pulse shaping

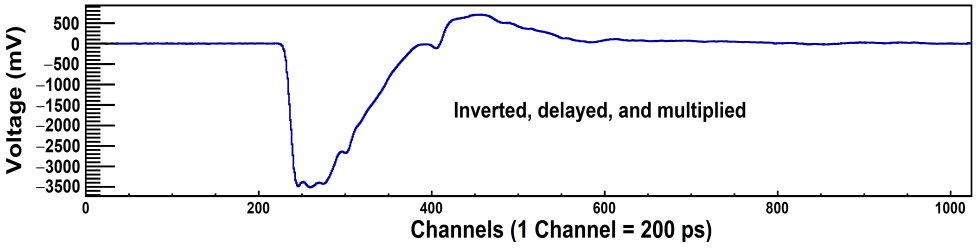

(b) Orginal signal was inverted, delayed and amplified.

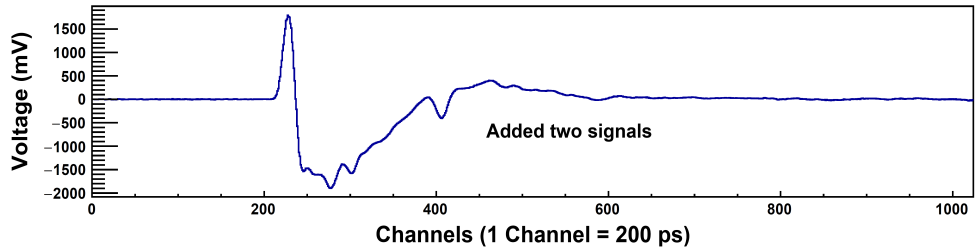

(c) Added two signals, whhich one is the original signal, and second one is inverted-delayed-amplified signal.

FIGURE 4.13: Signal processing in the constant fraction timing method. (a) A raw $LaBr_3$-PMT detector signal. (b) Inverted, delayed, and amplified signals. (c) Added resulting from top and middle signals.

had zero crossing points after the highest point, as shown in Figure 4.14. The software recorded the first zero crossing point in memory. A similar procedure was applied for the other detector's coincidence signals, and this was recorded in the second memory. Therefore, the time differences for the two detectors' signals were calculated by subtracting two recorded values. This calculation was repeated for 5000 coincidence signals after picking up only the 511 keV energy range as explained above. Time resolution was obtained using the constant fraction method, but the result was not as good as that obtained using the leading edge

method. For instance, intrinsic time resolution was found to be 127 ± 3 ps with the constant fraction method, but 70 ± 1 ps with the leading edge method. The constant fraction method can lead to very poor timing resolution if there is a pulse shape distortion, poorly shaped, or noisy pulses [72]. SensL fast readout signal of SiPM is not as good as the standard readout mode, the pulse shape changes from pulse-to-pulse. Therefore, we preferred to use the results calculated from the leading edge method, rather than that obtained using the constant fraction method.

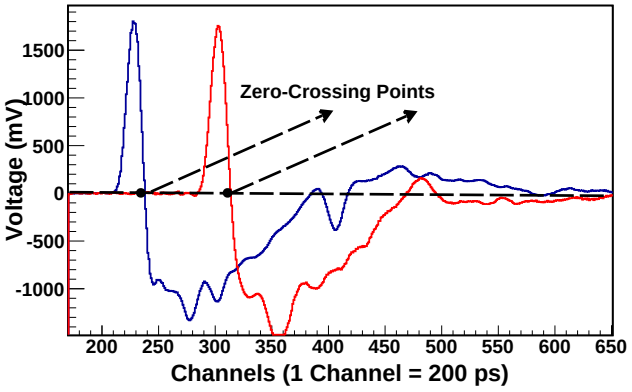

FIGURE 4.14: First zero crossing points of the signals after the peak. Difference between these two points gave the time differences between two signals.

4.3.3 Filtering Noise

In the software, a filtering procedure for the signal noise was also used, and then the signal was amplified. The common digital filter method known as a moving average filter was applied for a specific data length (from 3 to 10 data length). In this filtering, the average value of the data length was subtracted from the original data. Therefore, the new data was much smoother than the raw data without high frequency noise. Figure 4.15 illustrates an example of the moving average filter method applied to 10 data length.

However, coincidence-resolving time (FWHM) did not improve after filtering the noise; for example, 616 ± 9 ps was found for C-SiPM coupled with a $LaBr_3$ and a Hamamatsu fast PMT-R9880U-210 coupled with the other $LaBr_3$ that was found at 338 ± 7 ps without a moving average filter.

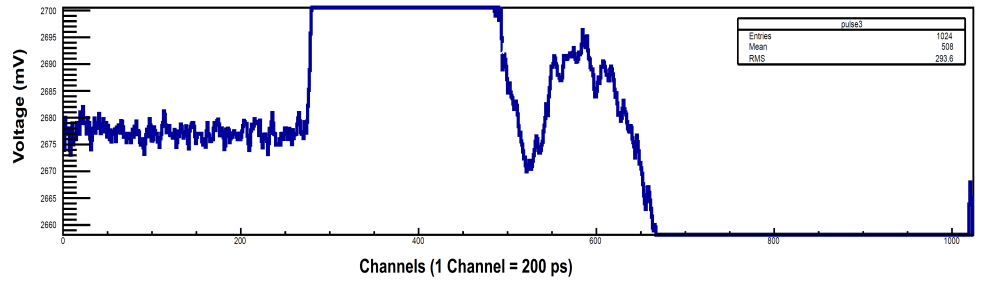

(a) $LaBr_3$-C SiPM detector fast timing terminal readout signal.

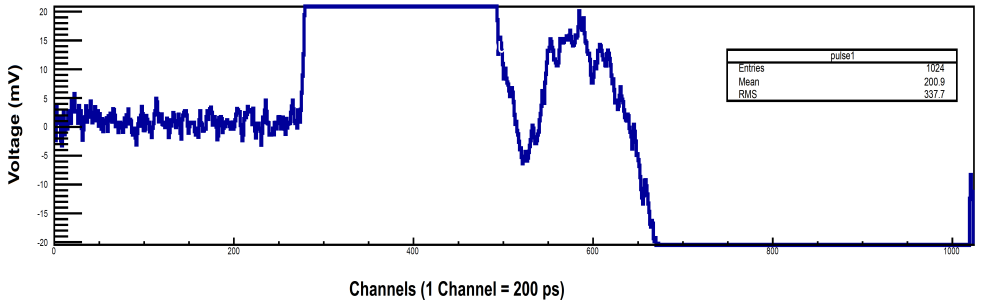

(b) Original signal subtracted for moving to the baseline.

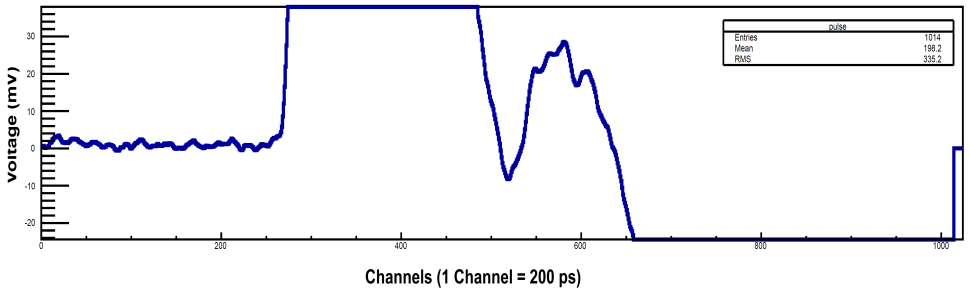

(c) Digital filter method (moving average filter) was applied to 10 data length.

FIGURE 4.15: (a) $LaBr_3$-C SiPM detector signal from fast timing terminal. (b) Signal subtracted for baseline and inverted if necessary. (c) Digital filter method, known as a moving average filter was applied to 10 data length resulting in smooth data and eliminating the high frequency noise component. It is also amplified 1.5 times higher than the raw signal to obtain a better rise time for the lowest threshold level as possible.

4.3.4 C-Series SiPMs without Balun

For the case of the fast Hamamatsu PMTs optically coupled with $LaBr_3$, there was a coincidence-resolved time or resolution (FWHM) of 136 ps (Figure 4.7). After optimising the timing measurements for these detector systems, one of the Hamamatsu PMT-$LaBr_3$ detectors was replaced with $LaBr_3$-SiPM. An Ortec 820 fast timing amplifier (FTA) was used to obtain the desired signal from the timing output of SensL C type SiPMs, as schematically shown by an electronic block diagram

in Figure 4.16. Impedance matching is significantly important for RF/microwave

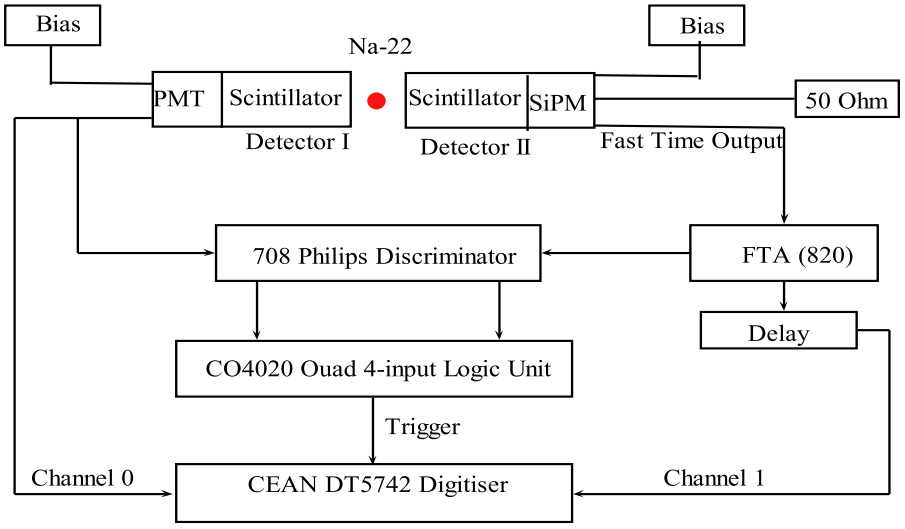

FIGURE 4.16: Electronic block diagram for coincidence time measurement of C type SiPM-$LaBr_3$ and PMT-$LaBr_3$ detectors. An Ortec 820 fast timing amplifier was used to generate an appropriate signal from a C-SiPM fast terminal readout to send to the discriminator and channel 1 in the digitiser system. Two different output signals of the discriminator fed into the coincidence unit. A CO4020 module was arranged for an AND logic unit. If the two detector signals occur at the same time, the digitiser trigger allows data to be recorded from channel 0 and channel 1. One of the detector signals was delayed to monitor both coincidence signals efficiently on the screen.

design when the digital signal is extremely fast. In higher frequency, tolerance will be less, so the PCB designer must be kept at 50 ohms during the transmission. The fast readout signal (48 pF) is significantly smaller than the standard readout signal (3400 pF) in C-SiPM. A transimpedance amplifier can not be used for low capacitance; instead, any RF style solution can be used with connecting 50 ohms impedance. That is why 50 Ω was connected to the standard signal during the data acquisition. FTA signals are fed into one channel in the digitiser and discriminator for the trigger. A CO4020 logic unit allowed the generation of coincidence triggers using AND logic. The trigger was then fed into the digitiser to acquire coincident-timing signals from the two detectors. The intrinsic time resolution (FWHM) of the electronics was found to be 70 ± 1 ps from the leading edge method (Appendix A.3). A Philips PM5786 pulse generator was used for electronic timing measurements. Coincidence-resolved time measurements were studied for several detector systems; the results are given in Table 4.3. According to Table 4.3, there was a major issue with the Ortec 820 FTA when it was used for C type SiPM's timing signal. The output from FTA module was rather different from the input signal in shape. There were two parts of the signal: inverted and

Scintillator ⟷ Photomultiplier	FWHM (ps)	FWHM after subtraction of intrinsic (ps)
$LaBr_3$ ⟷ PMT-R9880U-210 $LaBr_3$ ⟷ PMT-R9880U-210	136 ∓ 6	117 ∓ 7
$LaBr_3$ ⟷ PMT-R9880U-210 $CeBr_3$ ⟷ PMT-R9880U-210	150 ∓ 5	133 ∓ 5
$LaBr_3$ ⟷ PMT-R9880U-210 $LaBr_3$ ⟷ C-SiPM (With ORTEC 820 FTA non-inverted part)	869 ∓ 14	867 ∓ 14
$LaBr_3$ ⟷ PMT-R9880U-210 $LaBr_3$ ⟷ C-SiPM (With ORTEC 820 FTA inverted part)	486 ∓ 9	481 ∓ 9
$LaBr_3$ ⟷ PMT-R9880U-210 $LaBr_3$ ⟷ C-SiPM (Without amplifier)	338 ∓ 7	331 ∓ 7
$LaBr_3$ ⟷ PMT-R9880U-210 $LaBr_3$ ⟷ B-SiPM (Without Amplifier)	437 ∓ 4	431 ∓ 4

TABLE 4.3: Coincidence-resolved time for various detector systems measured by a digital system (without a transformer). Coincidence-resolving time resolution was very different from the PMT measurement. There was a major issue with an Ortec 820 FTA when it was used for C type SiPM's timing signal. The output from the FTA module reshaped the original signals with inverting them, but should not according to the module information provided by the manufacturer data. Therefore, the coincidence-resolved time resolution was found to be 338 ± 7 without using any amplifier, which is better than using the FTA.

non-inverted. That may be related to the fact that the raw signal has a bipolar shape while the module only processes a negative part as expected (Figure 4.17). When the non-inverted part made the coincidence-resolved time calculation in the

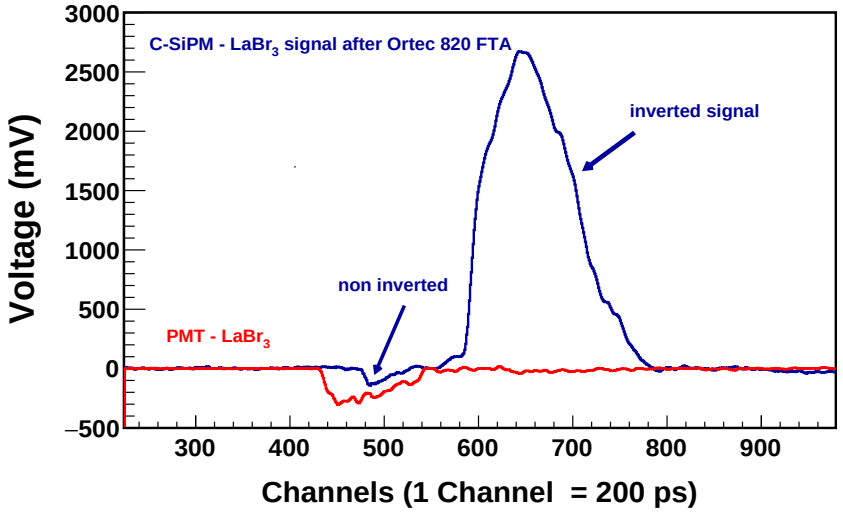

FIGURE 4.17: $LaBr_3$-C series SiPM fast-timing signal fed into the Ortec 820 fast-timing amplifier. The amplification part of the signal seemed to invert, but this module cannot invert the signal. Therefore, a small non-amplified part of the signal should be the fast component of the detector signal.

software, the timing result was lower than with the inverted section. That explains

the timing resolution we found was not accurate. Therefore, the Ortec 820 FTA was not suitable for a SensL fast-timing signal. The coincidence resolving time resolution was found to be 338 ± 7 ps at 5 mV threshold level and without using any amplifier, which is better than using FTA.

In addition, we investigated how the bias voltage affects coincidence-resolving time measurement (FWHM): Figure 4.18 shows this parabolic relationship. In this

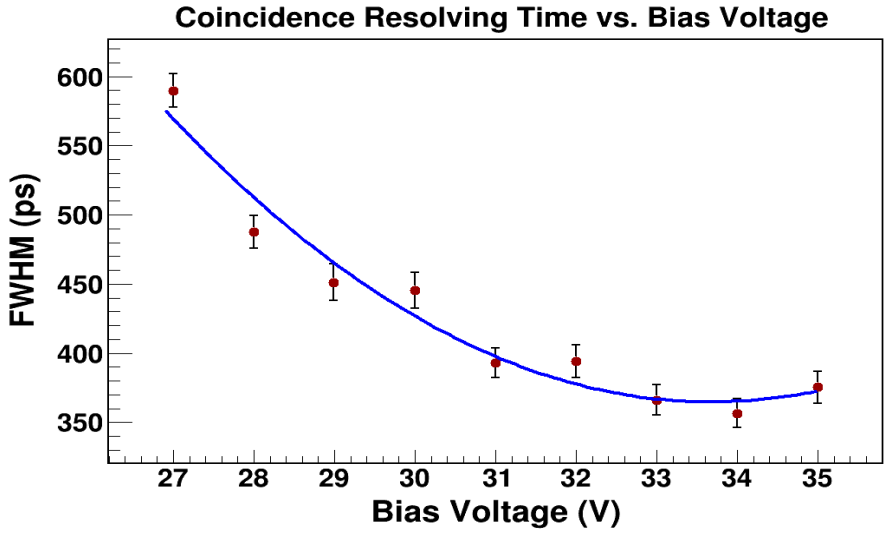

FIGURE 4.18: Dependence of the coincidence resolving time resolution (FWHM) and applied bias voltage from 27 V to 35 V. The detector systems were $LaBr_3$-SensL C-series SiPM and $LaBr_3$ optically coupled to PMT. An Ortec 820 fast-timing filter amplifier (FTA) was not used in the measurement.

measurement, the SensL C-type SiPM-$LaBr_3$ detector's timing output is directly connected to the digitiser without any amplification (the Ortec 820 fast timing filter amplifier was not used. Applied bias voltage was adjusted from 27 V to 35 V to find the optimum bias voltage, which minimises the coincidence resolving time resolution. In the data analyses process, the leading edge method was used with setting threshold level at 20 mV. The trend was found what expected, and the result is consistent with the literature [66, 73, 74]. When the applied reversed voltage increases, the detector gain and photodetection efficiency (improvement in the photon statistics [73]) also increase. The higher gain gives a better rise time and signal-to-noise ratio [74]. Noise becomes less important in the higher pulse amplitude. Consequently, coincidence resolving time resolution becomes lower until the noise becomes more dominant in the signal. After that bias voltage, the noise negatively impacts the time resolution. According to the plot, a 6 mm^2 SensL C-SiPM does not need to be used with very fast amplifiers between 33 V

and 34 V bias voltage. However, current amplifiers must use to minimise the noise in the signal for good time resolution.

4.3.5 C-Series SiPMs with a Balun

Photodiode current is commonly converted into the usable voltage by a transimpedance amplifier; however, a very low capacitance of the fast terminal does not allow that. Therefore, a microwave-RF style solution was applied by connecting 50-ohm impedance directly connected to coaxial cable. However, for optimum performance from the fast timing signal of SiPM with 3 mm^2 or 6 mm^2 effective area, that is not a suitable solution as this is a higher capacitance than a 1 mm^2. In that situation, it is highly recommended to connect an RF transformer, such as the RFXF9503, into the fast output for providing impedance matching and improving the fast output signal amplitude [50, 54, 76]. The standard readout signal and fast timing signal work against each other (this is not important ground and the currents are equal in magnitude), which is called a balanced signal. A balun is an electric device which converts a balanced signal into an unbalanced signal or vice versa. After connecting the balun to the circuit, the standard output work against the electrical ground and the fast readout carries the signal, which is called an unbalanced signal. That allows the electronic impedance matching for the efficient transfer of power and reduces the signal reflection from load [50, 54]. Therefore, the rise time of the detector pulse improves with the balun by routeing the signal trace (because timing output is extremely fast, it needs to be routed on a PCB). Figure 4.19 represents the recommended readout circuit by the manufacturer for optimum timing performance of the SensL SiPM. After the balun (transformer) was connected to the circuit, the signal rise time dramatically decreased from 40-35 ns to 10-6 ns. Balun connected SensL C-SiPM optically coupled with a $LaBr_3$ scintillator. This detector system was irradiated by a ^{22}Na radioactive source. A standard output signal and fast-timing signal of the detector were generated by the same event as shown in Figure 4.20, which exhibits different rise times. The rise time of the fast-timing signal obtained much faster than the standard signal and the fast readout signal generated without balun. SensL recommends a negative bias voltage for the optimum performance of the fast readout mode as illustrated in the biasing scheme in Figure 3.4 in Chapter 3. When the negative bias voltage is applied to the anode with the cathode at 0V, the signal polarity of the fast

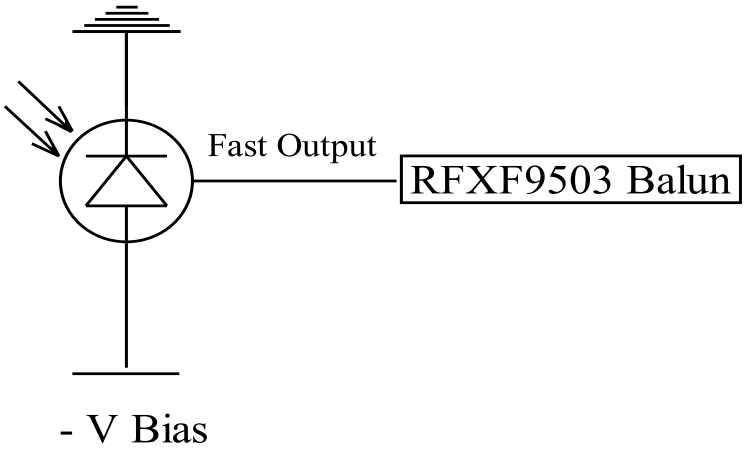

FIGURE 4.19: Recommended readout circuit for fast time output [54].

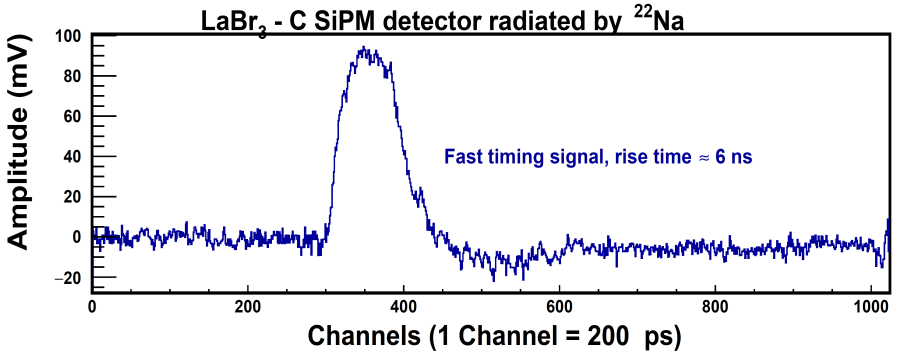

(a) Fast terminal readout signal.

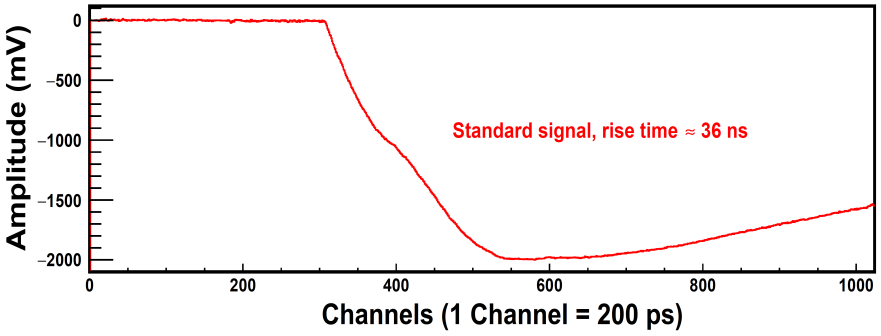

(b) Standard signal, the anode readout signal with negative polarity (negative bias voltage applied for optimum performance in fast timing mode)

FIGURE 4.20: Balun connected SensL 6 mm^2 C-SiPM was optically coupled with $LaBr_3$, and then the detector system was irradiated by ^{22}Na. (a) Standard and (b) fast-timing readout signals were obtained from the same event.

terminal will be positive, and a standard signal will obtain from the cathode with negative polarity.

Although the better rise time is obtained with the balun, the fast readout signal needs to be amplified and the noise filtered out to achieve the optimum

performance in coincidence-resolving time measurement. It seems that using the Ortec 820 fast-timing amplifier could not be compatible with the fast terminal signal of the SensL C-series SiPMs, as explained in section 4.3.4. Mini-Circuits ZFL-1000LN and ZX60-43-S+ amplifiers were used to obtain an adequate signal for coincidence resolving time measurement [54]. The circuit schematic of a 6 mm SensL SiPM and fast timing signal processes with the amplifier is illustrated in Figure 4.21. The fast output signal of SiPM was first fed to Mini-Circuits

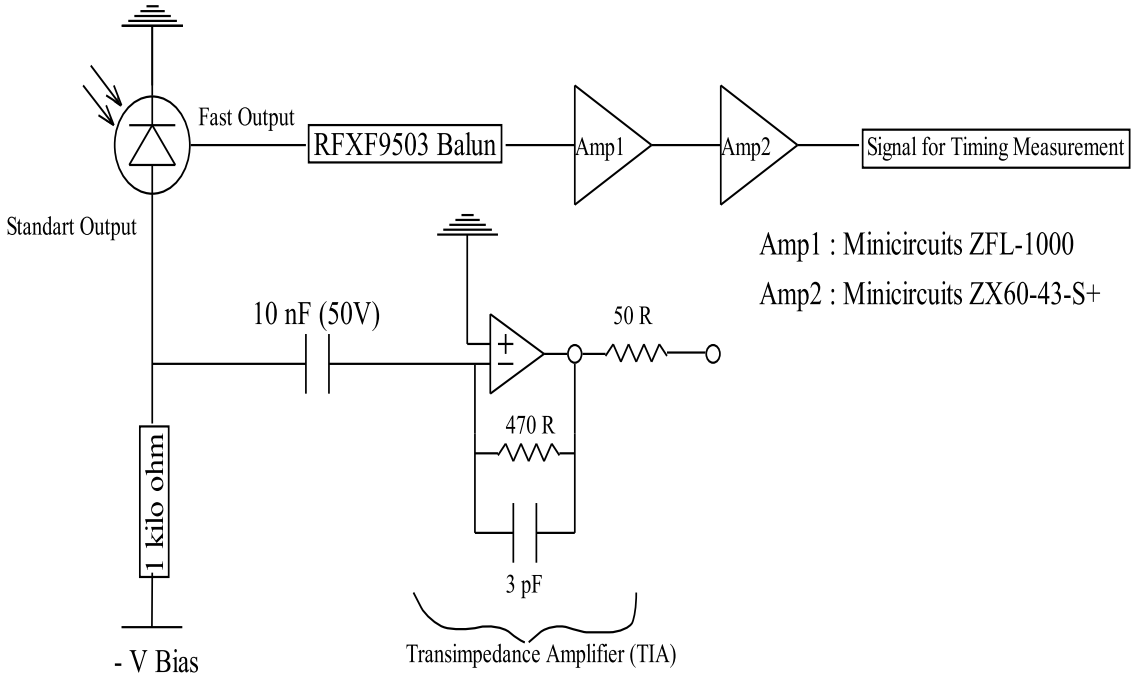

FIGURE 4.21: AC coupled readout for 6 mm SiPM circuit schematic with transimpedance amplifier. The fast signal transits to Mini-Circuits ZFL-1000LN and ZX60-43-S+ amplifiers obtain an appropriate signal for coincidence measurement.

ZFL-1000 and then ZX60-43-S+: Figure 4.22 shows the signal processes for each devices. The first amplifier was used to amplification of the signal, so the signal to noise ratio becomes a large. Therefore, the noise would not be significant in the signal (elimination of the high-frequency noise). Then the signal was sent to the second amplifier. The second amplifier used for the low-frequency noise within the fast frequency bandwidth to 4000 MHz. If the signals pass through a non-linear phase device, the signal frequency will delay in the output signal. The two amplifiers used were not in the linear phase. In addition, the signal output of the second amplifier was inverted resulting in an 180° phase shift. Therefore, the extra delay in the signal was observed as illustrated in Figure 4.22(c).

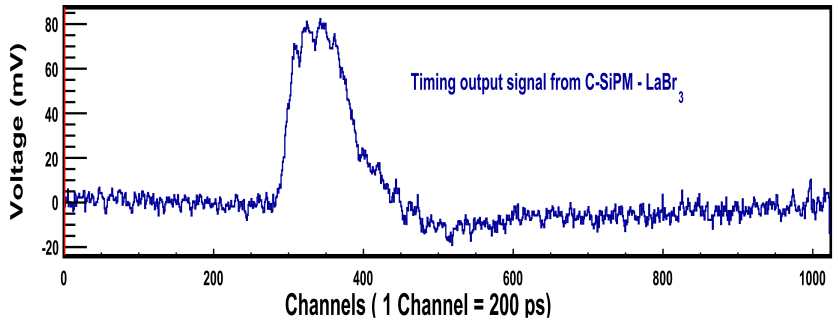

(a) Original fast timing readout signal.

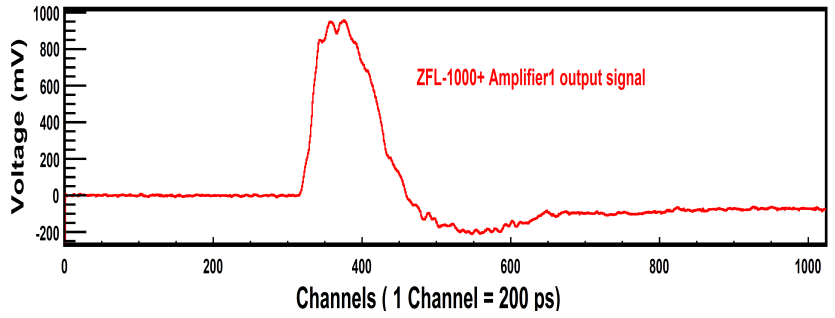

(b) Mini-Circuits ZFL-1000LN amplifier output.

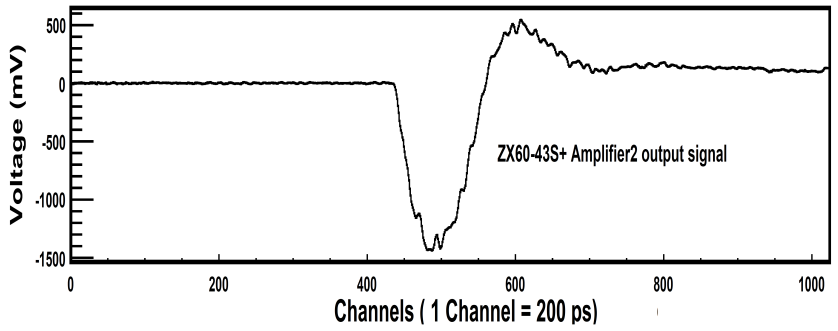

(c) Mini-Circuits ZX60-43-S+ amplifier output.

FIGURE 4.22: $LaBr_3$-C type SiPM detector was irradiated by ^{22}Na, the silicon photomultiplier then generated a fast timing signal. (a) Detector fast-timing readout signal (without signal processes). (b) The output signal of the first amplifier; original fast-timing signal fed to the first amplifier (Mini-Circuits ZFL-1000LN). The high-frequency noise was filtered out and the signal amplified. (c) The first amplifier signal was sent to the second amplifier (Mini-Circuits ZX60-43-S+). The low-frequency noise (with fast frequency bandwidth to 4000 MHz) was filtered out from the input signal. The output signal was amplified and inverted with time delay. If the signals pass through a non-linear phase device, the signal frequency will delay. The signal is also inverted during the signal process in the second amplifier, resulting in 180° additional phase shift. That is why delay time is greater than the first amplifier's delay time [77].

An appropriate fast timing signal was obtained after the usage of the two different amplifiers. The first detector system ($LaBr_3$-Hamamatsu PMT-R9880U-210)

was fixed and the second detector system used various combinations of scintillation materials and SiPMs. The electronic block diagram of the coincidence time measurement is shown in Figures 4.23 and 4.24.

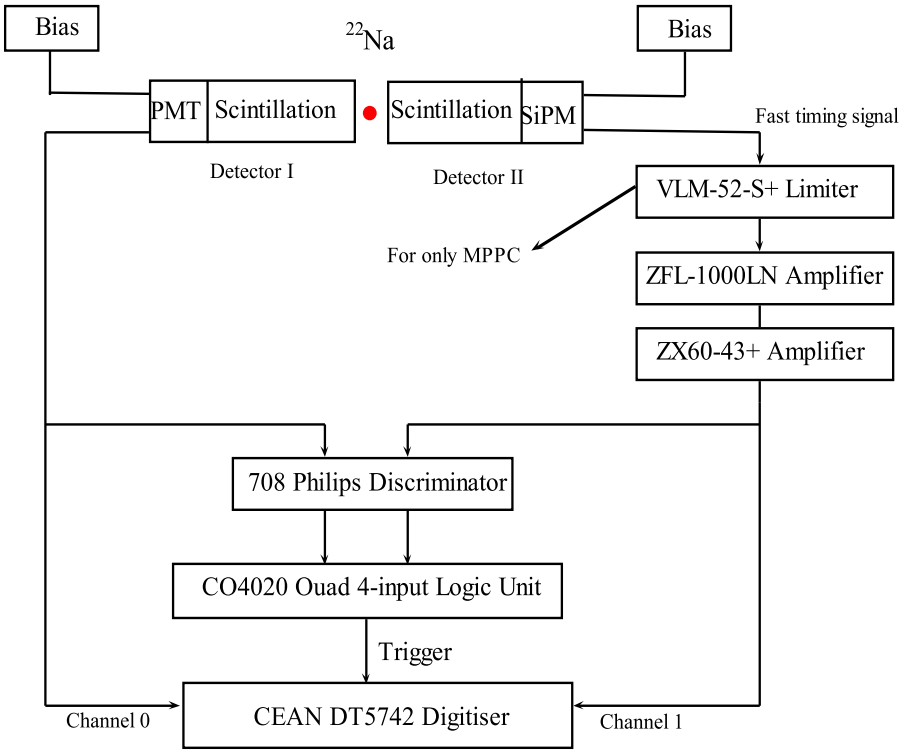

FIGURE 4.23: Electronic block diagram of the coincidence timing measurement. $LaBr_3$-Hamamatsu R9880U-210 PMT detector system was fixed and various scintillation crystals optically coupled with SensL C series SiPM. A Hamamatsu S12572-010P MPPC 2x2 array was also tested in coincidence resolving time measurement. When the Hamamatsu MPPC readout signal was fed into the first amplifier (ZFL-1000LN), this amplifier suddenly stopped working. According to the technical report obtained from the manufacturer, a VLM-52-S+ limiter should have been used before the amplifier to protect it against possible overstress from the MPPC. This limiter can operate at a low frequency, down to 100 kHz [75].

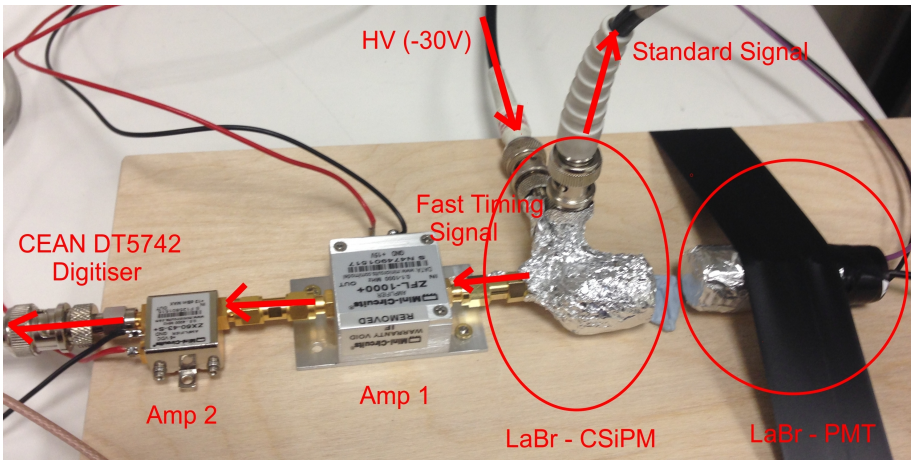

FIGURE 4.24: Experimental set-up of the coincidence resolving time measurement. Two different detector systems, a $LaBr_3$-Hamamatsu PMT and a $LaBr_3$-SensL C-SiPM were placed (0.5 cm) at the each side of the radioactive source (^{2}Na). The SiPM fast signal was fed into two amplifiers, and then sent to a digitiser. The standard readout signal was also sent to the other channel of the digitiser as well as a PMT output.

The intrinsic time resolution (FWHM electronic devices) was calculated as 68 $\mp$ 1 ps (Appendix A.4). The lowest possible threshold was chosen, between 10 mV and 15 mV in the software, depending on the noise level of the detector signals. However, in the electronic intrinsic time measurement the threshold level was set to 5 mV. The energy gate, or energy window does not need to be set due to having only true coincidence (the radioactive source did not generate signals). A Philips PM5786 fast pulse generator was used for electronic timing measurement, as in the electronic block diagram shown in Figure 4.25. A pulse generator generated signals with 3-2 ns rise time, and then divided into two identical signals. One of the signal was fed to Mini-Circuits amplifiers, and then to the digitiser and discriminator, which is the same as the $LaBr_3$-SensL C-SiPM detector's experimental set-up. The other pulse was sent to the Philips discriminator, then the logic unit for coincidence and finally to the digitiser. This was similar to the $LaBr_3$-Hamamatsu detector's set-up. Subtracting intrinsic time resolution of the electronics from the actual measurement (with scintillation detector systems) gives the intrinsic time resolution for both detector systems. The results of coincidence-resolved time measurement are listed in Table 4.4.

Thallium doped CsI scintillation crystals were also investigated, even though these are known as slow scintillators. Figure 4.26 shows different rise times for standard and timing output of SensL C-series SiPM coupled with 25 mm CsI. The $LaBr_3$-PMT detector was again fixed and the second detector was replaced by the

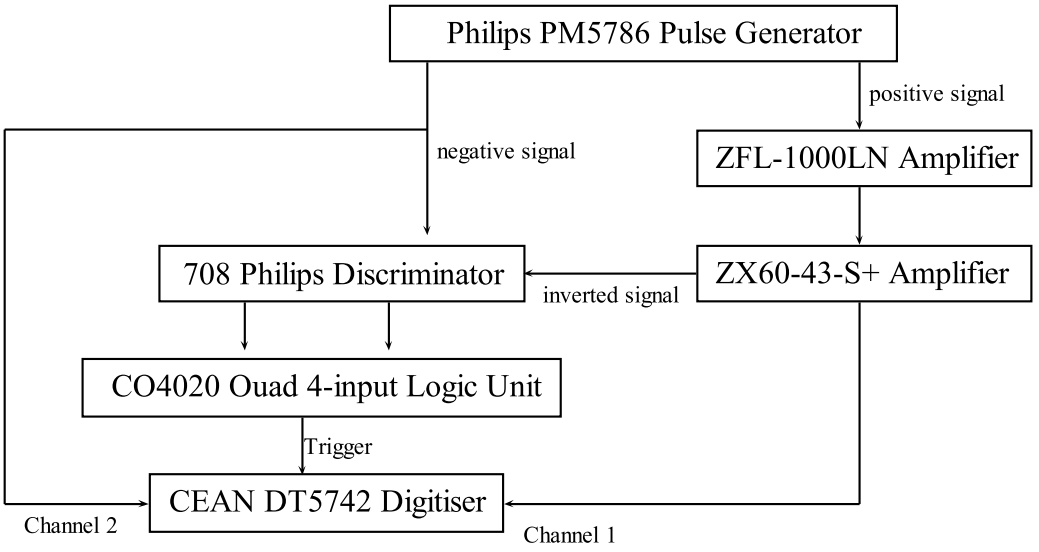

FIGURE 4.25: Setup for measuring intrinsic time resolution from the electronic modules used for timing measurement with Mini-Circuits amplifiers.

Scintillator ⟷ Photomultiplier	**FWHM (ps)**	**FWHM after subtraction of intrinsic (ps)**
$LaBr_3$ ⟷ PMT-R9880U-210 $LaBr_3$ ⟷ C-SiPM	**284 ± 8**	**276 ± 8**
$LaBr_3$ ⟷ PMT-R9880U-210 LYSO ⟷ C-SiPM	**301 ± 15**	**293 ± 15**
$LaBr_3$ ⟷ PMT-R9880U-210 $CeBr_3$ ⟷ C-SiPM	**348 ± 27**	**341 ± 27**
$LaBr_3$ ⟷ PMT-R9880U-210 $LaBr_3$ ⟷ MPPC(2x2 Arrays)-S12572-010P	**1222 ± 55**	**1220 ± 55**
$LaBr_3$ ⟷ PMT-R9880U-210 CsI(Tl) ⟷ C-SiPM	**3572 ± 94**	**3571 ± 94**

TABLE 4.4: Coincidence resolved time for various detector systems measured by digital system (with a transformer).

CsI(Tl) – C-series SiPM detector system. Timing resolutions were successfully calculated for standard and timing signals separately. The timing resolution could improve $\sim$ 3.6 ns by fast terminal (Figure 4.27). Gaussian-distributions were obtained after applying the leading edge method and energy gate for both outputs.

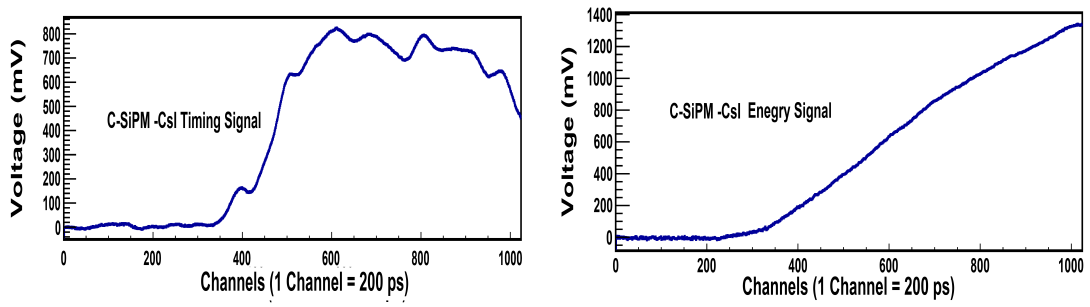

(a) Fast terminal readout signal.

(b) Standard readout signal.

FIGURE 4.26: CsI(Tl) - C SiPM detector irradiated by ^{22}Na. Fast-timing and standard readout signals generated by the slow scintillation detector with two different rise times. The original fast timing output signal had to be fed by the time filter amplifier to obtain a signal in the digitiser. (a) Timing signal after time filter amplifier. (b) Standard output.

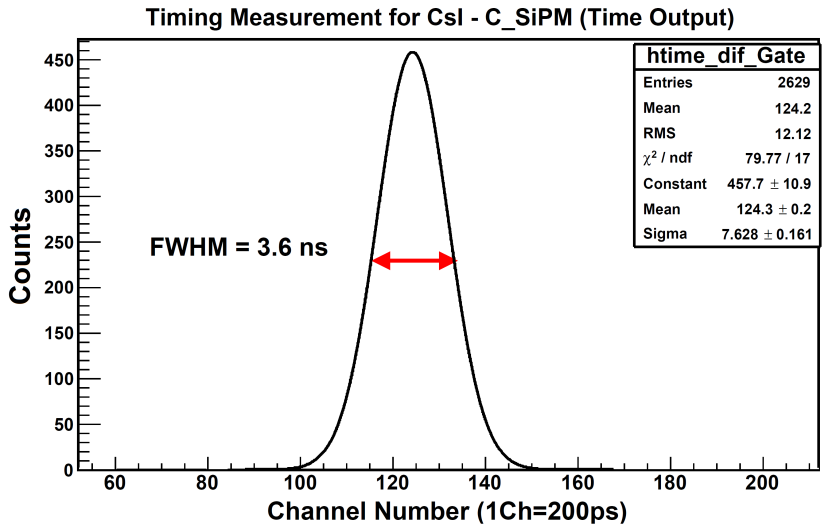

(a) Time resolution was obtained by fast time output of SensL C-series SiPM coupled with CsI and $LaBr_3$-PMT detectors.

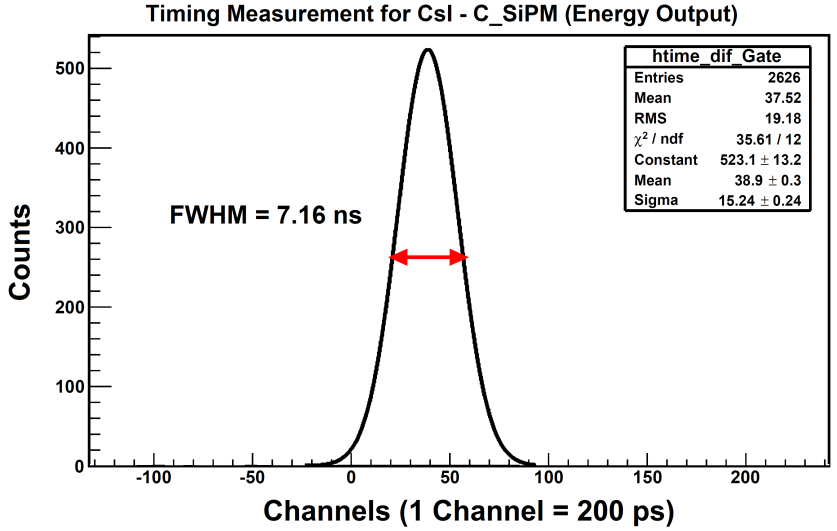

(b) Time resolution is obtained by standard output of SensL C-series SiPM coupled with CsI and $LaBr_3$-PMT detectors.

FIGURE 4.27: Timing measurement for CsI(Tl)-SensL C-type SiPM detector system and $LaBr_3$-PMT detector. (a) Fast-timing terminal signals of CsI-SiPM and $LaBr_3$-PMT signal were used to obtain Gaussian distribution, and found 3.6 ns. (b) Standard terminal signals of CsI-SiPM and $LaBr_3$-PMT signal were used to obtain Gaussian distribution and calculated as 7.2 ns.

4.4 Conclusion and Summary

Obtaining fast timing resolution is an essential requirement for medical and nuclear physics applications. Silicon photomultipliers have many advantages over photomultiplier tubes, but the timing performance is not yet similar to PMTs' response to simultaneous measurement of fast light pulses. In this research, a new generation SensL blue-sensitive silicon photomultiplier was optically coupled with various scintillation crystals to investigate timing resolution performance from the separate fast timing readout signal of SiPMs. For these measurements, analogue and digital system setups were used. Timing resolution performance obtained by a digitiser was completed with remarkable progress. The first critical approach was adding the transformer in the circuit and using Mini-Circuits amplifiers for different reasons in the set-up. Second, an appropriate threshold level for the analyses was sought (between 10 mV and 15 mV depending on the noise level, just above the noise), and the correct energy gate (only 511 keV energy window to mitigate the accidental coincidences) in the software applied. The code for analysing data was carefully written to find an accurate interpolated value; for example, a quadratic fitting equation rather than a linear equation was used. Similar to the findings of the literature review, the leading edge method gave better results, even though the constant fraction technique was employed independently. After the intrinsic time resolution was subtracted from the measured coincidence time resolution (FWHM), the resolved time for the unknown detector system was calculated from Equation 4.4.

$$Unknown\ Detector = \sqrt{M^2 - R^2} \tag{4.4}$$

where M measures coincidence timing resolution of two detector systems (FWHM), and R is the reference detector's time resolution. $LaBr_3$-PMT-R9880U-210 was used as a reference detector. The diversity of detector systems was then computed, as given in Table 4.5. Time resolution directly correlates with the square root of the SiPMs' capacitance. In consequence, CRT measurement doubles by using 6 mm SiPM instead of 3 mm, as detailed in the introduction. If it is considered that the slow decay time, the length of the scintillation crystal, and capacitance of a 6 mm active area SiPM adversely affect the coincidence resolving time, 264 ± 9 ps is a highly promising result for a 12.7 mm length $LaBr_3$-C series SiPM detector system. According to the CRT measurement result, the timing performance of

Scintillator $\longleftrightarrow$ Photomultiplier	$\frac{\textbf{FWHM}}{\sqrt{\textbf{2}}}$**(ps)**
$LaBr_3$ $\longleftrightarrow$ PMT-R9880U-210	**82 $\mp$ 5**
$CeBr_3$ $\longleftrightarrow$ PMT-R9880U-210	**94 $\mp$ 4**
$LaBr_3$ $\longleftrightarrow$ C-SiPM	**264 $\mp$ 9**
LYSO $\longleftrightarrow$ C-SiPM	**281 $\mp$ 16**
$CeBr_3$ $\longleftrightarrow$ C-SiPM	**331 $\mp$ 28**
$LaBr_3$ $\longleftrightarrow$ Hamamatsu SiPM (2x2 Array)	**1217 $\mp$ 55**
CsI $\longleftrightarrow$ C-SiPM	**3570 $\mp$ 94**

TABLE 4.5: Timing resolution performance for diverse detector systems used in the CRT measurements. The best result was found when the digitiser system was used with balun and Mini-Circuits amplifiers for the SensL C-series silicon photomultiplier.

the detector system based on SensL C-series SiPM is better that standard silicon photomultiplier (Hamamatsu MPPC).

Furthermore, the investigation was completed that the bias voltage affects on the coincidence resolving time measurement (FWHM). If the bias voltage increases, photon statistics, detector gain and photodetection efficiency rise with applied voltage [73]. Therefore, the signal rise time will be faster with less noise by a higher gain (or signal amplitude) [74] resulting in lower coincidence resolving time resolution. The resolution will improve until the noise again becomes more dominant in the signal. The coincidence resolving time relationship with the bias voltage in the experiment was consistent with the literature [66, 73, 74].

Chapter 5

Development of an Antimatter Detector for Nuclear Medicine

5.1 Introduction

Scintillation detector systems are employed in the radiopharmaceutical substance activity measurement as a part of the quality control protocol. After radioactive isotopes produced in a cyclotron, they are then formulated by specific chemical substances. For example, Fluorine-18 is a common radioisotope labelled with glucose (Fludeoxyglucose-FDG). After the radiopharmaceutical substance is injected into the patient circulation system, the radiochemical substance will accumulate around of the affected region. There must be acceptable quality control parameters to protect patients from the extra radiation. These parameters also include a reduction in the radiochemical impurity and radionuclide impurity to mitigate the adverse effect on the medical imaging. Therefore, PET radioisotopes quality control parameters must be checked for radiochemical purity, radionuclide purity, pH level, sterility, safety, efficacy, and radioactivity before the injection [22]. Furthermore, during the radiopharmaceutical substance investigation in the PET research centres, the activity of the radioisotopes must be measured in a short time to protect researcher from unnecessary radiation. In the quality control protocol, radiation detection instruments; thin layer chromatogram (radiochromatogram), scintillation counter, and dose calibrators, which are used for the determination of the radionuclide purity and the radioactivity. Radiochromatogram scanner, which

consists a long narrow piece of radiochromatography paper, is used for the quantification of the radioactivity distribution [23]. However, the measurement time with this expensive scanner is longer than the detection time with a scintillation counter. Although scintillation detector systems measure the radiation in a short period, there are also drawbacks of the using them, such as limited solid angle and the detector efficiency. These disadvantages seriously affect the medical image quality and the activity measurement.

The positron emission tomography research centre at the University of Hull scintillation detector system, LabLogic's Scan-RAM NaI optically coupled to PMT, is used for measuring the activity in radiopharmacologic research. Alternatively, novel plastic scintillation detector system is being developed to measure the activity directly from the emitted particles rather than annihilation photons. Radiolabelled substances are placed directly in contact with the scintillation detector to obtain a better detection efficiency. In standard detection design, there is not directly interaction between the detector and radiochemical substance. We have successfully finished initial measurements with encouraging results. It is a very simple detector system, cheap, user-friendly and an achievable nanoscale volume for a microfluidic chip application. Blood sample counting device or microfluidic system (based on silicon charged particle detector) has a few mL or less detection volume, being the useful tool for experimenting on small animals like rats and mice in PET research centres. These type of systems must take a time-dependent spectrum as a function of whole body radioactivity concentration from 0.70 μL to 0.22 μL sample volume precisely in a short time [78]. Very short measurement time with a low detection volume also helps to minimise the radiation exposure time for the researcher performing the process. In this application, the measurement time should be shorter than the decay time of the radioisotope and short delay time for diffusion of a blood curve [79].

In this chapter, there was an estimated positron range calculation with the empirical formula. Positron stopping power and range calculation by using ESTAR programme gave the similar result with the estimated positron range value. Monte Carlo simulation was studied with and without annihilation photons, generating optical photons, and without optical photons to find out the optimum thickness of scintillation. This approach gave the optimum thickness for measuring the positrons with the least effect of the annihilation photons on the measurement. Various detector designs were successfully studied with using MicroMCA software,

which was specially developed for activity measurement. Radiotracers continuous energy spectra (non-monoenergetic positrons) and decay curve obtained within the experimental uncertainty consistent with the literature. In the last part of this chapter, there is also the investigation into the novel scintillation detector system, which can be modified to a microfluidic chip with very low detection volume (from 94 $\mu\ell$ to 0.11 $\mu\ell$). A radioactive fluid contamination inside the scintillator underwent during the experimental measurement; that was a serious challenge. Microscopic cracks on the scintillation channel surface could cause the leakage or chemical reaction between scintillator material and radiochemical fluid. Various approaches were examined resulting in one of them addressed the issue.

5.2 Positron Range Calculation

The radiation absorption of β particles inside the medium can calculate by using Equation 5.1 in the specific energy region ($0.01 \leq E_\beta \leq 2.5$ MeV) [80]. This empirical formula might be used to estimate the range of the electron or positron in low Z (atomic number) material.

$$R = 0.412.E_\beta^{(1.265 - 0.0954\,.\,lnE_\beta)} \tag{5.1}$$

Where; E_β is the kinetic energy of positron (or electron) in the unit of MeV, and R is a positron (or an electron) range. The range of the charged particle in g/cm^2 can be converted to a distance using the material density (1.032 g/cm^3 for EJ212; which is the plastic scintillation material). According to Equation 5.1, approximately positron ranges were calculated at two different energies of positrons emitted from ^{18}F radioisotopes. The positron ranges have been computed to be 2.27 mm for the maximum energy (E_β = 634 keV), and 0.98 mm for the average energy ($E_{\beta\,average}$=350 keV) of ^{18}F.

Figures 5.1 and 5.2 show the range and energy loss as functions of energy in the plastic scintillation medium, respectively. Stopping power and range data are calculated from the ESTAR calculation program [81]. In ESTAR, the calculation of the stopping power is evaluated from the theory of Bethe with density effect correction. Positrons emit from ^{18}F are not mono-energetic, but their energy distribution is continuous energy spectrum from zero to maximum value or end point energy (as shown in Figure 5.22). According to the theoretical calculation

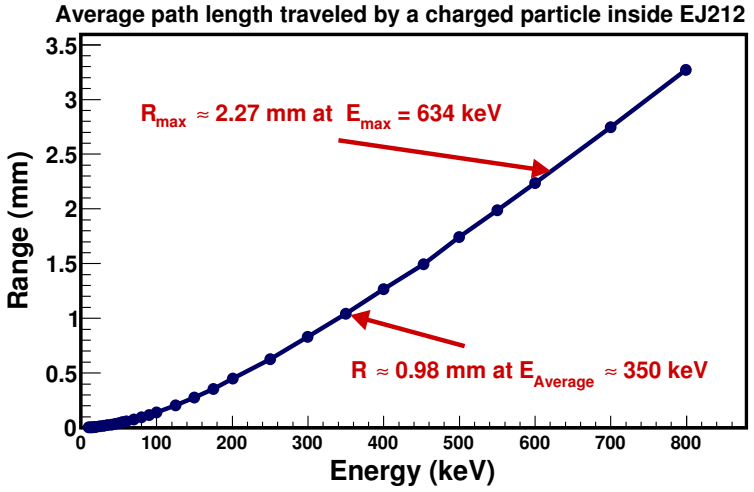

FIGURE 5.1: Positron (or electron) range in the plastic scintillation for low energy positron was obtained from the theoretical calculation.

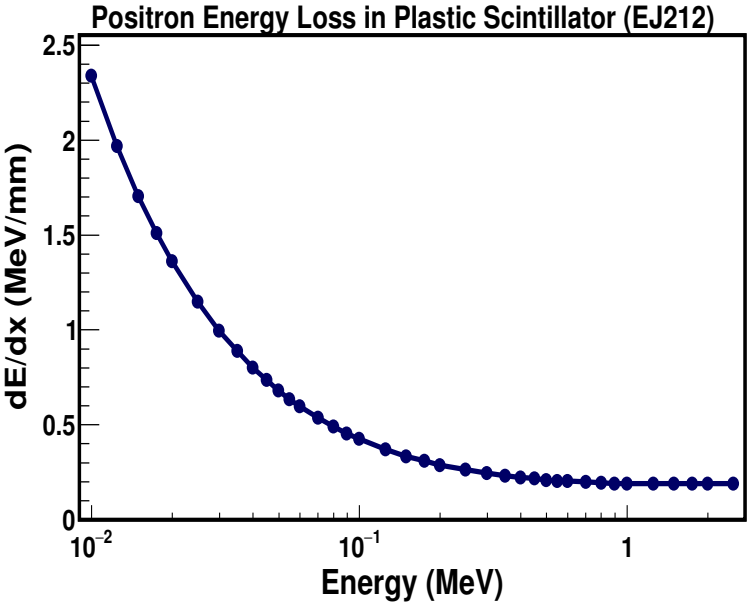

FIGURE 5.2: Energy loss (dE/dx) of positrons as a function of energy in the plastic scintillation obtained from the theoretical calculation in ESTAR.

obtained from the ESTAR data as illustrated in Figure 5.1 and estimated values of the positron range, between 1.0 and 2.3 mm plastic material could absorb 90-100% of positrons emitted with a distribution of energies from a ^{18}F source.

5.3 Simulation Work

A simulation code developed to study the response of a detector with basic geometry in which is SiPM coupled to EJ212 plastic scintillator (series number of the

plastic scintillators from Eljen Technologies) irradiated by cylindrical ^{18}F positron source. The code, based on the GATE 7.0 simulation package, was written and used to find out the optimum thickness of the plastic detector for beta particle detection. For this reason, the simulation is run with and without optical photons as explained in the following subsections.

5.3.1 Geant4 Simulation Without Optical Photons

A non-monoenergetic and cylindrical Fluorine-18 radioisotope is placed in front of the scintillation materials as visualized in Figure 5.3. Two different tracking paths (displacement or positron range) illustrate for plastic scintillation material (EJ212) and LYSO scintillation before positron annihilates. In Figures 5.3(a) and 5.3(b), positron displacement in plastic scintillation material is more than in LYSO scintillation due to having a low density. Several scintillation materials were also

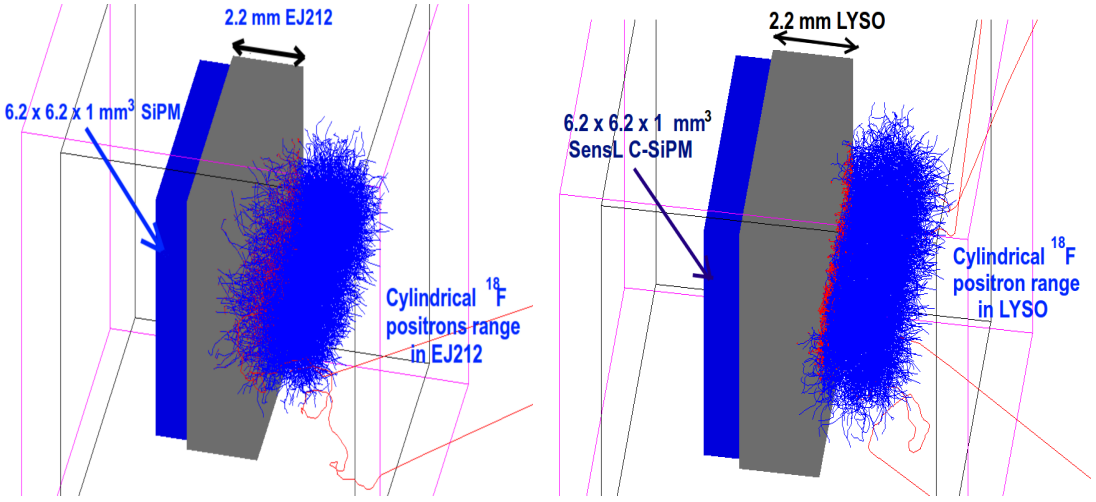

(a) Positron displacement in EJ212-Plastic scintillation. (b) Positron displacement in LYSO.

FIGURE 5.3: 6.2 x 6.2 x 1 mm^3 SiPM is coupled with 6.5 x 6.5 x 2.2 mm^3 dimension of the scintillator. (a) EJ212 and (b) LYSO scintillation materials were irradiated by cylindrical ^{18}F radioisotope. Positron range in EJ212 is more than in LYSO due to density differences. The red points are represented electrons; interaction points between positron and electron in the material. After positron interacts with electron, annihilation event occurs following that the creation of the two 511 keV annihilation photons. Gamma ray interactions will then start to affect the measurement. This simulation was run without annihilation events.

studied to find the optimum thickness for positrons emitted from ^{18}F. A positron's travel distance inside the medium depends on the material density as shown in Figure 5.4 for common scintillation crystals. Positrons have a small displacement

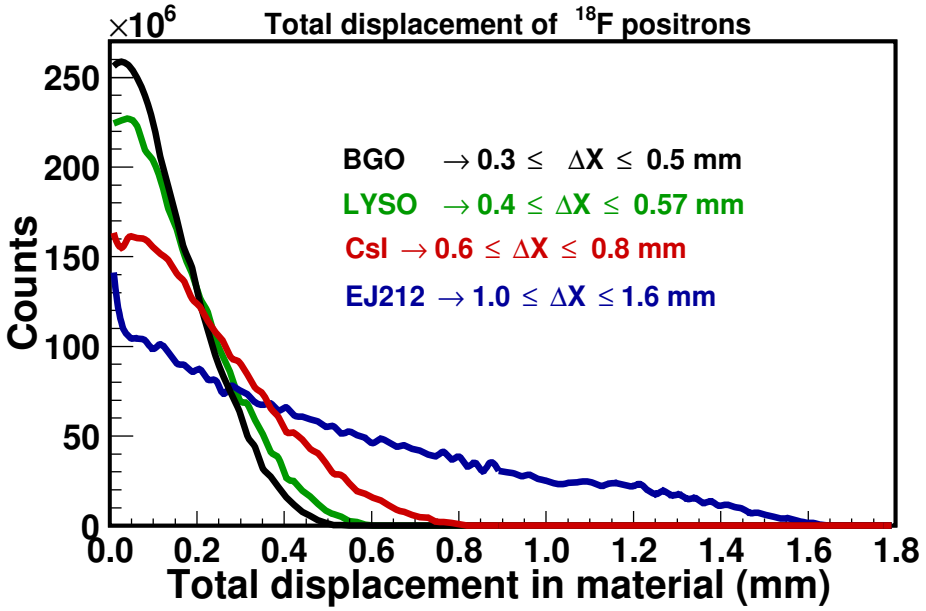

FIGURE 5.4: Various scintillation crystals with 10 mm thickness are investigated for positron range by using simulation without producing optical photons. This thickness will be sufficient to stop almost all positrons inside material because of short positron range in the medium. Beta particles are randomly emitted from non-monoenergetic ^{18}F radioisotopes. Calculated positrons displacement inside the CsI(Tl) is almost half of the EJ212 due to the density effect. Annihilation photons occur when the positron loses its total energy, so there must be more than one interaction before the annihilation events occur. In each interaction positron moves away from the source. The total displacement is defined as the distance between the radioactive source and the last interaction position. After the last interaction, positron annihilates (annihilation photons occur).

inside the high-density scintillators (inorganic scintillators). They usually prefer to detect gamma ray rather than charged particles because of their higher stopping power for gamma rays as explained in Chapter 2. If inorganic crystals are used to detect positrons emitted from fluorine 18, it would have very thin thickness. For example; several research groups developed beta microprobes separately using a very short LSO and plastic scintillation materials. Beta microprobes are used during the surgery operation as a very useful medical imaging tool. Using this device is an effective way to find the abnormal part of the surgery region by detecting accumulated radioisotopes. That kind of microprobes was focused on only measuring positrons rather than annihilation photons. Therefore, a very short LSO crystal had to be used to measure beta particles for the reduction in the effect of the annihilation photons [82, 83]. Successfully, beta microprobe device was designed in that research; however, LSO or LYSO scintillation crystals have an intrinsic radioactivity coming from ^{176}Lu. As a result of that, the activity curve must include some background radiation. The distance between the source and

detector is also critical during the operation. Therefore, the thickness must be less than 0.5 mm, or very close to examined region. Nearly 0.5 mm length of scintillation crystal can make it too fragile and difficult to design.

In the section 5.2, ESTAR calculation and estimated value show that the positron range is 1.0 - 2.3 mm for plastic scintillation (EJ212). That thickness will be sufficient to stop positrons which have the same energy range as the continuous energy distribution of ^{18}F (Figure 5.22). However, more than 90% of the positrons' kinetic energy is lower than 634 keV (the maximum energy of ^{18}F positrons), because of the continuous energy spectrum of beta particles. According to the simulation, Figures 5.5 and 5.6 show that the optimum thickness must be

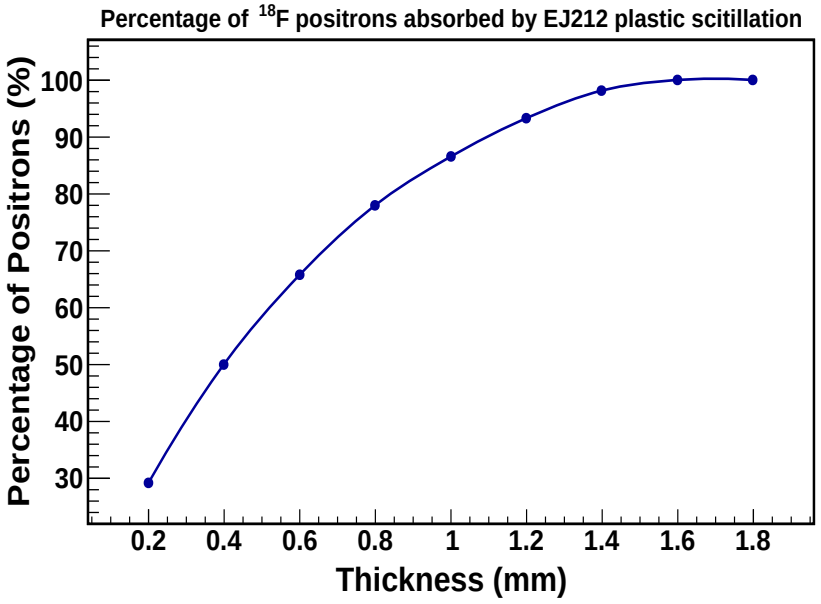

FIGURE 5.5: Percentage of the positrons is calculated as a function of thickness for 10 mm EJ212. Almost 90% of positrons stops at 1.2 mm according to the simulation without annihilation events.

between 1.0 to 1.8 mm to stop 90-100 % of positrons. The direction of positrons significantly changes with an elastic scattering (occurs between positrons and absorbing material's electrons). That is why the positron can not displace as a straightforward inside the material. Figure 5.3 illustrates that the displacement of the positron is sharply and suddenly turning in a various direction as same as the zigzag. Positron movement is also affected by the absorbing material density. Therefore, the positron displacement inside the plastic scintillators is more than in the inorganic scintillators (BGO, LYSO or CsI). Almost 10 % of high energetic positrons displacement will be more than the rest of the positrons in the energy distribution (90% of positrons). Therefore, the scattering points energy range is

between 250 keV and higher after 1 mm thickness of plastic scintillator as shown in Figure 5.6. The positron range simulation without optical photons is also studied

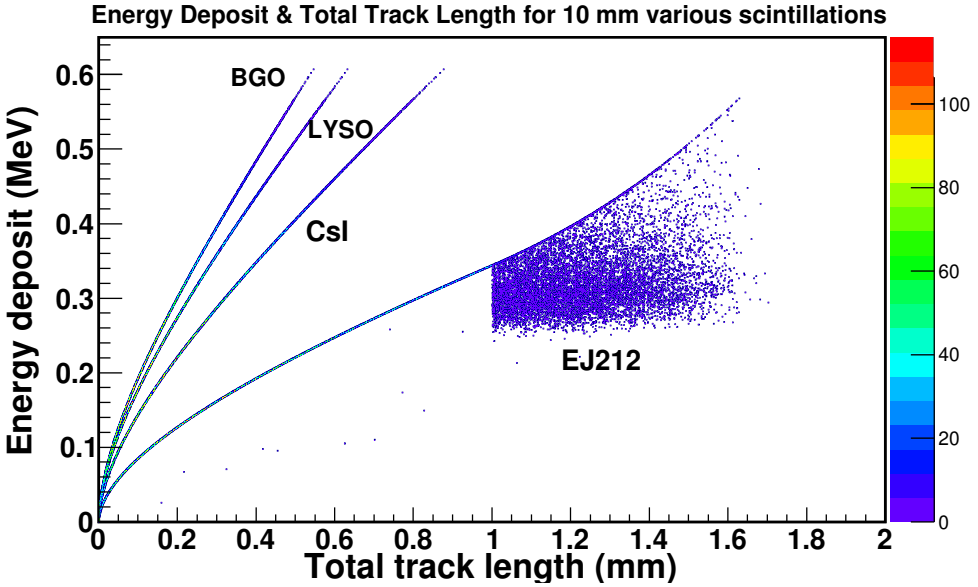

FIGURE 5.6: Positron energy deposition inside the absorbing material versus the total track length (displacement) of the particles inside 10 mm thickness for various scintillation materials. This plot's data obtained from Geant4 based simulation, used in Penelope model calculation (PENetration and Energy LOss of Positrons and Electrons at low energy) without scintillation and annihilation process. Positrons enter into the material at 0 mm, and particles then lose their energy with an each interaction. These interaction points represent a track length in the GEANT4 simulation. An elastic scattering between a positron and absorbing material electron becomes more dominant for the high energetic positron (almost 10 % of positrons from ^{18}F energy distribution) between 1.0 mm and 1.8 mm thickness of plastic scintillator (EJ212). It is also the effect of the density of the plastic scintillations (PVT). EJ212 plastic scintillator density is lower than others.

with the actual detector geometry. The same thickness range was concluded in Chapter 6 (see the Figure 6.3).

5.3.2 Geant4 Simulation With Optical Photons

Geant4 simulation (without optical photons) shows that almost ninety percent of the positrons stopped until 1.0 mm plastic scintillation material. The further simulation was also completed by generating optical photons. That is more close to the real experimental situation and allows us to investigate the annihilation photons effect on the measurement. The visualisation of the detector geometry and radiochemical source (F-18) are illustrated in Figure 5.7.

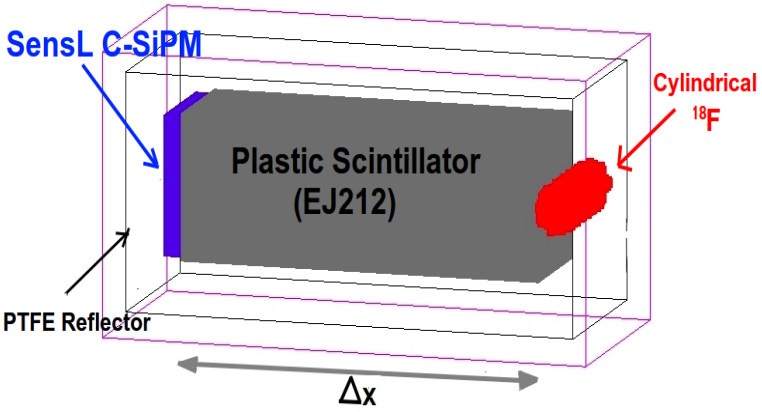

FIGURE 5.7: 6.2 x 6.2 x 1 mm^3 SiPM is coupled with 6.5 x 6.5 x $\triangle$X mm^3 EJ212. Two millimetre PTFE reflector surrounds the detector for keeping optical photons inside. Red cylindrical volume is defined as a ^{18}F radioactive source with two-millimetre diameter and 6.5 mm length. $\triangle$X is changed from 0.1 to 10 mm.

Two different physics lists in the simulation are defined to distinguish optical photons, produce by positrons and annihilation photons plus positrons (because the effect of the annihilation photons is in almost each thickness). Figures 5.8(a) and 5.8(b) show a single event with 511 keV and without respectively. In the

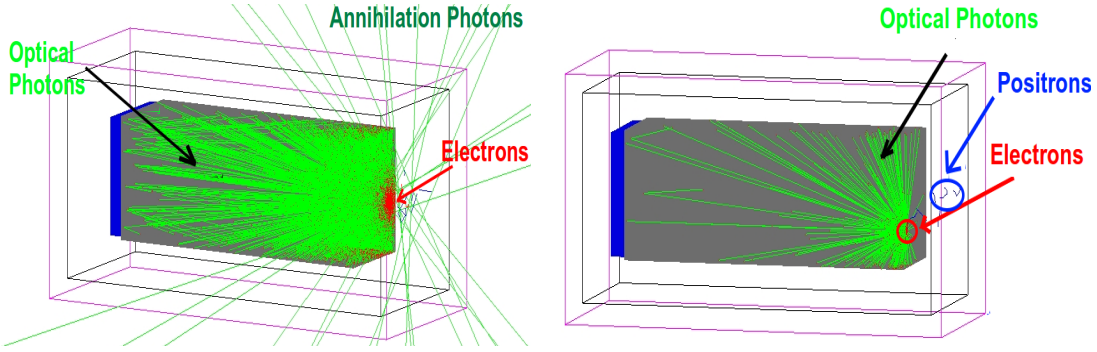

(a) With annihilation photons in physics list.

(b) Without annihilation photons in physics list.

FIGURE 5.8: With and without annihilation photons in the simulation physics list. (a) The physics list includes an annihilation event. Short green lines represent the optical (scintillation) photons inside the scintillator. Long cyan lines are 511 keV annihilation photons. Red points are electrons and a few of the blue zigzags (positrons). (b) Without annihilation in the physics list; only positrons generate optical photons (short bright green lines inside the scintillator).

simulation, there are different colours to represent particles and photons. Red points are electrons which collide with the low energetic positrons, then annihilation events occur. Long cyan lines, which can penetrate the detector, are 511 keV

annihilation photons. Short green lines inside the detector represent florescences (optical photons).

The light yield of EJ212 plastic scintillation is 10 000 photons per MeV of deposited energy [84]. The total number of optical photons for with and without annihilation events is individually plotted at various length as shown in Figure 5.9. The optical photons number sharply increases until 1 mm thickness of the plastic

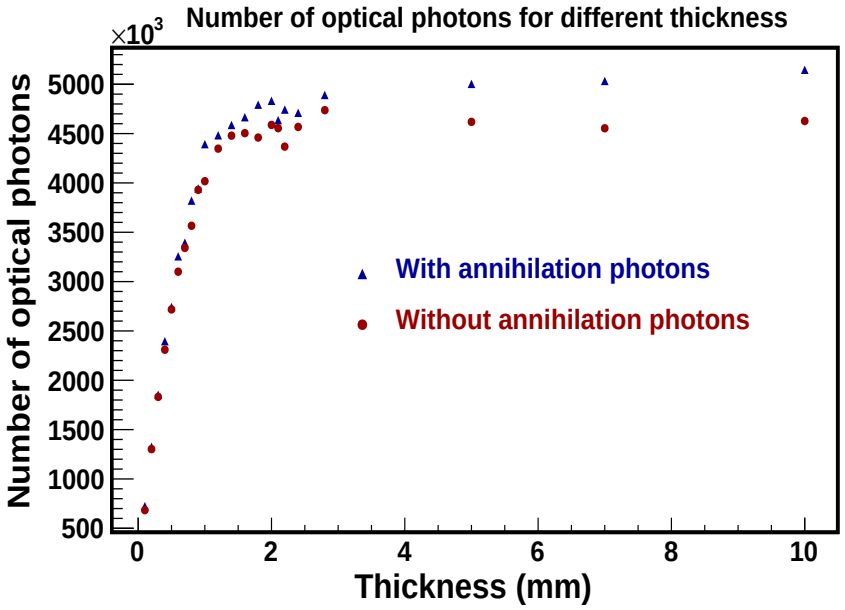

FIGURE 5.9: The number of optical photons in various thickness of scintillator with and without annihilation photons. The optical photons number sharply increases until 1 mm thickness of the plastic scintillator. 90% of positrons, which is the positron energy distribution of ^{18}F, creates the optical photons until 1 mm. After that thickness, the optical photons number gradually increases until the 10% of positrons (from F-18 energy distribution) losses their energy by interaction with the absorbing material's electrons. The optical photons number after that thickness remains nearly constant (because there is a statistical variation). Plot points with annihilation photons, however, slightly increases due to the interaction between 511 keV annihilation photons and scintillator

scintillator. After that thickness, the number of scintillation photons gradually increases, the 10% of positrons stop by annihilation events occur between the positron and the electron, which is inside the absorbing material. That is why the optical photon number nearly stays the same after whole positrons losses their energy with interactions (ionisation) in the simulation without annihilation events. However, in the case of annihilation event, there is steadily increase in the number of optical photons. That is the effect of the annihilation photons (511 keV). Therefore, more scintillation photons occur with annihilation events as shown in Figure 5.10. Interactions betweenγ-rays and the material are different from

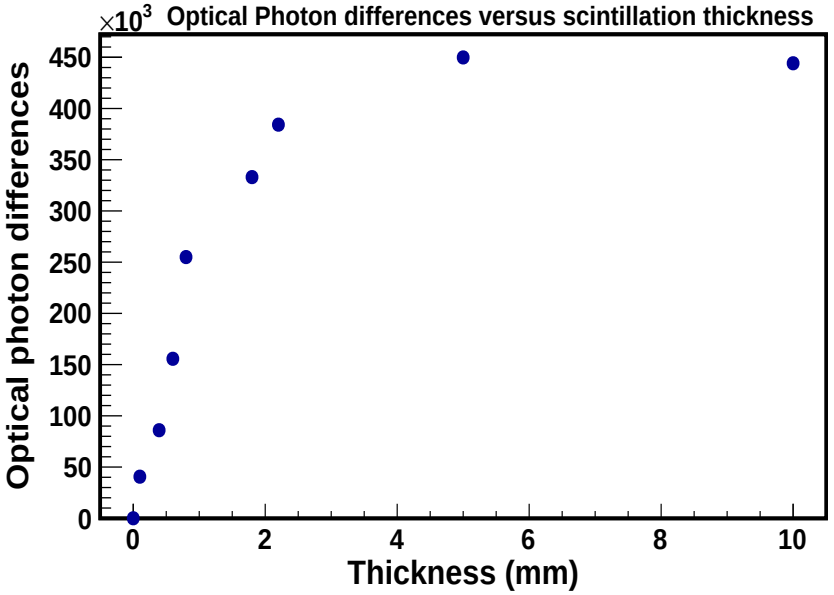

FIGURE 5.10: The effect of the annihilation photons as the number of optical photons for different thickness. This plot's data obtained from the statistical calculation and created randomly positrons by random number generator in the simulation. Almost 90 % of positrons interacts with scintillator by generating optical photons until 1 mm thick of plastic scintillator (Ej212). After that thickness optical photons number growth less than the number of optical photons trend between 0 and 1 mm.

positron interactions with the material. The main interactions are the Compton scattering, photoelectric effect and pair production for electromagnetic radiations. The major impact of annihilation photons in the number of optical photons comes from the Compton scattering, as illustrated in Figure 5.11. In simulation without annihilation photons, there are a few photoelectric effect and Compton scattering events as a result of X-ray interactions which arise from Bremsstrahlung scattering as shown in Figure 5.11. Generating optical photons within the actual detector geometry was also researched in Chapter 6. The result of the simulation conducted with the simple detector geometry was consistent with the conclusion of the simulation investigated with the real detector geometry as discussed in the next chapter.

Approximately, 90% of positrons lost their energy and stopped before 1 mm. Optical photons between 1 and 2 mm depth of the plastic scintillator are generated by annihilation photons (511 keV gammas) plus 10% of the positrons from the ^{18}F positron energy distribution (high energetic positrons in the distribution). After that thickness, optical photons are only produced by gamma rays. In conclusion, the optimum thickness must be approximately 1 mm to detect optical photons

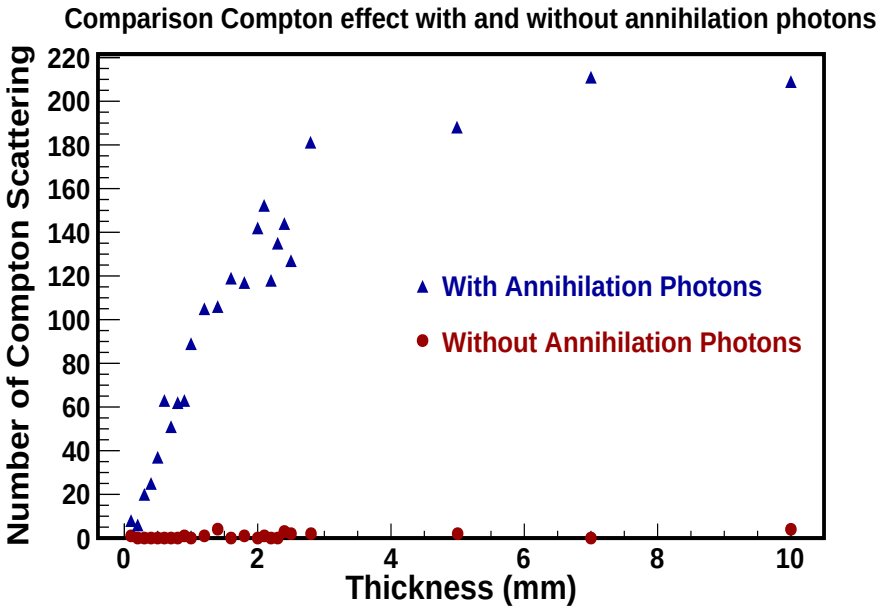

FIGURE 5.11: The graph shows the number of the Compton scattering events as a function of thickness for with and without annihilation photons. The main differences on the optical photons come from the Compton scattering events. Gamma radiation mainly loses its energy by Compton scattering, however, positron loses its energy by the interaction with absorbing material electrons (ionisation).

produced by positrons and the lowest effect of the annihilation photons on the measurement resulting in almost 90% of positrons measured. After 1.0 mm, the effect of the annihilation photons increases.

5.4 Detector Design

In order to eliminate the effect of the annihilation photons, optimum thicknesses were investigated with Geant4 based GATE Monte Carlo simulation program (for more details see the section 5.3). Before studying the simulations, the first experiment was conducted with 2.25 mm wall thickness as shown detector design in Figures 5.12 and Figure 5.13. A cylindrical channel was made in the middle of the plastic scintillator for the radioactive liquid to pass through. After interactions between radiation and scintillation material, scintillation photons (or optical photons) were created. The SensL C series SiPM were used to convert optical photons into the electrical signal which is related to the amount of the radiation absorption. The signal then sent to the multi-channel scale to measure the activity. In this stage, assuming that there was not interaction between needle and positrons

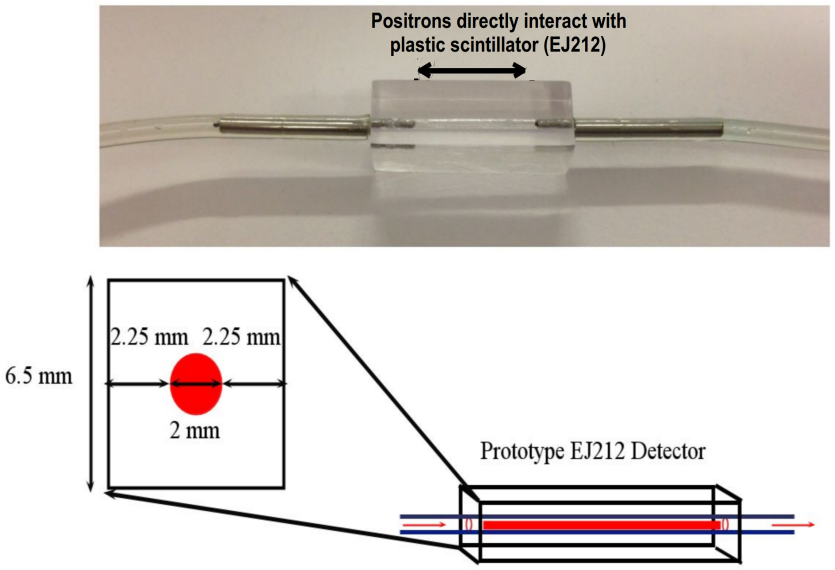

FIGURE 5.12: The dimension of the plastic scintillation detector, 2.25 mm wall thickness and cylindrical empty volume for flowing positron source inside the detector. Two needles are used for joining plastic and tubing system together. They are glued and then leakage is tested with water.

while the radioactive liquid was passing thought inside the plastic scintillator. If there is interaction, positrons will displace shorter than the positron displacement inside the plastic scintillator because of the density effect. Also, particles can not directly interact with the fluoropolymer tubing system, when the particle was inside the plastic scintillator (Figure 5.13). If there is interaction, it will again be quite weak due to very short positron range. However, the measurement must be slightly influenced by annihilation photons (511 keV gamma radiation), because annihilation photons are detected in the each part of the system.

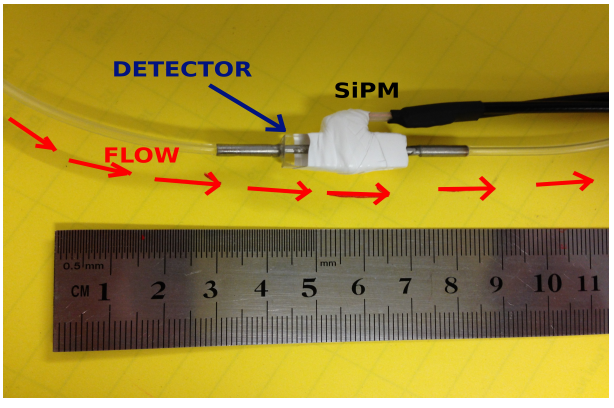

FIGURE 5.13: First prototype plastic scintillation detector system. Plastic scintillator and fluoropolymer tubing system (with 0.51-0.66 mm inside diameter and 0.25-0.31 mm wall thickness [85]) were connected each other by gluing between needles and fluoropolymer tubing.

The electronic board (Figure 5.14) contains 527 miniature multichannel analyser modules with pre-amplifier (the signal process details are shown schematically in Appendix. B.1). The module can be adapted to the different SiPM with

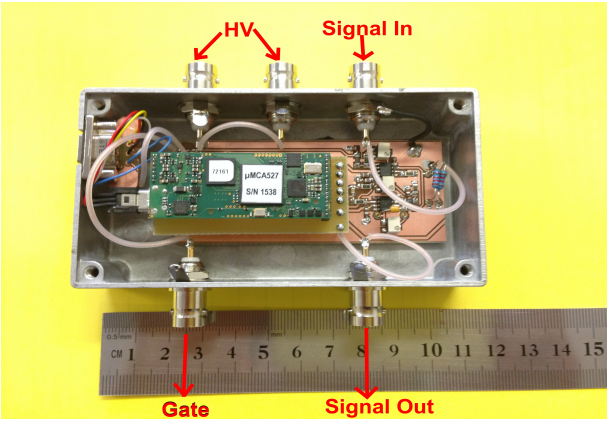

FIGURE 5.14: 527 MicroMCA module to measure the number of detected particles as a function of time. This electronic board can be easily adapted to the different types of SiPMs with negative and positive bias capability.

negative and positive bias capability. The signal readout can also be monitored with the oscilloscope while the data accusation is recording. WinSPEC software was used to record multi-channel analyser for energy spectrum and multi-channel scale for the activity measurement at the same time. The MCS (multi-channel scale) module is used to convert the output signal into the number of detected particles in a particular time. Figure 5.15 shows the spectra obtained from detector system irradiated by ^{137}Cs radioactive source. In this measurement, detector system was EJ212 plastic scintillator optically coupled with the SensL 6 mm C type SiPM. During the data acquisition time, radioactive source was being quickly moved away from the detector. This source displacement effects on the number of detected particle per millisecond as shown in Figure 5.15(a). At the same time an energy spectrum was also accrued (Figure 5.15(b)). The Compton Edge and backscattering are clearly seen in Figure 5.15(b). The full energy peak or photopeak is not observed because positrons interactions are dominantly the Compton scattering rather than Photoelectric effect. The composition of the plastic material contains low Z elements as opposed to the most of the inorganic scintillators [24].

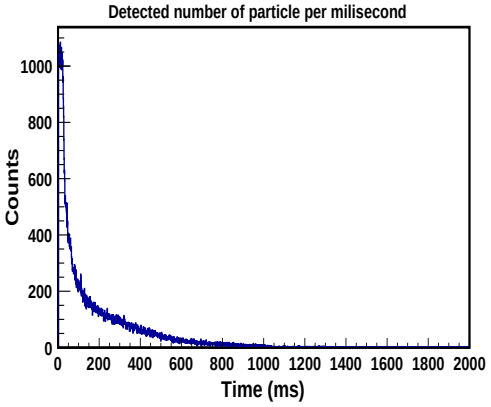

(a) When ^{137}Cs source was suddenly moved away from the detector, the number of detected particles was dramatically decreased in every millisecond, to obtain the activity curve. In the software called WinSpec, the number of photoelectrons, which are the proportional to the amount of the radiation absorption or generated optical photons in the scintillator, are measured by the SensL C-series SiPM. The number of photoelectrons is recorded in each millisecond by the multi-channel scale. Therefore, the number of the generated optical photons or the number of photoelectrons will be affected by the source position.

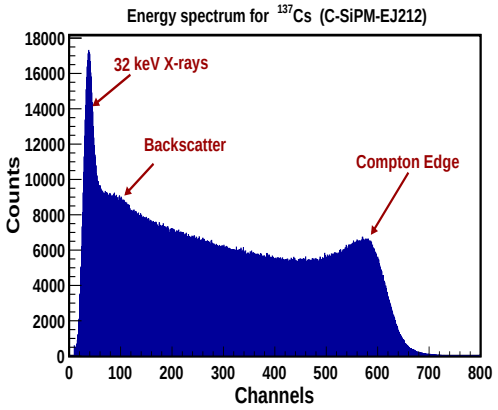

(b) While the multi channel scale was recording the variation in the number of the photoelectrons as shown in Figure 5.15(a), multi channel analyser was taking the energy spectrum of ^{137}Cs radioactive source. The WinSpec software of 527 MicroMCA module has a capability to record both at the same time.

FIGURE 5.15: The performance of the MCS module obtained by the EJ212-SiPM detector. (a) While the data acquisition, radioactive source was being suddenly moved away from the detector system. Taking away the source from the detector was dramatically reduced the number of the detected particles in every millisecond. In this part of the measurement, multi channel scale (MCS) was used. (b) The energy spectrum of the ^{137}Cs radioactive source was taken by using MCA module. While the MCS was recording the photoelectrons number in every millisecond, the data acquisition was also taken by MCA (multi-channel analyser). In the energy spectrum, backscattering and the Compton edge are clearly observed. Plastic scintillator and gamma radiation interaction primarily is Compton Scattering, that is why the full energy peaks (photopeaks) are not observed.

5.5 Detector Performance for Annihilation Photons in Experiment and Simulation

Various thickness of plastic scintillation (EJ212) materials were irradiated by the ^{22}Na radioactive source, which produces annihilation events similar to ^{18}F. Sodium-22 decays predominantly to the 1275 keV level of ^{22}Ne by emitting positrons and γ-rays with high probability. 511 keV annihilation photons occur after 546 keV energetic β^+ emission (with high positron yields of 90%). Additionally, ^{22}Na emits 1274 keV gamma ray with high probability. The MCS module was used to measure the number of the photoelectrons in every second while the MCA module

was recording an energy spectrum. There are several options for channel numbers (from 64 to 4096) in the software (WinSpec) depending on the acquisition time (or exposure time from microseconds to hours). Therefore, acquisition time was set to 17 minutes and 4 seconds, so obtained one channel was a second resulting in 1024 channels. The MCA module recorded the number of created optical photons inside the detector (or photoelectrons) in every second. Five various thickness of plastic scintillator from 2 mm to 30 mm were irradiated by ^{22}Na. The exposure time for each measurement was set to 17 minutes and 4 seconds. The total number of photoelectrons were then calculated by adding each recorded photoelectrons number in every channel. The total number of optical photons as plotted as a function of scintillator thickness (Figure 5.16). The blue exponential growth and fitting coef-

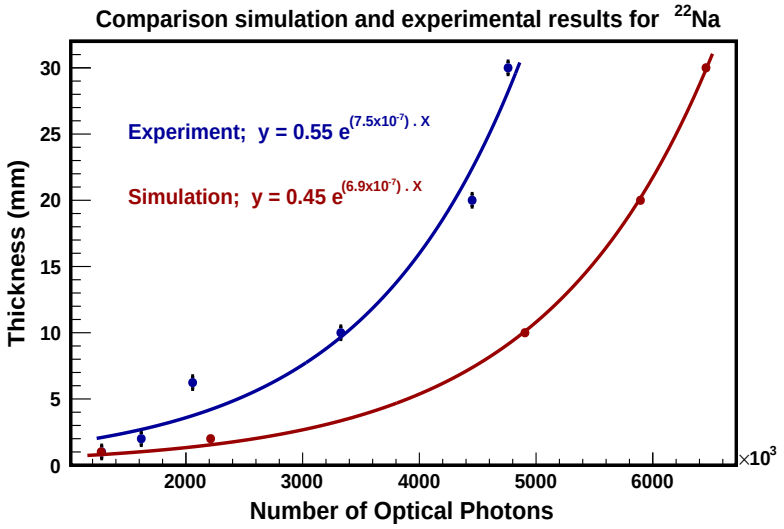

FIGURE 5.16: The number of optical photons versus the thickness of the plastic scintillation. The various thickness of plastic scintillation material was irradiated by the ^{22}Na. The MCS module with WinSPEC software recorded the number of optical photons in every second. After 17 minutes and 4 seconds, the total number of optical photons was calculated by accumulating every recorded number in a second. The optical photon number was then plotted as a function of thickness. The same measurement was conducted by using simulation. The exponential function fitted data points of measurements. Experimental fitting parameters are similar to the fitting parameters obtained by the simulation as shown in Figure 5.16.

ficients in the Figure 5.16 represent the experimental measurement. Equation 5.2 defines this exponential relationship between number of optical photons created by plastic scintillator and scintillator thickness;

$$T = 0.55\ e^{(7.5\ \ 10^{-7})\ .\ OP_{exp}} \tag{5.2}$$

Where OP_{exp} is the number of optical photons generated in experimental measurement and T is the thickness of the plastic scintillator. For comparison between experimental and simulation results, the same conditions in the experiment were successfully defined in the simulation. Besides, several relevant parameters must be defined for the optical photon generation, such as scintillation quantum efficiency (0.8), photodetector quantum efficiency (0.8), transfer efficiency (1) , and light yield (10 000 scintillation photons per MeV). However, data acquisition time or exposure time could not be set longer than one minute due to very slow simulation running time for optical photon's calculation. The simulation time was fixed to a minute for each thickness (it took a day in the real time). The relationship between thickness and optical photons will be independent of data acquisition time unless setting different exposure time. Therefore, the simulation data acquisition time remained constant as a minute. The exponential growth fitting coefficients obtained by the simulation well match with fitting coefficients obtained by the experimental measurement as indicated in Figure 5.16. Equation 5.3 defines the exponential fitting function acquired by the simulation.

$$T = 0.45\ e^{(6.9\ \ 10^{-7})\ .\ OP_{sim}} \tag{5.3}$$

Where OP_{sim} is the number of optical photons generated in the simulation and T is the plastic scintillation thickness. Only annihilation photons interacted with the plastic scintillator because the distance between the detector and the source was approximately 1 cm. The short positrons range does not allow the positrons to reach the detector. Therefore, only annihilation photons produce optical photons, and the number of optical photons will change with the scintillation thickness (variation in the number of Compton scattering). The sensitivity of gamma-ray for the plastic detector is also studied and obtained the graph as shown in Figure 5.17. ^{22}Na gamma ray (511 keV) source placed in front of the detector and then moved away after five minutes acquisition time to plot the average number of detected particle versus to various source-detector distance. According to the graph, there are gamma ray interactions (mainly Compton scattering) with the plastic scintillation until 25 cm. Therefore, it should be considered for making appropriate gamma ray shielding to eliminate the background radiation. In PET research centre, the background radiation can arise from the other radioisotopes or impurity of the radiochemical substance. Various radioisotope contaminations can occur during the reaction in the cyclotron because of the target impurity. The shielding box not only requires to minimise the background radiation, but it also

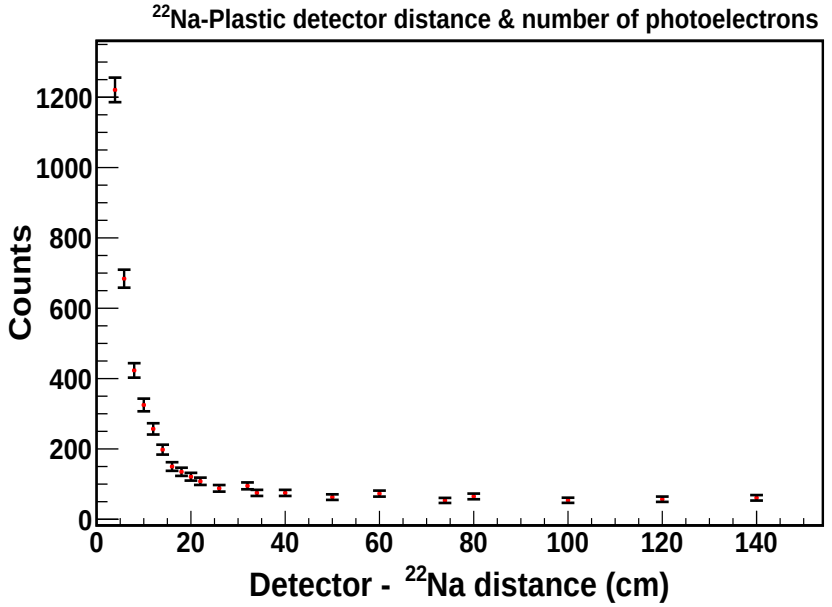

FIGURE 5.17: ^{22}Na source moved away from the detector and plot shows the total optical electrons number in the various distance. MCS spectra were taken nearly five minutes for each distance.

needs to reduce the effect of the annihilation photons. While the radioactive fluid is passing through the circulation system, there must be annihilation photons effect in everywhere of the system. There will be more discussion later about the radiation contamination arises from the tubing circulation system.

5.6 Testing Detector in Hull PET Research Centre

The new antimatter detector system was tested at the university of Hull PET research centre as shown in Figure 5.18. Before the experiment, the detector and shrinkable tubes were carefully wrapped with several layers of PTFE Teflon tape resulting in the thickness of a few millimetres to reflect the scintillation photons inside the detector. Also, black tape and aluminium foil were used to cover the detector to minimise the ambient light leak. A ^{68}Ga radiotracer was injected into the cylindrical channel, the signal from which we obtained on the oscilloscope (Figure 5.19). However, this measurement was unsuccessful due to liquid leakage which then damaged the SiPM. In the second measurement, three various detectors were successfully tested with ^{18}F the experimental set-up as shown in Figures 5.20 and 5.21. Figure 5.20 illustrates the first and second plastic detector designs with

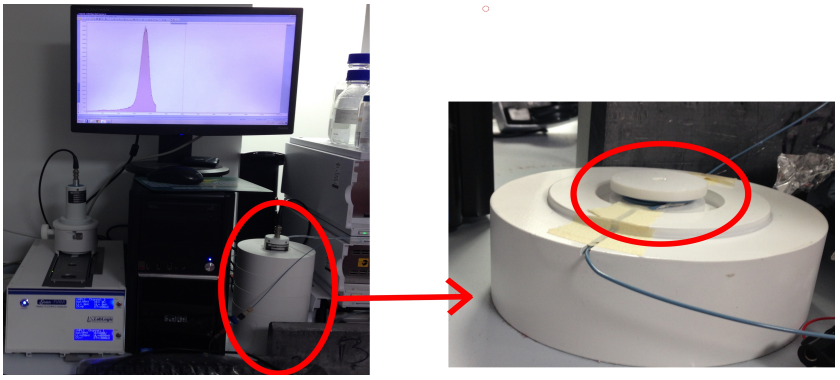

(a) LabLogic detector systems.

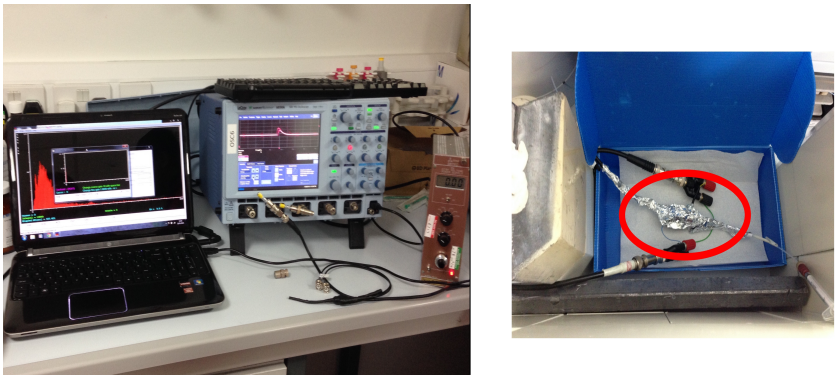

(b) New detector system.

FIGURE 5.18: NaI and new plastic detector systems set-up at the University of Hull PET research centre. (a) LabLogic (NaI/PMT) detector system is used for the gamma ray spectroscopy. (b) The new plastic detector system is adjusted to the LabLogic NaI detector system. The NaI detector first detects radioactive fluid. Then radiochemical substance is being passed through the new plastic detector for the detection of positrons by the circulation system with a constant flow rate (0.5 mℓ min^{-1}).

several detection volume. The detection volume of the first detector is 78 $\mu\ell$, and it is optically coupled with 3 mm Hamamatsu S12572-010P MPPC. That detector was used to compare standard LabLogic NaI-PMT detector system with newly designed plastic scintillator-SiPM. The second detector's detection volume is higher than the first detector (94 $\mu\ell$), and it is optically coupled with SensL 6 mm C-SiPM. This detector was used only for measuring energy spectrum and the decay curve of ^{18}F.

The last detector; 2$\mu\ell$ channel volume is designed for the blood sample counter application as illustrated in Figure 5.21. These detectors were carefully glued around the connection between needle (Figure 5.12) and tubing (fluoropolymer) to prevent fluid leakage; they were then tested with water for safety.

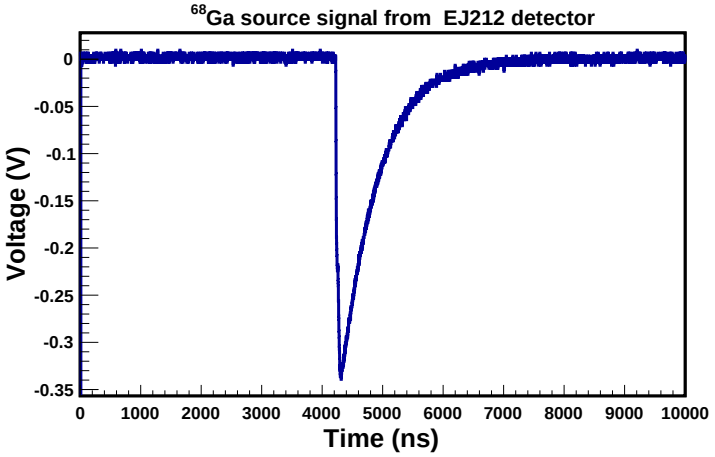

FIGURE 5.19: The first plastic scintillator design was optically coupled to the 6x6 mm^2 SensL blue sensitive SiPM. While ^{68}Ga radioactive fluid source was passing through inside the plastic scintillation detector, SiPM readout signal was obtained by oscilloscope.

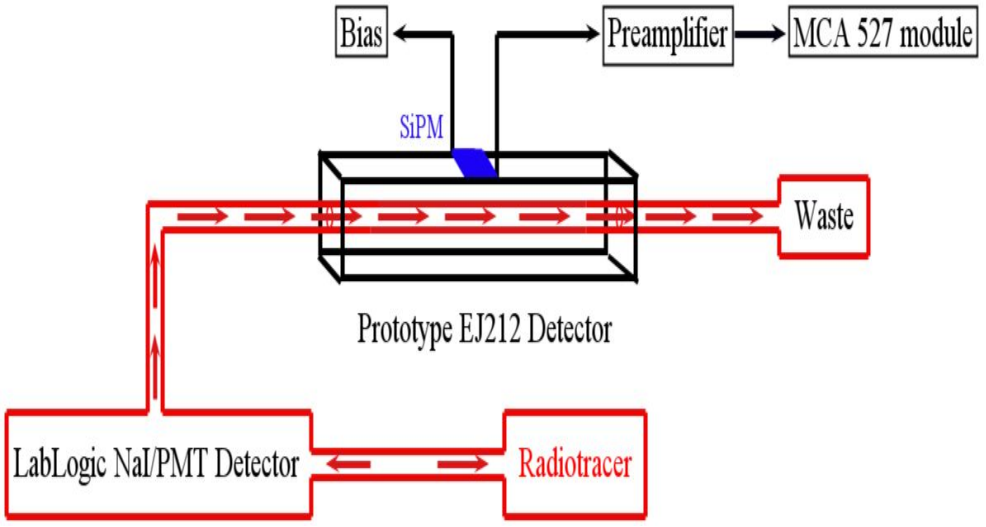

FIGURE 5.20: Experimental set-up for EJ212 plastic scintillation detector coupled with 3x3 mm^2 Hamamatsu SiPM ($\sim$ 69V) with 78 $\mu\ell$ cylindrical detection volume. The low volume of radioisotope was injected into the water circulation system. This radiochemical volume first passed through the NaI-PMT detector with the flow, then plastic scintillation detector system. The second detector design was the same as this detector device; however, the detection volume was 94 $\mu\ell$ and it was optically coupled to the SensL C-types SiPM. The second detector was only used to measure the energy spectrum and the decay curve of ^{18}F .

The comparison measurement between standard LabLogic detector system (NaI-PMT) and the new detector system (plastic scintillator-SiPM) was completed by using the first detector (78 $\mu\ell$ detection volume) and third detector (2$\mu\ell$ channel volume). The measurement result will present in the next section 5.6.1. However,

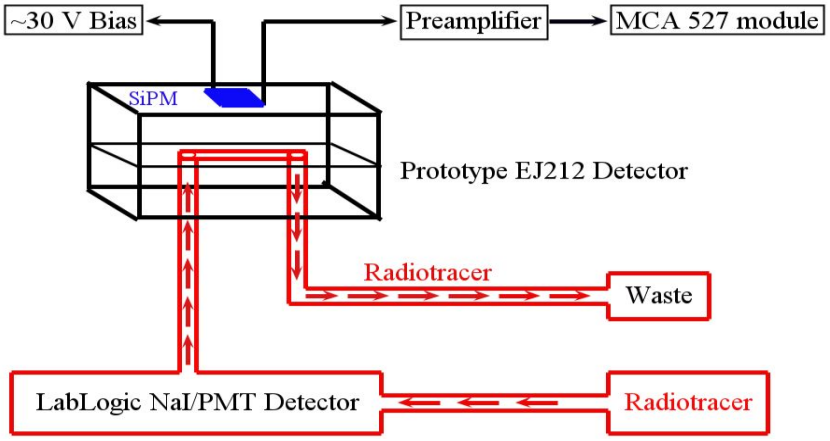

FIGURE 5.21: Experimental set-up for the EJ212 plastic scintillation detector was coupled with 6x6 mm^2 SensL C series SiPM. Detector channel volume is only 2 $\mu\ell$. Radiochemical fluid volume was first passed through NaI-PMT detector system, then the plastic chip detector system by the flow in the circulation system.5.20

the second detector was constructed for obtaining the energy spectrum and the decay curve of the radiochemical substance. The second detector device is the same as the detector design in Figure 5.20. The detection volume, however, was 94 $\mu\ell$ with 6 mm blue sensitive C series SiPM was optically coupled to that detector. After ^{18}F (1.167 MBq/ml) was injected into the plastic detector, the energy spectrum and decay curve were obtained (exposure time was 4096 seconds) as shown in Figures 5.22 and 5.23 respectively, Positrons have a continuous energy spectrum starting with zero up to the end point (maximum energy of positrons). This end point depends on the nuclei (^{18}F the end point is 634 keV). Experimental measurement of ^{18}F energy distribution was the same as the energy spectrum conducted with the simulation with a lower statistic. These energy spectra are consistent with the expected energy spectrum of ^{18}F. MicroMCA module with WinSpec software recorded for both applications, multi-channel analyser (MCA) and multi-channel scale (MCS), at the same time as we discussed previously. While the energy spectrum of ^{18}F was recording, the multi-channel scale was being recorded the generated number of photoelectrons in every second. Therefore, MCS gave the information about the activity (decay curve of ^{18}F) as presented in Figure 5.23. ^{18}F was inside the detector for 4096 seconds, and the detector was then cleaned up with the solution, which contains 40% acetonitrile and 60%water dilutions. However, there must be some radioactive fluid leakage from the surface to the inside of the detector. After flushing the solution inside the detector, the activity or counts number in normal condition could switch back to the ground radiation level or

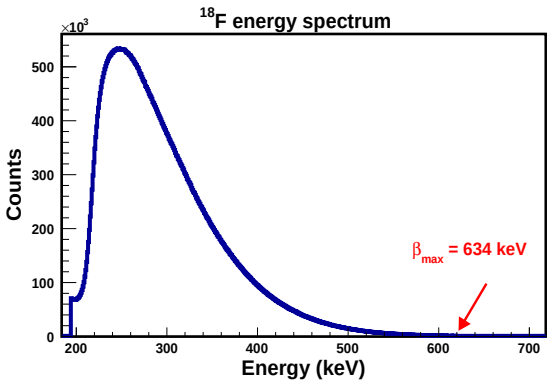

(a) ^{18}F energy spectrum obtained from experiment.

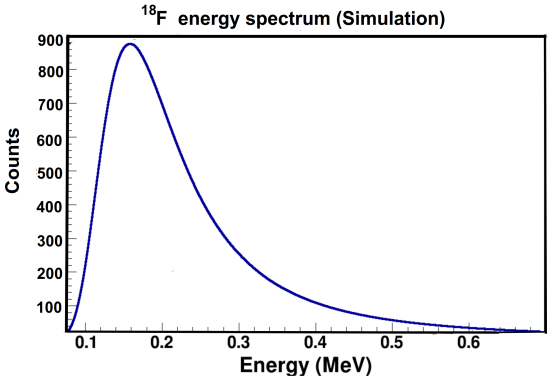

(b) ^{18}F energy spectrum obtained from simulation.

FIGURE 5.22: ^{18}F energy spectra were obtained from experiment and simulation. Plastic scintillation design (94 $\mu\ell$ detection volume) was optically coupled with 6 mm blue sensitive C series SiPM. The source of positrons; ^{18}F (1.167 MBq/ml) was placed inside the detector. (a) Almost one hour later energy spectrum obtained from the experimental measurement. (b) In the simulation, detector design and conditions were defined the same as the experimental conditions, but the data acquisition time had to be set only 2 seconds due to the slow optical photon calculation. Positrons have a continuous energy spectrum (not monoenergetic) from zero to a definite maximum energy value (β_{max}), depending on the nuclide. The highest energy of positrons, which emit from ^{18}F, is 634 keV. The continuous energy spectrum of ^{18}F obtained by the experimental measurement was the same as the energy spectrum conducted with the simulation. These energy spectra are also consistent with the expected energy spectrum of ^{18}F.

zero.

5.6.1 Comparison LabLogic Detector System with New Detector

Various detector designs were connected into the LabLogic circulation system as the set-up shown in Figures 5.20 and 5.21. During the experiment flow rate was stable with 0.5 mℓ min^{-1} and ^{18}F activity was 1.018 MBq per mL. A fraction of the fluid radioactive source was injected into the circulation system (only water). The radioactive volume was first detected by the NaI-PMT gamma detector system (the peak labelled with red), then passed through the new EJ212-Hamamatsu MPPC detector system (the peak labelled with blue) as shown in Figure 5.24. Although plastic scintillation detector had a low detection volume (78 $\mu\ell$), the detection counts with new detector system measured greater than the NaI-PMT

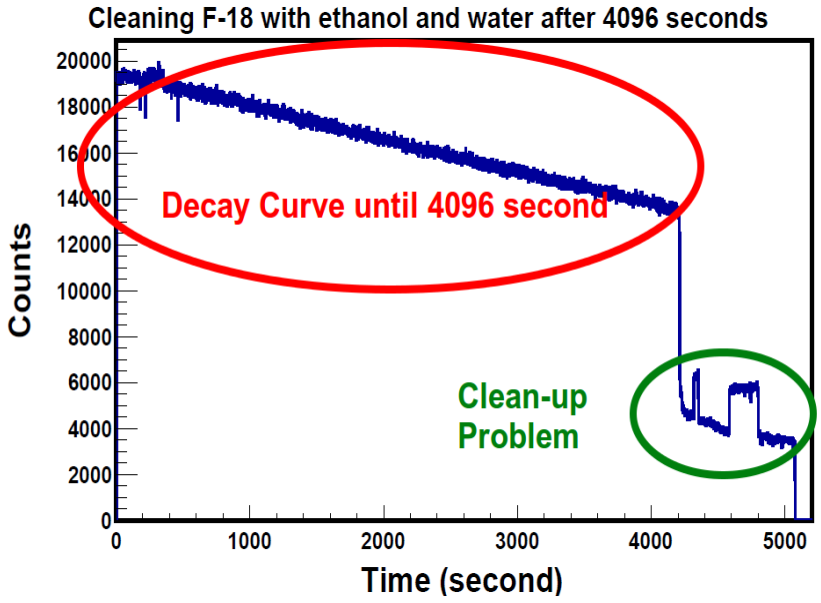

FIGURE 5.23: ^{18}F decay spectrum and cleaning up 4096 seconds later. When the MCA module recorded the energy spectrum, multi-channel scale (MCS) was also recording the decay spectrum of ^{18}F as detailed in Figure 5.22. The detector filled by radiochemical fluide was flushed with solutions, which contain 40% acetonitrile and 60%water dilutions, to clean up inside the plastic scintillation 4096 second later. However, after several second the activity unexpectedly increased instead of reduction. There must be fluid contamination on the detector surface. Therefore, there is a fluctuation in the number of counts (not switch back to the non-radioactive level) after cleaning up.

system. NaI-PMT system firstly detected a low fraction of radiochemical substance (^{18}F) inside the water circulation system, the activity level then switched back to the standard background radiation level (nearly zero) as illustrated in Figure 5.24 with red spectrum. After radiation completely left the tubing system, which was below the NaI-PMT system, ^{18}F passed through the new plastic scintillator detector system (at around 200 seconds). The radiochemical fluid should have flown away from the detector, by observing counts lever switching back to the background radiation level, similar to the NaI-PMT system. However, there must be radiochemical substance contamination (leakage problem) as illustrated in Figure 5.24. The radioactive fluid leaked in the vicinity of the plastic detected. While the plastic scintillator was being drilled to open a channel into it, the material (PVT) could have been damaged by the pressure and the force. That is why there must be cracks on the plastic scintillation surface. Therefore, after cleaning up the detector several times by flashing the solution inside, the contamination was still observed.

Measuring the activity is not the only important parameter, but it is also crucial

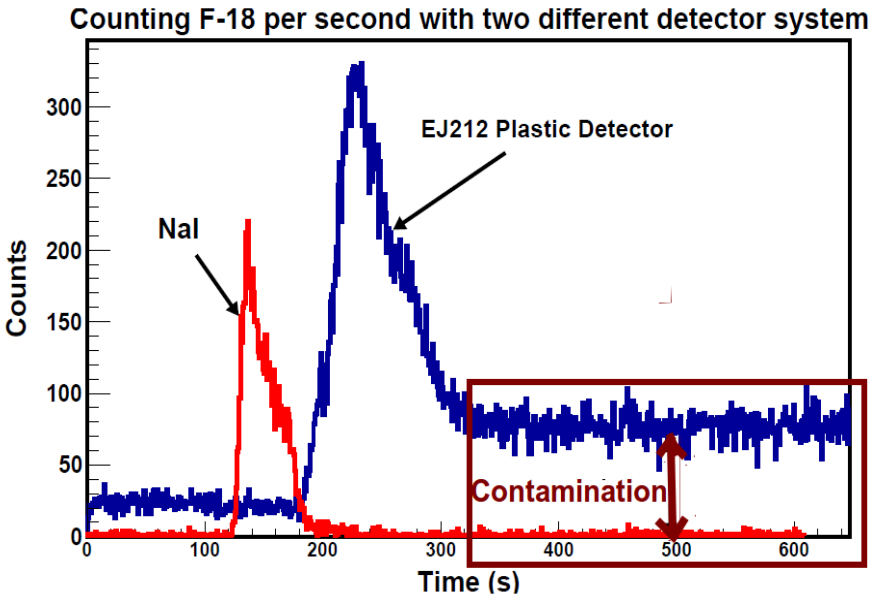

FIGURE 5.24: Comparison NaI-PMT detector system with the EJ212-SiPM detector in the same flow. The detection volume of the plastic scintillator was 78 $\mu\ell$. There must be fluid radiochemical fraction leakage from the detector surface into the plastic scintillator. Therefore, the number of counts did not switch back the background radiation $\sim$ 320 seconds later.

to detect the activity from the tiny blood volume of the small animal research such as microfluidic devices. For this reason, the other detector was designed with the channel volume was only 2 $\mu\ell$ as shown the experimental set-up sketched in Figure 5.21. The counts number of the low volume plastic was not greater than the counts number of NaI-PMT detector system as shown in Figure 5.25. However, this spectra indicates that the microfluidic system can be achievable with plastic detector approach (EJ212-SiPM). In the second run for testing the same detector, there was a flow rate issue as illustrated in Figure 5.25(b). The activity peak did not obtain, but the contamination was the same as the previous measurement radiochemical fluid contamination.

5.6.2 Low Detection Volume

New plastic scintillation detector was designed to measure the activity from very low detection volume (0.65 -0.70 $\mu\ell$) as shown in Figure 5.26. Nanotechnology was used to drill the detector, so there were not cracks on the surface of the plastic scintillation. To achieve a low detection volume in the half of the detector was made by PMMA (non-scintillation plastic). Therefore, there will be the only

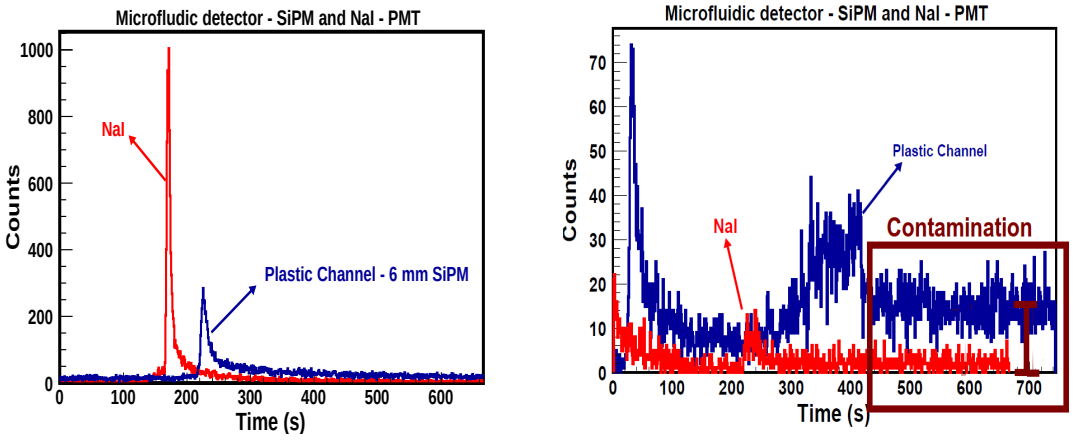

(a) (b)

FIGURE 5.25: (a) Activity of ^{18}F as measured by 2 $\mu\ell$ channel volume detector, and comparison with NaI-PMT detector system. (b) In the second measurement there was a flow rate problem. Activity peak could not obtained, but the contamination was again observed.

interaction between one surface area which is made by plastic scintillation. That means the detection volume might be approximately half 0.70 $\mu\ell$, because half of the positrons would pass through without scintillator interaction.

Figure 5.27 shows that the comparison between Lablogic NaI-PMT detector system and plastic detector which had very low detection volume. Total acquisition time was set to about 20 minutes and the circulation flow rate was 0.5 $\mu\ell$ min^{-1}. The acquisition started, after only 0.7 $\mu\ell$ ^{18}F radioactive concentration pumped into the circulation system (working with water). Radioactive volume was firstly passed through the tubing system, which was below the NaI-PMT detector system. Then second detector (plastic scintillation chip) detected the radiochemical substance activity. As a result, the number of counts per second was obtained for each independent systems. However, there are several important points which need to consider before the comparison of two detectors. The radiation interaction time for NaI-PMT system is nearly three times more than the new detector system. In addition, the plastic detector size is considerably smaller than the NaI scintillation detector as shown in Figure 5.18. Even though new detector has very low radiation interaction time, detection volume and small detector size, the new plastic detector allowed to measure the activity and the result could be improved in the future work. Furthermore, energy and decay spectra of ^{68}Ga were taken for one hour as illustrated in Figure 5.28. For that measurement 1.5 mm thickness of plastic scintillation was used instead of one millimetre. The positron energy

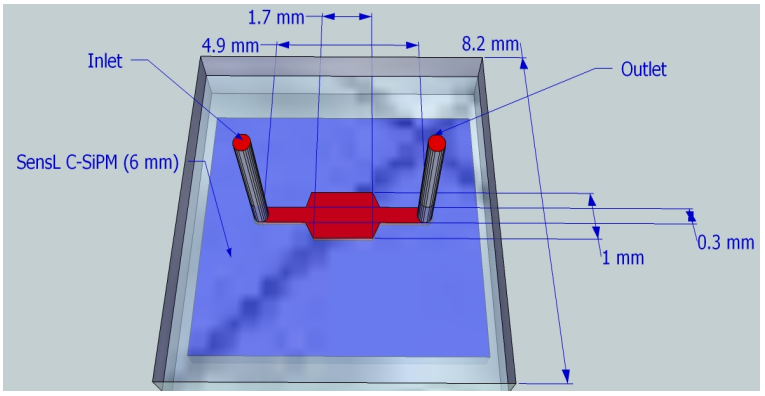

(a)

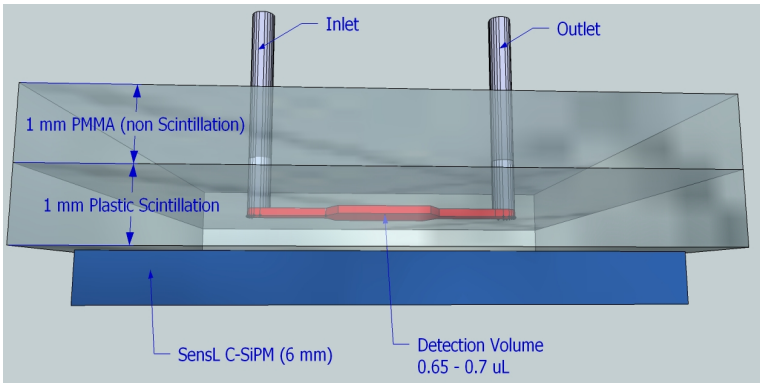

(b)

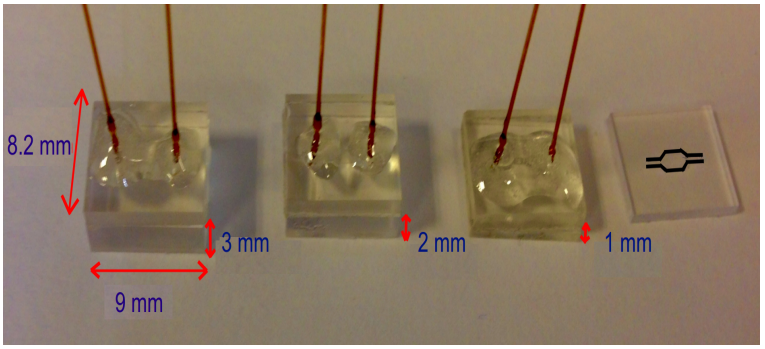

(c)

FIGURE 5.26: (a) - (b) A new detector is designed for low detection volume (0.65 - 0.70 $\mu\ell$) by nano technological approach. (c) Different thickness of plastic scintillation.

range of ^{18}F is lower than the positron energy range of ^{68}Ga. Data acquisition was obtained by using the multi-channel analyser (for energy spectrum) and the multi-channel scale (for decay curve). In Figure 5.28(b) blue spectrum represents the number of photoelectrons (measured by SiPM) as a function of time (counts per second). Radioactive nuclei decrease with the same fraction of radionuclides in every second so that the decay will be an exponential. ROOT software fitted

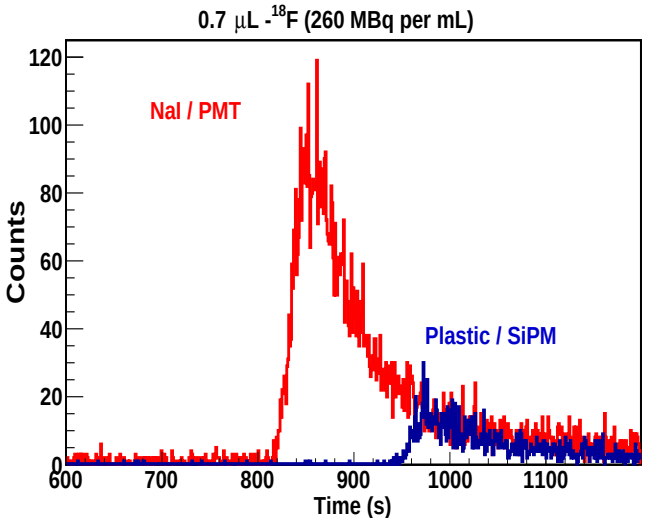

(a)

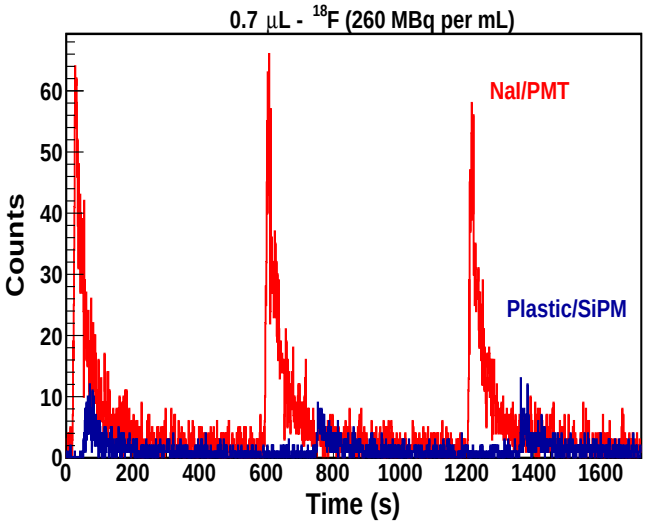

(b)

FIGURE 5.27: Comparison of two different systems; plastic detector with 0.70 $\mu\ell$ detection volume and standard NaI-PMT detector. (a) The acquisition time was nearly 20 minutes. (b) The chromatography column of the circulation system was removed, so acquisition time went down from 20 minutes to 10 minutes and three times the same loop was run.

exponential decay with fitting parameters as given by Equation;

$$Counts \;=\; 3463 \;.\; e^{-(1.86 \times 10^{-4}) \;.\; t} \tag{5.4}$$

Where; Counts is the number of photoelectrons (proportional to the activity), t is the time in second, and 3463 was the first counts number or N_0 which is the activity of the source at time 0. If the half of the activity of the source (N) is found at time t, that time will define as a half-life ($t_{1/2}$). Exponential fitting Equation 5.4

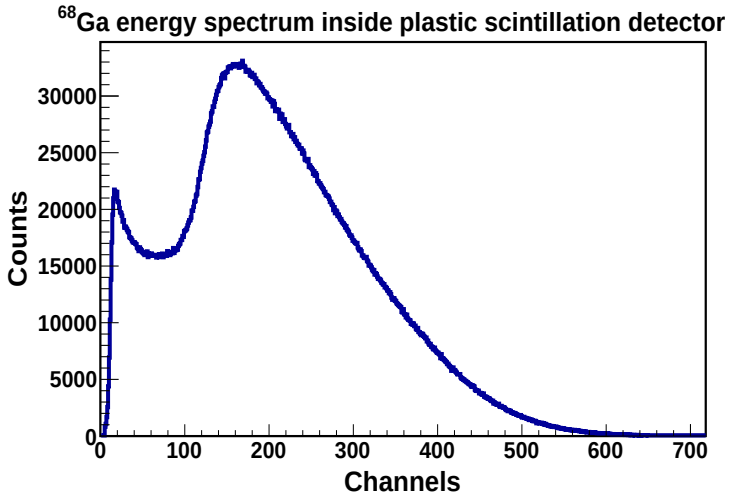

(a)

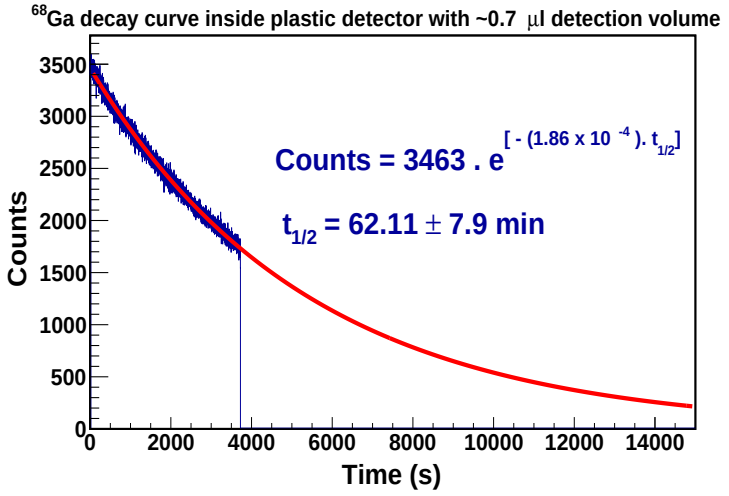

(b)

FIGURE 5.28: 0.7 $\mu\ell$ ^{68}Ga radioactive concentration was injected into the plastic detector system with 0.65 - 0.7$\mu\ell$ detection volume. (a) The energy spectrum of ^{68}Ga. (b) Decay curve and exponential fitting function with fitting coefficients.

can be modified by;

$$N = N_0 \, . \, e^{-(1.86 \times 10^{-4}) \, . \, t_{1/2}} \tag{5.5}$$

Calculated half-life of Ga-68 is 62.11± 8 minutes according to the fitting parameters (Equations 5.4 and 5.5). The excepted half-life for ^{68}Ga is 67.71 ± 9 minutes [86]. The decay curve is not quite sufficient, the data acquisition time should be more than an hour for better fitting parameters. Furthermore, the error could be more because of the statistical variation in the decay rate. However, half-life measurement was completed resulting in the literature value and the experimental value agree with each other if they overlap within their uncertainties.

5.6.3 Surface Treatment

According to the measurement we discussed in the previous section, there is a serious problem related to radiation contamination on the plastic scintillation surface. When radioactive fraction within water circulation system passes through plastic scintillator detection volume, radioactive fluid directly interacts with detector. If cracks occur during the drill (stress can damage the scintillator), radiochemical fluid could leak into the plastic scintillator. That contamination will not allow us to measure accurately radionuclide activity. Two different surface treatment approaches; plasma oxidation and cold fluoride were tested in Hull PET research centre. Plasma electrolytic oxidation is an electrochemical surface treatment to protect the surface from the physical and the chemical damage with the electrical isolation by a creating oxide layer on the surface. The dealkalization treatment with fluorine creates very thin alkali ions structure by using the lower concentration of alkali ions than ^{18}F concentration. That will change the features of the surface by increasing resistance against to the chemical reaction between fluid and the plastic scintillator. Instead of surface treatment, yellow PEEK tube was also used to make a barrier between scintillator and radiochemical liquid. In this approach, radioactive source can not directly interact with the plastic scintillator. Furthermore, yellow PEEK tubing wall thickness is only 360μm and this thickness could be ignorable comparing to the positron range [87] inside the plastic scintillator.

Acquisition time was nearly 20 minutes and each chip treatments were tested three times in order to make a clear observation by adding radioactive contamination on the detector surface. 10 $\mu\ell$ ^{18}F injected inside the circulation system. The radioactive tracer first passed through tubing system, which is located under the NaI-PMT detector. Then radiochemical volume was detected by the cold fluoride treated chip (0.65-0.70 $\mu\ell$ detection volume). Figure 5.29 shows that the two individual detector's activity spectra and radiotracer contamination defined as a background counts after radiochemical volume poured the waste container. According to Figures 5.29(b) and 5.30(b), radiotracer contamination could be inside the entire tubing system, not only surface of the plastic detector. That is why the observed background radiation increased in every circulation loop. The background radiations, measured by the first counter (NaI-PMT), were 107, 135, and 170 counts after each loop as shown in Figure 5.29(b). This trend is also seen in Figure 5.30(b), counted activity number increases from 238 to 286. Radiotracer

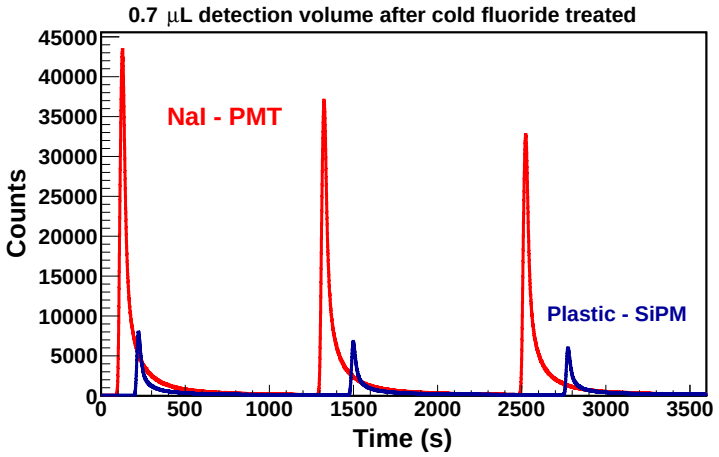

(a)

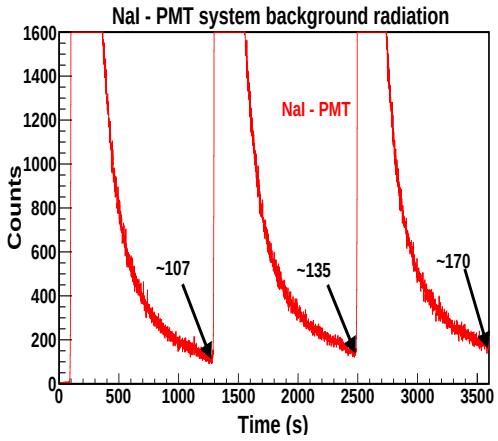

(b)

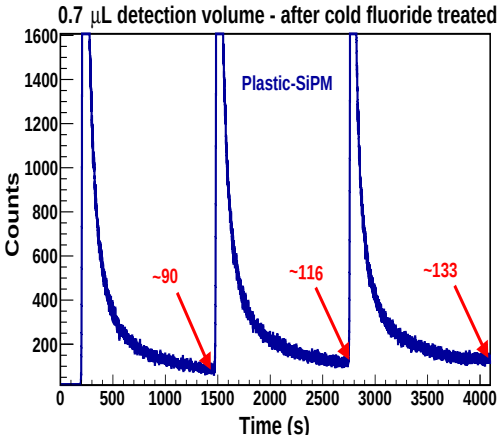

(c)

FIGURE 5.29: 10 $\mu\ell$ ^{18}F (157 MBq mL^{-1}) injected inside the circulation system. Cold fluoride treated chip's detection volume is 0.65-0.70 $\mu\ell$. (a) Background radiation for NaI-PMT detector. (b) Background radiation for plastic detector.

contamination was also observed in plasma oxidisation and cold fluoride treated plastic scintillator chips as shown in Figures 5.30(c) and 5.29(c). However, there is more contamination in the plastic detector, which is treated by a plasma oxidation despite measured lower activity. Background radiation contamination increased from 262 to 331 counts for the plastic scintillator chip, which has been processed by plasma electrolytic oxidation. However, radioactive fluid contamination for the plastic chip applied dealkalisation treatment by fluorine is slightly increase from 90 to 133 counts. As a result, surface treatments (dealkalisation and oxidation) did not succeed the leakage or contamination problem. According to the background radiation activities, not only plastic scintillation material has radiation contamination, but also the entire circulation system (or tubing system) has radioactive fluid contamination.

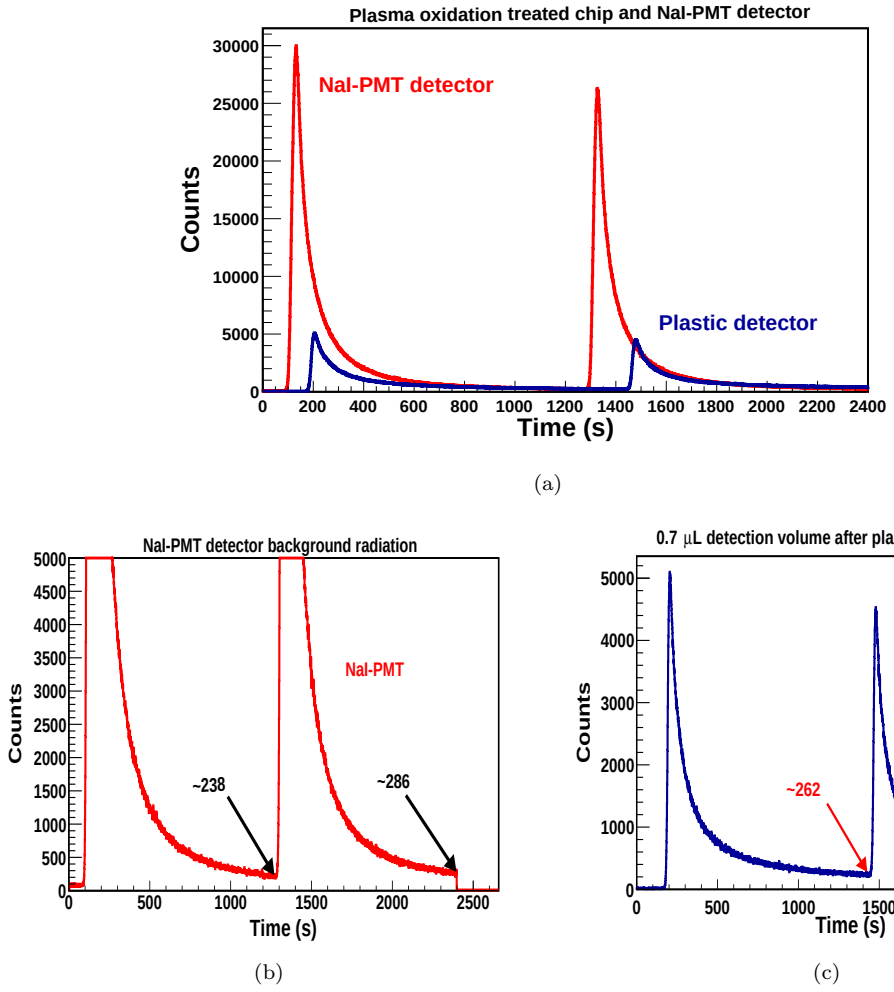

FIGURE 5.30: 10 $\mu\ell$ ^{18}F (158.9 MBq mL^{-1}) was injected into the circulation system. Plasma oxidation treated chip detection volume is 0.65-0.70 $\mu\ell$. (a) Background radiation for the NaI-PMT detector system. (b) Background radiation for the plastic scintillator chip.

Another approach is using the silicon PEEK tubing, which has 360μm wall thickness and 0.006" diameter. The detection volume of tubing is nearly 0.11 $\mu\ell$. The effect of the PEEK wall on the positron detection measurement can be ignored because of remarkably thin wall thickness. In Figure 5.31, there is not radiochemical contamination or leakage problem between the activity peaks. In conclusion, contamination problem is solved by using PEEK tubing. Because after source passed through the detector the level of activity turned back to background level. There is not any contamination on the surface of the tubing. It is highly possible to use that silicon tubing for blood counter device application with a low volume.

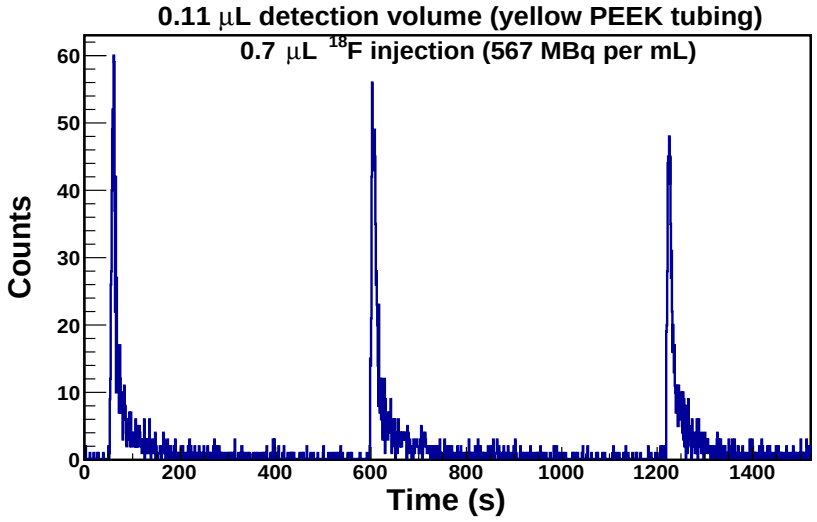

FIGURE 5.31: Yellow PEEK tubing was mounted inside the plastic detector chip. 0.7μL ^{18}F was injected into the circulation system. Three same loops were run to see the accumulated contamination on the detector surface. Yellow PEEK tubing was the best approach to deal with the leakage problem. Because there was not observed radiochemical fluid counts between activity peaks.

5.6.4 Testing Different Thickness of Plastic Scintillation

The experiment in Hull PET research centre was successfully conducted by using different thickness of detector to clarify the effect of the annihilation photons. According to the simulation work, optical photons are produced by 511 keV gamma ray as a result of Compton scattering and the detector thickness. The number of counts (proportional to the generated optical photons) for 3 mm thickness of plastic scintillator is greater than optical photons produced in 2 thickness of plastic scintillator even though using less source activity (Figure 5.32). Photoelectrons difference between 2 and three 3 mm plastic scintillation detectors gives the annihilation photons' effect. According to the simulation, approximately %10 percentage of positrons with higher energy did not stop within 1 millimetre plastic scintillation. It was the conclusion of the simulation, and these positrons would reach the SiPM by direct interact. The high energy positron losses their energy by interacting with absorber material electron, then positron hits the SiPM with lower energy. These positrons measured by the SiPM as shown in Figure 5.33. In a short period, it could be ignorable, but for long term silicon photomultiplier performance will be affected badly. Consequently, plastic scintillation thickness should be between 1.4 mm to 1.6 mm to minimise annihilation photons effect and stop all positrons inside the detector.

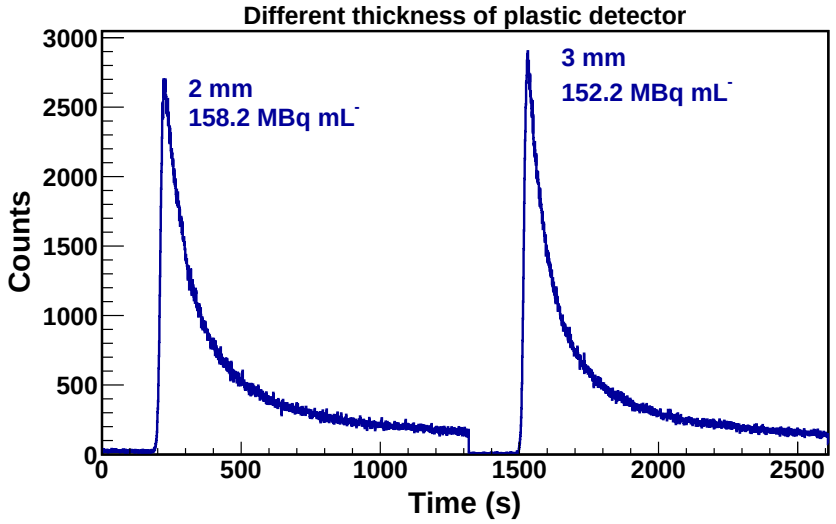

FIGURE 5.32: 2 and 3 mm plastic scintillation detector systems independently measured the activity curve of ^{18}F.

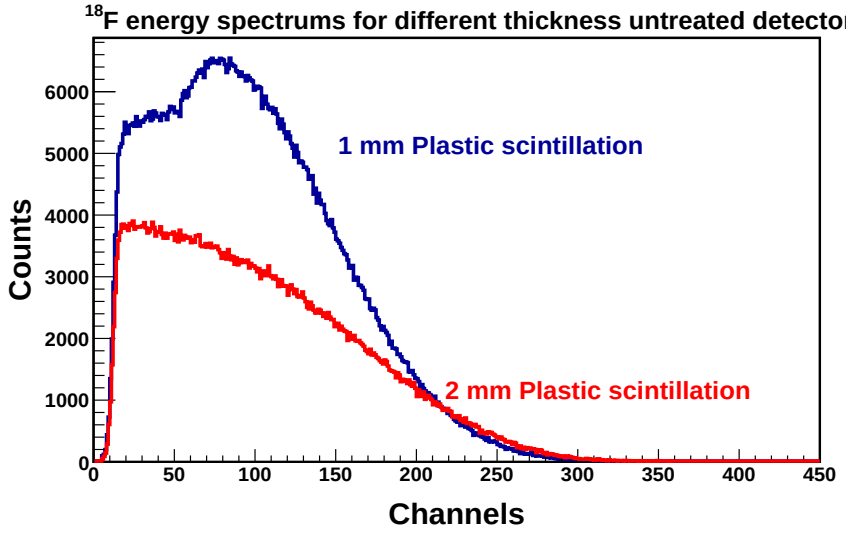

FIGURE 5.33: Untreated chip with 1 and 2 mm thickness of plastic scintillations. The energy spectrum of ^{18}F (157.1 MBq mL^{-1}) for different thickness. It is obvious that 1 mm plastic scintillation detector is not suitable concerning SiPM's performance.

5.7 Summary of the Tests on the Antimatter Detector and Conclusion

Scintillation detector systems are regularly used in the medical application such as; Compton camera, positron emission tomography (PET), beta camera and microprobes. These useful medical imaging tools measured gamma radiation or annihilation photon. Furthermore, scintillation detector is also measured the radiotracers

activity in PET research centres as a standard quality control procedure to obtain acceptance parameters from the radiochemical substance. Clinical quality control parameters must be in the acceptable value before using; these parameters are radiochemical purity, pH level, sterility, safety, radionuclide purity (occurs during the reaction in cyclotron if the target is impure), and radioactivity. Accurate radioactivity measurement is critically necessary to protect the patient against to the unnecessary radiation. In addition, during the investigation of the radiopharmaceutical in the research centre, activity measurement must be completed in a short time to protect researcher from the extra radiation. Thin layer chromatograph, dose calibrator or scintillation counter are used to measure the activity. However, these useful medical devices are very expensive. Also, measurement with radiochromatograph is slower than the scintillator. Scintillation counters have the limit in the detection efficiency and the solid angle. Therefore, a novel antimatter detector system is being developed to use in PET research centre and medical applications. That detector system is measured radiochemical substance activity from direct positrons rather than annihilation photons to increase the detector efficiency and the solid angle for more accurate measurement. Radiopharmaceutical fluid directly interacts with the antimatter detector (PVT or plastic scintillation material - EJ212) for better detection efficiency. It is very simple detector system, user-friendly, cheap and very easy to modify into the other system.

Empirical formula theoretically calculates estimated positron range for ^{18}F. This estimated position range is well-matched with the range calculation obtained from ESTAR stopping power and range calculation programme, based on the theory of Bethe with density effect correction. Then GEANT4 based Monte Carlo simulation programme, GATE 7.0, is used to investigate annihilation photons effect on the positron measurement. Therefore, simulation code is written in two different ways; generating annihilation photons and without creating annihilation photons. Data obtained from the simulation was analysed in ROOT software. Non monoenergetic positrons (with continuous energy spectrum) displacement inside the plastic scintillator (1-1.6 mm) is found longer than displacement in inorganic scintillator (0.5 mm or less) such as LYSO. As a result of the comparison, detector design will be easy with plastic scintillator than others because it would not be too fragile.

Simulation without generating optical photons is found that 1.2 mm thickness of scintillator suffices to stop nearly 90% of positrons emit from ^{18}F (because of

its non-monoenergetic energy distribution). Approximately 10% of positrons emit from radionuclide with higher energy will scatter more than other positrons inside the material with low Z and density. Elastic scattering is related to the positron range direction, so movement inside the medium will be sharply different directions not straightforward by elastic scattering between positron and electrons of plastic scintillator. Although generated optical photons calculation in the simulation was too slow, important several results successfully obtained and compared to the experimental data.

Optical photons are created by nearly 90% of positrons and annihilation photons until 1 mm thickness of plastic scintillator. Between 1 mm and 2 mm plastic scintillation, 10% of positrons (from ^{18}F energy distribution) and annihilation photons generate scintillation photons. All positrons will stop around 2 mm, and then optical photons are produced by only annihilation photons. Annihilation photons interaction with plastic scintillator is dominantly Compton scattering and slightly Photoelectric effect. For without annihilation photons there is a few number of Compton Scattering and Photoelectric effect as a result of X-ray interactions which created by Bremsstrahlung scattering. After completed the investigation of the appropriate thickness of plastic scintillator, antimatter detector design was performed with developing 527 MicroMCA module. In that module, there is a capability to run two different functions at the same time (multi-channel analyser for energy and multi-channel scale for activity measurement). Detector construction was varied depending on the application, and then Hamamatsu MPPC and SensL C-SiPM were optically coupled to plastic scintillator to obtain readout signal.

Initial measurement of new detector system was successfully tested with encouraging results. An expected continuous energy spectra for ^{18}F and ^{68}Ga obtained very nicely. Furthermore, the half-life of ^{68}Ga radioisotope was experimentally calculated resulting good agreement with accepted value. Plastic scintillator with 0.65 -0.70 $\mu\ell$ detection volume was also devised for the low volume of sample blood counter and microfluidic chip applications. During the measurement, we found out that there must be radiochemical fluid contamination inside the whole tubing circulation system in particularly plastic surface which directly contact with the radiochemical liquid. For this reason, various surface treatment (plasma oxidation and cold fluoride) were tested. Instead of surface treatment, different approach was also examined that yellow PEEK tubing with very thin wall thickness was mounted inside the scintillator. In this measurement detector

with 0.11 $\mu\ell$ detection volume was achieved without observing any radiochemical fluid contamination.

Chapter 6

GEANT4 Based Monte Carlo Simulation with GATE for Medical Applications

Monte Carlo simulation method is widely used in scientific research to identify the scatter distribution, model the new medical imaging device, and improve the image quality. That can be the most efficient technique in the investigation if the study is not be experimented, such as; scatter components and their effect on the medical image. Various type of particles and radiation interaction with the material can simulate by a well known Monte Carlo simulation toolkit package program called GEANT4. It has worldwide users in applications from the high-energy physics to the medical physics (accelerator, shielding, space and radiation technologies). The GEANT4 package includes particular tool structures which must contain the system geometry, material properties, physics processes, models, particle tracking, hits and visualisation.

GATE, based on GEANT4, is an open-source advanced numerical simulation software, which is developed by OpenGATE collaborators. It commonly uses in medical physics and radiotherapy (dose calculation). Recently, GATE has played a critical role in the optimisation of acquisition protocols, the new medical imaging device design with its complex image reconstructions techniques, and the radiotherapy dose calculation. The other simulation, GAMOS, is also built upon GEANT4 libraries for medical applications. However, GEANT4 improvement is

frequently updated in GATE software, and writing code in GATE is more user-friendly than in GAMOS.

In this chapter, there will be overview explanation about the GATE simulation. In the last section, further simulation work related to the antimatter detector system, as given in the previous chapter, will be presented.

6.1 GATE

GATE is a combination of the GEANT4 simulation toolkits including well-defined physics models, complex geometry definitions and medical visualisations. In GATE, the time dependent parameters can define, such as radioactive source decay kinetics and movements of the source or detectors. The Monte Carlo simulation controlled by the macro language without advanced C++ knowledge, macro codes create commands for the GEANT4 interpreter. That is why defining a sophisticated geometry of the detector, radioactive source, and phantom construction in GATE is easier than in GEANT4. Various critical sections merged into the GATE simulation, such as detector geometry and materials, physics processes, digitiser, a radioactive source, data output, visualisation, and experiment acquisition [88].

6.1.1 Definition of Geometry and Materials

The definition of the geometry is necessary because simulated particles track inside the predefined volume, these tracking data are then used to provide medical imaging or other applications. First the world volume must be defined, and other volumes called daughter or granddaughter have to be inside the word volume. That gives a hierarchical structure without overlapping each others, so the world volume should be as broad as to cover all volumes in the simulation. Particle tracking data will capture inside the world volume, but it will stop outside the volume. Geometrical volume daughter or granddaughter in the world volume can be repeated, placed or moved in the specific systems such as PET. If detector system has a movement during the experiment, all volumes defined in the world will update within the certain time interval. The volume geometry must define as an element, molecule or mixture with material properties in the material database. In the more complicated detector definition, a surface boundary must be defined

for two different volumes. For example, the surface boundary between scintillation crystal and silicon photomultiplier must be determined for optical photons transfer. Further definitions will require in the simulation such as reflectivity, and the backscatter constant if optical photons and scintillation are studied.

6.1.2 Physics Process

The physics lists are chosen depending on either the particle or radiation energy and type. Each physics process has the final state model and the interaction probability (cross section).

6.1.2.1 Electromagnetic Physics Process

The particle interactions with the matter in the physics list define as an electromagnetic process, which includes photoelectric effects, Compton scattering, ionisation, and so on. In the physics list, each process can be set as a default. For instance, positron annihilation photons were set as a default after recording the data with annihilation photons to search the effect of the annihilation photons on the measurement. Each electromagnetic process has three different models depending on the energy; the standard model (from 1 keV to 100 TeV), the low-energy model (from 250 eV to 100 GeV) and the Penelope model (from 250 eV to 1 GeV) [89].

6.1.2.2 Optical Physics Process

Optical photons and optical physics processes are used to investigate the scintillation detector properties, such as energy resolution. The optical photon generation and tracking must determine, before the definition of the optical photon physics process. The optical photon tracking is extremely fast, but the tracking process completes after a factor of thousand or more photons tacked. Consequently, the optical photons process in the simulation is always slow, and it takes a long time. There is a fast analysis option in the digitiser architecture. However, that cuts the data acquisition time without recording all information into the output files such as coincidence.

Various parameters must be known to define the scintillation material properties and boundary surface. Finding these parameters can be difficult if there is

no literature or measurement about them. The optical absorption is the critical parameter, which is the travel distance of the optical photons in the material before absorbed. The optical boundary between scintillator (dielectric) and SiPMs (metal) is also important because generated optical photons could either reflect back into the scintillator or be absorbed by the SiPM depending on the surface boundary parameters and incoming optical photon's angle and wavelength. As discussed in Chapter 5, two optical boundary surface are defined for antimatter detector system; interference between SiPM and scintillator and interference between scintillator and reflector (PTFE material). Therefore, generated optical photons undergo the total internal reflection; reflection into the scintillator with high probability and reflection into the PTFE with low probability [90].

6.1.2.3 Hadronic Physics Process

Hadron or ions interaction process defines as the decay process in the hadronic physics list. The main processes for fusion are fragmentation and inelastic scattering, which includes Cascade, thermalisation and deexcitation.

6.1.3 Radioactive Sources and Particles

There are various source forms in GATE simulation, such as voxelised, linacBeam, Pencilbeam and GPS (general particle source). A source manager is responsible for generating randomly radioactive decay. The definition of the source first defines followed by source energy, the angular distribution of emission, shape and position. If the source has a movement, it must be attached to the daughter or granddaughter volume with its movement. For medical imaging and radiotherapy applications, a voxelised source and phantom are defined as an attached sensitive detector to provide the absorbed dose in the output file.

6.1.4 Digitiser

Detector pulses or digitiser algorithms use for the particle interaction with the material. Each track inside the sensitive volume (defined as a sensitive detector as shown in Figure 6.1) records as a hit in the output file. All critical information of the interaction obtains from the hits such as deposited energy, position and time of

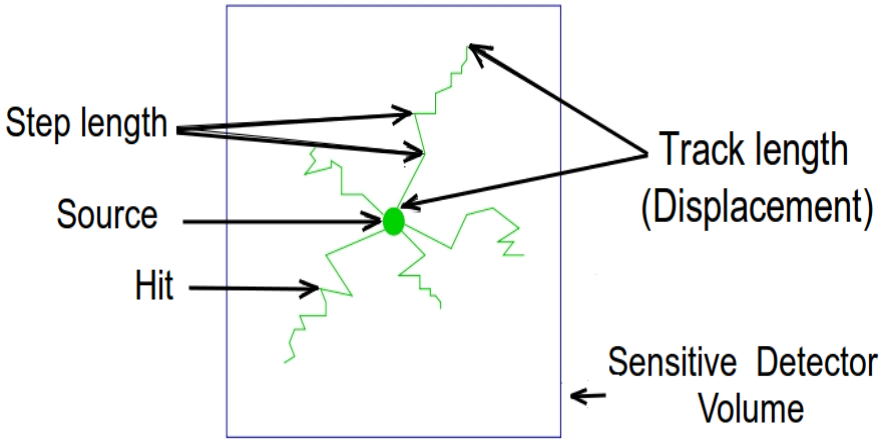

FIGURE 6.1: Recording particle interaction process inside the sensitive detector. After defining the system, some volumes must be chosen as a sensitive detectors, which allow the storage of particle interaction information. If a volume defines as a sensitive detector, the signal processing chain begins to digitise. Therefore, particle interaction inside the sensitive detector volume is recorded as namely; hits, singles and coincidences [89].

the step, momentum and energy of the track, and interaction type. However, the hits information do not relate to the real detector response. The digitiser module (a series of signal processors) must be used to obtain an actual detector interaction response. A chain of the module begins with hits, followed by the adder, readout, energy response, spatial response, threshold electronics, dead time and singles.

When the optical photons study with GATE, relevant parameters must be determined, such as light yield (LY), transfer efficiency ($\bar{e}$) and quantum efficiency (QE) of the detector. If these parameters define in the simulation, the energy variable of the pulse represents the number of photoelectrons (N_{pe}).

6.1.5 Data Outputs

Readout data are the most important aspect of the software applications. In GATE simulation, there are various data output formats such as ASCII, binary, interfile output of projection set and image CT.

6.1.5.1 Root

In this research, readout files in GATE simulation obtained and analysed in root software to investigate annihilation photon effects. Root is a particular structure of systems for processing large amounts of data, born at CERN and forming the main part of research in high energy physics [91]. In GATE simulation, a root output file is generated with histograms and trees that allow extremely fast access to a huge amount of data. In that output file, Coincidences, Hits and Singles trees contain numerous histograms related to particle tracking data, such as energy, position, time and angle.

Using MakeClass in root classes, two files are generated as MyClass.h (the class definition) and MyClass.C (allows the user to loop over tree entries). When a MyClass.C file is modified and improved in C++, the specific information inside each tree of recorded events can be obtained, as shown in our simulation results, which were gained using this knowledge of MakeClass.

6.1.6 Radiotherapy Applications

Initially, GATE simulation is started for positron emission tomography, before special tools developed for radiotherapy dose calculations. When a simulation is running, actor tools save specific information regarding interactions in the volume, such as the number of created particles, an amount of energy deposited, simulation statistics, dose measurements, secondary productions, Q-value and cross section production. In radiotherapy, energy and dose deposited (E_{dep}) provided by dose measurement actors in 3D images.

6.2 Investigation of the Positron Displacement in Antimatter Detector System

6.2.1 Without Generating Optical Photons and Annihilation Photons

In Chapter 5, simulation works were successfully conducted with the simple detector geometry, and placing the radioactive source in front of the scintillator (see the Figure 5.3). In this section, the scintillation detector geometry defined the same as the real detector geometry with detector channel. Radiochemical substance (non-monoenergetic cylindrical Fluorine-18) placed at the centre of the scintillation materials (filled the channel space homogeneously) similar to the experimental conditions as discussed in Chapter 5. Figure 6.2 illustrates a real detector geometry and radiochemical source visualisation in the simulation. The grey box was the plastic scintillation (EJ212) material, and its properties were determined in the material database. The small blue box on the top of the scintillator was the SensL C-series SiPM with 1 mm thick and 6 mm^2 photosensitive area. Blue non-linear tracking paths indicate the positron displacement inside the EJ212 plastic scintillator.

Beta particles randomly emitted from the ^{18}F radioactive source in the simulation. These particles (positrons) travel distance (displacement) in the material depends on the absorber material density and the particle energy. The positron displacement in the high density scintillator (inorganic scintillator) is shorter than in the low-density scintillator as discussed in the previous chapter. Figure 6.3 shows the positron movement in the EJ212 with the real detector geometry. In each hit (or interaction) positron moves away from the source. The track length or displacement defines as the distance between the first position of the particle and the last position as illustrated in Figure 6.1. In the last interaction, positron annihilates and annihilation photons occur. In this simulation, the generation of annihilation photons and optical photons (or scintillation) events were set as a default, so after the last interaction positrons will stop. Figure 6.3 shows the total displacement of the positrons in the EJ212 plastic scintillator. As discussed in Chapter 5, the low energetic positron's displacement will be shorter than the high energetic positrons' because of the beta particles continuous energy spectrum. Almost 90% of positrons emitted from ^{18}F stop before 1.2 mm thickness of the plastic

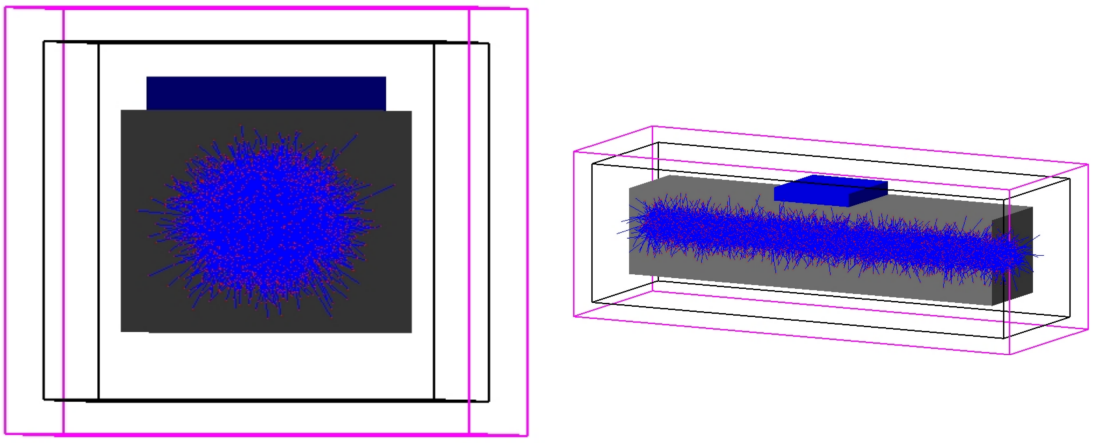

(a) (b)

FIGURE 6.2: Investigation of the positron displacement in the real detector geometry. The non-monoenergetic Fluorine-18 source (blue cylindrical volume) placed at the centre of the detector (homogeneously filled the channel). Positrons displacement inside the EJ212 plastic scintillator (grey box) showed with blue non-linear tracking paths visualisation; (a) from the centre of the detector and (b) from the left side of the detector. The small blue box, at the top of the scintillator, defined as the SensL C-SiPM with 1 mm thickness and 6 mm ^{2} sensitive area. The pink box frame is the world volume and other volumes placed inside the world volume. This simulation was set to run without annihilation and scintillation events (not generated optical photons).

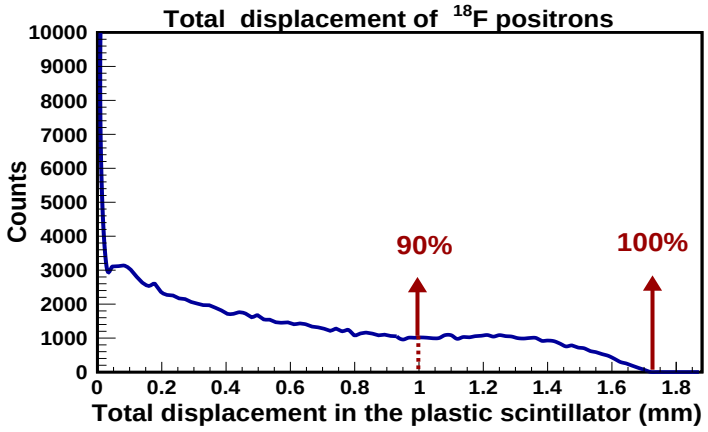

FIGURE 6.3: The total tracking length (displacement) of the positrons inside the plastic scintillation material. Simulation code was defined for real detector dimension and without annihilation photons and optical photon generation.

scintillator. Nearly 10% of positrons will lose its energy between 1.2 and 1.8 mm. This result is consistent with the conclusion of the simulation completed with the basic geometry.

6.2.2 Generating Optical Photons

There are several disadvantages of the using optical photons in the simulation. Optical photon generation is very fast, but tracking optical photons is too slow. That dramatically increases the simulation time. To perform the optical photons in the simulation many parameters must be defined, and some of them may be difficult to determine. Though drawbacks of the using optical photons in the simulation, generating optical photons is the only way to investigate the scintillation detector properties in the simulation.

First, plastic scintillation material (EJ212) properties determined in the material database such as scintillation light yield, absorption length, emission spectrum with probabilities, and so on. Scintillation features and optical properties (surface and surface boundary for optical photon transfer) of the plastic scintillation defined in the macro codes. The detector geometry and generated optical photons illustrate in Figure 6.4. The blue box volume defined as the SensL C-SiPM and

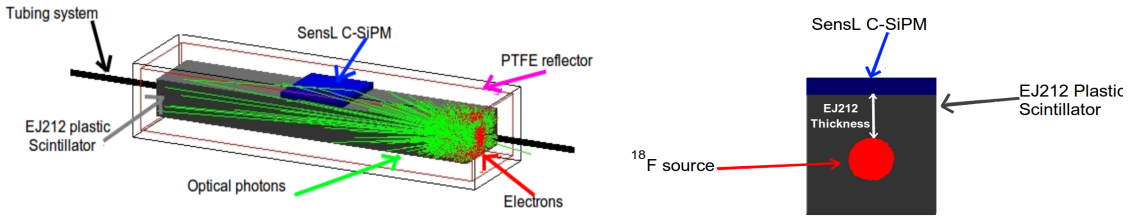

(a) Scintillation events resulting in optical photons, (source was not visible)

(b) The source position shifted to change the scintillator thickness.

FIGURE 6.4: Optical photon simulation with real detector geometry: blue box volume defined as the SensL C-SiPM, and grey material was plastic scintillator (EJ212). Radioactive source placed at the centre of the detector, which is in the black tubing system. After simulation source became invisible, and only particle interactions observed. Pink frame defined as a 2 mm PTFE reflector to keep optical photons inside the detector. (a) There are only a few scintillation events resulting in many optical photons (green lines) generations inside the plastic scintillation. (b) ^{18}F source position changed to investigate the optimum thickness of the scintillator.

grey material was plastic scintillator (EJ212). The pink frame defined as a 2 mm PTFE reflector to keep the scintillation photons inside the detector. The interference between two volumes must be defined to transfer optical photons from the scintillator to the SiPM (scintillator and SiPM) and keep optical photons inside the scintillator (scintillator and PTFE). Positron interaction with the plastic scintillator creates optical photons as indicated with green lines inside the detector.

Additional physics processes need to define to produce optical photons such as scintillation process and optical boundary.

The thickness was altered from 0.1 mm to 4 mm to find the optimum thickness of the scintillator by changing the ^{18}F source position as shown in Figure 6.4(b).

Figure 6.5 illustrates the number of optical photons versus the scintillator thickness. Until 1 mm almost 90% of positrons produces scintillation photons the same as the simulation result with simple detector geometry given in the previous chapter. The 10% of positrons emitted from the continuous energy spectrum generates

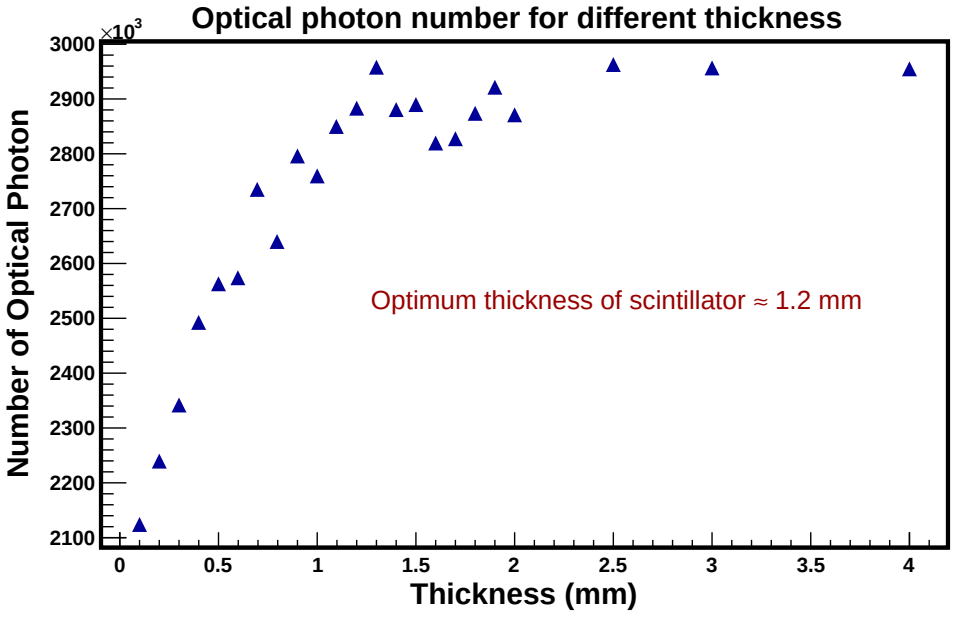

FIGURE 6.5: The number of optical photons versus the scintillator thickness. Until 1 mm almost 90% positrons produced scintillation photons, between nearly 1 mm and 2 mm thickness the rest of positrons (10% with high energy) from the continuous energy spectrum of the ^{18}F generated the optical photons. That is why after 2 mm thickness of scintillator the number of optical photons remained constant. In this simulation, annihilation photons were set as a default.

the less optical photons between approximately 1 mm and 2 mm with statistical variation. Optical photon simulation acquired for each thickness of scintillation, source decays randomly and the random generator also used in the simulation as a Monte Carlo tool. After 2 mm thickness, the number of optical photons remains constant because all positrons generate optical photons. In this part of the simulation, annihilation photons were set as a default.

6.3 Summary and Conclusion

In Chapter 5, the simple detector geometry used to investigate the effect of the annihilation photons on the optical photons measurement. In this chapter, there was a further investigation for positron range with and without generating optical photons within the actual detector dimension. The simulation results with the real detector geometry are the same as the simulation performed with the simple detector geometry. Consequently, almost 90% of positrons (from continuous energy spectrum) generate optical photons and then annihilate with electrons in the material. Defining optical and scintillation properties of the EJ212 plastic scintillator and finding parameters were not difficult, but the data acquisition time in the simulation was extremely long. That is why the simulation time set in seconds or incoming particle numbers set as a constant (5000 primaries particles).

Chapter 7

Summary and Future Plans

7.1 Summary and Experimental Results

In this work, several important properties of the scintillation detector system were experimentally investigated to enhance their potential for use in HELIOS spectrometer and PET-MRI medical imaging system. The integration of the functional imaging technique (PET) into the magnetic resonance imaging (MRI) opened the door to lead an innovative approach to the spectrometer technology. This new concept has become an important part of the nuclear structure research. A solenoidal spectrometer, called HELIOS, is now being used to investigate the exotic nuclear structure and deeply understanding of the stable nuclei by single nucleon transfer reactions, pair transfer, inelastic scattering, and knockout-reactions. In general, scintillation detection systems are widely employed in nuclear, particle, and medical physics for radiation detection, cross-sectional images and the activity measurement of the radiopharmacy. The optically combined scintillation material and photomultiplier tube (PMT) or silicon photomultiplier (SiPM) can operate inside a strong magnetic field (such as PET-MRI system or HELIOS spectrometer). Regarding PMT, it needs to be shielded to eliminate the effect of the magnetic field on the PMT current or must be operated outside of the field [15]. However, the combination of the scintillator and SiPM (or APD) can work in the magnetic field because of photodiode's insensitivity of the magnetic field [8, 16, 17].

Silicon photomultipliers have many advantages over photomultiplier tubes, so they are an attractive replacement for photomultiplier tubes. In this research, scintillation detector system, which is the combination of novel scintillators and new

generation silicon photomultiplier are studied. The work is particularly focused on the characterisation of the SensL 6 mm blue sensitive silicon photomultiplier and the coincidence time measurement with using unique fast timing readout signal of the SensL SiPM. In addition, novel scintillation detector system was successfully modified into the medical applications to measure the radiopharmacy activity and microfluidic chip applications in the PET research centre. Primary measurement of this new detector system was completed with encouraging results.

First, various scintillation detector systems were examined as detailed in Chapter 2. A simple PET detector module (4 x 4 matrix) was constructed by using sixteen LYSO crystals. The previous generation SensL position sensitive silicon photomultiplier was optically coupled to this detector module. That detector construction was the same as PET detector module performed by Hong and Choi [16]. The readout board of the SensL 4x4 array MPPC had already broken, and one signal output only used in the energy spectrum. Additionally, the wrapping material was not sufficiently completed because of the little space between the scintillator and plastic grid resulting in excessive loss of scintillation light yield. Therefore, the PET detector module performed insufficiently. After that, a new generation scintillator, $LaBr_3$, was optically coupled to 5 mm Hamamatsu avalanche photodiodes to examine inside a magnetic field. The $LaBr_3$-APD detector system was used to take the energy spectra of the standard radioactive source (^{137}Cs with 370 kBq activity) inside approximately 1 Tesla magnetic field. The energy resolutions were calculated with and without magnetic field at 662 keV gamma energy; 6.67% and 6.66% respectively. Therefore, the energy performance of the detector system was not affected by the magnetic field. After a simple positron emission detector had been placed inside the phantom, which is the plastic ball filled with paramagnetic substance, an MRI image was also obtained to investigate the interference in the magnetic resonance image. A hospital MRI machine successfully acquired horizontal cross section images. The magnetic field homogeneity was slightly deteriorated by the scintillation detector system, as observed in the reconstructed MR image of the phantom. Magnetic field degradation must be the effect of the detector current and its connectors placed inside the field. High-frequency noise, which originated from the Larmor frequency, was observed on the readout signal of the scintillation detector, so the shielding box could be used to reduce the noise [16]. Furthermore, scintillation detector system operating with the electronic modules such as power supply, amplifier, and MCA module should be shielded to minimise the effect of the electronic oscillations on the detector measurement. Furthermore,

experimental phoswiches data, gathered by the PARIS collaboration was analysed using ROOT software. Additional experimental data has been obtained by using the phoswich cluster and new-generation scintillators, such as SrI_2, CLYC, and GYGAY. However, these data are yet to undergo analysis.

Using novel technological techniques (such as complementary metal oxide semiconductor (CMOS)) and innovative designs in the manufacturing process of the photodiode gain the several advantages in the SiPM applications. CMOS technology reduces damage to the depletion region during the fabrication process, so dark current (improved from 10-24 μA to 0.68-1.75 μA) and noise decrease with SensL C series SiPM by using CMOS technology. Also, P-N junction can be constructed extremely close to the surface of the SiPM, that dramatically increases the blue sensitivity via detecting shorter wavelength photons (from blue light to UV). In Chapter 3, various types of SiPM were characterised in terms of the energy performance, temperature dependence, and bias voltage and gain dependencies by generally focusing on SensL SiPM. SensL B-series SiPM energy resolution for 662 keV at room temperature (21.6 $\pm$ 0.1 °C) versus bias voltage measurement is not as fluctuated as at low temperature (6.1$\pm$ 0.1 °C) measurement. The bias voltage against the dark current at different ambient temperatures from 6 °C to room temperature 21°C measurement was completed for SensL B series 6 mm SiPM. The dark currents were measured almost zero before the breakdown voltage. However, after the breakdown voltage dark current electrons (thermally generated) become more dominant, that is why the dark current suddenly increases after V_{BR}. The dark current rises if the environment temperature increases. Overall, the dark current increases as a square of the bias voltage (V^2) after breakdown voltage as a similar trend measured with the literature [29]. The detector gain, defined as a channel number (at the FWHM of the 662 keV full energy peak), is significantly influenced by the voltage variation and change in the temperature. If the detector gain changes, the performance of the detector will vary. Therefore, the gain must be kept a stable by modifying the voltage or temperature. For SensL B series SiPM, the breakdown voltage was calculated to be 26.2 $\pm$ 0.6 V at room temperature (4.8 % agreement with the technic data) and 25.8 $\pm$ 0.2V at low temperature (3.2 % agreement with the technic data value). One channel shifts with each 2.84 $\pm$ 0.05 mV variation at room temperature and 1.94 $\pm$ 0.01 mV variation at low temperature according to the experimental measurement. The similar measurement was conducted for SensL 6 mm C type SiPM and 6 mm Hamamatsu

MPPC module (2x2 array made by four 3 mm S12572-010P MPPC). The breakdown voltage was found to be 26.23 ± 1.02 V for SensL C-SiPM and 66.29 ± 6.30 V for Hamamatsu MPPC. Experimental breakdown voltage calculations are well-matched with the technical data values obtained from manufacturers. The dependence of the detector gain and voltage is also found to be 2.85 ± 0.10 mV for SensL C series SiPM, which is very close to the SensL B type SiPM voltage-gain relationship. Hamamatsu MPPC sensor is less affected by the voltage variation, one channel shifts with every 8.5 ± 0.6 mV. The temperature dependence of the gain and the connection between temperature and bias voltage were also investigated. If the temperature decreases, the detector gain will increase or vice versa. A single centigrade variation will shift 3.72 ± 0.13 channels for SensL B-series SiPM. According to the measurement, only one centigrade variation in the temperature will change 0.52 ± 0.02 percentage of gain, which is not in agreement with the technical data value (0.8 %/°C [50]). This error could originate from the thermally-isolated temperature controller chamber, so the temperature stabilisation could not accurate. The fact that the detector gain does not directly change with the temperature, the breakdown voltage variation will directly alter the detector gain. For SensL B-series SiPM the breakdown voltage was found to be 22.73 ± 0.72 mV growth with every centigrade variation. Various detector systems' non-linearity corrections were calculated with the experimental data. Energy linearity of Hamamatsu MPPC (2x2 arrays)-$LaBr_3$ detector system is found to be much better than SiPMs. This conclusion is also consistent with the similar research [59].

The coincidence-resolved time is a critical measurement in nuclear research subjects and ToF-PET systems. In many experiments, time-of-flight measurements are required. If the coincidence time resolution of scintillation detector (γ radiation detector system) is sufficiently higher than the lifetimes of excited nuclear states, in some cases, decay cascades can be ordered and identified distinctly. Regarding medical applications, the quality of the positron emission tomography's image increases with a better time resolution of the PET detector. This parameter directly affects the line of response (LOR) by reducing Compton scattering and random coincidence effects on the medical imaging. A coincidence time resolution is influenced by the SiPM capacitance because the silicon photomultiplier capacitance affects the photodiode rise time. SensL producer successfully achieved the lower capacitance silicon photomultiplier by innovative design. For instance,

SensL silicon photomultiplier's capacitance for 6x6 mm^2 photosensitive area is reduced from 3400 pF to 48 pF. The effect of the SiPM capacitance could be less in timing measurement, which is conducted by SiPM with the lower photosensitive area (such as 1 mm^2), but this effect will be more if SiPM has large sensitive area. That is why the timing resolution is found poor by using SiPM with a large photosensitive area. SensL B and C series blue sensitive SiPMs structure has a great advantage with the additional signal output (lower capacitance readout for timing applications) beside of the standard output (used for energy spectrum). In Chapter 4, the coincidence time resolutions of the various scintillation detector systems were investigated by analogue and digital timing methods. Timing resolution performance of the SensL C series SiPM with 6 mm^2 photosensitive area was completed by using the digitiser with remarkable progress (from 512 ps to 331 ps). The first critical approach was combining the transformer in the circuit. Secondly, Mini-Circuits amplifiers for different purposes were used in the set-up to obtain the better rise time of the signals. The coincidence time resolution was improved from 481 $\pm$ 9 ps to 276 $\pm$ 8 ps by using these amplifiers. Finally, an appropriate threshold level during the analyses was sought depending on the signal amplitude, and the correct energy gate (only 511 keV annihilation photons) in the software applied during the data analysing process. The code for analysing data was carefully written to find an accurate interpolated value; a quadratic fitting equation was used instead of a linear equation. The leading edge method gave the better results, even though the constant fraction technique was employed independently. The coincidence time resolution (FWHM / $\sqrt{2}$) was found to be 264 $\pm$ 9 ps for $LaBr_3$-C series SiPM detector after the intrinsic time resolution subtracted from the measured coincidence time resolution. Furthermore, the coincidence-resolved time measurement (FWHM) dependence of the bias voltage was investigated. When the bias voltage increases, the detector gain and photodetection efficiency also increase due to the improvement in the photon statistics [73]. Therefore, the higher gain gives a better rise time and signal-to-noise ratio [74] because noise becomes less dominant in the higher pulse amplitude. Consequently, coincidence-resolved time resolution becomes lower until the noise again becomes more dominant in the signal. The coincidence-resolved time relationship with the bias voltage obtained by the experimental measurement was consistent with the literature [66, 73, 74].

Scintillation detector systems are also used to measure the activity of the radiopharmacy in the radioisotope or research centres as a standard quality control procedure. Clinical radiochemical and radionuclide parameters must be in the

acceptable value. These parameters, which are radiochemical purity, pH level, sterility, safety, radionuclide purity, and radioactivity, must be checked before injected into the patient circulation system [22]. Radioactivity measurement must be accurately conducted for the patients health to protect them from the extra radiations and minimisation of the adverse effect on the medical image. In addition, the activity measurement in a short time is crucial for researchers to protect them from the unnecessary radiation during the investigation of the radiopharmaceuticals in the research centres. In general, expensive radiochromatogram scanner and scintillation counter systems are used for the quantification of the radioactivity distribution [23]. However, the measurement time with radiochromatogram scanner is longer than the scintillation counter, and scintillation detector system has a limited detector efficiency and solid angle. Therefore, a novel antimatter detector system is being developed to use in PET research centre and medical applications. In this detector design, radiochemical substance activity is measured from positrons rather than annihilation photons, and radiochemical substance directly contacts with the scintillator without any interference between the detector and the radioactive source. These are the major differences between the new detector system and standard detector systems used in nuclear medicine; such as blood counter, beta probes and scintillation detector system. Furthermore, this detector design is obviously cheaper than standard detectors, and it has a very simple working principle with being user-friendly, easy to modify into another systems, and achievable nanoscale volume for a microfluidic chip application. Blood sample counting device or microfluidic systems must precisely take a time-dependent spectrum as a function of the whole body radioactivity concentration from 0.70 μL to 0.22 μL sample volume in a short time [78]. In PET research centre, the standard scintillation detector system, which is LabLogic's Scan-RAM NaI optically coupled to PMT, is used for measuring the activity in radiopharmacologic research. The initial measurements were completed with various new detector designs, and results compared with the standard NaI-PMT detector system. First, empirical formula theoretically calculated the positron range in the plastic scintillator and that well-matched with the calculation obtained by ESTAR stopping power and range calculation program. Then GEANT4 based Monte Carlo simulation program, GATE 7.0, is used to examine the annihilation photons effect by two different ways in the simulation; generating annihilation photons and without annihilation photons. That gave the optimum thickness for the least effect of the

annihilation photons on the positron measurement. Various detectors were designed, and they were then tested in the PET research centre at the University of Hull. During the experiment, we observed the radiochemical fluid contamination inside the whole tubing circulation system especially on the plastic scintillator surface, which directly contact with the fluid. The novel scintillation detector designs were also tested for the low volume blood sample counter and microfluidic chip applications (measured from 94 $\mu\ell$ to 0.11 $\mu\ell$). Surface treatments (plasma oxidation and cold fluoride) were applied on the plastic scintillator surface before the experiment to remove the radiochemical contamination. Moreover, PEEK tubing with very thin wall thickness were tested resulting in successfully measurement with 0.11 $\mu\ell$ detection volume without radiochemical fluid contamination. Continuous beta particle spectra from ^{18}F and ^{68}Ga were obtained as what expected. Besides, the half-life of ^{68}Ga radioisotope was experimentally calculated to be 62.11$\pm$ 8 minutes (accepted half-life is 67.71 $\pm$ 9 minutes [86]). Therefore, the literature value and the experimental value agree with each other if they overlap within their uncertainties.

7.2 Future Plans

A patent application has been completed following a collaborative agreement between the University of York and Hull University for this new concept scintillation detector design, which is used in the PET radioisotopes research centre. Further investigation must be conducted with different thickness of scintillator, designing prototype microfluidic blood counter device and the calibration of the detector systems. This new detector system is also highly possible to modify into a complex gradient microfabricated device. That medical device is used to vary the radioactivity level of the radiopharmacy as illustrated in Figure 7.1. There are two inlets; radiochemical sample (showing with the blue solution) is injected into the first inlet and radioisotope labelled sample (showing with the red solution) is injected into the second inlet. When red and blue colour samples pass through inside the tubing system, radioisotope and radiochemical concentration will change in gradually. Consequently, six different concentration levels are obtained in the outlets. From the first outlet to the last outlet, radioactivity level reduces, but radiochemical concentration increases. The new detector design must measure the activity in the each outlet. The standard complex gradient microfabricated device

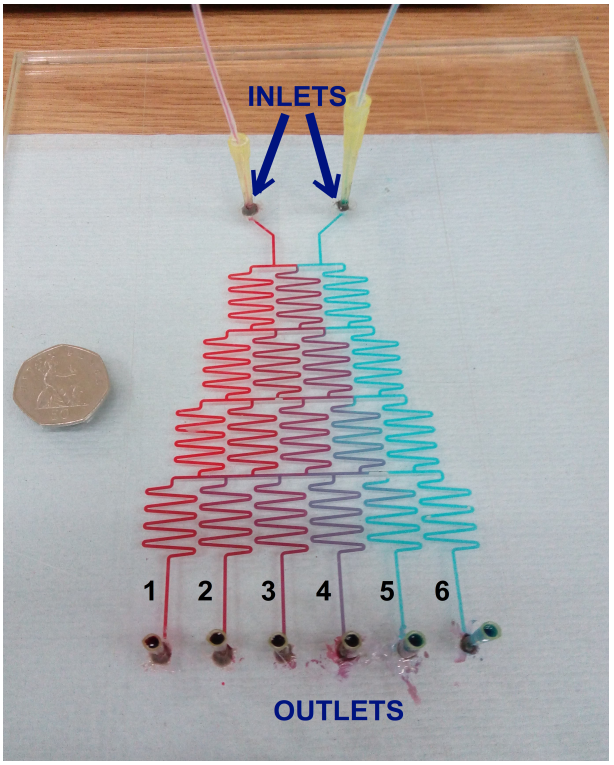

FIGURE 7.1: A complex gradient microfabricated device. Two different samples are injected into the inlets; one sample contains radiochemical component (represents with blue solution), and the other is radioisotope sample (represents with red solution). When red and blue colour samples pass through inside the tubing system, the main sample mixes each other with different concentrations. This device is used as a mixer or concentration gradient generator. There are six different radioactivity levels with the different chemical concentration in the each outlet. The highest radioactive isotope concentration and the lowest radiochemical concentration is in the first outlet. Radioactivity concentration will decrease from the first outlet to the last outlet.

is produced from the non-scintillator material such as plastic. Figure 7.2 shows the detector design with two different size of SensL silicon photomultiplier array is coupled with scintillator. In this detector design, the main board is scintillation material. When the fluids mix in the way of the each path, the activity level can be monitored by using scintillation material coupled with the silicon photomultiplier. Figure 7.2(a) shows the detector for the SensL C-series 1 mm^2 active area 4 x 4 array SiPM. Four outlets monitor activity variation as a movement of time. Radioactivity level at the last region of the outlet can be measured with the second design, as shown in Figure 7.2(b).

Measurements with these devices are more complicated than a single detector measurement. At least six channels of digital readouts must be used for data acquisition. Furthermore, a new scintillator material is being made in the Hull

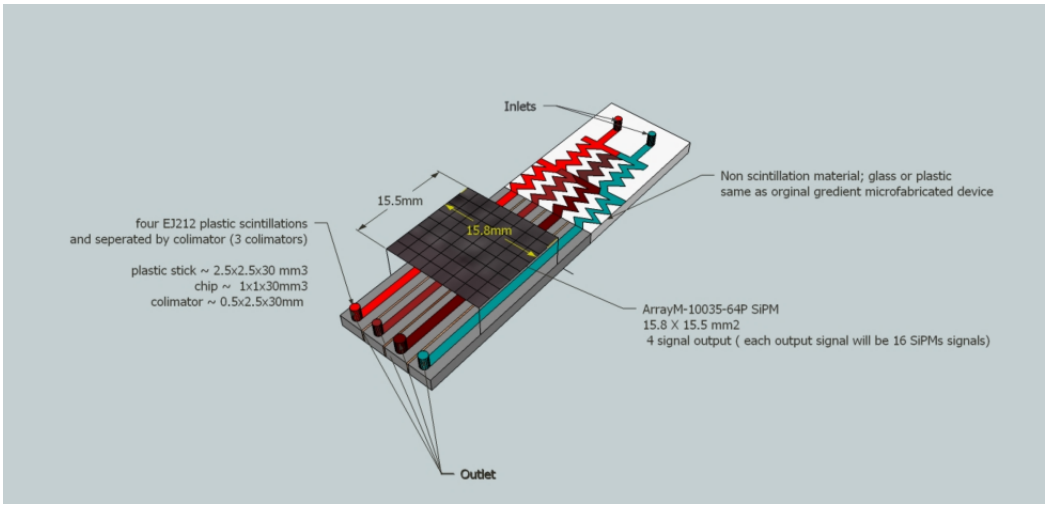

(a) For a 1 mm^2 active area, a 4 x 4 matrix array of SensL C-series blue sensitive SiPMs.

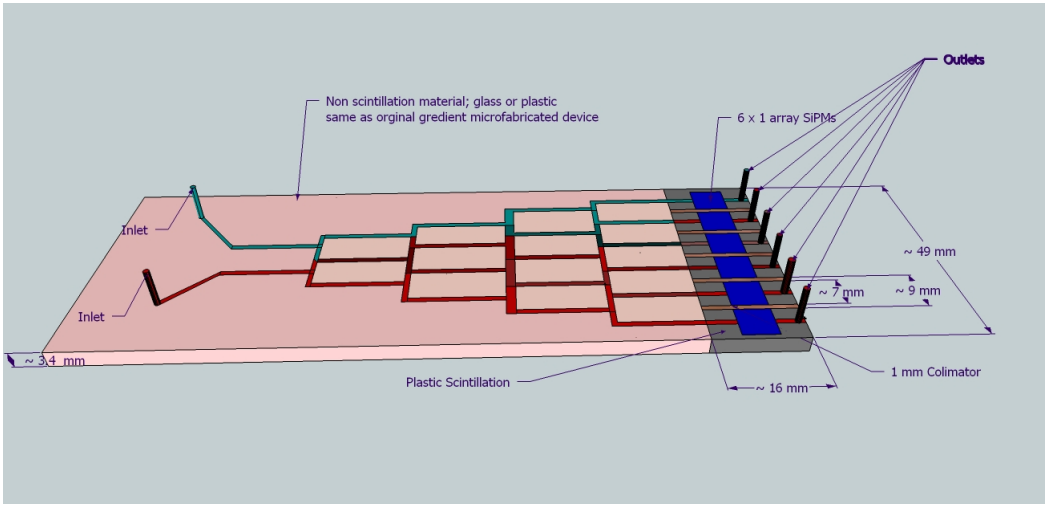

(b) For a 6 mm^2 active area,a 6 x 1 matrix array of SensL C-series blue-sensitive SiPMs.

FIGURE 7.2: A complex gradient microfabricated device. Two different samples with different radioactivity levels are injected inside the inlets. Six outlets are obtained with various activity levels.

research centre as an alternative to the plastic scintillation (EJ212). There was a radiochemical contamination on the surface of the scintillator detector as we discussed in Chapter 5. Two different possibilities can cause of that problem. The first probability is that the scintillation material reacts with the radiochemical fluid resulting in radiopharmacy contamination into the detector (called the leakage problem). The second possibility is that the plastic scintillator can be damaged (cracks on the surface) by the drill. That is why we were searching different scintillation material. Until now, encouraging result has been obtained, but the light output of the scintillator is insufficient.

Appendix A

Signal Processing and Coincidence Time Measurement

Choosing a suitable amplifier in the specific measurement (such as, energy and time spectroscopy) is a critical point to optimise the signal during the data acquisition. Figure A.1 shows the electronic block diagram for specific measurements with pre-amplifiers, amplifiers, and discriminator, which are commonly used in nuclear physics and particle physics as discussed in Chapter 2and Section 2.4.

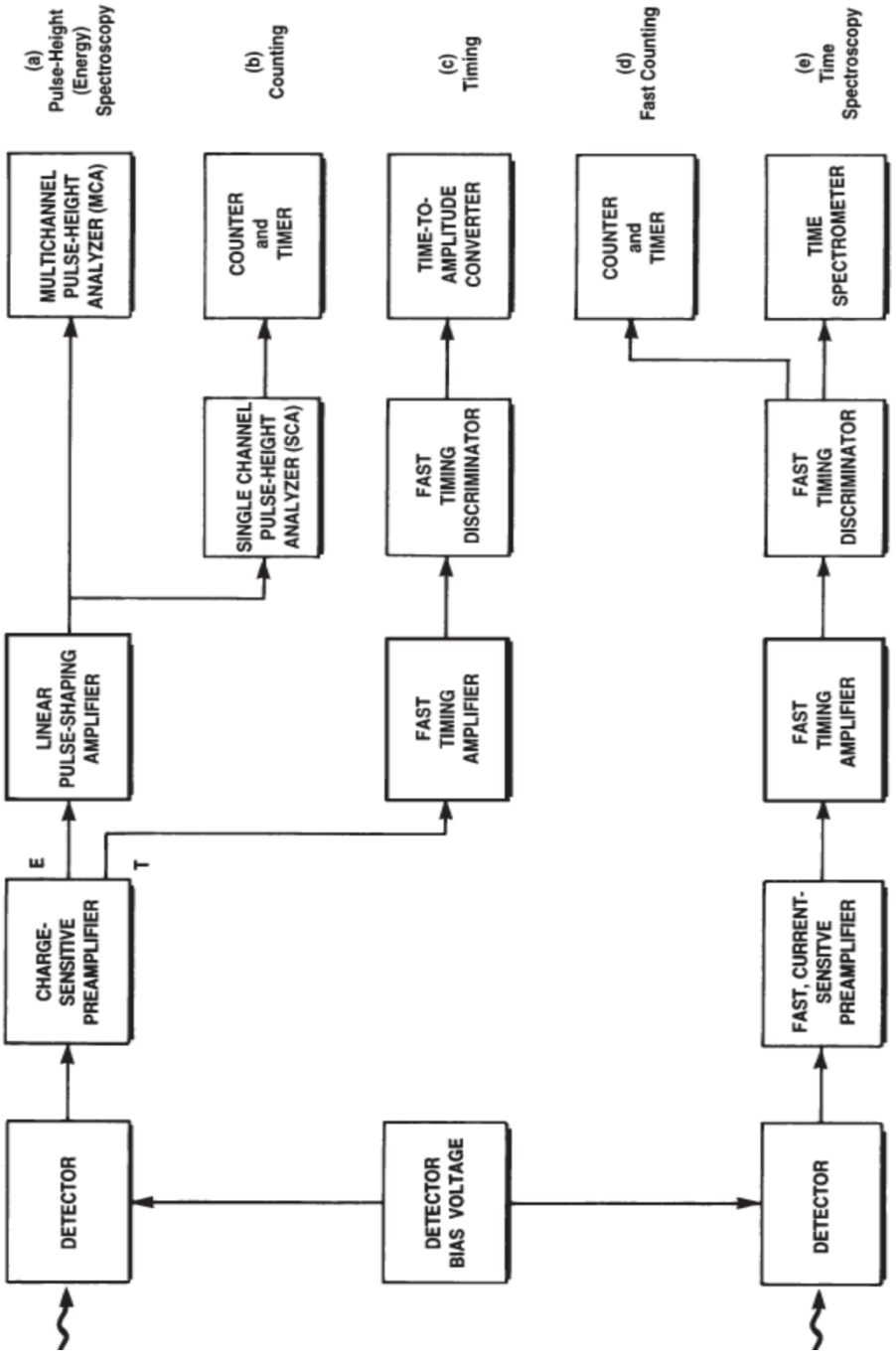

FIGURE A.1: Common amplifiers used in nuclear and particle physics applications for signal shaping processes [37].

Hamamatsu does not release large photosensitive area (6 mm ^{2}) multi-pixel photo counter (MPPC or SiPM). Therefore, we constructed 2x2 arrays from four S12572-010P MPPC with 3 mm^2 photosensitive area (Figure A.2). These MPPCs connected in parallel to obtain a combination of the four signal outputs (because the circuit readout will be the total of the each MPPC currents). Therefore, SensL C and B series SiPM with 6 mm^2 photosensitive area was compared with 6 mm^2 Hamamatsu MPPC as shown in Chapter 4 in Figure 4.1(a).

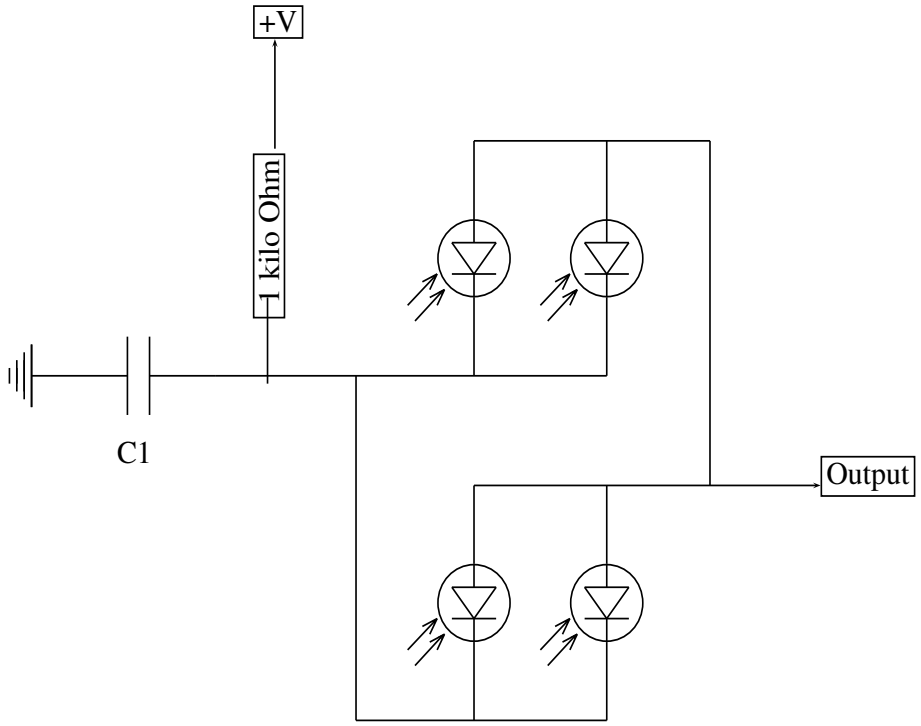

FIGURE A.2: Readout circuitry for the 2x2 array of Hamamatsu multi-pixel photon counter (MPPC conventional SiPMs). A single S12572-010P MPPC has 320 pF terminal capacitance, 90000 number of pixels, 3 mm ^{2} active area. Four MPPC have been connected parallel.

Philips PM5786 pulse generator used for electronic time resolution measurement. Two identical pulses first obtained, generator pulses were then fed into the digitiser (CEAN DT5742), Ortec 820 fast timing amplifier, and Philips 708 discriminator, which is the same electronic block diagram as shown in Figure 4.16. The digitiser recorded 5000 pulses, data was then analysed with leading edge method as detailed in Chapter 4 in Section 4.3.1. Calculated time difference between two identical pulses was histogrammed and created the Gaussian distribution for intrinsic time resolution, which illustrates in Figure A.3

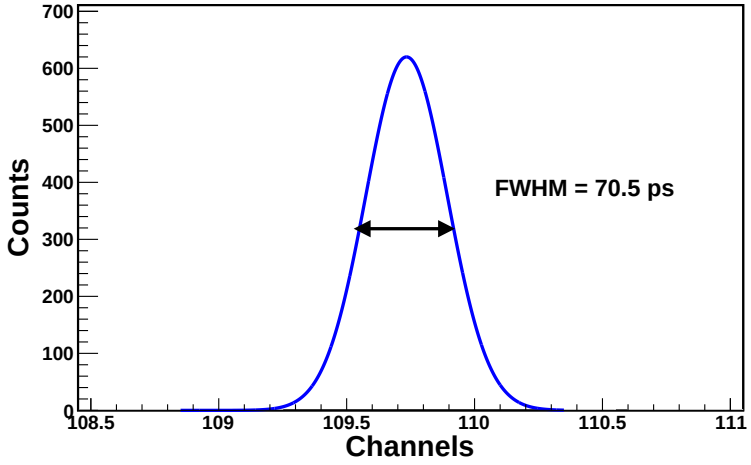

FIGURE A.3: Intrinsic time resolution (Full-Width-Half-Maximum (FWHM)) of the electronics. Philips PM5786 pulse generator used for producing simultaneous two identical pulses.

The Philips PM5786 pulse generator used for electronic time resolution measurement (intrinsic time resolution) with the different experimental set-up. After obtained two identical pulses, these signals were fed into Mini-Circuits amplifiers (ZFL-1000LN and ZX60-43-S+), digitiser, and discriminator as shown the electronic block diagram in Figure 4.25 in Chapter 4. The digitiser recorded 5000 pulses, data then analysed with using leading edge method. Calculated time differences between two identical pulses were histogrammed and created the Gaussian distribution for intrinsic time resolution, which illustrates in Figure A.4.

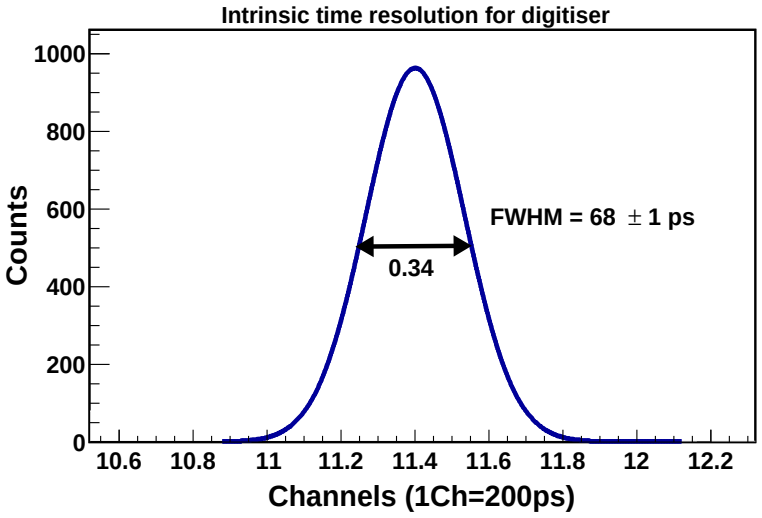

FIGURE A.4: Intrinsic resolved time measurement of the electronics. The Philips PM5786 pulse generator used to produce simultaneous two identical pulses. For the experimental set-up see Figure 4.25. The Full-Width-Half-Maximum (FWHM) is calculated to be 0.34 channels (68 $\mp$ 1 ps).

Appendix B

Antimatter Detector

527 MicroMCA module was developed to measure the number of photoelectrons as a function of time in per seconds or microseconds (for activity measurement). Figure B.1 shows the layout diagram of the electronic board, which used in activity measurement. This module can modify for different SiPM by negative or positive bias voltage capability. The readout signal can also be monitored by oscilloscope when MCA acquisition records the data. The software called WinSPEC used for the record of the data. It has the capability to record the energy spectrum with multichannel analyser and activity spectrum with the multi-channel scale at the same time.

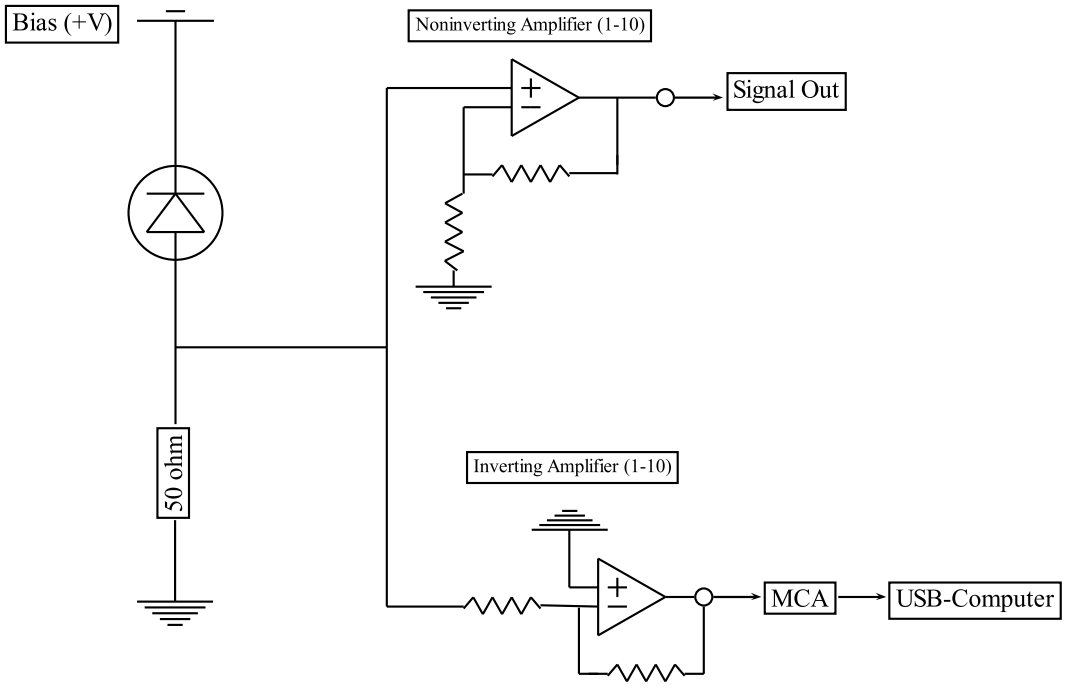

FIGURE B.1: The layout diagram of the developed MCS model. The SiPMs signal can be monitored by oscilloscope when MCA acquisition records the data by using WinSPEC software.

Abbreviations

MRI	**M**agnetic **R**esonance **I**maging
PET	**P**ositron **E**mission **T**omography
PET-MRI	**P**ositron **E**mission **T**omography integrated **M**agnetic **R**esonance **I**maging
HELIOS	**HELI**cal **O**rbit **S**pectrometer
ATLAS	**A**rgonne **T**andem **L**inac **A**ccelerator **S**ystem
rp-process	**r**apid **p**roton capture **process**
FDG	**F**luro**D**eoxy**G**lucose
PMTs	**P**hoto**M**ultiplier **T**ubes
SiPM	**Si**licon **P**hoto**M**ultiplier
APDs	**A**valanche **P**hoto**D**iodes
MPPC	**M**ulti **P**ixel **P**honton **C**ounter
LOR	**L**ine **O**f **R**esponse
PET-CT	**P**ositron **E**mission **T**omography **C**omputed **T**omography
ToF-PET	**T**ime **O**f **F**light **P**ositron **E**mission **T**omography
SPECT	**S**ingle **P**hoton **E**mission **C**omputed **T**omography
GEANT	**GE**ometry **AN**d **T**racking
NIM	**N**uclear **I**nstrumentation **M**odules
QE	**Q**uantum **E**fficiency
PDE	**P**hoton **D**etection **E**fficiency
MCA	**M**ulti **C**hannel **A**nalayser
SCA	**S**ingle **C**hannel **A**nalayser
TAC	**T**ime **A**mplitude **C**onverter
ADC	**A**nalogue to **D**igital **C**onverter
PARIS	The **P**hoton **A**rray for the studies with **R**adioactive **I**on and **S**table beams
CMOS	**C**omplementary **M**etal **O**xide **S**emiconductor
FTA	**F**ast **T**iming **A**mplifier
GDG	**G**ate and **D**elay **G**enerator
CFD	**C**onstant **F**raction **D**iscriminator
CRT	**C**oincidence **R**esolving **T**ime

Bibliography

[1] A.H. Wuosmaa *et al. Proposal for a Solenoidal Spectrometer to Study Reactions with Short-Lived Beams.* Argonne National Laboratory (ATLAS), 2005.

[2] J.C. Lighthall *et al. Commissioning of the HELIOS spectrometer.* Nuclear Instruments and Methods in Physics Research A, 622:97-106, 2010.

[3] A.H. Wuosmaa *et al. A solenoidal spectrometer for reactions in inverse kinematics.* Nuclear Instruments and Methods in Physics Research Section A, 580(3):1290-1300, 2007.

[4] S.J. Freeman *et al. A HELIcal Orbit Spectrometer (HELIOS) for HIE-ISOLDE.* CERN-INTC-2010-031 / INTC-I-099, 2010.

[5] B.B. Back *HELIOS:The Helical Orbit Spectrometer at ATLAS.* Argonne National Laboratory (ATLAS), 2010.

[6] J.C. Lighthall, *Commissioning of the helical orbit spectrometre: a new device for measuring nuclear reactions in inverse kinematics.* PhD thesis, Western Michigan University, 2011.

[7] B.B. Back *First Experiment with HELIOS: The Structure of* ^{13}B. The American Physics Society (Physical Review Letter), 2010.

[8] C. Catana *et al. Simultaneous in vivo positron emission tomography and magnetic resonance imaging.* Proceedings of the National Academy of Sciences (PNAS), 105(10):3705-3710, 2008.

[9] *Positron Emission Tomography PET image gallery.* [Online] Available at: http://www.healthgalleries.com/positron-emission-tomography-pet [Accessed 10 April 2013].

[10] E.C. Paul *Nuclear Medicine and PET/CT Technology and Techniques.* USA: Elsevier Mosby, 2012.

[11] J. Sæterstøl *Characterization of Scintillation Crystals for Positron Emission Tomography.* MSc thesis. Norway: University of Bergen; 2010.

[12] O.J. Roberts, *Investigations of Detector Methods for Gamma-Ray Spectroscopy with PARIS.* PhD thesis. York: University of York; 2010.

[13] N.L. Christensen *et al. Positron emission tomography within a magnetic field using photomultiplier tubes and lightguides.* Physics in Medicine and Biology, 40(4):691, 1995.

[14] M. S. Judenhofer *et al. Simultaneous PET-MRI: A new approach for functional and morphological imaging.* Nature Medicine, 14(4):459-465, 2008.

[15] Y. Shao *et al. Simultaneous PET and MR imaging.* Physics in Medicine and Biology, 42(10):1965-1970, 1997.

[16] K.J. Hong *et al. A prototype MR insertable brain PET using tileable GAPD arrays.* Medical Physics, 40(4):042503, 2013.

[17] C. Woody *et al. Preliminary studies of a simultaneous PET/MRI scanner based on the RatCAP small animal tomograph.* Nuclear Instruments and Methods in Physics Research A, 571:102-105, 2007.

[18] Y. S. Huh *et al. Development of Filtering Methods for PET Signals Contaminated by RF Pulses for Combined PET-MRI.* IEEE Nuclear Science Symposium Conference Record, M13-258:3812-3815, 2009.

[19] H. S. Yoon, *et al. Initial results of simultaneous PET/MRI experiments with an MRI-capatible silicon photomultiplier PET scanner.* The Journal of Nuclear Medicine (NSS/MIC), 608-614, 2012.

[20] N. Ojha *et al. PET Performance of the GEMINI TF PET-MR: The World's First Whole Body PET-MRI Scanner.* Nuclear Science Symposium Conference Record (NSS/MIC), 2013-2015, 2010.

[21] S. Suleman *et al. Performance of Philips Gemini TF PET/CT Scanner with Special Consideration for Its Time-of-Flight Imaging Capabilities.* Journal of Nuclear Medicine, 48(3):471-480, 2007.

[22] J. Shukla *et al. Quality Control of Positron Emission Tomography Radiopharmaceuticals: An Institutional Experience.* Indian Journal of Nuclear Medicine, 28(4):200-206, 2013.

[23] S. L. Vivian *Quality control of compounded radiopharmaceuticals*. The University of New Mexico Health Sciences Centre Continuing education for nuclear pharmacists and nuclear medicine professionals, 2009.

[24] G.F. Knoll, *Radiation Detection and Measurement*. John Wiley & Sons: The United States of America, 2000.

[25] N. A. Syed, *Physics & Engineering of Radiation Detection*. Canada: Elsevier, 2015.

[26] K. A. Olive *et al. Particle Data Group Collaboration*. Review of Particle Physics, Chin, Phys. C, 38:090001, 2014.

[27] L. John *Nuclear Physics Principles and Applications*. John Wiley & Sons: Manchester, 2009.

[28] T. Stefaan *Experimental Techniques in Nuclear and Particle Physics*. Springer: Berlin, 2010.

[29] *Introduction to the SPM.* SensL Technical Note, 2011.

[30] *Microcell Construction* [Online]. Available at: http://www.ketek.net/products/sipm-technology/microcell-construction/ [Accessed 18 August 2015].

[31] *How to Evaluate and Compare Silicon Photomultiplier Sensors* SensL Technical Documentation, 2015.

[32] *Si Photodiode, Si APD and MPPC.* Hamamatsu; Opto-semiconductor Handbook.

[33] *Characteristics and use of Si-APD (Avalanche Photodiode).* Hamamatsu; Technical Information SD-28, 2004.

[34] A. Intermite *et al. Influence of Dark count on the Performance of Silicon Photomultipliers.* Paper In Conference Proceedings, In Beam Instrumentation Workshop (BIW10), Santa Fe, NM, USA, 2010.

[35] *Advanced Silicon Detectors; Introduction to the SiPM.* AdvanSiD, Application Note, 2014.

[36] H. T. Yen, S. D. Lin and C. M. Tsai *A Simple Method to Characterize the Afterpulsing Effect in Single Photon Avalanche Photodiode.* Journal of Applied Physics, 104:054504, 2008.

[37] *Introduction to Amplifiers*. Ortec Application Notes.

[38] *Fast Timing Discriminator Introduction.* ORTEC, AMETEC (Advanced Measurement Technology), 2013.

[39] Z. H. Cho *et al. A Hybrid PET-MRI: An Integrated Molecular-Genetic Imaging System with HRRT-PET and 7.0-T MRI.* International Journal of Imaging Systems and Technology, 17(4):252–265, 2007.

[40] R. Slates *et al. Chemical Polishing of LSO Crystals to Increase Light Output.* Nuclear Science, IEEE Transactions on Nuclear Science, 47(3):1018-1023, 2000.

[41] N. J. Cherepy *et al. Scintillators with Potential to Supersede Lanthanum Bromide.* IEEE Transactions on Nuclear Science, 56(3):873-880, 2004.

[42] *Wrapping Scintillator Crystals to Optimize Light Collection.* SensL Technical Note.

[43] K. J. Hong *et al. Performance evaluation of a PET detector consisting of an LYSO array coupled to a 4x4 array of large-size GAPD for MR compatible imaging.* IOP Publishing Ltd and SISSA, 6:P05012, 2011.

[44] G. R. Gilmore *Practical Gamma-ray Spectrometry.* Nuclear Training Services Ltd, John Wiley & Sons: Warrington UK, 2008.

[45] *CsI(Tl) and CsI(Na).* ORTEC, AMETEC (Advanced Measurement Technology), 2007.

[46] *Radiation Background in a $LaBr_3$(Ce) Gamma-ray Scintillation Detector.* The radiation Safety Journal Health Physics, 101(6):703-708, 2011.

[47] E. S. Kurt, A. K. Eugene and P. U. Blass *Radiation Effects in Solids.* Springer, 2007.

[48] M. Zieblinski *et al. Testing of the PARIS LaBr3-NaI Phoswich Detector with High Energy Gamma-rays.* ACTA PHYSICA POLONICA B ,44(3):651-656, 2012.

[49] C. Jackson et al. *Ultra-low noise and exceptional uniformity of SensL C-Series SiPM sensors.* SensL, 2015.

[50] *B-Series Fast, Blue-Sensitive Silicon Photomultiplier Sensors; Datasheet* SensL Technical Documentation, 2013.

[51] *C-Series Low Noise, Blue-Sensitive Silicon Photomultipliers; Datasheet* SensL Technical Documentation, 2014.

[52] *MPPC (multi-pixel photon counter), S12572-010, -015C/P, Low afterpulses, wide dynamic range, for high-speed measurement, Photosensitive area: 3 × 3 mm, Datasheet* Hamamatsu, 2015.

[53] K. O'Neill and C. Jackson *SensL B-Series and C-Series silicon photomultipliers for time-of-flight positron emission tomography* Nuclear Instruments and Methods in Physics Research A, 787(2015):169-172, 2014.

[54] *C-Series Low Noise, Fast, Blue-Sensitive Silicon Photomultipliers; User Manual* SensL Technical Documentation, 2014.

[55] G. Collazuol *The SiPM Physics and Technology.* PhotoDet, LAL Orsay, 2012.

[56] P. Eckert *et al. Characterisation Studies of Silicon Photomultipliers.* Nuclear Instruments and Methods in Physics Research Section A 2.620:217-226, 2010.

[57] M. Petasecca *et al. Thermal and electrical characterization of silicon photomultiplier.* IEEE Transactions on Nuclear Science, 55(3):1686-1690, 2008.

[58] V.R. Vanin *et al. Table of radionuclide, Eu-152 decay scheme.* The National Laboratory Henri Becquerel, Atomic & Nuclear Data, 2001-2004.

[59] X. Chen *et al. Comparison of Digital and Analog Silicon Photomultiplier For Positron Emission Tomography Application.* IEEE Nuclear Science Symposium and Medical Imaging Conference (NSS/MIC), 1-7, 2013.

[60] *A software package for interactive graphical analysis of gamma-ray coincidence data(^{152}Eu Full-energy peak efficiency calibration)*; http://radware.phy.ornl.gov/gf3/gf3.html (Accessed: 12 June 2015).

[61] R. Emilie and S. R. Cherry *Application of Silicon Photomultipliers to Positron Emission Tomography.* Annals of Biomedical Engineering, 39(4):1358–1377, 2011.

[62] M. Ito *et al. Timing Performance Study of New Fast PMTs With LYSO for Time-of-Flight PET.* IEEE Transactions on Nuclear Science, 60(1):30-37, 2013.

[63] I. Deloncle *et al. Fast timing: Lifetime measurements with LaBr3 scintillators.* XVIII International School on Nuclear Physics, Neutron Physics and Applications, 205:012044, 2010.

[64] O.J. Roberts *et al. Development of a fast-timing LaBr3(Ce) array for NuSTAR.* Journal of Physics: Conference Series, 381:012124, 2012.

[65] Q. Peng, W.Choong and W. W. Moses *Evaluation of the Timing Properties of a High Quantum Efficiency Photomultiplier Tube.* IEEE Transactions on Nuclear Science, 60(5):3212–3219, 2013.

[66] S. Dolinsky, G. Fu, and A. Ivan.*Timing Resolution Performance Comparison for Fast and Standard Outputs of SensL SiPM.* IEEE Nuclear Science Symposium and Medical Imaging Conference (NSS/MIC), 1-6, 2013.

[67] E. Berdermann *et al. Time Resolution of Diamond Detectors for Relativistic Ions and Protons.* GSI Scientific Report, Instruments-Methods-09, 2009.

[68] K. O'Neill *et al. SensL New Fast Timing Silicon Photomultiplier.* International Workshop on New Photon-Detectors, Proceedings of Science, 2012.

[69] J. Y. Yeom *et al. Performance of Fast Timing Silicon Photomultipliers for Scintillation Detectors.* IEEE Science Symposium and Medical Imaging Conference (NSS/MIC), M13-2:2845-2847, 2012.

[70] D. R. Schaart *et al. LaBr(3):Ce and SiPMs for time-of-flight PET: achieving 100 ps coincidence resolving time.* Physics in Medicine and Biology, 55(7):N179-N189, 2010.

[71] P. S. Jeffrey *et al. Timing and Energy Resolution of new near-UV SiPMs coupled to LaBr3:Ce for TOF-PET.* IEEE Transactions on Nuclear Science, 61(5):2426–2432, 2014.

[72] *Timing and Coincidence Counting Systems.* Canberra Industries, 2010.

[73] P. Avella *et al. A study of timing properties of Silicon Photomultipliers.* Nuclear Instruments and Methods in Physics Research Section A, Detectors and Associated Equipment 695:257-260, 2012.

[74] L. Cosentino *et al. High-resolution Time-Of-Flight PET with Depth-Of-Interaction becomes feasible: a proof of principle.* 2012.

[75] *Mini Circuits VLM-52+ Limiter Technical Datasheet.*

[76] I. Krxysztof *Medical Imaging: Principles, Detectors, and Electronics.* John Wiley & Sons: The United States of America, 2009.

[77] H. Zumbahlen *Phase Response in Active Filters.* Analog Dialogue, 43-09, 2009.

[78] L. Convert *et al. Blood compatible microfluidic system for pharmacokinetic studies in small animals.* LabChip, 12:4683-4692, 2012.

[79] W.Hsiao-Ming *et al. In Vivo Quantitation of Glucose Metabolism in Mice Using Small-Animal PET and a Microfluidic Device.* The Journal of Nuclear Medicine, 48(5):837–845, 2007.

[80] L. Katz and A. S. Penfold *Range-Energy Relations for Electrons and the Determination of Beta-Ray End-Point Energies by Absorption.* Reviews of Modern Physics, 24(1):28-44, 1952.

[81] *The ESTAR program calculates stopping power, density effect parameters, range, and radiation yield tables for electrons in various materials.* Available at:physics.nist.gov/PhysRefData/Star/Text/ESTAR.html (Accessed: 11 February 2015).

[82] C. L. Woody *et al. A Study of Scintillation Beta Microprobes.* IEEE Transaction on Nuclear Science, 49(5):2208-2212, 2002.

[83] C. S. Levin *et al. Optimizing Light Collection from Thin Scintillators Used in a Beta-Ray Camera for Surgical Use.* IEEE Transactions on Nuclear Science, 43(3):2053–2060, 1996.

[84] *EJ-212 Plastic Scintillator Technical Data Sheet.* Eljen Technology, 2007.

[85] *PTFE AWG Series Sleeving.* Adtech Fluoroplastics Technical Data Sheet, 2007.

[86] B. E. Zimmerman, J. T. Cessna, and R. Fitzgerald *Standardisation of $^{68}Ge/^{68}Ga$ Using Three Liquid Scintillation Counting Based Methods.* Journal of Research of the National Institute of Standards and Technology (NIST). 13:265-280, 2008.

[87] *Yellow PEEK tubing; 0.006" (152.4μm) ID, 360μm OD.* Kinesis Scientific Experts, Technical Data Sheet, 2015.

[88] J. S'ebastien, S. Simon, D. Albertine, B. Ir'ene *GATE Training 12-14 February.* The OpenGATE collaboration, INSTN-Saclay, February (2013).

[89] *GATE User Guide V7.0* GATE collaborative documentation (2014).

[90] D. J. Van der Laan *et al. Optical Simulation of Monolithic Scintillator Detectors Using GATE/GEANT4.* Physics in Medicine and Biology, 55:1659-1675, (2010).

[91] ROOT User's Guide *ROOT Data Analysis Framework.* (2011).